# Hazards from catastrophic failure of high-pressure hydrogen storage

Donatella Maria Chiara Cirrone (BSc, MSc)

Faculty of Computing, Engineering and the Built Environment
of
Ulster University

Thesis submitted for the degree of Doctor of Philosophy
September 2018

I confirm that the word count of this thesis is less than 100,000 words excluding the title page, contents acknowledgements, summary or abstract, abbreviations, footnotes, diagrams, maps, illustrations, tables, appendices, and references or bibliography.

# Thesis outline

# Acknowledgments

I am grateful to a large number of people without whom I would not have been able to go through this PhD study.

First of all, I owe my deepest gratitude to my supervisors, Prof. Vladimir Molkov and Dr. Dmitriy Makarov. Without your continuous and extraordinary guidance, support and sometimes encouragement I would not have completed this study and most of all enjoyed it. Thank you for the chance to work with you at HySAFER and for everything you taught me about physics, CFD and life!

I would like to express my gratitude to Dr. Volodymyr Shentsov, whom I have considered an advisor, even if not written on paper. Many studies I have conducted during my PhD thesis were possible thanks to your help and collaboration.

I am grateful to all my colleagues at HySAFER and FIRESERT, in particular Dr Sergii Kashkarov, (almost Dr.) Konstantinos Chotzoglou, Dr. Mohammad Dadashzadeh, Harem Hussain, Wulme Dery, Dr. Brennan Sile and especially Dr. Svetlana Tretsiakova-McNally, without whom I would not have done my Master Thesis here and have the chance to come back for the PhD study. As promised, a particular thanks to Dr. Eleni Asimakopoulou, who assisted me in the printing/submission final rush.

It is a pleasure to thank all the friends I met here, the friends I left in Turin and the friends I left home.

I would like to express a huge thanks to my parents, brother and sister for all their love, encouragement and support. Thank you for everything you have given me not only during the last years but in all my life. Last but not least, I would like to thank Giuseppe, who has been always by my side, even if 2000 km apart!

# Abstract

This doctoral study investigates and closes a number of knowledge gaps identified in hydrogen safety engineering and associated with the employment of high pressure storage systems. Analytical and Computational Fluid Dynamics (CFD) models were implemented and developed to assess the hazards from catastrophic failure of high-pressure hydrogen storage, i.e. an event concerning "*failure of a vessel so severe to necessitate replacement or major repair*" (Smith and Warwick, 1983). The developed models were validated against experiments. Parametric studies were conducted where relevant to provide insights into the investigated phenomena and into the effect of sub-models and parameters, identifying appropriate numerical requirements for such modelling studies.

In case of release from a damaged tank or a Thermal Pressure Relief Device (TPRD), hydrogen is likely to ignite producing a jet fire, causing life-threatening conditions by the flame length and thermal radiation. A predictive CFD tool was developed and validated against experimental tests on hydrogen jet fires from several storage conditions, i.e. low temperature (48 K) and high pressure (900 bar). However, ignition delay of the jet may occur which produces a significant overpressure. Numerical simulations were conducted to investigate the formation of the turbulent non-uniform mixture and subsequent ignition for 200 bar and 40 bar releases. Two CFD approaches were proposed and their response tested.

A numerical study was conducted on ignition of a quiescent hydrogen-air mixture by spark discharge. The study provided insights into the flame kernel formation and propagation. A contemporary tool was developed for numerical evaluation of Minimum Ignition Energy (MIE).

In case of a continuous and/or established fire involving the tank, the TPRD activates venting the gas and preventing the catastrophic rupture of the tank. If it fails to activate and no adequate thermal protection is provided, the tank can catastrophically rupture with devastating blast wave and fireball. A CFD tool was developed to predict the associated hazards and it was validated against experiments on rupture of 70 MPa tanks.

Keywords: CFD, hydrogen safety, under-expanded jet, jet fire, spark ignition, delayed ignition, blast wave, fireball.

# Nomenclature

## Latin

| | |
|---|---|
| A | area ($m^2$) |
| $A_r$ | pre-exponential factor (consistent units) |
| $c$ | progress variable, speed of sound (m/s), specific heat (J/kg/K) |
| $C$ | capacitance (F) |
| $C^*$ | non-dimensional radiant power (-) |
| $C_d$ | discharge coefficient (-) |
| $C_{j,r}$ | molar concentration of the specie $j$ in reaction $r$ (-) |
| $c_p$ | specific heat at constant pressure (J/kg/K) |
| $C_{RNG}$ | RNG constant, $C_{RNG} = 0.157$ |
| $C_s$ | Smagorinsky constant, $C_s = 0.1$ |
| $C_\mu$ | k-ε turbulence model constant |
| $C_\xi$ | volume fraction constant, $C_\xi = 2.1377$ |
| $C_\tau$ | time scale constant, $C_\tau = 0.4082$ |
| $C_{1\varepsilon}, C_{2\varepsilon}, C_{3\varepsilon}$ | k-ε turbulence model constant (-) |
| $D$ | diameter (m), molecular diffusivity ($m^2/s$) |
| $d$ | distance (m) |
| $e$ | radiative emissive power ($W/m^2$) |
| $E$ | total energy (J/kg), expansion coefficient (-) |
| $E_r$ | activation energy for reaction $r$ (J/mol) |
| $Fr$ | Froude number |
| $G$ | generation term (consistent unit) |
| $g$ | acceleration due to gravity ($m/s^2$) |
| $h$ | enthalpy (J/kg) |
| $H(x)$ | heaviside function |
| $I$ | radiation intensity ($W/m^2$) |
| $k$ | turbulent kinetic energy ($m^2/s^2$), thermal conductivity (W/m/K) |
| $k_{f,r}$ | forward reaction rate (consistent units) |
| $k_{b,r}$ | backward reaction rate (consistent units) |
| $K_r$ | equilibrium constant of reaction $r$ (-) |
| $L$ | length (m), mean beam length (m) |
| $L_f$ | flame length (m) |
| $L_{IR}$ | infrared flame length (m) |
| $L_{sgs}$ | subgrid scale mixing length (m) |
| $L_{UV}$ | ultraviolet flame length (m) |
| $L_{vis}$ | visible flame length (m) |
| $\dot{m}$ | mass flow rate (kg/s) |
| $n$ | refractive index (-) |
| $N$ | number of chemical specie in the mixture (-) |
| $P, p$ | absolute, partial pressure (Pa) |
| $Pr_t$ | turbulent Prandtl number |
| $\dot{q}$ | heat flux ($W/m^2$) |

| | |
|---|---|
| $\vec{r}$ | position vector |
| $\hat{R}_{i,r}$ | molar rate of reaction for species *i* |
| $R_m$ | rate of species production/consumption source term (kg/m$^3$/s) |
| $Re$ | Reynolds number |
| $\vec{s}$ | direction vector |
| $Sc_t$ | turbulent Schmidt number (-) |
| $S$ | source term (consistent unit) |
| $S_E$ | source term for energy (J/m$^3$/s) |
| $\tilde{S}_{ij}$ | rate of strain tensor (s$^{-1}$) |
| $S_m$ | source term for specie (kg/m$^3$/s) |
| $S_{mass}$ | source term for mass (kg/m$^3$/s) |
| $S_{rad}$ | radiant power emitted by the flame (W) |
| $S_t$ | turbulent flame speed (m/s) |
| $S_u$ | laminar flame speed (m/s) |
| $t$ | time (s) |
| $T$ | temperature (K) |
| $t_f$ | flame residence time (s) |
| $ts$ | time step (s) |
| $U$ | velocity (m/s) |
| $u_{i,j,k}$ | velocity components (m/s) |
| $u'$ | velocity fluctuating component (m/s) |
| $V$ | voltage (V) |
| $W_f$ | flame width (m) |
| $X$ | distance (m), mean beam path length (m) |
| $x_{i,j,k}$ | spatial coordinates (m) |
| $\chi_{rad}$ | radiant fraction (-) |
| $Y$ | mass fraction (-) |

## Subscripts

| | |
|---|---|
| $0$ | initial condition |
| $ax$ | axial |
| $b$ | black body, buoyancy |
| $c$ | progress variable |
| $eff$ | effective |
| $fb$ | fireball |
| $fract$ | fractals |
| $fuel$ | fuel |
| $i,j,k$ | cartesian coordinates |
| $karl$ | Karlovitz |
| $lp$ | leading point |
| $m$ | index of chemical species |
| $N$ | actual nozzle |
| $r$ | reaction, reservoir |
| $rad$ | radiant |
| $S$ | surrounding air |
| $t$ | total, turbulent |
| $turb$ | turbulence |

| | |
|---|---|
| $u$ | unburnt |
| $\lambda$ | monochromatic quantity |

**Greek letters**

| | |
|---|---|
| $\alpha$ | gas absorptivity (-) |
| $\beta$ | extinction coefficient (1/m) |
| $\beta_r$ | temperature exponent of reaction *r* |
| $\Gamma$ | net effect of third bodies on the reaction rate |
| $\delta_{ij}$ | Kronecker symbol |
| $\Delta$ | local grid scale (m) |
| $\Delta H_c$ | heat of combustion (J/kg) |
| $\varepsilon$ | turbulent dissipation rate ($m^2/s^3$), emissivity (-) |
| $\Xi$ | turbulent flame speed wrinkling factor |
| $\eta'_{j,r}$ | rate exponents for reactant *j* in reaction *r* (-) |
| $\eta''_{j,r}$ | rate exponents for product *j* in reaction *r* (-) |
| $\vartheta$ | polar angle |
| $\kappa$ | absorption coefficient (1/m) |
| $\kappa_c$ | von Kármán constant, $\kappa_c = 0.4187$ |
| $\lambda$ | wavelength (m) |
| $\gamma$ | ratio of specific heats (-) |
| $\gamma_{j,r}$ | third body efficiency of species *j* in reaction *r* (-) |
| $\nu$ | kinematic viscosity ($m^2/s$), frequency (Hz) |
| $\upsilon'_{i,r}$ | stochiometric coefficients for reactant *i* in reaction *r* (-) |
| $\upsilon''_{i,r}$ | stochiometric coefficients for product *i* in reaction *r* (-) |
| $\xi$ | length scale of turbulent structures (-) |
| $\mu$ | dynamic viscosity (Pa·s) |
| $\mu_s$ | RNG SGS coefficient |
| $\mu_t$ | turbulent viscosity (Pa·s) |
| $\emptyset$ | shape factor (-), scattering phase function (-), azimuthal angle (-) |
| $\pi$ | pi number $\pi = 3.14$ |
| $\rho$ | density ($kg/m^3$) |
| $\sigma$ | Stefan-Boltzmann constant $\sigma = 5.67 \cdot 10^{-8} \frac{W}{m^2 K^4}$ |
| $\sigma_s$ | scattering coefficient (1/m) |
| $\psi$ | empirical coefficient for Karlovitz wrinkling factor (-) |
| $\Omega$ | solid angle (sr) |

**Bars**

| | |
|---|---|
| ‾ | Reynolds averaged parameter |
| ~ | Favre averaged parameter |
| * | fine scale parameter |
| ^ | Arrhenius reaction |

**Acronyms**

| | |
|---|---|
| AUSM | Advection Upstream Splitting Method |
| BLEVE | Boiling Liquid Expanding Vapor Explosion |
| CFD | Computational Fluid Dynamics |
| CFL | Courant-Friedrichs-Lewy number, $CFL = \frac{\Delta t \cdot u}{\Delta x}$ |

| | |
|---|---|
| CNG | Compressed Natural Gas |
| CPU | Central Processing Unit |
| CV | Control Volume |
| DO | Discrete Ordinates |
| DTRM | Discrete Transfer Radiation Model |
| EDC | Eddy Dissipation Concept |
| E-EWB | Efficient Exponential Wide Band |
| EOS | Equation of State |
| EWB | Exponential Wide Band |
| FCHV | Fuel Cell Hydrogen Vehicle |
| FCT | Fuel Cell Technology |
| FRR | Fire Resistance Rating |
| HSL | Health and Safety Laboratory |
| IE | Ignition Energy |
| IR | Infra-Red |
| LBL | Line By Line |
| LES | Large Eddy Simulation |
| LFL | Lower Flammability Limit |
| $LH_2$ | Liquified Hydrogen |
| MIE | Minimum Ignition Energy |
| MUSCL | Monotonic Upwind Scheme for Conservation Laws |
| PISO | Pressure-Implicit with Splitting of Operators |
| PRD | Pressure Relief Device |
| RANS | Reynolds Averaged Navier-Stokes |
| RMS | Root Mean Square |
| RNG | Renormalization Group |
| RTE | Radiative Transfer Equation |
| SIMPLE | Semi-Implicit Method for Pressure-Linked Equations |
| SNL | Sandia National Laboratories |
| STP | Standard Temperature Pressure |
| TD | Thermal Dose $((kW/m^2)^{4/3}s)$ |
| TDU | Thermal Dose Unit $((kW/m^2)^{4/3}s)$ |
| TI | Turbulent Intensity |
| TLS | Turbulent Length Scale (m) |
| TPRD | Thermal Pressure Relief Device |
| UDF | User Defined Function |
| URF | Under Relaxation Factors |
| UV | Ultra Violet |
| VLES | Very Large Eddy Simulation |
| VS | Volumetric Source |

# Publications

The results of the present research have been disseminated in the form of the following conference publications and presentations.

**Journal papers:**

- Cirrone, D., Makarov, D., Molkov, V. (2018), Thermal radiation from cryogenic hydrogen jet fires, *International Journal of Hydrogen Energy* [Accepted in August 2018]
- Cirrone, D., Makarov, D., Molkov, V. (2018), Simulation of thermal hazards from hydrogen under-expanded jet fire, *International Journal of Hydrogen Energy* [Accepted in August 2018]

**Conference papers:**

- Cirrone, D., Makarov, D., Molkov, V. (2018), Thermal dose in the near field of cryogenic hydrogen jet fires, *International Seminar on Fire and Explosion Hazards*, April 21-26, Saint Petersbourg, Russia
- Molkov, V., Cirrone, D., Shentsov, V., Dery, W., Makarov, D. (2018), Blast wave and fireball after hydrogen tank rupture in a fire, *11th International Colloquium on Pulsed and Continuous Detonations (ICPCD)*, September 17-21, St. Petersburg, Russia
- Cirrone, D., Makarov, D., Molkov, V. (2017), Thermal radiation from cryogenic hydrogen jet fires, *International Conference on Hydrogen Safety*, September 11-13, Hamburg, Germany
- Cirrone, D., Makarov, D., Molkov, V. (2017), Simulation of thermal radiation from hydrogen under-expanded jet fire, *International Conference on Hydrogen Safety*, September 11-13, Hamburg, Germany
- Shenstov, V., Cirrone D., Makarov, D., Molkov, V. (2016), Simulation of fireball and blast wave from a hydrogen tank rupture in a fire, *7th International Symposium on Non-equilibrium Processes, Plasma, Combustion, and Atmospheric Phenomena*, October, Sochi, Russia

**Communications at international conferences:**

- Cirrone, D., Makarov, D., Molkov, V. (2018), Numerical evaluation of MIE of hydrogen-air mixture, *Hypothesis XIII*, 24-27 July, Singapore

- Cirrone, D., Makarov, D., Molkov, V. (2017), CFD modelling of thermal hazards from cryogenic hydrogen jet fires, *H2FC SUPERGEN Researcher Conference*, 11-13 December, St. Andrews University, Scotland
- Cirrone, D., Makarov, D., Molkov, V. (2017), Simulation of cryogenic hydrogen jet fires, *IOP One-day meeting on current research in combustion*, 27 September, Imperial College, London, United Kingdom
- Cirrone, D., Makarov, D., Molkov, V. (2017), Thermal radiation from cryogenic hydrogen jet fires, *International Conference on Hydrogen Safety*, 11-13 September, Hamburg, Germany
- Cirrone, D., Makarov, D., Molkov, V. (2017), Simulation of thermal radiation from hydrogen under-expanded jet fire, *International Conference on Hydrogen Safety*, 11-13 September, Hamburg, Germany
- Cirrone, D., Shenstov, V., Makarov, D., Molkov, V. (2017), Thermal and pressure hazards in accidents with high-pressure hydrogen tank in a fire, *Hypothesis XII*, 28-30 June, Siracusa, Italy
- Cirrone, D., Makarov, D., Molkov, V. (2016), Numerical study of thermal hazards from hydrogen jet fires, *H2FC SUPERGEN Researcher Conference*, 12-14 December, Ulster University, Northern Ireland

# List of Tables

# List of Figures

# 1 Introduction

*Project background*

Hydrogen has been widely used in the process and energy industry. In recent years, the attractive idea of energy production with high efficiencies and without the consistent pollution resulting from combustion of hydrocarbon fuels has led to the development and improvement of the Fuel Cell Technology (FCT) employing hydrogen as a fuel for automotive applications. Many countries and organizations have launched programmes aimed to the enhancement and deployment of Fuel Cell Hydrogen Vehicles (FCHV) and the associated infrastructure. For instance, London has already employed a fleet of eight hydrogen fuel buses (tfl.gov.uk). Another example is given by the HyFIVE project, (hydrogen for innovative vehicles) which involves the deployment of 185 fuel cell vehicles and a network of hydrogen refuelling stations across Europe (www.hyfive.eu).

Hydrogen is odourless and colourless. In standard conditions hydrogen density is 0.084 $kg/m^3$. Therefore, hydrogen is generally stored as a compressed gas or as a liquid to achieve large capacities. The most common technique used to store hydrogen for stationary and automotive purposes is the high-pressure compression of the gas. The operating pressure can range in a wide interval according to the final employment, as reported in a recent study published in 2012 (Rawls et al., 2012). The vessels commonly used in the petroleum industry are designed to stand around 17 MPa, whilst pressures up to 70 MPa are employed in hydrogen-powered vehicles. This value could be even higher when dealing with fuelling stations, achieving values of 85 MPa (www.fuelcells.org). The installation of a non-reclosing thermally activated pressure relief device (TPRD) is required by Regulations to release the gas and prevent catastrophic rupture of the tank in case of a continuous/established fire involving the high-pressure hydrogen storage (ISO/TR 15869:2009 and GTR 2013).

Other properties distinguishing hydrogen from other fuels are a low minimum ignition energy (MIE=0.017 mJ) and a wider flammability range corresponding to 4-75% by volume of hydrogen in air (ISO/TR 15916, 2004). Because of these characteristics, an unintended release of hydrogen results in a serious danger of jet ignition and accident escalation. In addition, it must be considered that the high pressure of the containment system leads to different approaches and models for the study of the effects of the storage tank failure, preventing the use of models and engineering tools obtained and employed for low-pressure releases.

Furthermore, it should be considered that the development of the $H_2$ automotive sector involves the decentralization and diffusion of the facilities in an urban context with likely severe life safety and property protection issues in case of accident.

In case of release from a damaged tank or a TPRD, as well as in the case of full bore rupture of a pipeline, the released hydrogen is likely to ignite producing a jet fire. The consequent flame length can cover distances of tens of meters (Royle et al., 2011a), and cause life-threatening conditions by the flame itself and thermal radiation. If a delay occurs between the opening of the TPRD/beginning of the release and ignition, explosion hazards arise along with the above mentioned thermal hazards. The produced overpressure can be as high as 0.2 bar at 4 m from the ignition point (Takeno et al., 2007), which is enough to cause eardrum rupture according to the thresholds indicated by (LaChance et al., 2011). A further scenario to be considered involves the TPRD failure to activate and/or an inadequate thermal protection of the tank to withstand the fire. In this case the tank can catastrophically rupture with devastating blast wave, fireball and projectiles. The mentioned events are identified as catastrophic failures, according to the definition given by Smith and Warwick (1983): "*failure or destruction of a vessel or component so severe to necessitate replacement or major repair*".

Taking into account the considerations stated above, a thorough and comprehensive study has been conducted to help the understanding of the hazards associated to a hydrogen system catastrophic failure and to develop engineering tools to be used in hydrogen safety engineering. The final aim is to support the inherently safer deployment of high pressure hydrogen systems and infrastructure. The approach of this study is outlined below.

## *Organisation of the thesis*

The thesis consists of 8 chapters:

Chapter 1 provides an introduction to the topic, giving an overview of the hydrogen economy and the safety issues arising due to the growing associated infrastructure;

Chapter 2 is a literature review of the state of the art of hydrogen systems and associated infrastructure, the experimental studies and predictive tools currently available for the scenarios involving damage or rupture of such systems: unignited and ignited hydrogen releases, ignition of hydrogen-air mixtures, delayed ignition of high-pressure hydrogen releases and catastrophic rupture of the storage tank in a fire. The aim and objectives are formulated on the basis of the identified knowledge gaps and they are presented at the end of this chapter;

Chapter 3 provides a description of the CFD approach and sub-models implemented throughout the study;

Chapter 4 focuses on the development and validation of a CFD approach to model thermal hazards from free jet fires. Both "mildly" under-expanded cryogenic (P<6 bar) and high pressure under-expanded (P=900 bar) jet fires are investigated;

Chapter 5 presents the results of CFD simulations of spark ignition in a quiescent and stoichiometric hydrogen-air mixture, providing insights on the flame kernel formation and the calculation of MIE;

Chapter 6 aims at the development of a CFD tool to model dispersion of high pressure hydrogen jets and the overpressure produced by delayed ignition of such releases. The formulated CFD approaches are applied to releases from 200 bar and 40 bar storage tanks;

Chapter 7 proposes and validates a CFD model for prediction of the blast wave and fireball originated by rupture of high-pressure hydrogen storage tanks. The process of development of the CFD approach included preliminary evaluations on a 35 MPa tank rupture in a fire and tests on quasi 1D blast wave propagation;

Chapter 8 synthesises the research performed in the previous chapters, presenting the outcomes and conclusions of the PhD study.

# 2 Literature review

As a result of its reactivity and unique physical properties, hydrogen has been used for a wide range of applications, such as in chemical and petroleum industries. The processes often require high pressures and pure hydrogen to enhance reactions. Hydrogen is also employed in the metallurgical industry and nuclear power plants as chemical consumer or deactivator of oxygen (Ramachandran et al., 1998). Furthermore, hydrogen has been largely employed as fuel in the aerospace industry. Nowadays, the employment as a fuel is destined to widen, owing to the great and increasing development of the Fuel Cell Technology (FCT), which leads to the spread of new devices for the stationary energy production and for automotive purposes.

## 2.1 Hydrogen storage systems and associated infrastructure

The most common technique used to store hydrogen for stationary and transport purposes is the high-pressure compression of the gas. The vessels used for hydrogen containment are divided in four typologies: seamless vessels made of metal (type I), vessels made of metal with hoop wrapped resin filaments (type II), vessels made of metal matrix composite with fibre resin (type III) and composite vessels made of polymer liner with carbon fibre windings all over the cylinder (type IV) (Barthélémy, 2011). The different employed materials and designs address the choice of a certain vessel typology to its final use. Type II and type IV are suitable for high pressure operating conditions and when high resistance is needed, making them the obvious choice for automotive purposes. Thus far, the mainstream nominal working pressure employed in hydrogen-powered vehicles is either 35 or 70 MPa, with hydrogen as a compressed gas at ambient temperature; however, this value can be exceeded in the case of fuelling stations, achieving 85 MPa or even more (www.fuelcells.org). The necessity of high storage capacities, especially for stationary purposes, has led to the employment of super-insulated vessels storing hydrogen as cryo-compressed or liquid. The first storage option employs pressure ranging between 1 and 35 MPa and temperature <230 K, according to the classification suggested by BMW (Kunze and Kircher, 2012). Considering vessel pressure equal to 35 MPa, the storage density increases from 24 kg/m$^3$ to 41 kg/m$^3$ for a decrease of temperature from 288 K to 150 K. Values up to 82 kg/m$^3$ are reached for temperature down to 40 K. Liquid hydrogen tank pressures span from 0.1 to 1 MPa. Typical storage conditions are ambient pressure and temperature at 20 K, which corresponds to a density equal to 71 kg/m$^3$. The mentioned capacities make cryogenic and liquified hydrogen storage attractive for large fuelling stations (>400 kg/day) or transport trailers (~3500 kg of $LH_2$/trailer) (Kunze and Kircher, 2012). On the other hand, transport of hydrogen as compressed gas in tube trailers usually involves quantities of approximately 500-1000 kg for, respectively, container and tube

trailers. In this case the employed operating pressure is in the range 20-50 MPa (Adolf et al., 2017). Hydrogen transport can also take place through carbon steel pipeline networks. Rawls et al. (2012) study reported an existing network of about 3200 km, operating at pressures up to 10 MPa. Gerboni and Salvador (2009) used for their studies on hydrogen pipelines pressures of 10, 20 and 50 bar for respectively 0.2, 0.3 and 0.7 m diameters.

## 2.2 Gaseous hydrogen releases

### 2.2.1 Under-expanded jet theory

At the operating pressure mentioned in Section 2.1, a release from the hydrogen storage system originates an under-expanded jet. At the nozzle exit, velocity is sonic, and pressure is higher than the atmospheric one. The critical pressure ratio for sonic flow at the nozzle is 1.9 for STP conditions, as calculated from the following equation:

$$\frac{P_R}{P_N} = \left(\frac{\gamma+1}{2}\right)^{\frac{\gamma}{\gamma-1}} \tag{2.1}$$

where $P_R$ is the pressure in the storage vessel, $P_N$ is the pressure at the nozzle and $\gamma$ is the specific heats ratio. However, the critical pressure ratio can be up to 4.1, as observed by Ishii et al. (1999) for diatomic gases jets characterised by $\gamma$=7/5. Deviation from ratio 1.9 can be attributed to the losses in the release tube between the high and low-pressure chambers, as discussed in (Molkov, 2012).

Since pressure at the nozzle exit is higher than ambient, the gas must expand outside the nozzle, forming a series of shock waves while reaching the atmospheric pressure. The shock waves originated by the expansion, reflect on the flow boundary free surfaces, conjoining and forming a barrel shock culminating in a Mach disk. After crossing this area, the flow Mach number becomes lower than 1 in the core of the jet while it is higher than 1 in the layer surrounding it. The numerical studies reported in (Molkov, 2012) showed that if the critical pressure is below 40 MPa, the jet presents a repetition of the described pattern, denominated diamond structure. This condition was not observed for ratios above 40 MPa.

Several theories have been developed to simplify the above process for engineering calculations. Birch et al. (1984) described the gas behaviour and concentration decay through an expanded jet originated by a corresponding source, called pseudo-diameter or notional nozzle, which dimensions depend on the storage conditions. Indeed, it corresponds to a nozzle with section equal to the area occupied by the mass flow rate released from the real nozzle with uniform sonic velocity at ambient temperature and pressure. The scheme of the under-expanded jet and the related nomenclature are given in Figure 2.1. Birch et al.'s (1984) results

have shown that the concentration decay trend was well represented considering the fictional nozzle value in the equation for expanded releases and an entrainment constant of 4.9. In a following study, published in 1987, the new experimental data led to a different constant, 5.4, and the notional nozzle evaluation included the conservation of momentum in the expansion region (Birch et al., 1987). Whilst Birch et al. (1987) described the gas behaviour as ideal, Schefer et al. (2007) used a similar approach introducing the Abel-Noble equation of state to take account of the non-ideal behaviour of the gas given the high storage pressure.

The methodology elaborated in Molkov et al. (2009) also employs the Abel-Noble equation of state. The flow at the actual nozzle is chocked. Then it undergoes an isentropic expansion to the notional nozzle, where ambient pressure and uniform velocity equal to the local speed of sound are reached. The system of equations to evaluate the flow characteristics is closed by the conservation of mass and energy. A complete description of the model is available in the referred publication.

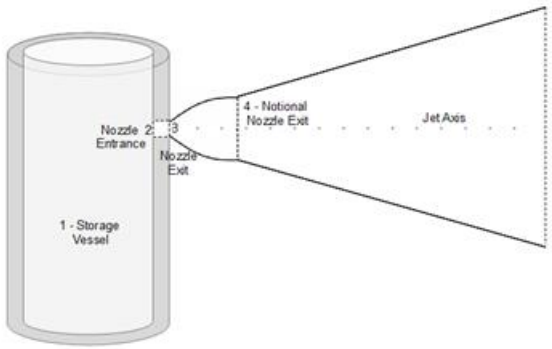


Figure 2.1 The under-expanded jet scheme

### 2.2.2 Numerical studies on under-expanded jets

Capturing the shock structures may be a problem in numerical simulation of under-expanded jets. Cumber et al. (1995) used an adaptive finite-volume grid algorithm to capture the shock waves, obtaining the grid independency when decreasing the grid spacing from 1/32 to 1/64 of the diameter. Taira et al. (2015) suggested that the diameter should be subdivided in at least 13 nodes to correctly describe the diffusion process of a release at the sonic speed. Another numerical study (Xu et al., 2005) solved the under-expanded zone close to the orifice using a RANS simulation on a 200,000 control volumes unstructured grid with extension of the cylindrical domain equal to 0.5 m as diameter and 0.8 m as axial extension. The results are in line with the experimental observation, but the authors also noticed the presence of air entrainment, which is neglected in the pseudo-source model. Afterwards, the outcomes have been used as input parameters for a LES modelling of the remaining part of the jet.

As shown from the mentioned studies, the reproduction of highly under-expanded jets requires a high level of grid refinement and consequent long calculation time. This may become impractical when the object of the study extends to the far field zone of the jet, as in the study of jet fires with length achieving distances up to 10 m. Thus, several studies have implemented the notional nozzle approach to provide the boundary conditions to CFD simulations. Brennan et al. (2009) successfully reproduced the length and width of the jet fires presented by Schefer et al. (2007). Papanikolau et al. (2012) have studied the performances of three turbulence models using several notional nozzle approaches to represent a set of experiments they have conducted. During the study it was observed that, for the same turbulence and notional nozzle approach, the prediction capability worsen as the release diameter decreases. The results have shown that the hydrogen concentration was better predicted by the SST turbulence model, while the k-ε model performance was the worst. On the other hand, k-ε model had better prediction capability when analysing the flow velocity and the approach proposed by Birch et al. (1984) was employed. Pope (1978) discussed the k-ε turbulence model limited capability to reproduce correctly the spreading rate of axisymmetric jets. The physical explanation given by the author is that the vortex stretching causes a decrease of the effect of viscosity and consequently a lowering of the spreading rate in comparison to plane jets. The spreading rate definition is given by Papanikolau et al. (2012) as "the value of radial distance from the centreline where hydrogen mass fraction and velocity are half of their centreline values". Owing to the previously mentioned physical considerations, Pope proposed and justified a modified expression for the dissipation equation, which is based on the introduction of a new constant $C_{\varepsilon 3}$ equal to 0.79, evaluated fitting the experimental observations made by the author.

### 2.2.3 Similarity law for concentration decay in unignited under-expanded jets

The major risk related to unignited gaseous jet is the formation of a flammable hydrogen-air cloud, which constitutes a serious danger of jet fires, deflagration and detonation. Thus, it is of primary interest to have a tool able to evaluate the distances where the dangerous hydrogen concentration in air is achieved. Chen and Rodi (1980) developed a similarity law for evaluation of the axial concentration decay in expanded jets, showing that for round jets, the mass fraction $C_{ax}$ at a given distance x is linearly proportional to the orifice diameter D:

$$\frac{C_{ax}}{C_N} = 5.4\sqrt{\frac{\rho_N}{\rho_S}}\frac{D}{x} \tag{2.2}$$

where $\rho_N$ and $C_N$ are the density and concentration at the nozzle, and $\rho_S$ is the ambient density. Molkov et al. (2012) validated the similarity law by Chen and Rodi (1980) for momentum controlled expanded and under-expanded jets, providing that the density at the nozzle is calculated according to the under-expanded jet theory presented in (Molkov et al., 2009).

Based on the validation, a simple and effective engineering tool was developed under the form of a nomogram for the concentration decay calculation. The diagram is shown in Figure 2.2. The inputs for the distance evaluation are the density at the nozzle exit and the diameter of the leak. The former parameter can be evaluated from the bottom diagram shown in the same graph. A practical example is presented by the author himself for the evaluation of the distances for the hydrogen concentrations in air: 4 % and 11%.

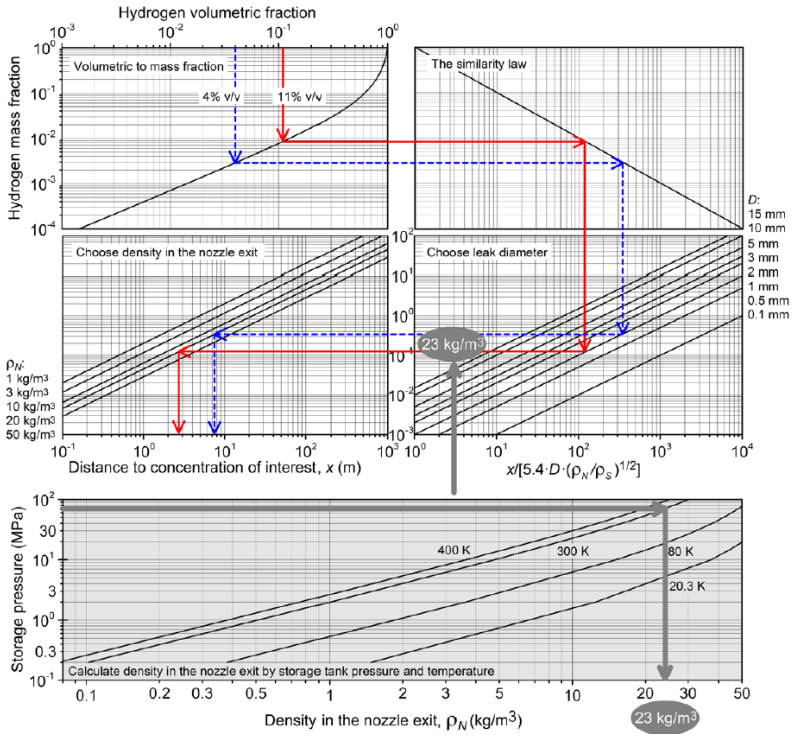


Figure 2.2 Nomogram for calculation of concentration decay for hydrogen jets (Molkov, 2012).

## 2.3 Ignition of hydrogen-air mixtures

Hydrogen has some peculiar characteristics, distinguishing it from other fuels, such as its low value of minimum ignition energy (MIE) and wide range of flammability. The ISO reported 0.017 mJ as the lowest value of MIE for a hydrogen-air mixture close to the stoichiometric composition. Other flammable gases, such as methane or ethane, are usually characterised by MIE greater than 0.1 mJ (Lewis and Von Elbe, 1961). The flammability limits for hydrogen in air are 4% and 75% by volume (ISO/TR 15916, 2004). However, the former limits are strictly influenced by the apparatus adopted to determine them and the gas temperature, as shown by Coward and Jones' study (1952). Therefore, an unforeseen release of hydrogen in air can easily ignite. Research by Astbury et al. (2007) analysed the 81 incidents involving hydrogen releases reported by the Major Hazard Incident Database Service (MHIDAS). The totality of the releases involved combustion and only 5% of them recorded a delay in ignition.

However, it has to be considered that the database regards only the major incidents, thus, unignited releases might have not been recorded as not leading to major hazards. Furthermore, the authors report that it was not possible to establish the ignition cause in 86% of the events, conversely to the 65% of other flammable gaseous releases. This confirms the different propensity of hydrogen releases to ignite. An exhaustive analysis of hydrogen ignition mechanisms is given in Astbury et al. (2007). The present section will focus on ignition by spark discharge.

### 2.3.1 Ignition by spark discharge

As reported by Kumamoto et al. (2011), spark capacitive discharge is the most common technique to determine MIE for flammable mixtures in experiments. From a safety point of view, it is the most common type of electrostatic discharge associated to ignition hazards (Pratt, 2000). Furthermore, the deployment of hydrogen-powered vehicles rises the importance of conducting studies on electrostatic discharge hazards. The energy released by a spark can be evaluated as $E=(CV\text{^}2)/2$, where $C$ is capacitance and $V$ voltage. Two phases can be individuated in spark discharges (Figure 2.3). The first phase is called "capacity component". It is characterised by the discharge of potential of several thousand volts during a very short period. In the following phase, denominated "inductance component", energy is released at a lower and approximately constant potential for a longer period. Several authors have investigated which component gives the greater contribution to ignition. However, experimental evidence has led to the conclusion that each component can equally contribute as long as energy is sufficient to obtain ignition (Terao, 2007).

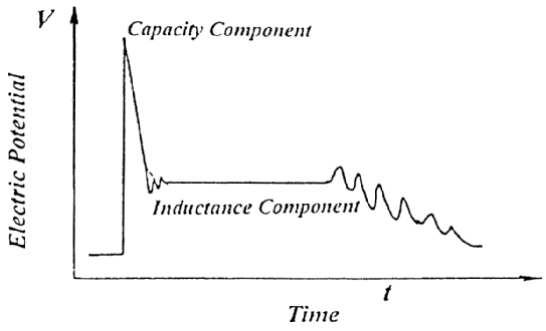


Figure 2.3 Electric potential variation between discharge electrodes through induction coils (Terao, 2007)

During the first stage of the capacitive discharge, a plasma channel with diameter of order of magnitude about 50 μm forms between the electrodes. This brief stage (about 1-10 ns) is denominated breakdown phase and it is characterized by high level of ionization and dissociation of molecules and high temperature (up to 60000 K). A shock wave is produced by the strong expansion of the discharge zone. Due to the high conductivity of plasma, the

voltage imposed by the circuit in the gas decreases. Diffusion and conduction in the electrodes start to dominate the process, initiating the arc phase, which is characterised by lower temperature (~6000 K) and ionization level (~1%). The final stage is denominated glow phase, which corresponds approximately to the inductance component of the discharge and is characterised by longer durations with order of magnitude of 1 ms. Gas temperature decreases to about 3000 K along with the ionized molecules (HySafe, 2007). For the exact determination of MIE it is important to highlight the possible presence of losses in the circuit resistance. Roth et al. (1951) measured that 95% of the nominal energy was released into the gas. Later studies correlated the energy delivered in the spark to the resistance. It was found that the energy increases with the increase of resistance, although not monotonically and that the optimal resistance to minimize losses depends on the discharge duration. For instance, Rose and Priede (1958) found that, maintaining a capacitance of 5pF, the delivered energy increased from 50% of the stored energy to 90% when the resistance was changed from 50 Ω to 100 Ω. On the other hand, Ono et al. (2007) observed that in all their experiments more than 99% of the stored energy was discharged.

### 2.3.2 Minimum ignition energy

MIE of a hydrogen-air mixture depends on numerous factors. First of all, the hydrogen concentration causes the MIE to vary from 0.017 mJ in proximity of the stoichiometric composition to infinite towards the lower and higher flammability limits. A second parameter to consider is the oxygen content in the mixture. This parameter rises in significance in the case of spurious $LH_2$ or cryogenic releases, where the oxygen boiling temperature higher than nitrogen may cause a local enrichment of oxygen in the mixture. Kumamoto et al. (2011) measured a decrease of MIE to 0.0057 mJ for air containing 35% by vol. of oxygen. It was not possible to measure the corresponding value for hydrogen combustion in oxygen as it was below the minimum limit of energy supplied by their experimental apparatus. Kuchta (1986) reported that it can be as low as 0.0012 mJ. The presence of humidity in air was found to not significantly contribute to the MIE. Ono et al. (2007) showed that hydrogen in dry air presented slightly lower MIE compared to air with 90% relative humidity. The same authors presented a comparison of their MIE measurements with previous studies conducted by Lewis and von Elbe (1951) and Calcote et al. (1952), observing up to twice difference for lean mixtures. This discrepancy may be originated by differences in the experimental apparatus, such as the electrodes distance or material. Effect of gap distance for needle to needle electrodes was analysed by Ono et al. (2007) and is represented in Figure 2.4. It can be observed that MIE decreases with the shortening of distance between the electrodes, until a minimum is reached for 0.5 mm. A further decrease in gap distance causes an increase of MIE, highlighting that

not enough mixture is excited by the spark and there is a greater contribution of losses to the electrodes.

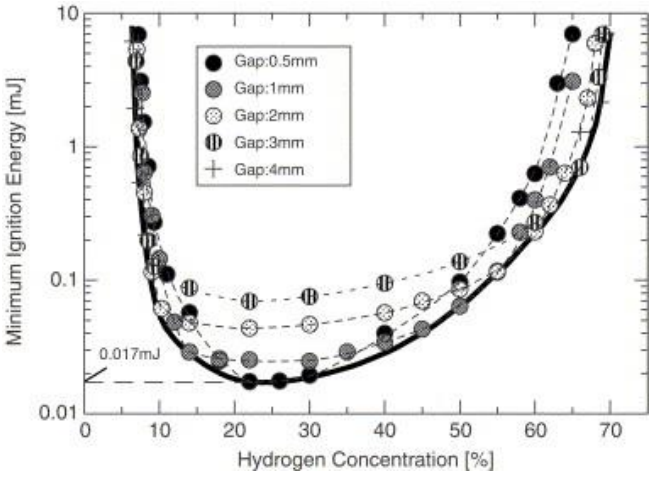


Figure 2.4 Effect of gap distance on MIE (Ono et al., 2007)

### 2.3.3 Numerical studies on spark ignition and MIE evaluation

Numerical reproduction of spark ignition processes represents an arduous challenge due to the interaction of complex processes such as plasma kinetics, presence of high temperatures and large gradients, chemical kinetics, molecular transport, short processes duration etc… One of the earliest studies on spark ignition modelling was carried out by Frendi et al. (1990) on methane-air mixtures, employing only a 1-step chemical reaction and neglecting any radiation or heat losses. The latter assumption might have been the cause of their MIE estimation 70 times lower than the experimental value for a kernel radius of about 63 μm and 27.5 μs as duration of the spark. Better agreement was found for a kernel radius of 0.5 mm. Thiele et al. (2002) investigated both experimentally and numerically the transition from spark kernel to flame propagation in hydrogen-air mixtures. The authors observed that for a spark arc release with duration 50 μs, an initial phase lasting approximately 80 μs is dominated by the expansion of the high temperature spark kernel. Afterwards, the flame kernel detaches from the spark core, moving with flame propagation speed. The transition phase was well reproduced by their 2D numerical model, which couples equations for reacting flow, composed by 9 species for 38 elementary reactions, to electrodynamics of the spark. The authors further analysed the losses to the electrodes, concluding that up to 130 μs they do not affect the simulation results, conversely to other factors such as the electrodes geometry or spark intensity. A more detailed chemical kinetics model has been employed by Han et al. (2011) in their study on calculation of MIE: 53 species and 325 elementary reactions. The authors found that the energy supply procedure significantly affect the MIE calculation, in opposition to what was observed previously for methane-air mixtures. The electrode size was found to affect the estimated MIE only for gap lengths within the quenching distance. However, the calculated MIE for a

stoichiometric hydrogen-air mixture overestimated by over 135% the experimental measurement. Hence, further numerical studies are needed to address a more accurate and conservative calculation of MIE to be used in hydrogen safety engineering. Owston and Abraham (2009) extended the study of spark ignition to stratified hydrogen-air mixtures, observing that, after an initial transient and provided that enough energy to ignite the mixture has been released, the flame propagation is not affected by the spark intensity and location in the mixture.

## 2.4 Free hydrogen jet fires

The main events involving flames in gaseous hydrogen applications are jet flames and fireballs. As suggested by Lees (1996), it is crucial to characterise the flames in terms of shape and dimensions, heat release rate, radiative fraction, temperature, surface emissive power and location/arrangement of the target. The present section will focus on the characterisation of jet flames according to the above listed parameters.

If ignited, the gaseous hydrogen release from damaged high-pressure storage originates a non-premixed (diffusion) jet flame characterized by momentum-dominated regime. The flame jet release is likely characterised by a consistent length. An experimental study on hydrogen jet flames conducted in 2011 reported that an 11 m long flame was produced by the 9.5 mm diameter release from a 205 bar storage (Royle and Willoughby, 2011a). Earliest studies on diffusion jet flames were conducted by Hottel and Hawthorne (1949), characterising the transition from laminar to turbulent flames. The authors concluded that the flame length is proportional to the nozzle velocity in laminar flames, whereas it is proportional to only the nozzle diameter when the nozzle velocity is great enough to produce a turbulent jet.

### 2.4.1 Flame length and width

Schefer et al.'s (2006) evaluation of the flame length recalls the observations and correlations developed by Delichatsios (1993) for turbulent jet flames, as reported by the authors. The experiments made on 7.94 mm and 1.91 mm diameters outlined that the flame length is well represented by the correlations developed for other fuels and based on the Froude number and a non-dimensional flame length. Hydrogen flames can be non-luminous. The condition might be different when dust or other particles are entrained in the flame. Thus, the visible flame length results are different from the one individuated through thermal cameras. This is well shown in Figure 2.5 for a jet fire studied at the HSL facility (Moonis et al., 2010).

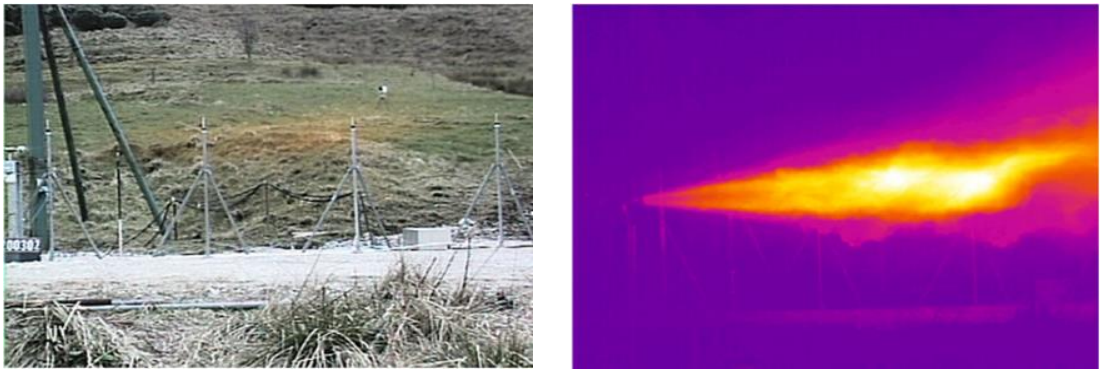

Figure 2.5 Comparison between the visible flame (left) and the flame extent obtained through thermal imaging (right) (Moonis et al., 2010)

Schefer et al.'s (2006) investigated the flame length using UV and IR images, finding out that the IR flame length is longer than the visible flame length ($L_{vis} = 0.88\ L_{IR}$) and that the width can be evaluated as $0.17\ L_f$, confirming the experimental results of Turns and Myhr's study (Turns and Myhr, 1991). The UV length has been found to be $0.78\ L_{IR}$. According to the authors, the difference is consistent with the consideration that $L_{IR}$ should indicate the flame portion where the high temperature combustion products are located and $L_{UV}$ the area where the oxidation is mainly taking place. Hawthorne et al. (1949) noted that the visible flame length was 10% greater when observed in a darkened room. A following study conducted in 2007 (Houf et al., 2007) confirmed the same flame width correlation ($0.17\ L_f$) observed by Schefer et al. (2006). In Mogi and Horiguchi' s research, the correlation has been found to be approximately $0.18\ L_f$, in agreement with the studies mentioned above (Mogi and Horiguchi, 2009). The authors also concluded from their experiments that the flame length is proportional to both the release diameter and spouting pressure. However, if the pseudo-source is considered, the flame length is influenced only by the pseudo nozzle diameter. A following study (Proust et al., 2011) investigated the flame geometry of the releases produced by a 25 l storage system at 900 bar and different release diameters: 1, 2 and 3 mm. The authors observed that the flame lengths were well represented by the correlations proposed by the previous mentioned studies (Schefer et al., 2006 and Mogi and Horiguchi, 2009) for the smaller diameters but they incurred in significant overestimations for the 3 mm release.

Molkov and Saffers (2011) have proposed a novel correlation for the evaluation of the flame length with respect to the previous correlation depending only on the Froude number. The innovation is given by the consideration of the Reynolds and Mach number and by the use of the actual nozzle parameters rather than the notional nozzle. The similarity group, indicated as X in Figure 2.6, is expressed as function of Reynolds number (Re) and the Froude number (Fr) in the following equation:

$$\frac{\rho_N}{\rho_S} \cdot \left(\frac{U_N}{C_N}\right)^3 = \frac{g \cdot \mu_N}{\rho_S \cdot {C_N}^3} \cdot Re \cdot Fr \tag{2.3}$$

The flame length is hence correlated to the ratio of the densities at the actual nozzle, $\rho_N$, and of the surrounding air, $\rho_S$, times the ratio at the third power of the velocity at the actual nozzle, $U_N$, and the corresponding velocity of sound $C_N$. The other parameters presented in Equation (2.3) are the gravity acceleration, $g$, and the dynamic viscosity, $\mu_N$.

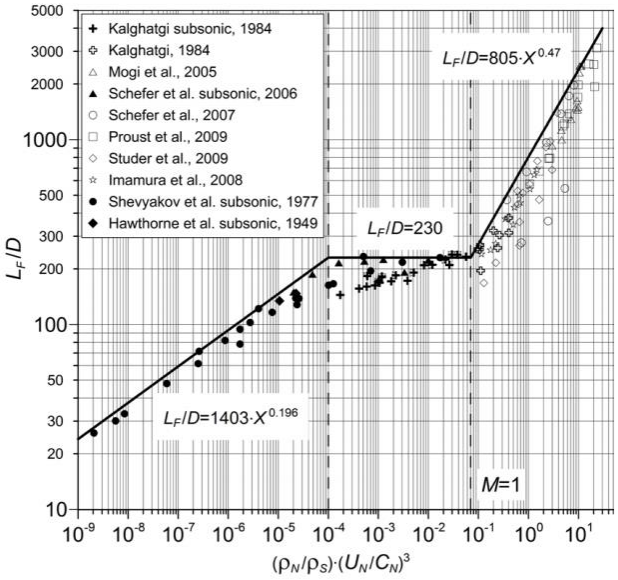


Figure 2.6 The dimensionless correlation for hydrogen jet flames (Molkov and Saffers, 2011)

2.4.1.1 Numerical investigations on turbulent free jet flames

The LES modelling implemented by Brennan et al. (2009) used the mixture fraction approach to investigate the flame length of jet fires. The heat losses were not considered in the simulation. The comparison between the numerical and the experimental results from Schefer et al. (2007), showed that a good agreement has been achieved using a turbulence intensity of 25% and turbulent length scale equal to 7% of the equivalent diameter. However, the variation of turbulence intensity in the range 0-20% had limited influence on the resulting flame length and width, showing that for values below 20%, turbulence developed in the flow overcomes the turbulence level applied at the release nozzle. The same experiment has been numerically reproduced by Houf et al. (2009) using a RANS approach. In this case, the heat losses have been considered coupling a discrete ordinates radiation model. The calculated temperature on the jet axis was compared to experiments. Better predictions were given by RNG k-ε turbulence model rather than standard k-ε model for a turbulent intensity equal to 20%. Zheng et al. (2012) studied the jet fires experimented by Schefer et al. (2007) through the k-ε model for the high Reynolds number region and using a weight function when switching to the k-ω

turbulence model in the near wall zone. The final prediction showed good agreement with the experimental result. The model has then been applied to several discharge pressures, varying from 10 to 40 MPa.

### 2.4.2 Temperature distribution

The presence of the jet flame obviously influences the temperature distribution in its surroundings and leads to the production of hot air currents that could be very dangerous for whom is exposed. Molkov (2012) analysed the temperature distribution along the jet trajectory measured in the experiments made by Barlow and Carter (1996), Imamura et al. (2008) and LaChance (2010). The distance from the release is normalized by the flame length and the resulting temperature profile is shown in Figure 2.7. The study also correlates the temperature distribution to the following proposed harm criteria for people:

- "no harm" limit: 70°C for any exposure duration;
- "pain" limit: 115°C for 5 minutes exposure;
- "death" limit: 309°C, third degree burns for 20 s exposure.

As shown in Figure 2.7, the death limit condition is achieved at a distance (x) equal to twice the flame length ($L_f$), the pain limit at x=3$L_f$ and the no harm limit at 3.5$L_f$. If the thermal hazard related to the distribution of temperature along the jet trajectory is well investigated and defined, to the author's knowledge, there is not a model or experimental investigation about the temperature rise around the jet flame axis.

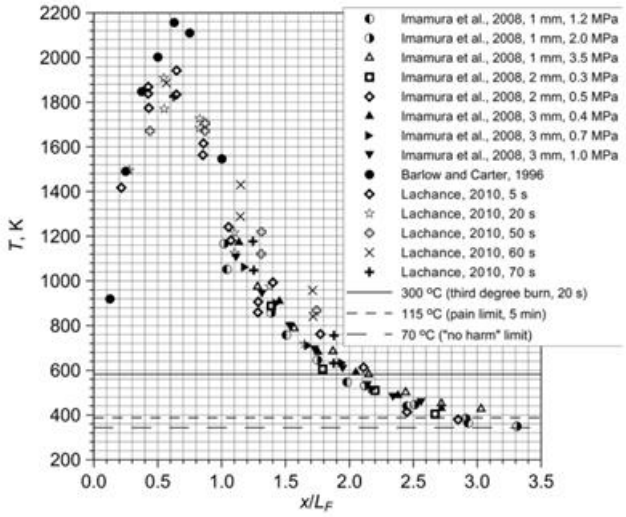


Figure 2.7 Temperature distribution along the jet axis in hydrogen jet fires (Molkov, 2012)

### 2.4.3 Thermal radiation

The main studies on flames non-premixed combustion have regarded fires characterised by limited size, in order to be investigated in laboratory facilities. The actual employment of

hydrogen as a fuel might lead to higher characteristic length of jet fires. In this scenario, the contribution of heat transfer exchange modality will be different from the small scale flames. SFPE Fire Protection Handbook (2002) indicates that the thermal radiation is the dominant contributor for fires with characteristic length higher than 0.2 m. A similar conclusion has been achieved by Frank et al. (2000), who reported that for distances greater than 40D the heat losses due to radiation affect significantly the temperature distribution in the flame. Yeoh et al. (2009) indicated that radiative heat transfer becomes increasingly dominant for temperature higher than 400°C. Houf and Schefer (2007) assessed that radiation is the primary heat transfer mechanism when dealing with hydrogen gaseous flames. The radiation is defined in terms of wavelengths (λ) and frequency $\nu$ (Hz). Thermal radiation wavelengths range approximately from 0.1 μm to 100 μm, covering the infrared, visible (0.4 -0.7 μm) and a portion of the ultraviolet spectrum range (Howell et al., 2016). Thus, a monochromatic treatment would be the most precise way to deal with radiative properties and quantities. However, a first analysis can be done on the main radiative transfer laws considering the integration over the whole spectrum and the idealized bodies, as the black body which emits the maximum energy at a defined temperature T, called the total emissive power, evaluated through the Stefan-Boltzmann equation:

$$e_b(T) = n^2 \sigma T^4 \tag{2.4}$$

where n is the refractive index and $\sigma$ is the Stefan-Boltzmann constant. Equation (2.4) can be further simplified considering n=1, realistic condition in most of all the engineering applications (Lees, 1996). By definition, the black body is a perfect absorber and radiator of energy. The introduction of the gray body assumption, which properties are independent of wavelength, and emissivity (also named emittance by Modest, 2003) allows to quantify how the real emitting body differs from the black body through the correlation $\varepsilon = e/e_b$. Hence, the total radiation emitted by a gray body per unit of area (W/m$^2$) is evaluated as $e = \varepsilon \sigma T^4$.

The heat flux, $q$, received by a target at distance $r$ from the body emitting $e$ is evaluated considering the geometrical disposition of the emitter and the receiver through the so-called shape factor or configuration factor, $\emptyset$, (Drysdale 2011):

$$\dot{q} = \emptyset \, e \tag{2.5}$$

The study of burning or hot gases poses new issues on the radiation evaluation. First of all, not all the components of the gas mixture under study give the same contribution when interacting with thermal radiation. For instance, water vapour is the main source of radiation from gaseous hydrogen flames (Schefer et al., 2007). Secondly, the molecules are characterised by a finite

number of energy state levels. Only photons defined by certain energy, so specific wavelengths and frequencies, will be able to change the internal energy of the molecular gas. This peculiar feature causes the great discontinuous distribution of their radiative properties in the spectrum, making the radiative properties, such as the emissivity, deeply dependent on the wavelength considered. In the case of water vapour, the significant bands are centred at 1.4 – 1.9 – 2.7 – 6.3 -10 $\mu m$ (Coppalle and Vervisch, 1983). According to Hottel and Sarofim (1967) the principal radiation bands are 2.55-2.84, 5.6-7.6, 12-25$\mu m$, range confirmed by Taylor and Foster (1974). Few data are available on the contribution of each band to the measured heat flux. Gore et al. (1987) observed from their investigations that 6.3 $\mu m$ band can weight up to the 30% the overall heat flux, while bands at more than 10 $\mu m$ did not significantly contribute to the heat flux. Hence, a monochromatic study would be more suitable. Also the consideration of constant temperature in Equation (2.5) might lead to miscalculations, since as it has been shown in Figure 2.7, temperature varies substantially along the jet axis and, thus, inside the flame. Furthermore, the burning gases are not generally characterised by a certain shape or emitting surface. They are rather characterised by complex geometries, making arduous the evaluation of the correct shape factor.

In participating media, the radiation might be absorbed, emitted or scattered, attenuating it while passing through the body, making the radiative properties dependent on the "depth" of the body or the "path length" that a photon might cover. Precisely, the initial radiation intensity, $I_{\lambda,0}$, decreases by a factor $\exp(-\beta_\lambda x)$, where x is the mean beam path length (or mean free path as defined by Modest (2003)) and $\beta_\lambda$ is the extinction coefficient, sum of the absorption and scattering coefficients, respectively, $\kappa_\lambda$ and $\sigma_{s,\lambda}$. Assuming that scattering is negligible, the monochromatic absorptivity of the gas can be defined as the ratio of the absorbed radiation intensity to the total amount:

$$\alpha_\lambda = \frac{I_{\lambda,0} - I_{\lambda,x}}{I_{\lambda,0}} = 1 - e^{-\kappa_\lambda x} \tag{2.6}$$

Recalling Kirchhoff's law, the monochromatic emissivity will be defined as:

$$\varepsilon_\lambda = 1 - e^{-\kappa_\lambda x} \tag{2.7}$$

Generally, the term $\kappa_\lambda x$ is defined as the optical path-length or opacity (SFPE, 2002), leading to the definition of optical thickness. According to Tien et al. (2002), the medium can be considered as optically thin if $\kappa_\lambda x \ll 1$; according to the authors, the penetration of the beam ray is of the same order as the characteristic length of the medium. Thus, the gas starts to behave as a non-participating medium and the emissivity can be approximated equal to the optical path-length. If $\kappa_\lambda x \gg 1$, the medium is considered optically thick, indicating that the

penetration of the beam ray is much shorter than the characteristic length of the medium. Thus, the transmitted portion of radiation decreases as the optical thickness increases. The same definition is proposed by (Howell et al. 2016).

The radiative heat transfer in a participating medium is governed by the local intensity balance, expressed through the Radiative Transfer Equation (RTE):

$$\frac{dI_\lambda(\vec{r},\vec{s})}{ds} = -\left(\kappa_\lambda + \sigma_{s,\lambda}\right) I_\lambda(\vec{r},\vec{s}) + \kappa_\lambda\, I_{b,\lambda}(\vec{r}) + \frac{\sigma_{s,\lambda}}{4\pi}\int_{4\pi} \phi\,(\vec{s}',\vec{s})\, I_\lambda^-(\vec{s}')d\Omega' \tag{2.8}$$

where the first term on the right side of the equation represents the reduction of intensity due to the absorption ($\kappa_\lambda$) and scattering ($\sigma_{s,\lambda}$) of the incident radiation, the second term indicates the gain of energy due to the emission of radiation from the body at temperature T and the third term indicates the gain of energy due to the inscattering phenomena, i.e. when the radiation is scattered in such a way it is addressed to the direction $\vec{s}$ of interest. The scattering phenomenon is usually negligible compared to absorption (Hubbard and Tien, 1978) and this assumption is reasonable in hydrogen combustion modelling, where the production of soot (main scattering cause) is limited, if not totally inexistent.

The Radiative Transfer Equation (RTE) is characterised by a high grade of complexity, due to the presence of either integral and differential terms in its expression, the dependence of the radiative properties on the spectrum and the three-dimensional nature of the problem which generally could not be approximated with simpler geometries. Thus, several methodologies have been developed for the resolution of the RTE, having different grades of accuracy, applicability to the problem and computational efforts requirements. An exhaustive overview of the available methods is given in Viskanta and Mengüc (1987). A first class of methods consists in evaluating the exact solution of the RTE. However, these methods use several assumptions that hardly coincide with the considerations that could be done for most of the engineering problems, as simplified geometries and homogeneous properties. The methods based on the statistical approach, such as the Monte Carlo method, allow a wider range of applicability. Monte Carlo prediction involves the generation of photons from the source and randomly distributes it in the surrounding space. The photons are characterised by a certain probability of being absorbed or scattered by the objects located along is path. The zonal method consists in dividing the emitting and transmitting medium in zones characterised by homogeneous properties. Once each zone has been solved, the total heat exchange can be evaluated. A further method for the RTE resolution is considering the radiation intensity uniform over a certain solid angle width. An application of this concept is given by the discrete ordinates method, which discretises the 4π solid angle according to a certain number of ordinates directions. Fiveland et al. (1991) proposed the discrete ordinates method applied to

3D objects considering the spectral nature of the participating media radiation. A similar concept is implemented in the Discrete Transfer Radiation Model (DTRM), where the intensity over a solid angle is represented by a single ray.

The spectral nature of the RTE makes evaluations too expensive in terms of computational cost. Thus, the use of spectral properties is usually not practical in engineering problems. On the other hand, global gas radiation properties evaluated from the high discontinuous spectral distributions of the gas under study might present either low accuracy or restricted range of validity. A summary of the different methodologies for radiative properties calculation will be attempted in the following section. In absence of in-scattering and out-scattering, emissivity and absorption are the main players in the RTE resolution. Therefore, the following section will focus only on such radiative properties for water vapour, as it is the main source of radiation from gaseous hydrogen flames (Schefer et al., 2007). Line by line calculation consists in the evaluation of the properties for each line of the spectrum, meaning high computational efforts for their evaluation. The narrow band models are based on the evaluation of radiative properties averaged on narrow spectral ranges. They are usually differentiated by the assumptions on the variation of the coefficient under study with the wave number, line intensity or line spacing. These assumptions will lead to different mathematical functions at the base of the models. However, they might not be valid out of certain range of conditions. For instance, Hottel and Sarofim (1967) noticed that the Elsasser model's assumptions has been mostly observed in low temperature gases, reason why the model was employed only for low temperature evaluations. Many studies have been conducted in this direction, such as Soufiani et al. (1997) and Leckner (1972). The wide band model consists in the integration of the narrow band model outcomes across whole bands. Yan et al. (2015) implemented an Efficient Exponential Wide Band (E-EWB) model for the evaluation of the Planck mean absorption coefficient, $\kappa_p$, and the effective mean absorption coefficient, $\kappa_e$. The evaluation of the radiative properties for $H_2O$ resulted in a deviation from the Line By Line method (LBL) within, respectively, 0.78% and 0.22%. However, the novel evaluation methodology speed is about 350 times faster than the EWB model. Tien (1969) reports the Planck mean absorption coefficients and the Rosseland absorption coefficient as a function of temperature. Sparrow and Cess (1978) compares the values obtained by Tien (1969) from spectral data with the data reported by McAdams (1964) obtained from emittance data, showing that for temperature lower than about 1000 K, McAdams' evaluations resulted in lower Planck mean absorption values. The authors consider Tien's evaluations as more reliable, due to their evaluation procedure not correlated to the emittance evaluation.

Several authors attempted the empirical evaluation of a global emissivity value from the measured heat flux (Modest, 2003). Among these studies, it is worth to mention Hottel and

Sarofim (1967). In case of gas mixtures, such as water-vapour and carbon dioxide, or presence of soot, different considerations have to be made because of the bands overlapping (Modak, 1979). Relevant studies are Hottel and Sarofim (1967), Taylor and Foster (1974), Smith et al. (1982), Felske et al. (1973), Coppalle and Vervisch (1983), Rohsenow et al. (1998).

In conclusion, several studies on radiative properties are available in the literature. However, they must be handled carefully as they have been evaluated under certain conditions of pressure or temperature and assumptions.

2.4.3.1 Analytical models for thermal radiation calculation

As discussed in the section above, the RTE resolution can require high computational efforts due to the radiative characteristics depending on wavelength, gas composition and geometry of the flame. As a consequence, simpler analytical models have been developed for radiative heat flux evaluation. Mainly, the different methodologies to evaluate the radiated heat flux can be classified according to their key steps:

1. Determination of the radiated heat flux from global temperature and emissivity of the flame;
2. Evaluation of surface emissive power through empirical correlations;
3. Determination of the radiated heat flux from the total heat released and the radiative fraction of the flame.

As discussed previously, hydrogen jet fires are characterised by large variation of temperature and radiative properties across the flame; thus, the analytical evaluation of radiant heat flux through the methodology in point 1 might result in great inaccuracies. As a consequence, several authors efforts have been focused on the other two approaches.

Many non-dimensional correlations and scaling laws for hydrocarbon characteristics have been developed for hydrocarbon fuels. Schefer et al. (2006) have investigated the application of the scaling correlations developed by Sivathanu and Gore (1993) to the prediction of heat flux from hydrogen flames. The study defines the radiant fraction, $\chi_{rad}$, as:

$$\chi_{rad} = \frac{S_{rad}}{\dot{m}_{fuel} * \Delta H_c} \tag{2.9}$$

where $S_{rad}$ is total power emitted by the flame, $\dot{m}_{fuel}$ is the fuel mass flow rate and $\Delta H_c$ is the combustion heat. Therefore, the radiant fraction is the ratio of the energy effectively emitted by the flame and the chemical energy associated to the fuel stream. Zabetakis and Burgess (1961) reported that the radiant fraction (defined as radiative output over total thermal output) for gaseous hydrogen diffusion flames is included in the range 9.5 – 16.9% for burner diameters ranging from 5 mm to 400 mm. Proust et al. (2011) observed the evolution of radiant

fraction for diameters in the range 1-3 mm, noticing larger radiant fractions (up to 15%) for larger orifices. Similar values were noted by Gore et al. (1987) with fractions equal to 8.7% and 10.2%, corresponding respectively to the mass flow rates 200 and 105 mg/s for a 5 mm release. Houf and Schefer (2007) reported a radiant fraction in the range 4-10% for a residence time between 30 to 100 ms. The study compared hydrogen flames to hydrocarbon flames, which are characterised by approximately twice the radiant fraction. Zabetakis and Burgess (1961) found that the value is higher when flames originate from liquid hydrogen spillages, in this case 25% of the combustion heat is radiated to the surroundings.

According to Houf and Schefer (2007), the heat flux at the radial location *r* with respect to the jet axis and at the axial distance *x* from the nozzle, $\dot{q}_{rad}$, can be evaluated using a non-dimensional radiant power, $C^*$, described by Sivathanu and Gore (1993) and Schefer et al. (2006). The equation is given as follow:

$$\dot{q}_{rad}(x,r) = C^* \cdot \frac{S_{rad}}{4\pi r^2} \tag{2.10}$$

Experiments conducted on hydrocarbons showed that the non-dimensional radiant power may be considered only dependent on the term x/L and expressed using the definition of radiant fraction. Houf and Schefer (2007) collected the empirical data from a 7.94 mm vertical release (15 MPa reservoir) to build the curve of $C^*$ as function of $\chi_{rad}$ (Figure 2.8). Schefer et al. (2006) found that the radiant fraction well fits a linear correlation in function of the flame residence time, defined as:

$$t_f = \frac{\pi}{12}\frac{\rho_f \cdot W_f^2 \cdot L_f \cdot Y_s}{\dot{m}} \tag{2.11}$$

where $Y_s$ is the hydrogen stoichiometric mass fraction ($Y_s$ =0.0281), $L_f$ is the visible flame length, $W_f$ is the visible flame width, $\dot{m}$ is the mass flow rate and $\rho_f$ is the flame density. Thus, the methodology proposed by Houf and Schefer (2007) employs the evaluation of the jet and flame parameters through available engineering models, such as Delichatsios' correlations (as reported from the authors) for the flame length calculation. The flame residence time can be calculated through Equation (2.11) and used in Figure 2.8 (right) to evaluate the radiant fraction. Afterwards, $S_{rad}$ can be evaluated from Equation (2.9) and $C^*$ from Figure 2.8 (left). Finally, the heat flux can be evaluated according to Equation (2.10). The authors assess that calculation uncertainty is within $\pm 18\%$, according to the studied jet diameter.

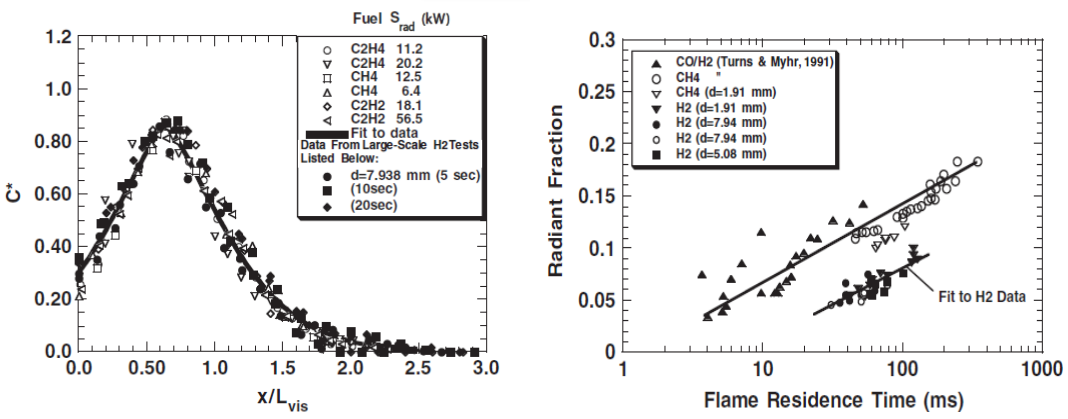


Figure 2.8 Axial normalized radiative heat flux (left) and radiant fraction as function of residence time for hydrocarbon and hydrogen flames (right) (Houf and Schefer, 2007)

Further studies on radiative fraction have concluded that it should be evaluated taking account of the Planck mean absorption coefficient, $\kappa_p$, in addition to the flame residence time. Furthermore, a decrease in the radiative fraction was observed when the flame size increased, as consequence of the enlargement of optical thickness (Molina et al., 2007). Ekoto et al. (2014) reported the following empirical correlation for the radiant fraction evaluation for hydrogen jet fires:

$$\chi_{rad} = 0.08916 \log_{10}\left(t_f \, \kappa_p \, T_{ad}^4\right) - 1.2172 \tag{2.12}$$

where the subscript *ad* denoted the adiabatic flame temperature. The experimental studies investigating the thermal radiation of the jet flames are in a minor quantity if compared to the studies on the flame length. Mogi and Horiguchi (2009) investigated both the issues. The experiments regard several hydrogen releases with pressure in the range 4-40 MPa and diameter from 0.1 to 4 mm. For circular nozzles, it has been observed that the flame length is proportional to the release diameter and pressure, and that the flame width is approximately 0.18 the length of the flame. The heat flux was found to be proportional to the mass flow rate according to the following equation:

$$Er^2 = 6.0 \times 10^5 \, m^{1.3} \tag{2.13}$$

where $E$ is the thermal flux at the radial distance $r$ from the jet axis and $m$ is the mass flow rate. Using the heat flux and temperature measurements, the authors also evaluated the emissivity of the flame, 0.08. A lower value has been evaluated by Zabetakis and Burgess (1961) for hydrogen diffusion flames, reporting 0.01 for temperature equal to 1900 K.

2.4.3.2 Experimental studies on thermal radiation

Gore et al. (1987) made several evaluations on the spectral and total radiation of turbulent hydrogen diffusion flames in air. The authors measured the radiative heat flux at several axial and radial locations from a vertical flame produced by a 5 mm diameter release. It was observed that for low Reynolds number, the radiative heat flux was lower due to the reduced dimensions of the flame. Houf and Schefer (2007) reported data on the radiative heat flux as function of the distance normalized to the flame length at different times during the storage tank blowdown for a turbulent vertical jet flame. Proust et al. (2011) investigated the heat flux determined by the jet fires produced by a 90 MPa hydrogen storage with capacity 25 l for three release diameters: 1 mm, 2 mm and 3 mm. The data were recorded at different distances from the jet axis and for all the duration of the tank blowdown. The closest sensor (1 m from the jet axis) recorded a peak value of about 13 kW/m$^2$ during the 2 mm diameter release. It has also been observed that the radiant fraction increases for larger release diameters, so larger mass flow rates, and decreases with the reduction of flame length for the same release nozzle. Studer et al. (2009) investigated the radiative characteristics of hydrogen and hydrogen/methane mixtures jet fires with initial release pressures up to 100 bar. The results showed that the addition of methane to hydrogen sensibly increases the measured heat flux achieving differences up to 7 kW/m$^2$ for the radiometer closer to the jet axis and 50:50 mixtures.

2.4.3.3 Numerical investigations on thermal radiation

Thus far, few numerical investigations present the implementation of radiation model. Frank et al.'s calculations (2000) highlighted the importance of considering the radiative heat losses while modelling jet fires, presenting significant lower temperature profiles with respect to the adiabatic evaluations for distances greater than 40D. However, the investigations regarded relatively small flames, with stoichiometric flame lengths up to 0.6 m. Xiao et al. (2015) have investigated the heat losses mechanisms in sonic hydrogen flames. The comparison of the numerical results with the outcomes of the experiments conducted in the ENACCEF facility showed that radiation and convective heat losses contribute differently in the various stages of the combustion (Bentaib et al., 2014); the convective heat losses have been found to prevail for the early stage of combustion, whilst the radiative losses increases their contribution while the combustion advances. However, the long term combustion time needs to be further investigated. Ilbas (2005) investigated the temperature distribution in a combustion chamber of 2 m length and 0.3 m radius, for pure hydrogen and pure methane. The third and latter case considers a mixture made of 30% by volume of hydrogen and 70% by volume of methane. The numerical simulations were run without the activation of radiation model, with P-1 radiation model and with the discrete transfer radiation model. The results show that the temperature profiles predicted without modelling radiation are generally higher than the

estimations including radiation. The discrepancy between the evaluations is higher as the axial distance increases. The two radiation models results do not present considerable differences. The temperatures predicted at the chamber exit have been compared with experimental results. Overall, for all the fuel compositions, the experimental average temperature has been better represented by the numerical investigations considering radiation. The discrete transfer radiation model has been further implemented by Muthusamy et al. (2011). The experiment they reproduced was performed at the Health and Safety Laboratories and published in 2011 (Royle and Willoughby, 2011b). The employed software presented a considerable limitation, precluding the evaluation of the radiative heat flux but solely the total heat load. Comparisons with the experimental results highlighted an increasing deviation for larger release orifices. According to the authors, the reason is given by the increasing contribution of convective heat flux, highlighting the limitation of the software. The same radiation model has been implemented by Jang et al. (2015) for the numerical evaluation of the heat flux caused by a hydrogen pipe rack failure. However, the models have not been validated against experimental evidence. Ekoto et al. (2014) proposed a novel methodology for prediction of the heat flux to compensate the poor predictive capability shown by previous analytical models for large-scale flames and the near field. Jet fires with length greater than 10 m were defined as large-scale flames. The proposed flame integral model consists in the resolution of the conservation equations governing the phenomena for the evaluation of the flame trajectory, which is curved due to buoyancy. A weighted multi source model was then applied for the evaluation of the heat flux in the surroundings. The predictions of the heat flux by two hydrogen jet flames with diameters 20.9 mm and 52.5 mm resulted to be strictly dependent on the pseudo-source model implemented. The best results showed that the under-prediction was of about the 6.5 % for 20.9 mm and 0.4 % for 52.5 mm. Wang et al. (2014) reproduced numerically the radiative characteristics of the jet fires experimentally investigated in (Studer et al., 2009) and (Ekoto et al., 2014). The implemented radiation model was the finite volume discrete ordinates model coupled to the eddy dissipation concept accounting the presence of multi-components in the combustion. The predicted radiative fractions strongly agreed with the results presented in (Studer et al., 2009) and (Ekoto et al., 2014), showing over predictions of respectively 8% and 5%. Furthermore, the study investigated the effect of the ground reflectance on calculations, comparing them with the experimental results obtained in (Ekoto et al. 2014). The results pointed out that the variation of ground reflectance has a wide influence on the heat flux predicted at the radiometers, causing additions up to 50%, whereas it has a controversial effect on the radiant fraction and surface emissive power. Indeed, the increase of ground reflectance did result in oscillating predictions of the above quantities; however, the values vary in a narrow range, such as 0.9% for the surface emissive power.

### 2.4.4 Tank blowdown

The internal pressure of a damaged high-pressure hydrogen storage releasing gas decreases, causing variations of the related parameters. Thus, the resulting mass flow rate and gas concentration distribution or flame length, whether the jet has been ignited, varies during the tank blowdown. Proust et al. (2011) investigated the tank blowdown of 90 MPa hydrogen storage with capacity 25 l for three release diameters: 1 mm, 2 mm and 3 mm. A similar study has been conducted by Schefer et al. (2007) on a hydrogen vertical flame from 5.08 mm diameter release at 413 bar. As mentioned in Section 2.2 the notional nozzle theory can be used when characterising hydrogen jet fires. In the case of blowdown, applying the notional nozzle theory means a continuous change of the release diameter (notional nozzle dimensions). This circumstance might be challenging to reproduce in CFD simulations as it requires a computational grid changing in time. To remedy this issue, the volumetric source terms approach can be employed. Molkov et al. (2009) successfully validated the model for release volume size up to 4 times the effective diameter. The same model has been employed by Li et al. (2015) for the evaluation of unignited and ignited hydrogen jet released vertically downward. A correct reproduction of the whole release transient would require few considerations on the release start. This could be the valve opening or the rupture of the membrane, all phenomena needing a certain amount of time to actuate, meanwhile they are changing their spatial characteristics. Khaksarfard et al. (2012) investigated the expanding opening assuming 100 m/s, 200 m/s and 300 m/s as opening speeds. In addition to the previous observations, it must be considered that often hydrogen can be released through a piping system constituted by several components. This condition might sensibly change the outcomes of the experiments and consequences analysis. For instance, Schefer et al. (2006) employed the following release system in their experiments: the hydrogen was released from two cylinders, flowing through a 3.175 mm diameter manifold orifice into a 7.94 mm tube with length of 7.6 m. Assuming the chocked flow at the manifold orifice, the blowdown pressure prediction corresponds to the experimental pressure history, while the prediction with chocked flow at the 7.94 mm diameter appears to be really far from the experimental outcomes, resulting in a blowdown time of about 10 s against the 10 times longer duration observed in experiment. Numerical studies validating a predictive CFD tool for determination of thermal hazards from jet fires during tank blowdown are currently missing.

### 2.4.5 The interaction of hydrogen jet fires with barriers

In recent years, numerous research efforts have been made to provide efficient mitigation strategies for the thermal and overpressure hazards of hydrogen jet fires. Some of the studies concerned the reduction of flame lengths through smaller diameters of the Pressure Relief Devices (PRDs) employed on storage systems. A second class of study has been aimed to

mitigation strategies without modifying the storage tanks design, but through the location of barriers and walls. However, studying the interaction of jet fires with barriers is a powerful means to understand what happens to the jet in presence of obstacles along its path. Studies such as (Aleksandrov et al., 2009) assess that the combustion process is promoted by the presence of obstacles and that certain combinations of congestion and confined systems might result in a rise of the blast overpressure up to about 30 times. Royle and Willoughby's experiment (2011b) has concerned the interaction of hydrogen jet flames with two barriers with dimensions 3 x 2.4 m and tilted by 90° and 60°. Several pressure and heat flux sensors were located on the barrier and behind. The tests were conducted for three release diameters: 3.2 mm, 6.4 mm and 9.5 mm. The results showed that the maximum overpressures are higher with larger diameters. The 90° barrier showed better performance to limit overpressure with respect to the 60° wall configuration and, as expected, it also has shown higher overpressures than the free jet fire. The maximum overpressure on the wall behind the release was recorded for the 60° barrier and 9.5 mm diameter and it was equal to 0.572 bar, a value sufficient to provoke the displacement of cylindrical storage tank and failure of pipes, according to the threshold provided in (LaChance et al., 2011). The 60° barrier generally resulted in a higher heat flux recorded by the sensors behind the barrier. The same experiments have been numerically reproduced by Muthusamy et al. (2011). The pressure level predicted for the scenario concerning the 3.2 mm release and 90° barrier agreed with the experimental data. However, the analysis made on the heat fluxes on the wall showed an increasing deviation from the experimental data as the orifice diameter increases. According to the authors, this is due to the increasing contribution of the convective heat flux which cannot be distinguished from the radiative one, due to the software inability to evaluate the singular contribution of the radiation heat flux. Thus, the CFD models could not be validated. A second study was performed at the Sandia National Laboratories (Houf et al., 2011). The jet fire investigated was released through a 3.175 mm diameter and pressure equal to 13.8 MPa. Four barrier configurations were analysed. The maximum overpressure was recorded for the 90° barrier and the jet directed to the centre of the barrier: 6.89 kPa. The value corresponding to the free jet configuration was 2.78 kPa. The maximum mitigation was given by the 3-wall configuration (135° angle between the walls). The recorded pressure over the wall was about one order of magnitude minor than the value recorded upstream the wall. The same behaviours were observed for the heat flux analysis. The 90° wall showed the highest heat flux record, about 20 $kW/m^2$, whereas the 3-wall configuration showed the best reduction factor, in this case about 2.5. The experiments have been reproduced numerically through FUEGO simulations, showing a good agreement between the free jet heat flux measurements and the numerical prediction. The numerical simulation of the overpressure in the 90° barrier configuration showed a good agreement with the data collected by the sensor behind the

barrier. The simulation of the front wall sensor presented an overestimation of the peak pressure of about 1.5 kPa and a consistent under-prediction of the second pressure peak. Schefer et al. (2011) showed also the pressure and heat flux measurement history for the 1-wall configuration, the 3-wall 135° and the 3-wall 90° barriers. Zheng et al. (2012) have made a numerical study on the effect of a 1 x 1 x 0.2 m barrier located at 1 m from the jet release. The numerical model adopted the SST k-ω turbulence model for the near wall zone, while the k-ε turbulence model was employed for the high Reynolds number zone. The barriers were tilted by 90°, 60° and 45°. The results showed that the better configuration was given by the 45° tilted barrier, reducing the flame spread on the sides of the barrier with respect to the 90° wall and concentrating it on the upper part of the barrier. The high temperature region was also reduced with respect to the 60° configuration. However, the model was only validated against the free jet fire experiment. The same turbulence model has been employed by Li et al. (2015) for simulating the vertical downward hydrogen jet released from a vehicular TPRD. The presence of a surface as barrier in the jet path is not the only likely accident scenario. The surface might even only be the ground. If the horizontal release height is in close proximity to the ground, great effects might be produced on the jet extent. Royle and Willoughby (2011b) observed an extension of the flame length from 11 m to 13 m when the release height was changed from 1.2 m to 0.1 m for a 9.5 mm release at 205 bar. The same basic considerations can be done for surfaces in proximity of horizontal unignited releases. Numerical investigations made by Hourri et al. (2011) reported that the flammable extent (LFL) increased by 48% when in proximity of the ground. On the other hand, the hydrogen centreline extent is greatly affected by buoyancy if compared to methane. A previous study by Hourri et al. (2009) analysed the effect provoked by a vertical wall located on the side of the horizontal release. The LFL area extended by 90%, indicating that buoyancy effect has a limited reducing effect.

## 2.5 Delayed ignition of hydrogen jets

Overpressure originated by delayed ignition of high-pressure hydrogen jets was investigated in Takeno et al. (2007). The authors conducted an extensive study on the effect of leakage diameter, spouting pressure and ignition delay time. It was found that for release pressure equal to 40 MPa, orifice diameter 10 mm and ignition delay 2 s, a maximum overpressure equal to 0.2 bar was achieved at 3.9 m from the ignition point, which was located at 4 m from the release nozzle. After the high-pressure peak, a low pressure wave with longer duration was recorded, as a consequence of the after burning of the hydrogen which is continuously released. Hydrogen concentration in the ignition zone was numerically calculated as 40% while the gas speed was 120 m/s. At these conditions, the sonic speed of the gas and C-J detonation velocity were calculated as 740 m/s and 1980 m/s respectively. The flame front was detected during the experiment and the maximum flame propagation speed was

determined to be 978 m/s. Subtracting the gas flow speed, the net flame propagation velocity is yet higher than the sonic speed of the gas, while it is significantly lower than the detonation speed. The reason for such high flame propagation speed is believed to be the strongly turbulent premixed combustion given the high initial turbulence mixing of the jet. Therefore, it is of great importance to have a turbulence mapping of the flammable cloud, as turbulent intensities and length scales affect the turbulent flame speed and, consequently, the explosion overpressure. Daubech et al. (2015) assessed the turbulent intensity and length scale from measurements of the velocity field at same locations for different times. Release pressure and diameter were 40 bar and 12 mm. Turbulent intensity was found to be included in the range 15-30% on the jet axis, while it exponentially increased with the normalised radial distance (r/x). Turbulence length scale was proportional to the distance from the release by a factor equal to 0.05. Ignition was triggered at 1.8 m from the release point and the highest pressure (0.08 bar) was recorded 2 m downstream the ignition point. The recorded maximum flame speed was 280 m/s. Further experimental investigations on delayed ignition of hydrogen jets were performed by Royle and Willoughby (2011a). The releases were produced by a 205 bar storage through nozzles with diameter equal to 9.5 mm, 6.4 mm, 3.2 mm and 1.5 mm. The pressure sensors were located at 1.5 m, 2.6 m and 3.7 m from the jet axis. The sensors were all positioned at 0.5 m above the ground and 2.8 m from the release point. The overpressure of the 1.5 mm release experiment for the minimum ignition delay analysed (400 ms) was not recordable, while the maximum overpressure recorded for the same ignition delay rose with the increase of the release size, achieving a maximum value of 0.054 bar for the 9.4 mm release. The same proportionality was observed by Takeno et al. (2007) for the range of diameters 0.5-10 mm. However, for large diameters it was observed a larger effect of ignition delay time on recorded overpressure because of the larger variations of release conditions and flow turbulence characteristics during tank blowdown. As reported by Daubech et al. (2015), studies on diameters up to 100 mm measured overpressures up to 0.4 bar at 10.8 m from the ignition point.

### 2.5.1 Effect of ignition delay on overpressure

The effect of ignition delay could be significant on overpressure hazards. During the first phase of the release, the hydrogen concentration varies considerably along the jet axis. Thus, if the ignition position is fixed, variations of 100 ms order of magnitude of the ignition delay will determine if the ignition point is located in the poor or rich mixture portion of the jet.

Royle and Willoughby (2011a) investigated the effect of ignition delay on the overpressure produced by hydrogen jet fires (nozzle release 6.4 mm and pressure 205 bar). The pressure sensors were located at 2.8 m distance from the release point and 1.5 m from the jet axis. The

ignition delay was varied from 400 ms to 2000 ms and the maximum overpressures recorded for the range limits were, respectively, 0.037 bar and 0.095 bar. The peak value was achieved with an ignition delay of 600 ms. Similar ignition delay time was observed by Takeno et al. (2007). In their experiments, the maximum overpressure was recorded for ignition delay time equal to 850 ms. A more recent study (Grune et al., 2014) investigated the ignition delay effect on 4 mm release with initial pressure 200 bar and ignition distance 50 cm from the nozzle. The maximum overpressure recorded at 50 cm distance from the jet fire was around 0.180 bar for about 25 ms delay while it decreased to around 0.08 bar when the delay was more than 70 ms. Zabetakis and Burgess (1961) observed that ignition delay can also affect the total radiant energy and the rate of energy release of different masses of spilled liquid hydrogen.

### 2.5.2 Numerical studies on delayed ignition

Takeno et al. (2007) simulated the delayed ignition of hydrogen jets through k-ε equations for turbulence and Bray's definition for turbulent flame speed, $S_t$, as in Equation (2.14) to calculate the chemical reaction rate (Bray, 1990):

$$S_t = 1.8u'^{0.412} \cdot {L_t}^{0.196} \cdot {S_u}^{0.784} \cdot \nu^{0.196} \tag{2.14}$$

where $u'$ is the velocity fluctuation component, $L_t$ is the turbulence scale, $S_u$ is the gas laminar flame speed and $\nu$ is the gas viscosity. Simulation results well agreed with experiments. However, calculated pressure along the axis resulted approximately 1.5 times the pressure recorded in experiments. The same expression as in Equation (2.14) was employed by Daubech et al. (2015) to simulate the overpressure produced by the delayed ignition of a hydrogen release at 40 bar and with 12 mm diameter. Numerical grid resolution is generally greater than the flame thickness. Therefore, a factor β was chosen in such a way the flame thickness would be 3-5 grid cells, increasing diffusion by a factor β and decreasing the reaction rate by 1/β. Simulations well reproduced experiments, showing a slight underestimation of the pressure peaks equal to approximately 5%. However, the numerical modelling was limited to one experimental test, whereas a more comprehensive study shall be conducted to assure the model validity for a wider range of release conditions.

## 2.6 Rupture of storage tank in a fire

Tanks containing compressed gases are provided with devices aimed to the release of the substance when a certain temperature or pressure has been achieved. Thus, if the tank is engulfed by an established/ continuous fire, the devices intervene venting the gas and avoiding the tank rupture. According to their activation technique, the devices are classified in PRD (Pressure Relief Device) or TPRD (Thermally activated Pressure Relief Device). The possibility of the PRD/TPRD failure has to be taken into account. Another possible event to

be considered is the undermining of the tank material resistance provoked by a localized fire. In this circumstance, the erosion of the tank material might lead to the storage rupture before the pressure or temperature increase is sufficient to activate the safety devices. The consequences of this scenario are blast wave, fireball and projectiles. The fireball has to be defined in terms of size, lift-off, temperature, radiation and thermal dose in order to assess the related thermal hazards. One of the earliest studies on gas-filled tank burst was conducted by Boyer (1960). In experiments, the burst of glass spheres with 5 cm diameter was analysed. The spheres were filled by air or helium with pressure up to 2.8 MPa. Pittman (1972) investigated the blast pressure and fragments scattering for 5 tests involving nitrogen tanks with volume equal to 170 l and pressure up to 55 MPa. The damage to people was qualitatively assessed through the employment of anthropomorphic dummies located in the surroundings of the vessel. Minimum and maximum distance from the tank were 26 m and 46 m. The author concluded that the blast itself would have unlikely caused death at those distances. However, blast pressure would have been enough to cause at least eardrum damage. On the other hand, severe damage or death could have been caused by the projectiles, as proved by the travelled distance (up to 274 m) and the fragments hitting the dummies. Tank pressure was noticeably increased up to 345 MPa in following experiments on a 28 l vessel filled with Argon (Pittman, 1976). A lack of the previous experiments is the use of a non-flammable gas.

Given the complexity of the corresponding experimental set-up and extent of hazards, few experimental tests have been conducted to measure the hazards from hydrogen storage tank failure when involved in a fire. To the author knowledge, two tests conducted in USA (Weyandt, 2005- Weyandt, 2006) represent the only experimental studies available in the open literature on hydrogen gaseous storage tank rupture. In these tests, the hydrogen storage systems have been deprived of the PRDs to analyse the extent and magnitude of the tank burst consequences. Weyandt (2005) investigated a type IV stand-alone tank (72.4 l) with initial temperature of 300 K and pressure 34.5 MPa. During the tests, the appearance of black soot after 45 s indicated the beginning of the tank material combustion. The tank burst happened 6 min 27 s after the start of the bonfire. The generated fireball had diameter equal to 7.6 m and duration of 2 s when observed through the high-speed video camera. However, the infrared camera showed a longer duration (4.5 s). The recorded maximum overpressures showed values up to 300 kPa for the closest sensor (1.9 m). Cylinder fragments have been recovered to distances up to 82 m. The second test regarded a type III cylinder (88 l) installed in a SUV (Weyandt, 2006). In this scenario, the tank burst happened 12 min 18 s after the start of the bonfire test, conducted with a burner heat release rate of 265 kW (stand alone 370 kW). The heat flux from the fireball was measured through a transducer located 15.2 m from the vehicle location and the recorded maximum value was 210 kW/m$^2$, which was achieved in a peak

sensibly higher than the average. The presence of the vehicle combustion products could have caused the increase of the fireball size (24.4 m) with respect to the stand-alone test. 140 kPa was recorded as maximum overpressure at 1.2 m and the fragments were recovered at distances up to 106 m. Thus, the vehicle presence around the hydrogen cylinder might positively have affected the blast wave consequence but, as shown from the test results, it increased the magnitude of the consequences related to the fireball and the projectiles.

### 2.6.1 Pressure hazards

The energy of explosion in a vessel burst is dependent on the initial pressure of the storage system. In case of fire engulfment and TPRD failure to activate, pressure inside the tank may have grown by the moment of burst, thus increasing the explosion energy. In many applications, storage tanks are located on the ground or in proximity of it. In this case, the total available energy is usually calculated as twice the blast energy. A factor equal to 1.8 was suggested by Baker et al. (1983) to take into account the mechanical energy lost for cratering the ground. Baker et al. (1975) proposed a methodology for estimation of the blast wave pressure and impulse. The model assumes the high-pressure gas as ideal and it employs an empirical curve obtained from measurements of high explosive.

Molkov and Kashkarov (2015) refined the methodology presented in Baker et al. (1975) including in the model the non-ideal behaviour of the gas and contribution of combustion into the blast wave strength. The mass contained in the tank resulted 18% lower when evaluated using the Abel-Noble real gas equation, affecting the evaluation of the total mechanical energy, $E_m$, and the total chemical energy associated, $E_{ch}$. The portion of mechanical energy feeding the blast wave is quantified through the mechanical energy coefficient $\alpha$, while $\beta$ is the chemical energy coefficient quantifying the contribution given by the chemical energy. The authors applied the novel methodology to the experiments in Weyandt (2005) and (2006). The mechanical coefficient was found to be 0.14 for the tank installed in the SUV, compared to $\alpha$=1.8 for the stand-alone tank, which confirms Baker et al.'s (1975) observation. The reduction of α is consequence of the large quantity of energy required to displace the vehicle. The analysis on the chemical energy coefficient showed the opposite situation, with a value higher for the under-vehicle tank (0.09). The authors justified the increase through the enhancement of turbulence, therefore combustion, due to the vehicle presence. Comparing the evaluated mechanical energy and chemical energy, the authors found out that the chemical contribute to the blast wave is 30 times greater than the mechanical for the under-vehicle case, while it is only 1.4 times greater for the stand-alone tank.

### 2.6.2 Thermal hazards

The explosion of the storage tank in a fire results in the combustion of the hydrogen-air cloud. Owing the effect of buoyancy and combustion, the burning cloud rises and expands, assuming a spherical shape. The fireball growth process has been described by Roberts (1981). The first phase is mainly concerned by the mixing and combustion of air and fuel and it is dominated by momentum forces. Sequentially, the combustion interests the remaining fuel and entrained air; the fireball is mainly affected by combustion and buoyancy forces, while momentum forces decrease their influence. The third phase is defined by the end of combustion and decrease in temperature; buoyancy dominates the fireball behaviour.

Zalosh (2007) attempted the evaluation of the thermal hazards produced in Weyandt's test (Weyandt, 2006), calculating the surface emissive power ($E$) of the fireball as 339 kW/m$^2$. The evaluation considered the fireball as a solid flame, unitary atmospheric transmissivity and a view factor equal to 0.62. The view factor was evaluated as $D_{fb}^2/(2L)^2$, where $D_{fb}$ is the diameter of the fireball and $L$ is the distance from the fireball centre. However, a more simplified model exists for practical applications: the point source model. In this case the radiative heat flux at the target is evaluated only considering the distance from the fireball centre as $\frac{E}{4\pi L^2}$. A study by Zabetikas and Burgess (1961) attempted to define a correlation to evaluate the flame volume produced by the ignition of the hydrogen-air mixture created from the spillage of liquid hydrogen. Fireballs were observed when the cloud was ignited even if they rapidly disappeared. The flame volume ($ft^3$) was found to be proportional to the liquid hydrogen volume ($l$) by a coefficient of 750. If the same correlation is applied to the gaseous hydrogen volume of Weyandt (2005), the calculated diameter would be about twice the reality.

#### 2.6.2.1 Experimental investigations and models with other fuels

The majority of the previous studies about fireballs regard liquefied pressurised gas, thus, they are mainly associated with BLEVEs (Boiling Liquid Expanding Vapour Explosion). An analytical model for the evaluation of thermal hazards from propane fireballs has been proposed by (Hardee and Lee, 1973). The model assumes that the mixture fuel-air is stoichiometric and that it reacts completely. The burn out time $\tau_b$ has been estimated as 0.6 $m_b^{1/6}$and the radius of the flame $r_{fb}$ is evaluated as:

$$r_{fb} = \left(\frac{5\, m_b^{5/6}}{4\,\pi\,\rho}\right)^{1/3} {\tau_b}^{1/3} \tag{2.15}$$

where $m_b$ is the mass of fuel and air mixture before the ignition and $\rho$ is the density of the fireball, making the correlation dependent of the fuel type. The heat loss due to radiation is

evaluated following the Stefan-Boltzmann law for the whole surface of the fireball. In a following study made in 1978, the authors investigated the thermal hazards from 0.1-10 kg methane fireballs (Hardee et al., 1978). Conversely, Hasegawa and Sato (1978) observed from their and other authors' experiments that the fireball size can be expressed as function of only the initial fuel mass, $m_f$, independently from the fuel type ($D_{fb} = 5.28\, {m_f}^{0.277}$). The maximum irradiance ($\frac{W}{cm^2}$) at 15 m was found to follow the empirical correlation $0.31\ {m_f}^{0.661}$. However, the authors observed that the same conclusion cannot be achieved for the fireball duration, which deeply depends on the combustion processes. Hasegawa and Sato's (1978) data have been furtherly elaborated by Roberts (1981). The author concluded that the released thermal radiation corresponded to about 25% of the combustion energy. The author also observed that the emitted radiation becomes greater as the vapour pressure at the bursting increases and that the presence of fire surrounding the tank may affect the fireball size. The effect is related to the mass portion interested by flash evaporation, which is proportional to the temperature inside the tank. Thus, the phenomenon is associated to liquefied pressurised storage. Dorofeev et al. (1995) investigated the explosions of heterogeneous fuel air-clouds. Large scale experiments using gasoline, kerosene and diesel as fuel were performed varying the mass in the range 0.1-100 tonnes. The results allowed the definition of empirical correlations for the flame radius, duration and energy released. The tests made on 3-110 kg diesel resulted in the following equation for the emissive power of the produced fireball:

$$q = q_0 \varepsilon = q_0[1 - exp(-kx)] = (110 \pm 10)[1 - exp(-2 \cdot 6 \cdot R)] \tag{2.16}$$

where $q_0 = \sigma T^4$, $k$ is the extinction coefficient and $x$ is the flame size. Dorofeev et al. (1996) treated the thermal effects associated with gaseous propane. However, the analysis dealt with propane rich-air mixture detonation, resulting in scaling correlations quite different to those usually used for fireballs. If it has been observed that numerous correlations can be used for the whole class of hydrocarbons, the same cannot be extended to hydrogen. Indeed, the gas has always been discerned with a different treatment from other fuels. Hasegawa and Sato (1978) observed that different constants are needed to evaluate the fireball volume for hydrogen, whereas hydrocarbons can be approximated indistinctly by the same constants.

### 2.6.3 Numerical studies

The experiment performed by Weyandt (2005) has been reproduced through several numerical investigations. Kim et al. (2015) reproduced the blast wave and fireball phenomena implementing realizable k-ε as turbulence model and eddy dissipation model for combustion. The blast wave was reasonably reproduced in the near field, but it was underestimated as the distance progressively approaches the far field. The authors concluded that the temperature

increase was primarily produced by the adiabatic compression due to the blast wave, showing a weaker connection to the combustion phenomena. A discrepancy was found between the experimental diameter of the fireball (7.6 m) and the predicted one (5.3 m). The authors justified this difference through the presence of the smoke produced by the tank material combustion in the experiment. The same authors attempted to resolve the discrepancies highlighted above implementing a different approach for modelling combustion and turbulence. The CFD approach was based on Eddy Dissipation Concept (EDC) with finite chemistry and RNG k-ε turbulence model. The results are published in Shentsov et al. (2015) and they show good agreement with the experimental measurements at 4.2 and 6.5 m from the tank. On the other hand, pressure at the closest sensor was slightly overestimated (distance 1.9 m from the tank). According to the authors, this could be due to not considering the energy loss owe to the ground cratering and the ideal gas assumption. The fireball diameter was estimated through the OH concentration and temperature, resulting respectively 10.5 m and 12 m. Radiation modelling was not included in the mentioned numerical studies, preventing the assessment of the hazards related to thermal radiation from the fireball. Furthermore, numerical modelling was limited to an experimental test on a tank with storage pressure equal to 35 MPa, whereas vehicular applications involve storages with pressure up to 70 MPa. Therefore, further numerical investigations are needed to provide a validated CFD tool, including radiation modelling, capable to predict both blast wave and thermal hazards from rupture of tank with pressure up to 70 MPa.

## 2.7 Harm criteria

The main aim of predicting the consequences of a possible accident scenario is to analyse the potential harm to people and infrastructures to avoid the occurrence of injury to people and a domino effect. However, it is challenging to define globally applicable harm criteria. Indeed, the potential damage depends on the vulnerability of the target, which is determined for people by age, health conditions etc… LaChance et al. (2011) attempted the development of uniform harm criteria to be considered in the quantitative risk assessment of hydrogen infrastructures. Table 2.1 shows the harm criteria for people with regards to thermal radiation intensity and time of exposure.

Table 2.1 Radiative heat flux harm criteria for people

| *Thermal radiation intensity, kW/m$^2$* | *Damage* |
|---|---|
| 1.6 | No harm for long exposures |
| 4-5 | Pain for 20 s exposure; first degree burn |
| 9.5 | Second degree burn after 20 s |
| 25 | Significant injury in 10 s; 100 % lethality in 1 min |

The study proposed by Barry presents a comparison between different regulatory agencies (Barry, 2002). For instance, the exposure limit corresponding to the significant chance of fatality for prolonged exposures is reported as 12.5 kW/m$^2$ from the U.S. Department of Transportation and as 10 kW/m$^2$ from the UK regulatory agency. The potential harm to structures and equipment can be evaluated for the specific type of damage. LaChance et al. (2011) reported 35 kW/m$^2$ as threshold for damage to process equipment, such as storage tank, for exposition longer than 30 min. A lower value, 10 kW/m$^2$ is given as limit for the ignition of fuel oil with exposition time 120 s. Some authors attempted the evaluation of separation distances according to the radiation level. Gerboni and Salvador (2009) evaluated that the distance to a 30 mm leakage at the radiation level of 5 kW/m$^2$ is about 30 m. Zhiyong et al. (2010) evaluated that the scenario involving the maximum harm effects distances is higher for confined VCE and they increase as the release pressure becomes greater, achieving distances up to 45 m when dealing with 400 bar pressure. The hazard distances as function of the air temperature have already been presented in section 2.4.2.

The harm level is function of both thermal radiation intensity and exposure duration, thus it is usually expressed in terms of thermal dose (TD):

$$Thermal\ Dose = I^{\frac{4}{3}} \cdot t \tag{2.17}$$

where $I$ is the radiative heat flux (kW/m$^2$) and $t$ is the exposure time in seconds. The thermal dose unit (TDU) is equal to 1 (kW/m$^2$)$^{4/3}$s. Different thermal dose thresholds are reported in literature. Table 2.2 reports the thresholds provided by LaChance (2010) for infrared radiation.

Table 2.2 Thermal dose thresholds for people

| *Threshold Dose (kW/m$^2$)$^{4/3}$s* | *Burn Severity* |
|---|---|
| 80-130 | First Degree |
| 240-730 | Second Degree |
| 870-2640 | Third Degree |

Table 2.3 reports the thresholds identified in (Molkov and Kashkarov, 2015) for overpressure hazards. To the harm criteria for people, it could be added the threshold range corresponding to the displacement of cylindrical storage tank and failure of pipes as 50-100 kPa (LaChance et al., 2011).

The consideration of all the hazards connected to an accident scenario is essential for a correct estimation of the minimum distance according to the related and specified harm criteria. A

clear example is given by the hazard distances evaluated by Shentsov et al. (2015) for the rupture of a 72.4 l and 35 MPa hydrogen tank in a fire. The separation distance evaluated according to temperature (6 m) was evaluated to be 1.5 times longer for the "fatality" criteria related to the pressure wave. However, these considerations are reversed when considering the "injury/pain" criteria, with an overpressure hazard distance (12.5 m) twice longer than the one evaluated for temperature. Radiation hazards have not been considered in the previous study, leading to the need of further investigations for a complete understanding of the phenomena and validated tools for evaluation of hazard distances.

Table 2.3 Overpressure harm criteria for people

| *Overpressure, kPa* | *Damage* |
|---|---|
| 1.35 | No harm |
| 16.5 | Injury |
| 100 | Fatality |

## 2.8 Aim and objectives

The aim of this study is to identify and address the knowledge gaps in the safety of deployment and handling of high-pressure hydrogen systems. The investigated scenarios span from releases originated by damaged storage or TPRD, including full bore rupture of hydrogen pipelines, to catastrophic rupture of a hydrogen tank in a fire. The main outputs of the study are a deeper understanding of hydrogen behaviour and validated predictive tools to be used in hydrogen safety engineering. The research primarily takes place using numerical methods (CFD) and validating them against experiments. The first part of the study focused on the literature review of the hazards and risks associated to hydrogen storage, reporting the state-of-the-art of the research on unignited jets and dispersion, thermal and pressure hazards from ignited jets varying the ignition delay, spark ignition in quiescent mixtures and consequences from rupture of the tank in a fire. The literature review led to identification of the knowledge gaps to close and the main objectives to attain, which are defined as follow:

- Develop and validate models for the assessment of thermal hazards from steady and unsteady ignited releases from storage at different temperature and pressure.
- Study the phenomena of spark ignition in hydrogen-air mixtures and develop a tool for calculation of MIE.
- Propose and develop a model for prediction of overpressure effects from delayed ignition in turbulent hydrogen jets.
- Develop and validate a CFD tool capable to predict blast wave and fireball from rupture of a tank in a fire.

# 3 Description of a CFD model

The present section aims to provide an overview of the several models composing the CFD approaches developed in chapters 4-7. The investigated phenomena present significant differences among them, ranging from laminar to turbulent flows, from dispersion to combustion, from ignition in a quiescent mixture to ignition in a turbulent momentum dominated jet flow. The wide range of phenomena investigated resulted in a wide set of employed CFD sub-models. The CFD software employed for calculation is ANSYS Fluent. The software version may change from one study to another and it will be indicated in each section. The governing equations of the CFD model are described below.

## 3.1 Mass, momentum, energy and species conservation equations

The developed CFD approaches are based on the Navier-Stokes conservation equations for mass, momentum, energy and species, presented below:

$$\frac{\partial \bar{\rho}}{\partial t} + \frac{\partial (\bar{\rho}\tilde{u}_j)}{\partial x_j} = S_{mass} \tag{3.1}$$

$$\frac{\partial (\bar{\rho}\tilde{u}_i)}{\partial t} + \frac{\partial}{\partial x_j}\left(\bar{\rho}\tilde{u}_i\tilde{u}_j\right) = -\frac{\partial \bar{p}}{\partial x_i} + \frac{\partial}{\partial x_j}(\mu + \mu_t)\left(\frac{\partial \tilde{u}_i}{\partial x_j} + \frac{\partial \tilde{u}_j}{\partial x_i} - \frac{2}{3}\delta_{ij}\frac{\partial \tilde{u}_k}{\partial x_k}\right) + \bar{\rho}g_i \tag{3.2}$$

$$\frac{\partial (\bar{\rho}\tilde{E})}{\partial t} + \frac{\partial}{\partial x_j}\left(\tilde{u}_j\left(\bar{\rho}\tilde{E} + \bar{p}\right)\right) = \frac{\partial}{\partial x_j}\left(\left(k + \frac{\mu_t c_p}{Pr_t}\right)\frac{\partial \tilde{T}}{\partial x_j} - \sum_m \tilde{h}_m\left(-\left(\rho D_m + \frac{\mu_t}{Sc_t}\right)\frac{\partial \tilde{Y}_m}{\partial x_j}\right) + \tilde{u}_i(\mu + \mu_t)\left(\frac{\partial \tilde{u}_i}{\partial x_j} + \frac{\partial \tilde{u}_j}{\partial x_i} - \frac{2}{3}\frac{\partial \tilde{u}_k}{\partial x_k}\delta_{ij}\right)\right) + S_E \tag{3.3}$$

$$\frac{\partial (\bar{\rho}\tilde{Y}_m)}{\partial t} + \frac{\partial}{\partial x_j}\left(\bar{\rho}\tilde{u}_j\tilde{Y}_m\right) = \frac{\partial}{\partial x_j}\left(\left(\bar{\rho}D_m + \frac{\mu_t}{Sc_t}\right)\frac{\partial \tilde{Y}_m}{\partial x_j}\right) + R_m + S_m \tag{3.4}$$

where $\rho$ is the density, $t$ is the time, $i$,$j$ and $k$ correspond to the Cartesian coordinates and $u$ to the velocity components, $S_{mass}$ represents a source term that could be given by the addition of mass from a second phase or a function defined by the user, $p$ is the pressure, $\mu_t$ is the turbulent dynamic viscosity, $\delta_{ij}$ is the Kronecker symbol, $g_i$ is the gravity acceleration, $E$ is the total energy, $c_p$ is the specific heat at constant pressure, $Pr_t$ and $Sc_t$ are the energy turbulent Prandtl and turbulent Schmidt numbers equal to 0.85 and 0.7 respectively, $D_m$ is the molecular diffusivity of the species $m$, $Y_m$ is the corresponding mass fraction, $S_E$ is the source term in the energy equation, $R_m$ and $S_m$ are respectively the net production/consumption rate by chemical reaction for the species $m$ and the source term connected to any user defined source term of dispersed phase.

In the following chapters both laminar and turbulent flows are analysed. Therefore, the governing equations or the employed parameters vary according to the investigated flow. Furthermore, additional equations may be included when modelling turbulence, such as for k-ε turbulence models. The specifics of the models are presented in sections 3.2-3.3.

## 3.2 Laminar model

Laminar flows are characterised by smooth and regular paths, without the irregular fluctuations and swirls characterising turbulent flows. Reynolds (1883) reported that a water flow in a pipe is laminar for Re<2100. However, a limit of 1000 is generally accepted to define laminar flows, as it is not possible to define a distinct limiting value to characterise flows transitioning from laminar to turbulent regime. A range 1000<Re<4000 is indicated for transitional flows. The turbulent viscosity is absent in Equations (3.2)-(3.4) and diffusion is associated to the sole mass diffusion coefficient $D_{i,m}$. The laminar model will be applied in chapter 5 for the simulation of spark ignition in a quiescent hydrogen-air mixture.

## 3.3 Turbulence model

High Reynolds number flows involve small-scale turbulent fluctuations. In Direct Numerical Simulations the entire range of temporal and spatial fluctuations is numerically resolved, resulting in a computationally expensive and hardly attainable simulation for high Reynolds number and complex flows. On the other hand, the introduction of a turbulence model permits the treatment of Navier-Stokes equations without directly simulating the small scale turbulent fluctuations. In the following chapters both the currently possible approaches are employed: Reynolds-Averaged Navier-Stokes (RANS) and Large Eddy Simulation (LES) approaches. In a RANS approach, the whole range of turbulent scales is modelled and the averaged flow quantities are involved in the governing equations. The approach results in a significantly reduced computational effort, making it one favourable choice for many engineering applications. An LES approach resolves directly the large eddies, while the small eddies responsible for the turbulent kinetic energy dissipation are modelled. This approach requires a finer mesh than for RANS calculations, leading to more computationally expensive calculations. However, it bears the advantage of a more universal model for small eddies. The choice between the two approaches and the associated closure turbulence model is strictly dependant on several factors, such as the investigated class of problems, the required level of accuracy, computational time etc… Therefore, the following section is aimed to provide a mathematical overview of the models, while the reasoning behind the selection of a specific turbulence model will be discussed and justified along with the problem formulations.

### 3.3.1 RANS approach

In a RANS approach, the fluid variables are decomposed in two components: mean and fluctuating. In the selected approach, the mean velocity gradients in Equations (3.2) and (3.3) are related to the Reynolds stresses through the Boussinesq hypothesis. The RANS approach will be applied to fully turbulent flows. Therefore, k-ε turbulence models can be applied. They are selected for the study because of their robustness and less computationally expensive calculations. Two additional transport equations are solved for the turbulent kinetic energy, *k*, and turbulent dissipation rate, ε. Three variants of the model exist, and they mainly differ in the definition of turbulent viscosity, turbulent Prandtl number and generation/destruction terms in ε transport equation.

#### 3.3.1.1 Standard k-ε turbulence model

The standard k-ε turbulence model (Launder and Spalding, 1972) solves the transport equations for turbulence kinetic energy, *k*, and turbulent dissipation rate, *ε*, as follow:

$$\frac{\partial(\rho k)}{\partial t}+\frac{\partial(\rho k u_i)}{\partial x_i}=\frac{\partial}{\partial x_i}\left[\left(\mu+\frac{\mu_t}{\sigma_k}\right)\frac{\partial k}{\partial x_i}\right]+G_k+G_b-\rho\varepsilon-Y_M+S_\kappa, \tag{3.5}$$

$$\frac{\partial(\rho \varepsilon)}{\partial t}+\frac{\partial(\rho \varepsilon u_i)}{\partial x_i}=\frac{\partial}{\partial x_j}\left[\left(\mu+\frac{\mu_t}{\sigma_\varepsilon}\right)\frac{\partial \varepsilon}{\partial x_j}\right]+C_{1\varepsilon}\frac{\varepsilon}{k}(G_k+C_{3\varepsilon}G_b)-\rho C_{2\varepsilon}\frac{\varepsilon^2}{k}+S_\varepsilon \tag{3.6}$$

where $G_k$ and $G_b$ represent the generation of *k* by, respectively, mean velocity gradients and buoyancy, $Y_M$ is the contribution of the fluctuating dilatation in compressible turbulence to the overall dissipation rate, $\sigma_k$ and $\sigma_\varepsilon$ are the turbulent Prandtl numbers for *k* and *ε* equal to 1.0 and 1.3, $\nu$ is the kinematic viscosity. $C_{1\varepsilon}$and $C_{2\varepsilon}$ and $C_{3\varepsilon}$ are constants equal to 1.44 and 1.92, while $C_{3\varepsilon}$ is calculated as function of the flow velocity components with respect to the gravitational vector. $S_\kappa$ and $S_\varepsilon$ are user defined source terms. The turbulent viscosity is evaluated according to the following expression:

$$\mu_t=\rho C_\mu\frac{\kappa^2}{\varepsilon} \tag{3.7}$$

$C_\mu$is estimated empirically as 0.09. The application of the model is limited to fully turbulent flows.

#### 3.3.1.2 RNG k-ε turbulence model

The Renormalization Group method (Yakhot and Orszag, 1986) is characterised by the analytical calculation of the turbulent Prandtl numbers, $\alpha_\kappa$ and $\alpha_\varepsilon$, along with an improved formulation for ε. These modifications enhance the model performance for rapid strained

flows. Furthermore, the differential equation (3.8) for the effective turbulent viscosity widens the application of the turbulence model to low-Reynolds number flows:

$$d\left(\frac{\rho^2\kappa}{\sqrt{\varepsilon\mu}}\right) = 1.72\frac{\hat{\nu}}{\sqrt{\hat{\nu}^3-1+C_\nu}}d\hat{\nu} \tag{3.8}$$

where $\hat{\nu} = \mu_{eff}/\mu$ and $C_\nu \approx 100$. The turbulent viscosity evaluation at the high Reynolds number limit is evaluated as in Equation (3.7) with $C_\mu = 0.0845$. The transport equations for k-ε are defined as follow:

$$\frac{\partial(\rho k)}{\partial t} + \frac{\partial(\rho k u_i)}{\partial x_i} = \frac{\partial}{\partial x_i}\left[\alpha_\kappa \mu_{eff}\frac{\partial k}{\partial x_i}\right] + G_k + G_b - \rho\varepsilon - Y_M + S_\kappa \tag{3.9}$$

$$\frac{\partial(\rho\varepsilon)}{\partial t} + \frac{\partial(\rho\varepsilon u_i)}{\partial x_i} = \frac{\partial}{\partial x_j}\left(\alpha_\varepsilon \mu_{eff}\frac{\partial \varepsilon}{\partial x_j}\right) + C_{1\varepsilon}\frac{\varepsilon}{k}(G_k + C_{3\varepsilon}G_b) - \rho C_{2\varepsilon}\frac{\varepsilon^2}{k} - R_\varepsilon + S_\varepsilon \tag{3.10}$$

3.3.1.3 Realizable k-ε turbulence model

The realizable k-ε model (Shih et al., 1995) observes the transport equation for *k* as in standard k-ε model (Eq. 3.5) without involving the production of *k*, given by the term $G_k$. A different formulation for the ε destruction term is employed and it is given as:

$$\frac{\partial(\rho\varepsilon)}{\partial t} + \frac{\partial(\rho\varepsilon u_i)}{\partial x_i} = \frac{\partial}{\partial x_i}\left[\left(\mu + \frac{\mu_t}{\sigma_\varepsilon}\right)\frac{\partial \varepsilon}{\partial x_i}\right] + \rho C_1 S\varepsilon - \rho C_2\frac{\varepsilon^2}{k+\sqrt{\nu\varepsilon}} + C_{1\varepsilon}\frac{\varepsilon}{k}C_{3\varepsilon}G_b + S_\varepsilon \tag{3.11}$$

The turbulent Prandtl numbers $\sigma_k$ and $\sigma_\varepsilon$ assume the values 1.0 and 1.2, while the constants $C_{1\varepsilon}$and $C_{2\varepsilon}$ are equal to 1.44 and 1.90. A further improvement of the model is given by the alternative formulation for turbulent viscosity, which is based on a variable $C_\mu$. The model was validated against a wide range of flows, outperforming standard k-ε model particularly for the prediction of spreading rate in axisymmetric jets (ANSYS Fluent, Theory Guide, 2016) and solving the round-jet anomaly presented by Pope (1978).

### 3.3.2 LES approach

In the LES approach, the time-dependent Navier-Stokes equations (Eq. 3.1-3.4) are filtered out the eddies smaller than the applied filter or grid spacing. The filtering process results in unknown sub-grid stresses, which are modelled employing the Boussinesq hypothesis as in the RANS approach described above. Several models are available for the turbulent viscosity calculation. In the present study the RNG model, the Smagorinsky-Lilly model and the dynamic Smagorinsky-Lilly model are employed and they will be described in sections 3.3.2.1-3.3.2.3.

3.3.2.1 Smagorinsky-Lilly model

In the Smagorinsky-Lilly model (Smagorinsky, 1963) the turbulent viscosity is expressed as:

$$\mu_t = \bar{\rho} L_s^2 \sqrt{2\tilde{S}_{ij}\tilde{S}_{ij}} \tag{3.12}$$

$L_s$ is the subgrid scale mixing length and it is calculated as $L_s = min(\kappa_c d, C_s\Delta)$, where $\kappa_c$ is the von Kármán constant, $d$ is the distance from the nearest wall, $C_s$ is the Smagorinsky constant equal to 0.1 and Δ represents the local grid scale, which is calculated as the cubic root of the cell volume. $\tilde{S}_{ij}$ is the rate of strain tensor.

3.3.2.2 Dynamic Smagorinsky-Lilly model

In the Smagorinsky-Lilly model $C_s = 0.1$ was employed as it showed to better represent a wider range of flows compared to $C_s = 0.17$ as originally presented in the model (ANSYS Fluent, Theory Guide, 2016). However, its validity may change in certain conditions, such as in transitional flows. To obviate the model limitation, a dynamical formulation for $C_s$ as function of the resolved scales of motion was proposed by Lilly (1992). In Fluent, the range of variability of $C_s$ is 0-0.23. Complete description of $C_s$ calculation process is given in Lilly (1992).

3.3.2.3 RNG model

In RNG theory (Yakhot and Orszag, 1986) the effective viscosity $\mu_{eff} = \mu + \mu_t$ is calculated as:

$$\mu_{eff} = \mu\left[1 + H\left(\frac{\mu_s^2 \mu_{eff}}{\mu^3} - 100\right)\right]^{1/3} \tag{3.13}$$

where H is the heaviside function and $\mu_s$ is a parameter of the RNG SGS model given as:

$$\mu_s = \bar{\rho}(C_{RNG}\Delta)^2 \sqrt{2\tilde{S}_{ij}\tilde{S}_{ij}} \tag{3.14}$$

where $C_{RNG}$ is equal to 0.157 and $\tilde{S}_{ij}$ is the rate of strain tensor. For high Reynolds number $\mu_{eff}$ approaches $\mu_s$, reducing to the Smagorinsky-Lilly model, while for low Reynolds number $\mu_{eff}$ approaches the molecular viscosity, making the model suitable for reproducing not only turbulent but transitional and laminar regions too. Effective Prandtl and Schmidt numbers are evaluated according to the RNG theory and their complete description can be found in Bragin et al. (2013).

## 3.4 Combustion model

As shown in Equation (3.4), convection, diffusion and reaction source intervene in the mixing and transport of each of the chemical species. This section presents the models employed to define either the single or multiple chemical reactions occurring in the bulk phase of the flow.

### 3.4.1 Finite rate model

The Arrhenius expressions are employed to calculate the chemical source term $R_m$ in Equation (3.4). The net reaction term of the species *i* is evaluated as the sum of the $\hat{R}_{i,r}$ molar rates of the $N_R$ reactions involving species *i* times the corresponding molecular weight $M_{w,i}$:

$$R_i = M_{w,i} \sum_{r=1}^{N_R} \hat{R}_{i,r} \tag{3.15}$$

The molar rate of reaction is calculated as:

$$\hat{R}_{i,r} = \Gamma\left(\upsilon''_{i,r} - \upsilon'_{i,r}\right)\left(k_{f,r} \prod_{j=1}^{N} \left[C_{j,r}\right]^{\eta'_{j,r}} - k_{b,r} \prod_{j=1}^{N} \left[C_{j,r}\right]^{\eta''_{j,r}}\right) \tag{3.16}$$

where $\Gamma$ accounts for the effect of third bodies, evaluated as in Equation (3.17), $\upsilon'_{i,r}$ and $\upsilon''_{i,r}$ are the stochiometric coefficients for, respectively, reactant *i* and product *i* in the analysed *r* reaction, $k_{f,r}$ and $k_{b,r}$ are the forward and backward reaction rates and they are presented in Equations (3.18) and (3.19), *N* is the total number of chemical species, $C_{j,r}$ is the molar concentration of the species *j*, $\eta'_{j,r}$ and $\eta''_{j,r}$ are the rate exponents for reactant and product species *j* in reaction *r*.

$$\Gamma = \sum_{j}^{N} \gamma_{j,r} C_j \tag{3.17}$$

$$k_{f,r} = A_r T^{\beta_r} e^{-E_r/RT} \tag{3.18}$$

$$k_{b,r} = \frac{k_{f,r}}{K_r} \tag{3.19}$$

where $\gamma_{j,r}$ represents the third body efficiency of species *j*, $A_r$ is the pre-exponential factor, $\beta_r$ is the temperature exponent, $E_r$ is the activation energy for the reaction *r* and $K_r$ is the corresponding equilibrium constant, which depends on the change of free Gibbs energy. Combustion in Finite Rate model involves the whole CV volume, requiring fine meshes for an accurate calculation. Inaccuracy can be higher if the problem involves reactions with time scales much faster than convection and diffusion time scales, such as in multi-step reaction mechanisms, requiring smaller time steps.

### 3.4.2 Eddy Dissipation Concept

In turbulent combustion the reaction rate is controlled by the mixing of fuel and oxidizer. The Eddy Dissipation Concept (EDC) by Magnussen (1981) includes detailed chemical mechanisms in turbulent flows. The model is based on the assumption that chemical reactions take place in small turbulent structures, denominated fine scales, and not in the whole control volume. In RANS models, the fine-scale (indicated as *) length is modelled as:

$$\xi^* = C_\xi \left(\frac{\nu\varepsilon}{k^2}\right)^{1/4} \tag{3.20}$$

The volume fraction constant,$C_\xi$, is 2.1377 and $\nu$ is the kinematic viscosity. The time scale of the species reactions is evaluated as:

$$\tau^* = C_\tau \left(\frac{\nu}{\varepsilon}\right)^{1/2} \tag{3.21}$$

The time scale constant,$C_\tau$, is 0.4082. The rate of reaction of the species *i* is evaluated as follow:

$$R_i = \frac{\rho(\xi^*)^2}{\tau^*[1-(\xi^*)^3]}(Y_i^* - Y_i) \tag{3.22}$$

where $Y_i$ indicates the mass fraction of the species *i* and $Y_i^*$ is referred to the mass fraction over the time scale $\tau^*$.

In the LES approach the fine scale length is smaller than the filter width. It is modelled as function of the flow properties and cell size through the following expression:

$$\xi^* = C_\xi \left(\frac{u_\eta}{u_{sgs}}\right) \tag{3.23}$$

where $u_\eta$ is the Kolmogorov's velocity and is calculated as in Equation (3.24); $u_{sgs}$ is the residual velocity at the sub-grid scale level and it is given by Equation (3.25).

$$u_\eta = \left(\frac{\mu \cdot u_{sgs}^3}{\rho \cdot L_{sgs}}\right)^{\frac{1}{4}} \tag{3.24}$$

$$u_{sgs} = \frac{\mu_t}{\rho \cdot L_{sgs}} \tag{3.25}$$

The time scale of reaction in the fine scale structures is given by:

$$\tau^* = C_\tau \tau_\eta \tag{3.26}$$

where $\tau_\eta$ is the Kolmogorov time scale which is defined as:

$$\tau_\eta = \left(\frac{\mu \cdot L_{sgs}}{\rho \cdot u_{sgs}^3}\right)^{\frac{1}{2}} \tag{3.27}$$

A detailed description of the model is given in Bragin et al. (2013).

### 3.4.3 Multi-phenomena deflagration model

In this section the model developed in Verbecke et al. (2009) is presented and discussed. The model was originally developed for very large eddy simulation (VLES) of deflagration for non-uniform hydrogen-air quiescent mixture. In the present work, the multi-phenomena deflagration model will be adapted to RANS k-ε modelling of deflagration in turbulent flows. Modifications to the model will be discussed below.

The premixed flame propagation is modelled through the progress variable *c* equation:

$$\frac{\partial(\bar{\rho}\tilde{c})}{\partial t} + \frac{\partial}{\partial x_j}\left(\bar{\rho}\tilde{u}_j\tilde{c}\right) = \frac{\partial}{\partial x_j}\left(\frac{\mu_{eff}}{Sc_{eff}}\frac{\partial \tilde{c}}{\partial x_j}\right) + \overline{S_c} \tag{3.28}$$

The progress variable represents the mass fraction of products. The source term $\overline{S_c}$, representing the mass burning rate, is calculated with the gradient method as:

$$\overline{S_c} = \rho_u S_t |grad\tilde{c}| \tag{3.29}$$

where $\rho_u$ is the density of the unburnt mixture and $S_t$ is the turbulent flame speed. Transport equations similar to (3.28) are employed for conservation of air and hydrogen, considering the consumption of hydrogen and air through the addition of a source term calculated as function of the mass burning rate $\overline{S_c}$. The source term $S_E$ in the energy conservation equation (Eq. 3.3) is calculated as $\overline{S_E} = H_c\overline{S_c}$. The chemical kinetics is taken into account in the calculation of the laminar burning velocity, which depends on the local concentration of hydrogen, pressure and temperature ($S_u$). The laminar burning velocity is calculated as function of the relative hydrogen mole fraction so that the variation of composition in the flame front would not affect it. The data reported in (Lamoureux et al., 2002) are employed to evaluate the laminar burning velocity.

The turbulent burning velocity includes the effect of flow turbulence ($\Xi_{turb}$), turbulence produced by the flame front ($\Xi_{karl}$), preferential diffusion ($\Xi_{lp}$) and the increase of flame radius with respect to the flame thickness ($\Xi_{fract}$):

$$S_t = S_u \cdot \Xi_{turb} \cdot \Xi_{karl} \cdot \Xi_{lp} \cdot \Xi_{fract} \tag{3.30}$$

Verbecke et al. (2009) developed the model for modelling deflagration in non-uniform hydrogen-air mixture in quiescent conditions. In this work, the model is applied to simulate

the delayed ignition of a high-pressure hydrogen jet. By the time of ignition, a turbulent non-uniform mixture is formed. Therefore, the model was modified to omit the transition from laminar, but a self-similar fully developed turbulent combustion regime is considered in the calculation of the wrinkling factors $\Xi$ since the moment of ignition. The effect of turbulence is calculated as $\Xi_{turb} = \exp(u'/S_t)^2$, which originates from the equation for turbulent flame speed derived from the renormalization group theory for premixed turbulent combustion (Yakhot, 1988). The turbulent velocity was calculated as $u' = \sqrt{2/3\,k}$. The second mechanism considers the turbulence generated by the flame front itself which further increases its extension, as theorised by Karlovitz et al. (1951). The flame wrinkling factor is calculated as $\Xi_{karl} = \psi \cdot \Xi_{karl,max}$. $\psi$ is an empirical coefficient, which is computed as function of hydrogen concentration according to (Molkov and Bragin, 2015). The maximum theoretical value of the factor is given by $\Xi_{karl,max} = (E_i - 1)/\sqrt{3}$ where $E_i$ is the expansion coefficient of the combustion products, which is calculated as $E_i = \rho_u/\rho_b$. The products composition and properties, such as the density $\rho_b$, are calculated for a GRI mechanism with 18 species through Cantera. A further mechanism is represented by the preferential diffusion which increases in significance for lean-hydrogen mixtures. $\Xi_{lp}$ is calculated as function of hydrogen concentration according to (Zimont and Lipatnikov, 1995). Given the initial turbulence level of the mixture, it is assumed that the hydrodynamic instabilities produced by the leading flamelets are fully developed and maximum. The flame is assumed to be self-turbulent since the moment of ignition and to propagate with a fractal-like structure. Following the considerations made in (Verbecke et al., 2009), the fractal wrinkling factor was calculated as $\Xi_{fract} = \left(R_{flame}/\varepsilon\right)^{D-2}$. $R_{flame}$ is the radius of the flame, $\varepsilon$ is the inner cut-off and $D$ is the fractal dimension. The inner cut-off is supposed to be comparable to the flame thickness. However, the minimum scale that can be modelled corresponds to the control volume size, which was considered as the inner cut-off in this study. The fractal dimension is calculated according to the empirical parametrization defined by North and Santavicca (1990) as:

$$D = \frac{2.05}{\frac{u'}{S_u}+1} + \frac{2.35}{\frac{S_u}{u'}+1} \tag{3.31}$$

In conclusion, the turbulent flame speed including all the mentioned effects is defined as:

$$S_t = S_u \cdot \exp(u'/S_t)^2 \cdot (\psi \cdot \Xi_{karl,max}) \cdot \Xi_{lp,max} \cdot \left(\frac{R_{flame}}{CV_{size}}\right)^{D-2} \tag{3.32}$$

A detailed description of the model features and parameters can be found in Verbecke et al. (2009). A second formulation of the model employed a different definition for the fractals wrinkling factor. In this case the fractal coefficient was decomposed in the quantity $\frac{R_{flame}}{Cv\ size}$

which is assumed to be resolved in the calculation, whereas the quantity $\frac{CV_{size}}{\varepsilon}$ is modelled. The inner cut-off is considered to be proportional to the Kolmogorov length scale, calculated as in Equation (3.34).

$$\Xi_{fract} = \left(\frac{R_{flame}}{\varepsilon}\right)^{(D-2)} = \left(\frac{R_{flame}}{CV_{size}} \cdot \frac{CV_{size}}{\varepsilon}\right)^{(D-2)} \approx \left(\frac{CV_{size}}{\eta_k}\right)^{(D-2)} \tag{3.33}$$

$$\eta_K = \left(CV_{size}\left(\frac{\mu_t}{\rho_u u'}\right)^3\right)^{1/4} \tag{3.34}$$

A similar definition of $\Xi_{fract}$ as in Equation (3.33) was applied to a LES approach along with the RNG turbulence sub-grid model. In this case the turbulent SGS length, calculated as $L_{sgs} = C_{RNG} CV_{size}$, was considered as the limit resolution. The quantity $\frac{L_{sgs}}{\eta_k}$ was modelled and $\frac{R_{flame}}{L_{sgs}}$ was assumed to be resolved in the flow. The resulting fractals wrinkling factor is given in Equation (3.35). The Kolmogorov length scale (Eq. 3.36) was calculated considering the SGS parameters.

$$\Xi_{fract} = \left(\frac{L_{sgs}}{\eta_k}\right)^{(D-2)} \tag{3.35}$$

$$\eta_K = \left(L_{sgs}\left(\frac{\mu}{\rho_u u'_{sgs}}\right)^3\right)^{1/4} \tag{3.36}$$

The SGS turbulent velocity was calculated employing the definition of unresolved SGS turbulent kinetic energy, which leads to the expression:

$$u'_{sgs} = \sqrt{\frac{2}{3}}\,\frac{\mu_t}{\rho \cdot L_{sgs}} \tag{3.37}$$

## 3.5 Radiation model

In the present study, only the Discrete Ordinates (DO) model, as developed in Murthy and Mathur (1998), is employed to simulate radiation. The reason behind the selection is its applicability to a wide range of optical thicknesses. The participating medium is assumed as a gray gas. The Radiative Transfer Equation (RTE) is solved for a finite number of solid angles $\Omega'$ associated to the direction $\vec{s}$:

$$\nabla(I\,(\vec{r},\vec{s})\vec{s}) + (\kappa + \sigma_s) I\,(\vec{r},\vec{s}) = \kappa n^2 \frac{\sigma T^4}{\pi} + \frac{\sigma_s}{4\pi}\int_0^{4\pi} I\,(\vec{r},\vec{s}')\,\emptyset(\vec{s}\cdot\vec{s}')d\Omega' \tag{3.38}$$

where *I* is the radiation intensity, treated as transported quantity along the direction $\vec{s}$, $\vec{r}$ is the position vector in $\vec{s}$ direction, $\kappa$ and $\sigma_s$ are respectively the absorption and scattering coefficients, *n* is the refractive index and $\Phi$ is the scattering phase function. The direction $\vec{s}$ of

the control angle is determined by the polar and azimuthal angles, respectively $\theta$ and $\phi$. The number of divisions for each of these angles, respectively $N_\theta$ and $N_\phi$, is given as input by the user, allowing a finer spatial discretization and more accurate calculation when needed. On the other hand, increasing the number of divisions will vary the computational cost accordingly. Example of the effect is given in Section 4.2.3.1.4. The number of solid angles determined for each octant of the 4π space is $N_\theta N_\phi$ (at any spatial location). Considering all the directions solved in the 3D space, the number will be $8\,N_\theta N_\phi$ (ANSYS Fluent, Theory Guide, 2016).

A further aspect to consider in radiation modelling is the angle overhanging, due to the non alignment of global angular and control volume discretization as shown in Figure 3.1 (right). In this case, the solid angles (dashed lines) might be in part incoming and outgoing to the cell face. The solid angle is further subdivided in pixels, so that the incident radiation can be treated as incoming or not.

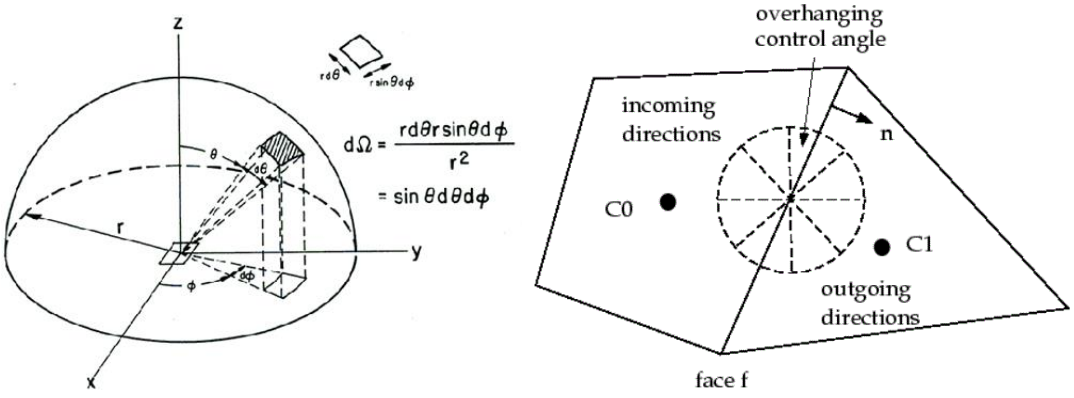


Figure 3.1 Left: solid angle representation (Thermopedia, 2016); right: face with control angle overhang (Fluent, 2016)

## 3.6 Gas state equations

The density for incompressible ideal gas is calculated as:

$$\rho = \frac{p_{op}}{\frac{R}{M}T} \tag{3.39}$$

where $p_{op}$ is the operating pressure, $R$ is the universal gas constant, $M$ and $T$ are the molecular weight and temperature of the gas.

For compressible flows, the gas law includes the local gauge pressure $p$ and it is given by:

$$\rho = \frac{p_{op}+p}{\frac{R}{M}T} \tag{3.40}$$

The ideal gas law results to higher inaccuracies with the increase of gas pressure and decrease of temperature. The study on rupture of tank rupture in a fire (Chapter 7) involves hydrogen pressurised up to 70 MPa, which rapidly undergoes an expansion to ambient pressure. Therefore, in preliminary calculations of the study two real gas equations of state are considered. Redlich-Kwong EOS (Redlich and Kwong, 1949) was selected because of the simple implementation and formulation. The equation of state is formulated as:

$$P = \frac{RT}{V-b} - \frac{\alpha}{V(V+b)T^{0.5}} \tag{3.41}$$

where $P$ is the absolute pressure, $V$ is the specific molar volume, $a$ and $b$ are constants associated to the critical pressure and temperature of the gas. However, Redlich-Kwong accuracy decreases for gases approaching or achieving the liquid state. On the other hand, Peng-Robinson equation (Peng and Robinson, 1976) yields to better prediction also for liquid density and it is written as:

$$P = \frac{RT}{V-b} - \frac{\alpha}{V^2+2V-b^2} \tag{3.42}$$

# 4 Free jet fire thermal hazards

## 4.1 Introduction

Cryo-compression is a competitive technique when storage of large quantities of hydrogen is needed, such as in stationary applications (DOE, 2006). On the other hand, the main currently considered technology for onboard hydrogen storage in automotive applications is the high-pressure gas compression (350-700 bar). In the case of release from a damaged pressurised storage system or Thermal Pressure Relief Device (TPRD) opening, hydrogen is likely to ignite producing a jet fire. The consequent flame length can cover distances of tens of meters and cause life-threatening conditions by the flame itself and thermal radiation. Predictive tools shall be developed to be used in hydrogen safety engineering to assure safer deployment of hydrogen technology and related infrastructure. Computational Fluid Dynamics (CFD) proved to be a practical predictive tool for modelling realistic accident scenarios and quantifying the related hazards.

The first section of this chapter (4.2) aims at a better understanding of consequences of potential accidents involving jet fires originated by releases of cryogenic hydrogen. Only a few experiments have been performed to investigate thermal hazards from cryogenic jet fires. Friedrich et al.'s experiments performed in Germany concerned releases with pressures from 7 to 35 bar abs and temperature in the range 34-65 K (Friedrich et al., 2012). Flame stability, combustion regimes and thermal radiation were analysed. The Health and Safety Laboratory (HSL) in UK performed experiments on 60 l/min spills of LH2 combustion and estimated that the minimum safety distance to avoid damage from jet fire thermal effects shall be about 14 m (Hall et al., 2014). The most recent experiments on cryogenic hydrogen jet fires were conducted at Sandia National Laboratories (SNL) in USA (Panda and Hecht, 2016). The radiative thermal heat flux and flame length were analysed for release temperature 37-295 K and pressures up to 6 bar abs. It was found that for a constant mass flow rate, the radiative heat flux increases for colder release temperatures, as consequence of the higher flame residence time. The present study simulated a selection of these experiments using Fluent as computational engine. Several numerical studies investigated liquefied (LH2) and cryogenic hydrogen unignited jets such as Venetsanos and Giannissi (2016), Giannissi and Venetsanos (2018), Venetsanos and Bartzis (2007), while there is a lack of investigations on ignited releases, i.e. jet fires. Therefore, the aim of this part of the research is to develop and validate a CFD model to predict radiative heat fluxes from a cryogenic jet fire at different locations from the flame. As part of the model development, a parametric study has been conducted, giving insights into the effect of several parameters and model assumptions on simulation results.

The second section of this chapter (4.3) moves towards applications involving higher storage pressures. Several numerical studies have been conducted on modelling and simulation of high pressure hydrogen jet flames targeting to reproduce the flame length and width, such as Brennan et al. (2009), Houf et al. (2009) and Zheng et al. (2012). However, fewer studies have analysed the emitted thermal radiation to validate radiation simulations against experiments (Wang et al., 2014). The present study is aimed to simulate dynamics of the radiative heat transfer and flame length of a hydrogen jet fire resulting from the high-pressure tank blowdown.

## 4.2 Cryogenic Jet Fires

This study is based on the conference publication "Thermal radiation from cryogenic hydrogen jet fires" (Cirrone et al., 2017a), submitted at the International Journal of Hydrogen Energy.

### 4.2.1 Validation experiments

The experiments were conducted at the Turbulent Combustion Laboratory of SNL in USA. The main aim of the experiments was to investigate the ignition and flame characteristics of cryogenic under-expanded jet fires. The analysed scenarios were concerned with hydrogen releases with temperature in the range 37-295 K and pressure 2-6 bar abs. The release temperature and pressure were maintained constant during each test and monitored upstream the interchangeable orifice of diameter 0.75 mm or 1 mm or 1.25 mm. The hydrogen was released vertically upward in the laboratory equipped with an exhaust gases collection system. The facility geometry and dimensions are presented in Figure 4.1. The exhaust hood volumetric flow rate was varied from approximately 5100 to 7650 $m^3$/h, depending on the hydrogen mass flow rate. The incident thermal radiation was monitored at 5 sensors located along the jet flame and at 0.2 m from the jet axis. The exact location of each sensor is shown in Figure 4.1. The flame length was given as average of the visible and infrared (IR) cameras images. 5 tests out of the entire set of experiments performed by SNL have been selected for the CFD model development and validation. Table 4.1 shows the details of the experimental operating conditions of the selected tests. Details of the experimental setting were provided by the author of the experiments in private communication (Panda, 2016). The orifice diameter for selected tests was 1.25 mm.

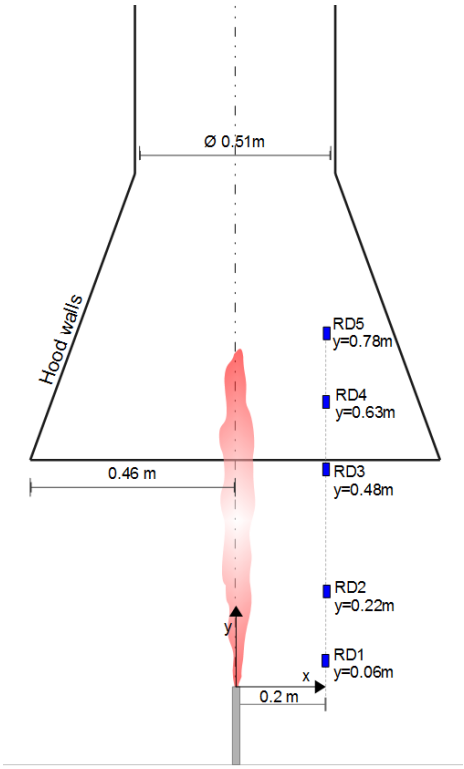


Figure 4.1 Scheme of the experimental set-up

Table 4.1 Experimental operating conditions of 5 validation tests (Panda, private communication, 2016)

| *Test No.* | *Mass flow rate, g/s* | *Temperature, K* | *Pressure, bar abs* |
|---|---|---|---|
| *1* | 0.33 | 64 | 2 |
| *2* | 0.38 | 48 | 2 |
| *3* | 0.45 | 75 | 3 |
| *4* | 0.56 | 78 | 4 |
| *5* | 0.64 | 82 | 5 |

### 4.2.2 Numerical details

4.2.2.1 Governing equations

The Reynolds-Averaged Navier-Stokes (RANS) conservation equations for mass, momentum, energy and species were solved (Eq. 3.1-3.4). A full description of the following models is given in section 3.3.1. Turbulence was accounted using the realizable k-ε model (Shih et al., 1995). Its performance was compared against standard k-ε model (Launder and Spalding, 1972) and RNG k-ε model (Yakhot and Orszag, 1986). Combustion was modelled through the Eddy Dissipation Concept (EDC) by Magnussen (1981), which includes detailed chemical mechanisms. In the present model, 18 elementary reactions and 9 species are considered for hydrogen combustion in air. Complete description of chemical reaction mechanism is given in Molkov et al. (2014). The DO model was employed to simulate radiation (Murthy and Mathur, 1998).

4.2.2.2 Modelling of release source

The operating pressure of the release in experimental tests is in the range 2-6 bar abs. At pressures above 2 bar abs an under-expanded jet is expected. The diameter of the notional nozzle was calculated using Ulster's under-expanded jet theory (Molkov, 2012), which assumes isentropic expansion, choked flow at the real nozzle, speed of sonic flow at the notional nozzle, and Abel-Noble equation of state (EOS) to describe the non-ideal behaviour of the high-pressure gas in the storage and at the real nozzle. Pressure and temperature in Table 4.1 were assumed as storage in stagnation conditions. As the release is cryogenic, the problem must be handled carefully. The stagnation conditions are all located in the vapour/gas phase. During expansion, the saturation curve may be crossed leading to a multiphase release. However, even considering the worst-case scenario, i.e. lowest recorded temperature (48 K), highest pressure (6 bar) and isentropic expansion to ambient pressure, the resulting point will be in the gaseous phase. In the experiments, the lower temperatures (< 60K) are coupled to pressure equal to 2 bar, distancing the nozzle conditions from the saturation curve. The second consideration regards the validity of Abel-Noble EOS for cryogenic releases. Abel-Noble EOS was compared to NIST EOS (NIST), which is generally employed to model $LH_2$ releases, such as in Venetsanos and Giannissi (2016), Giannissi and Venetsanos (2018), Venetsanos and Bartzis (2007). Density comparisons for several pressures are shown in Figure 4.2. The deviation is negligible for the range of pressure under study (2-6 bar) while it becomes significant as the pressure increases. For environmental pressure, as at the notional nozzle, Abel-Noble EOS, NIST EOS and ideal gas EOS density curves practically overlap, indicating interchangeability of EOSs. Thus, Abel-Noble EOS and the notional nozzle approach can be applied to the release cases under analysis.

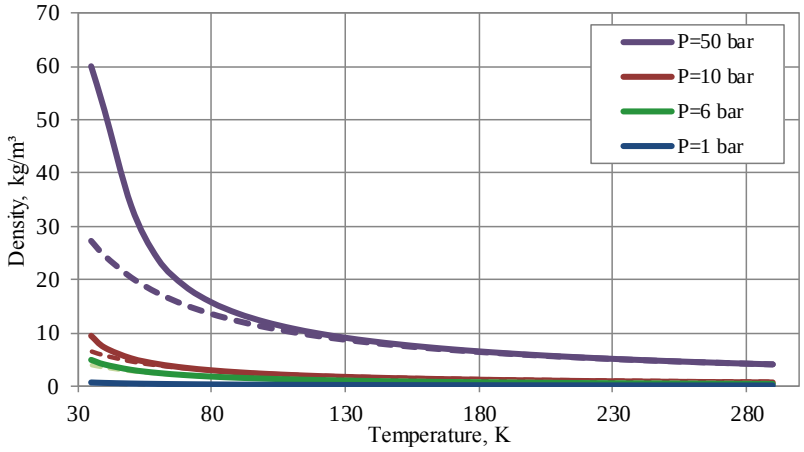


Figure 4.2 Effect of EOS on density evaluation: NIST (—) versus Abel Noble (--) equations

The calculated mass flow rate is compared against the experiments in Figure 4.3. The maximum deviation is about 10% and it is given for test 5. This discrepancy may be due to

measurements uncertainty, as the measured mass flow rate is lower than a test with equal diameter and pressure but higher temperature (T=91 K, m=0.66 g/s), while colder temperature should correspond to increase of released mass. The evaluated notional nozzle conditions are presented in Table 4.2.

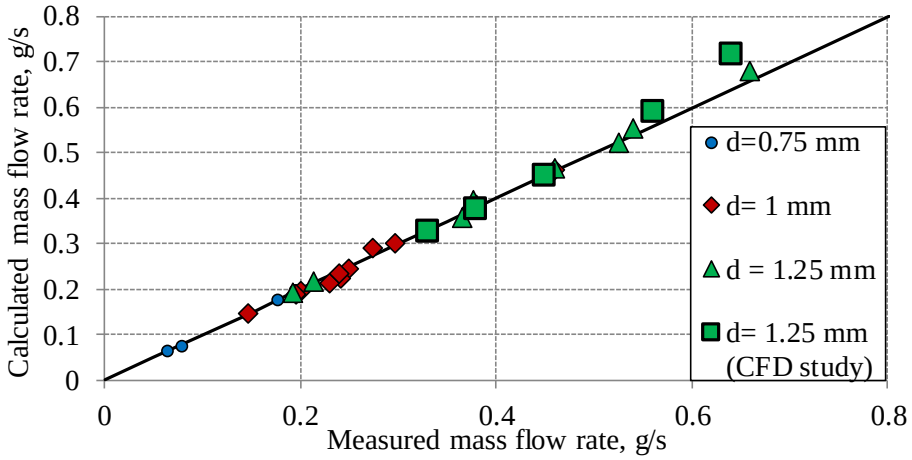


Figure 4.3 Calculated versus experimental mass flow rate

Table 4.2 Calculated notional nozzle conditions for the selected tests

| *Test No.* | *1* | *2* | *3* | *4* | *5* |
|---|---|---|---|---|---|
| *Inlet temperature, K* | 53 | 40 | 63 | 65 | 68 |
| *Inlet velocity, m/s* | 554.9 | 480.6 | 600.7 | 612.6 | 628.1 |
| *Density, kg/m$^3$* | 0.461 | 0.614 | 0.393 | 0.378 | 0.360 |
| *Notional diameter, mm* | 1.27 | 1.27 | 1.56 | 1.80 | 2.01 |
| *Calculated mass flow rate, g/s* | 0.326 | 0.376 | 0.451 | 0.589 | 0.717 |
| *Variation from experiment, %* | -1.26 | -1.10 | 0.25 | 4.93 | 10.78 |

4.2.2.3 Computational domain and grid

Given the axisymmetric nature of the problem, a quarter of the domain was considered for the analysis. Two calculation domains were used to perform simulations:

1. Rectangular domain with dimensions 0.5 m x 0.5 m x 3 m. The hood geometry was not included. The aim of the analysis was the investigation of the free jet fire characteristics without the effect of facility geometry and exhaust hood volumetric flow rate.

2. Rectangular domain with dimensions 1.2 m x 1.2 m x 2 m. The hood geometry was included in the numerical grid, as shown in Figure 4.4.

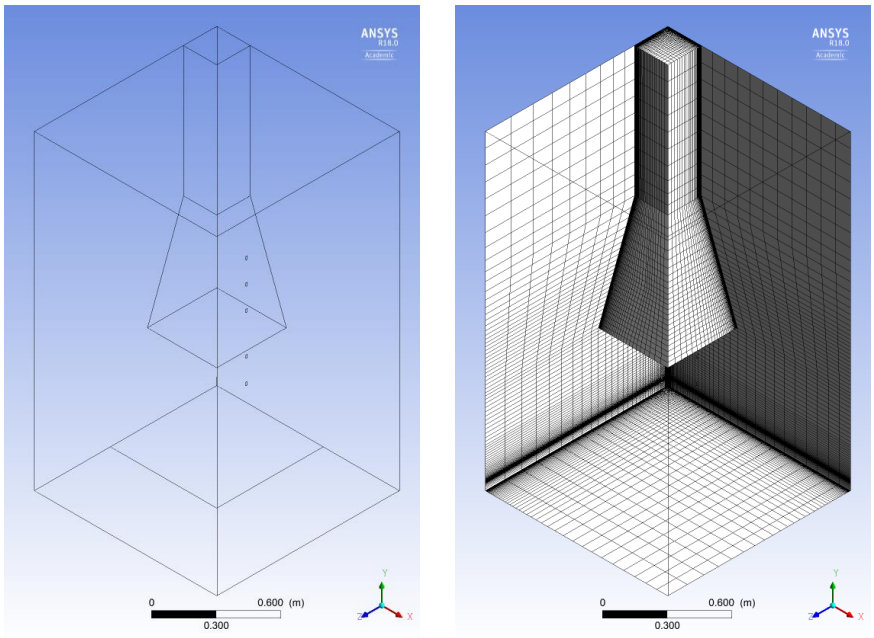


Figure 4.4 3D isometric view of computational domain and grid 2

The release source was approximated as square, with release area equal to the notional nozzle. As shown in Table 4.2, the 5 release tests resulted in 4 different notional nozzle diameters ($D_{eff}$). Thus, 4 numerical grids were created, adapting the release source and mesh to the test. The cell size varied from the notional nozzle size to about 10 cm in the far field. The maximum expansion ratio was 1.1 in the nozzle proximity. The number of control volumes (CVs) in the calculation domain varied, e.g. 267317 CVs in test 1, and 211587 CVs in test 5 for the domain including the hood. The releases were treated as steady-state, as the experimental facility was designed to release hydrogen at constant conditions. The velocity and temperature evaluated at the notional nozzle and indicated in Table 4.2 were imposed as inlet conditions at the nozzle. The turbulent intensity (TI) and turbulent length scale (TLS) were imposed as TI=25% and TLS=0.07$D_{eff}$, following the conclusions of the LES study on under-expanded hydrogen jet flame length and shape performed in (Brennan et al., 2009). TLS= 0.07$D_{eff}$ is usually indicated for fully developed pipe flows (ANSYS Fluent, Theory Guide, 2016). The domain boundaries were modelled imposing a gauge pressure=0 and dry air was considered. However, section 4.2.3.1.5 analyses the case with moist air. Possible condensation effect of $O_2$ and $N_2$ in proximity of the release was neglected, following the conclusions on horizontal liquid hydrogen release simulations by Ichard et al. (2012). The authors observed that condensation causes an increase of temperature up to 10 °C. The effect was restricted to a distance equal to 20$D_{exit}$, which corresponds to about 2.5 cm for the present case. Considering that combustion is present, it was assessed that condensation can be neglected. The surface beneath the release pipe was modelled as no slip adiabatic boundary. The radiometers were represented by 2x2 cm surfaces with 180° view, whereas in experiment their view was restricted to 150°. The

sensors were modelled as isothermal no slip walls with emissivity 1. In this way, no radiation will be reflected by the surface and the received radiative heat flux will take account of the entire incident radiation. The only absorbing/emitting species in hydrogen combustion is water vapour. In this study, it was treated as a grey gas with Planck mean absorption coefficient defined as function of temperature and $H_2O$ partial pressure. The function was determined from interpolation of Hubbard and Tien's data available in (Hubbard and Tien, 1978) and it will be indicated further in the text as HT. Scattering was not considered as it is negligible for combustion not involving soot. The Radiative Transfer Equation (RTE) was discretised using 5x5 angular divisions and 3x3 pixels, as suggested by (ANSYS Fluent, User's Guide, 2016). The radiative discretisation will be varied in the range 5x5-15x15 angular divisions and 3x3-10x10 pixels in section 4.2.3.1.4. SIMPLE procedure was chosen for velocity-pressure coupling and convective terms were discretized using the second order upwind scheme. The stainless-steel hood walls considered in section 4.2.3.2 were modelled as no slip walls with emissivity 0.6 (Omega, 2016). The above described characteristics constitute the initial settings of the problem. Several parameters were varied in the proposed sensitive study and they will be indicated and discussed in the following sections.

### 4.2.3 Results and discussion

The aim of this section is to analyse the effect of the modifications of a set of parameters on the simulated thermal radiation. The sensitivity study is presented for test 1, with the exception of section 4.2.3.2.2, where the results are shown for tests 4 and 5. The effect of each variation was investigated singularly and in sequence, selecting each time the best value/sub-model and applying it in the following part of the study. The effect of physical models or numerical features, such as the turbulence model or radiation discretisation, was assessed for a free jet fire configuration, to free results from further experimental uncertainties, such as the hood extraction velocity which is not known exactly for each release. Results are discussed in section 4.2.3.1. Analysis in section 4.2.3.2 includes the hood geometry, investigating the effect of the experimental settings, such as the exhaust gases extraction speed. Once the set-up of the model was completed, it was applied to the whole set of releases to validate it against experiments. Evaluations are shown in section 4.2.4.

#### 4.2.3.1 Free jet fire

The problem was formulated assuming incompressible ideal gas, thanks to the implementation of the notional nozzle approach, as explained in Section 4.2.2.2 However, to assure its correctness, the formulation was compared to the results obtained employing compressible ideal and real gas solvers. The axial temperature distribution was analysed as a term of comparison. It was noticed that the difference among the models is restricted to 5 cm distance

from the nozzle while it is negligible for the remaining part of the jet axis, confirmed by a maximum variation of 3% in flame length. In addition, the time required by the compressible solver was higher than the incompressible ideal gas formulation. Therefore, the assumption of incompressible ideal gas was maintained for the following analysis.

*4.2.3.1.1 Grid independency test*

A sensitivity study on the computational domain resolution was conducted at the initial stage, in agreement with the CFD model evaluation protocol (Baraldi et al., 2017). A finer mesh was created, heeding the regions where higher gradients and complex phenomena are expected. Thus, the length of the computational cells in proximity of the release point, the jet flame and the radiation sensors, was halved. An expansion ratio equal to 1.1 was maintained. The total number of CVs was increased from 196314 to 507524. The effect on the axial temperature distribution was found to be negligible, while slight differences were observed on its radial distributions. Figure 4.5 shows the radial distribution at 0.2 and 0.6 m from the release point for temperature and water vapour. The effect of the mesh refinement is limited to the proximities of the release point, resulting in a maximum difference of 5% for the radiative heat flux at the sensors RD1 and RD2 (y=0.22). Therefore, it is concluded that the built mesh using the minimum refinement (1 CV for the release point) can be used for the following analysis, as the mesh resolution is sufficient to solve accurately the problem.

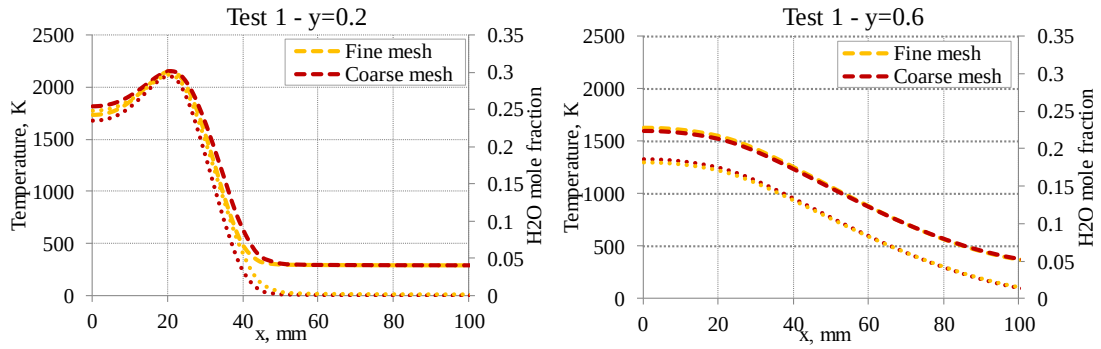


Figure 4.5 Grid independency study - radial temperature (---) and $H_2O$ mole fraction (...) distribution at 0.2 (left) and 0.6 m (right)

*4.2.3.1.2 Effect of turbulence model*

Simulations were performed for the standard k-ε, RNG k-ε and realizable k-ε turbulence models. The resulting axial temperature distribution is reported in Figure 4.6, showing significant differences. Considering a 1300-1500 K region as corresponding to the visible flame length (Schefer et al., 2004), the standard k-ε, RNG k-ε and realizable k-ε models resulted in flame length included in the range, respectively, 0.50-0.59 m, 0.38-0.44 m and 0.63-0.72 m. Experimental flame length, evaluated as average of visible and infrared

recordings, resulted 0.66 m. The realizable k-ε turbulence model gives the best result compared to experiment. However, it must be highlighted that flame length evaluations in experiments and simulations are somehow arbitrary and uncertain, mining the reliability of results. The different temperature distribution affects strongly the radiative heat flux, shown in Figure 4.7, where the 5 diamonds of each curve represent the records at the 5 sensors. The realizable k-ε model shows the best agreement with experiment. Visual representation of the flame is given in Figure 4.8 as comparison between standard k-ε and realizable k-ε models results.

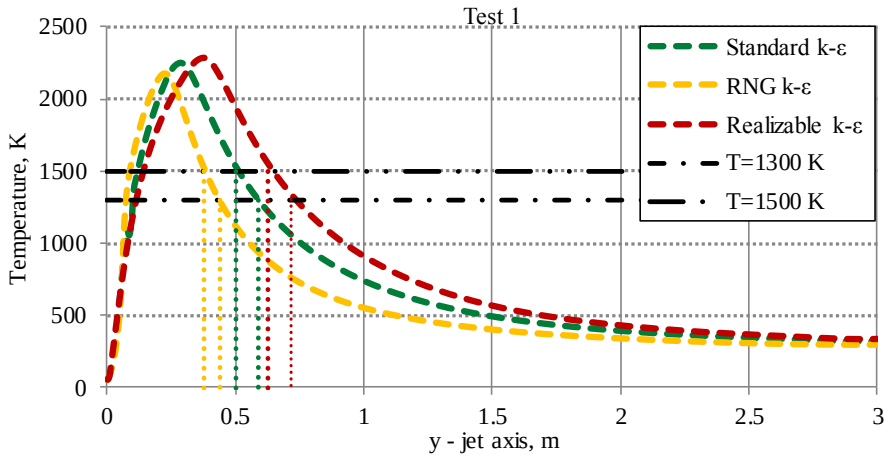


Figure 4.6 Effect of turbulence model on axial temperature distribution

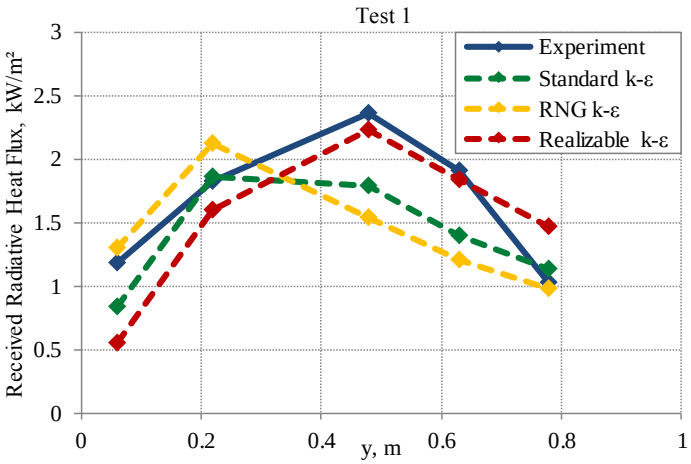


| Turbulence model | *Standard k-ε*<br>*RNG k-ε*<br>*Realizable k-ε* |
|---|---|
| TI and TLS | 25%, 0.07$D_{eff}$ |
| Angular divisions | 5x5 |
| Angular pixels | 3x3 |
| $mf_{H2O}$ | 0 |
| Absorption coefficient | HT |
| $Sc_t$ | 0.7 |

Figure 4.7 Effect of turbulence model on radiative heat flux

The temperature and velocity distribution along the jet axis were taken as indication of simulation convergence. The calculations were continued until no variation in the jet properties distribution was noticed. Furthermore, stabilisation of radiative heat flux at the 5 sensors was monitored, confirming convergence of properties on radial direction. The same convergence criteria were applied for all the following sections. For all the turbulence models, convergence was reached in about 40,000 iterations. However, the calculations differed in

terms of required computational time: standard k-ε and realizable k-ε turbulence models resulted in similar simulation durations, respectively 20 h and 22 h for 30 parallel processors machine, while RNG k-ε model resulted to be the most computationally expensive, requiring about twice the time.

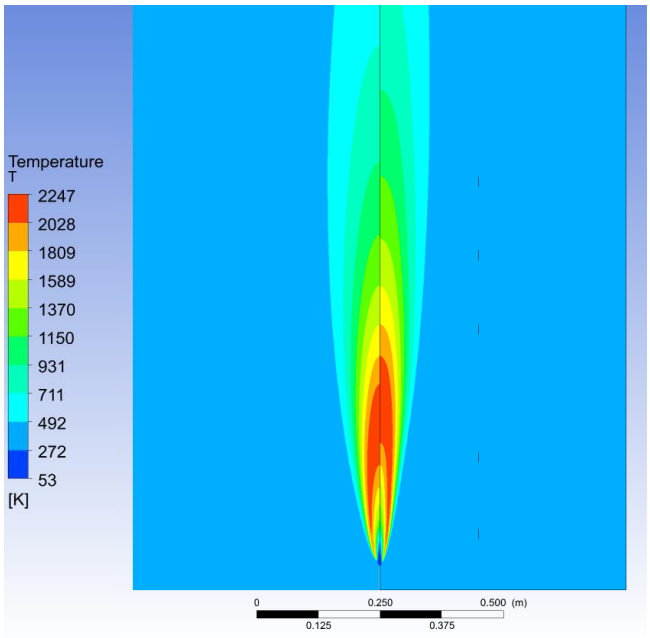


Figure 4.8 Temperature distribution on xy plane: standard k-ε (left) versus realizable k-ε (right)

*4.2.3.1.3 Effect of inlet turbulence intensity and turbulence length scale*

The current section is aimed to define the appropriate turbulence quantities at the inlet flow, i.e. at the notional nozzle exit. Indeed, these parameters affect the mixing occurring between the fuel and oxidizer, influencing the flame shape and species distribution in the jet fire. The flow perturbations at the inlet were modelled in terms of turbulence intensity and turbulence length scale. The case employing TI=25% and TLS=$0.07 \cdot D_{eff}$ was compared to: a) TI=4% and TLS=$0.07 \cdot D_{eff}$, based on experimental observations on air under-expanded jets (Chuech et al., 1989); b) TI=30% and TLS=$0.33 \cdot D_{eff}$, based on the results of a parametric study conducted at HySAFER on hydrogen jet concentration decay. Figure 4.9 demonstrates that the turbulence inlet parameters affect the radiative heat flux only in proximity of the release point. However, the difference is negligible for turbulence intensity and turbulence length scale lower than, respectively, 30% and $0.33 \cdot D_{eff}$. The effect on flame length was limited to ±2 cm variation. A further analysis was conducted for TI=30% and TLS=$0.07 \cdot D_{eff}$. The similarity of the results to the cases with equal TLS and different TI indicate that TLS is the cause of the variation for 30% and $0.33 \cdot D_{eff}$. However, if for 30% and $0.33 \cdot D_{eff}$ case the prediction improves for radiation sensor 2, it worsens for sensor 1. Therefore, the selected inlet conditions are turbulence intensity 25% and turbulence length scale $0.07 \cdot D_{eff}$.

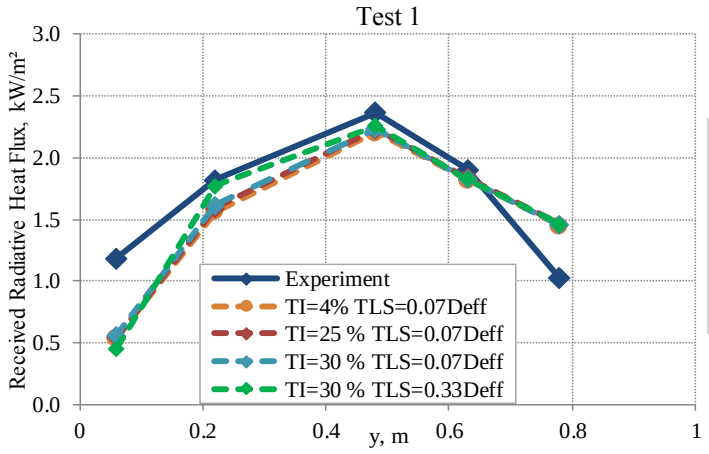


| Turbulence model | Realizable k-ε |
|---|---|
| TI and TLS | *4%, 25%, 30% 0.07D eff, 0.33D eff* |
| Angular divisions | 5x5 |
| Angular pixels | 3x3 |
| $mf_{H2O}$ | 0 |
| Absorption coefficient | HT |
| $Sc_t$ | 0.7 |

Figure 4.9 Effect of inlet turbulent intensity and turbulent length scale

*4.2.3.1.4 Effect of radiation model angular discretisation*

The number of Theta and Phi divisions determine the number of control angles associated to the RTE. 5x5 divisions are generally suggested for problems involving small geometry features and strong variation of temperature in space (ANSYS Fluent, User's Guide, 2016). Under-prediction of radiative heat flux at the radiometers located in proximity of the release point may be due to insufficient angular discretisation, preventing the sensors to receive the radiation emitted by the flame along all its length. Thus, the number of divisions was increased, maintaining the same number of pixels. Comparisons for 5x5, 7x7, 10x10 and 12x12 are shown in Figure 4.10. Case with 15x15 was also analysed but not reported in figure, as it practically overlaps the curves with 10x10 and 12x12 divisions. It was found that the angular discretisation has a great effect on the recorded radiative heat flux. Over 10x10 divisions the results are not sensitive to any further refinement. 10x10 was chosen as it is the adequate compromise between accuracy of the results and computational time (simulation time from 5x5 case increases by 1.9 for 10x10 and 2.4 for 12x12 angular divisions).

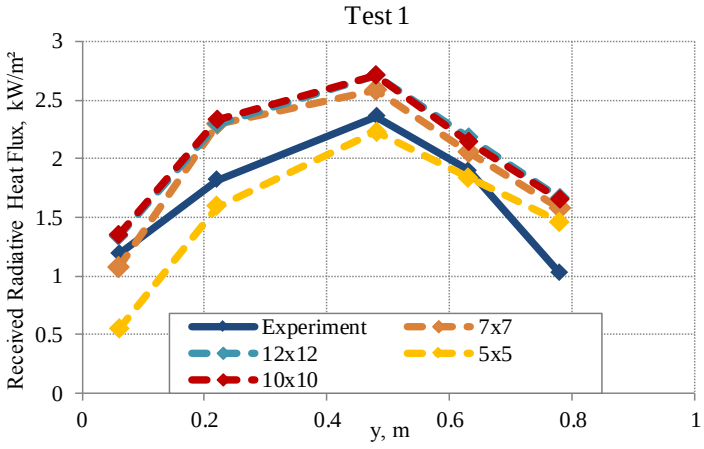


| Turbulence model | Realizable k-ε |
|---|---|
| TI and TLS | 25%, $0.07D_{eff}$ |
| Angular divisions | *5x5, 7x7, 10x10, 12x12, 15x15* |
| Angular pixels | *3x3, 10x10* |
| $mf_{H2O}$ | 0 |
| Absorption coefficient | HT |
| $Sc_t$ | 0.7 |

Figure 4.10 Effect of number of angular divisions (3x3 pixels)

The Theta and Phi pixels take account of any control angle overhang. When the control volume face is not aligned to the global angular discretisation, control angles may be partially outgoing and partially incoming to the face. Pixelation subdivides each control angle in smaller portions where energy can be treated as incoming or outgoing. 3x3 pixels are usually suggested for problems involving symmetry (ANSYS Fluent, User's Guide, 2016). The number of pixels was increased to 10x10 and no variation was sensed in the results. The reason may be due to the use of a rectilinear hexahedral mesh, where the control volumes faces are aligned to the angular discretization, preventing the control angle overhang problem to arise. Thus, 3x3 pixels are sufficient to obtain reliable results and they were used with 10x10 angular divisions in the following analysis.

*4.2.3.1.5 Effect of air humidity*

The initial assumption of dry air for a controlled laboratory environment may not be adequate and the effect of water vapour presence must be assessed. The amount of water vapour in air is highly variable, depending on location and time. Mass fraction equal to 0.008 was assumed, according to the average meteorological data for SNL location, i.e. relative humidity equal to 74% and temperature 288 K (Current Results, 2016). As shown in Figure 4.11, the presence of water vapour has a significant effect on simulation results, remarking how indispensable is the availability of accurate description of various test conditions from experimentalists, including relative humidity. In the following sections, moist air will be considered, as it is more realistic, and it provides better agreement with experiments.

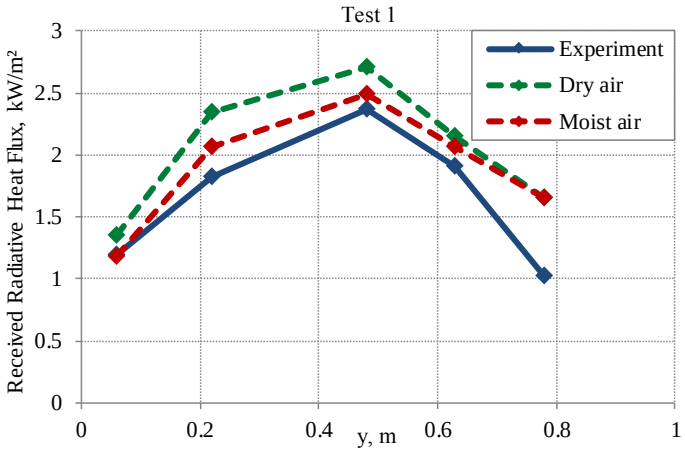


| Turbulence model | Realizable k-ε |
|---|---|
| TI and TLS | 25%, 0.07$D_{eff}$ |
| Angular divisions | 10x10 |
| Angular pixels | 3x3 |
| $mf_{H2O}$ | *0, 0.008* |
| Absorption coefficient | HT |
| $Sc_t$ | 0.7 |

Figure 4.11 Effect of water vapour presence in air

*4.2.3.1.6 Effect of absorption coefficient*

Hubbard and Tien's Planck mean absorption coefficient (HT) was compared to the coefficient evaluated according to Yan et al.'s (Y) calculations (Yan et al., 2015). The two coefficients mainly differ for temperatures lower than 800 K, where HT coefficient is higher than Y

coefficient. As shown in Figure 4.12, this difference is translated in less radiation at the sensors located close to the release point, as radiation from the flame has a longer distance to cover and, because of higher absorption coefficient, greater chance to be absorbed. Given the better agreement with experiments, HT formulation was selected for the model.

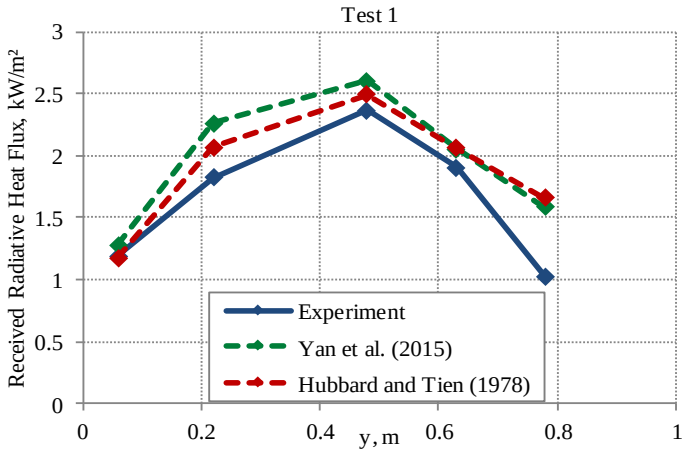


| Turbulence model | Realizable k-ε |
|---|---|
| TI and TLS | 25%, 0.07$D_{eff}$ |
| Angular divisions | 10x10 |
| Angular pixels | 3x3 |
| $mf_{H2O}$ | 0.008 |
| Absorption coefficient | *HT, Y* |
| $Sc_t$ | 0.7 |

Figure 4.12 Effect of absorption coefficient

*4.2.3.1.7 Effect of radiometer boundary conditions*

This section is aimed to quantify the effect of assumption for radiometers on the simulation results. As discussed in section 4.2.2.3, the sensors were modelled as isothermal no slip walls with emissivity 1. The isothermal assumption prevents the increase of sensors temperature because of absorbed radiation, maintaining the same temperature as for the environment, 288 K. However, if sensors are treated as coupled walls, their temperature would increase because of the absorbed energy. Therefore, there will be radiation losses from radiometers to their surroundings, affecting in a loop the net radiation received by the sensors. The simulation has shown that this contribution can cause increase up to 10% of the incoming radiation for sensor RD5, which is the most exposed to combustion products, while it is more contained for sensor RD1 (+2%). Further considerations were made on the typology of radiometers employed for the experiment. The window was made of Zn-Se, which is characterized by transmission between the useful wavelength range 0.5-22 μm and flat wavelength range 0.7-17 μm (Medtherm corporation, 2016). To assess the maximum effect on simulation results, a calculation was conducted restricting the absorbed radiation to the narrower wavelength range. It was observed a consistent decrease of the absorbed radiation in all the sensors (about -8%), reaching maximum variation equal to 13% for radiometer RD1.

4.2.3.2 Hood inclusion in the geometry

The laboratory was equipped with an exhaust gases system. Therefore, the combustion can be affected by the flow imposed at the hood. The extension of the computational domain

including the hood was decided according to a sensitivity study on the domain size. The width of the domain was changed from 0.7 m to 1.2 m. Maximum variation of radiative heat flux of about 8% was detected on sensor RD1, leading to the choice of domain size=1.2 m. To ensure that the domain boundaries are located sufficiently far from the area of interest, an additional sensitivity analysis was conducted on the domain boundary conditions. Turbulent kinetic energy and turbulent dissipation rate were varied from, respectively, $1.5 \cdot 10^{-4}$ $m^2/s^2$ and $3.0 \cdot 10^{-6}$ $m^2/s^3$ (evaluated for the analysis in section 4.2.3.2) to unitary values. The effect on radiative heat flux was confined to 4% variation, which was considered acceptable considering the needs to minimize the impact of boundary conditions on simulation results and to limit the required computational time. Figure 4.13 shows the comparison between the results of the free jet fire and the configuration including the hood. The removal of the combustion products by forced ventilation caused a decrease of radiative heat flux, reaching over 30% reduction. A further observation shall be made on emissivity for the stainless steel of the hood, as it may vary in a wide range according to the material composition and the maintenance status. A parallel analysis, not shown in Figure 4.13, on the variation of the hood surfaces emissivity was conducted, varying it from 0.60 to 0.07 (Omega, 2016). The maximum increase was +8% and it was detected on sensor RD5. Emissivity of 0.60 will be used in the following simulations.

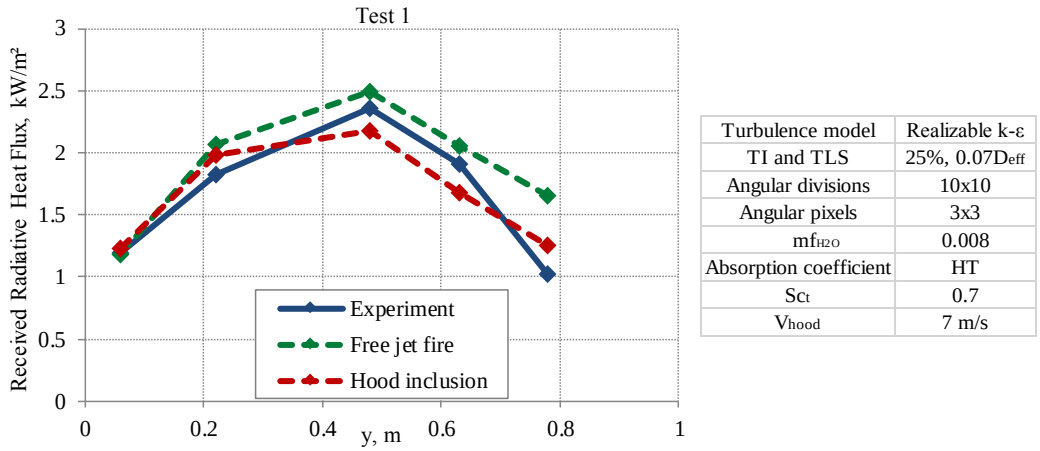


Figure 4.13 Effect of hood inclusion in the calculation domain (stainless steel emissivity=0.60)

*4.2.3.2.1 Effect of turbulent Schmidt number*

The turbulent Schmidt number, $Sc_t$, was changed in the range 0.7-1. The variation affected the temperature and species distribution in the jet. Figure 4.14 shows that the increase of $Sc_t$ causes the radiative heat flux from the first portion of the flame to decrease, while it has the opposite effect for the second half. The reason is due to the flame highest temperature region movement towards the flame tip, thus increasing the emitted radiation from the final part of the flame. $Sc_t$=0.9 was selected for the following analysis, as it reproduced better the experimental radiative heat flux distribution trend, decreasing the gap between simulation and experiment

for the sensors recording the highest radiative heat flux. In addition, $Sc_t$=0.9 gave the best reproduction for axisymmetric jets in the review proposed by (Tominaga et al., 2007).

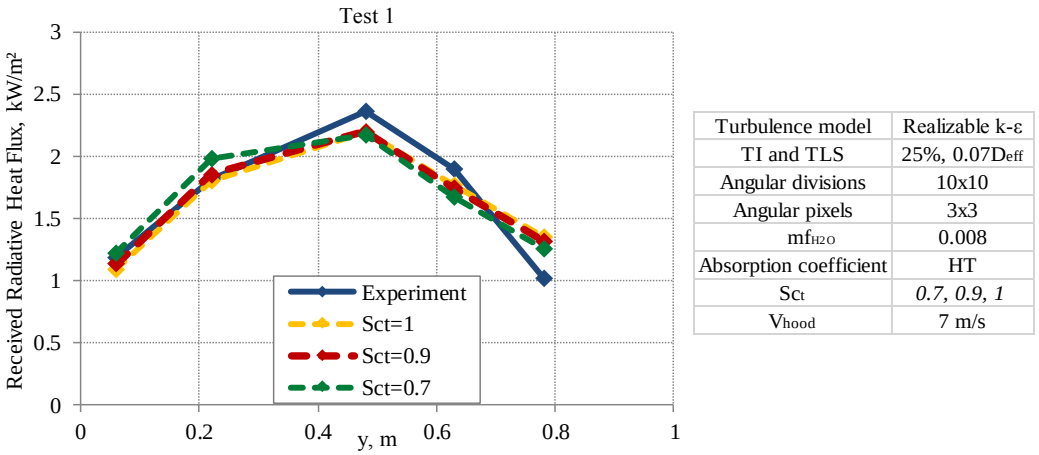


Figure 4.14 Effect of turbulent Schmidt number

*4.2.3.2.2 Effect of extraction velocity in the hood*

For each test, the volumetric flow rate of the ventilation system was adapted to the released mass flow rate of hydrogen. The only available experimental data is the range of variation of the volumetric flow rate, 5100-7650 $m^3/h$, corresponding to extraction velocity 7.0 m/s and 10.5 m/s respectively. No exact data for each test is available. Therefore, the minimum fumes speed has been considered in sections 4.2.3.2 and 4.2.3.2.1, based on the assumption that since the hydrogen mass flow rate (0.33 g/s) is closer to the minimum of the released mass range (about 0.1 g/s), the consequent extraction velocity will be more likely to be similar to the minimum of 7.0 m/s. However, tests 4 and 5 are characterised by a higher mass flow rate of 0.56-0.64 g/s, which is closer to the maximum mass flow rate of the overall tests set (0.7 g/s). Thus, fumes speed should be closer to 10.5 m/s rather than 7.0 m/s. This section aims to analyse the effect of the ventilation velocity on such releases, analysing the cases with minimum and maximum volumetric flow rate imposed at the hood as extreme cases. Figure 4.15 shows the effect of the hood extraction speed on the radiative heat flux. Since minimum and maximum limits were considered, the radiative heat flux curve simulating the actual fumes speed should be located between the green and red dashed curves, representing, respectively, the simulations for 7.0 and 10.5 m/s. For both the releases, considering the minimum extraction velocity led to a considerable overestimation (+36%) of the radiative heat flux for the sensors more exposed to the radiation from combustion products. The increase of the extraction velocity to the maximum limit, led to a reasonable reproduction of the experimental data, with deviations contained in the range ±14%. Therefore, extraction velocity of 10.5 m/s is considered for tests 4-5, while 7.0 m/s is considered for releases 1-3.

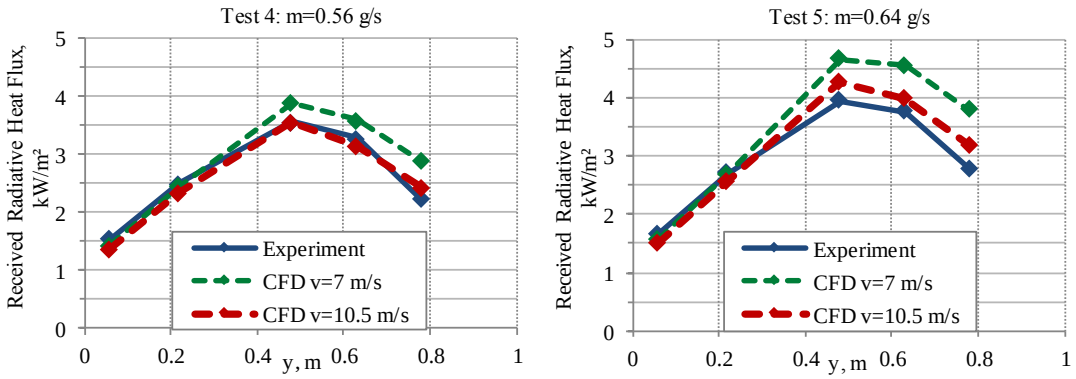


Figure 4.15 Effect of the hood extraction velocity in tests 4 and 5

### 4.2.4 Definition of model set-up based on the parametric study and validation

Following the conclusions of the previous sections, the best settings for the predictive model were identified and they are summarized in Table 4.3.

Table 4.3 Model set-up

| | |
|---|---|
| Turbulence model | Realizable k-ε |
| Turbulence intensity and length scale | 25% and 0.07$D_{eff}$ |
| Angular divisions | 10 x 10 |
| Angular pixels | 3 x 3 |
| Water vapour mass fraction | 0.008 |
| Absorption coefficient | Hubbard and Tien (1978) |
| Turbulent Schmidt number | 0.9 |
| Velocity at the hood | Tests 1,2,3: v=7.0 m/s<br>Tests 4,5: v=10.5 m/s |

Results for the 5 tests are shown in Figure 4.16. Experimental radiative heat flux is predicted in simulations within ±15%, which is acceptable for safety engineering design accuracy. There is one exception, i.e. the overestimations of flux at 5$^{th}$ sensor for tests 1 and 2, where radiation is 29% and 17.5% higher respectively. It must be reminded that this sensor is the most affected by the hood characteristics taken in simulations, such as the material emissivity or the hood geometry, which is approximated as square. In addition, the 5$^{th}$ sensor is the most exposed to the water vapour of the jet flame, strongly affected by the velocity field imposed by the extraction system. Since no precise volumetric flow rate was available for each test, the assumption of either minimum or maximum flow velocity in the hood can lead to inaccuracy of results. The water vapour, while accumulating and cooling down, may also be affected by condensation, which is not taken in account in simulation. Experimental data on relative

humidity were not available. Thus, the annual average for California (74%) was accepted. However, relative humidity is generally lower in environments where controlled air ventilation systems are present, such as combustion or chemical laboratories. Therefore, the slight under predicting trend present in most of the tests might be caused by such approximation.

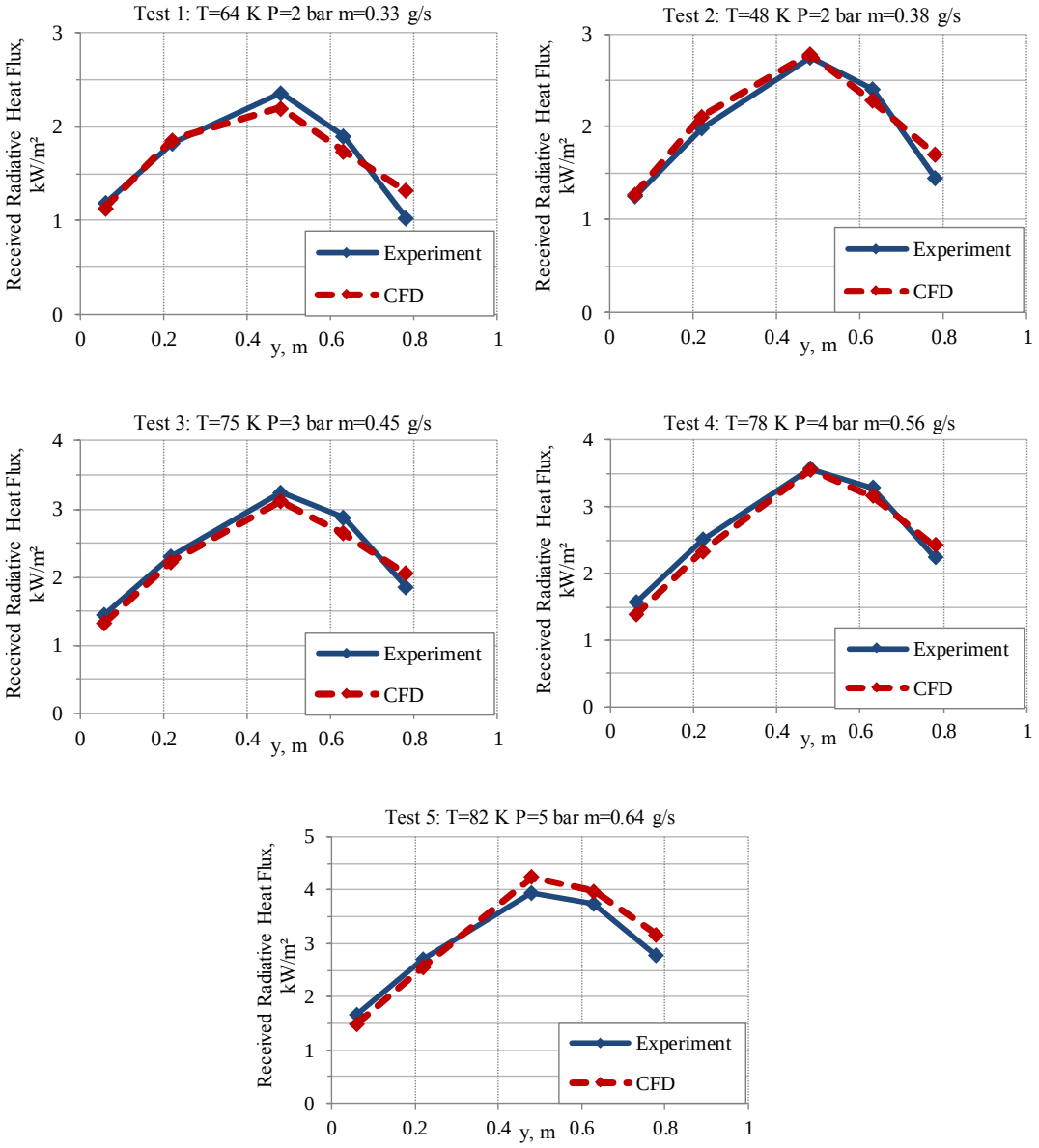


Figure 4.16 Radiative heat flux evaluation for validation experiments (model set-up: Table 4.3)

Table 4.4 reports the flame length evaluations based on the range of temperature 1300-1500 K and OH mole fraction=$10^{-3}$. In general, the simulated flame length resulted somewhat longer than reported by experimentalists. The difference becomes more significant for jet fires in tests 4 and 5. This can be due to the mass flow rate overestimations in simulations by, respectively, 5% and 10% of the release source modelling (Table 4.2). Similarly, overpredictions were

expected for the radiative heat flux, mainly for test 5. However, the maximum deviation was 14%, maintaining an acceptable accuracy of the results.

Table 4.4 Experimental and calculated flame length

| *Test No.* | *1* | *2* | *3* | *4* | *5* |
|---|---|---|---|---|---|
| *Experiment, m* | 0.66 | 0.70 | 0.72 | 0.74 | 0.78 |
| *CFD 1300 K, m* | 0.74 | 0.80 | 0.85 | 0.94 | 1.02 |
| *CFD 1500 K, m* | 0.65 | 0.70 | 0.74 | 0.82 | 0.88 |
| *CFD* $mf_{OH} = 0.001$*, m* | 0.67 | 0.76 | 0.78 | 0.88 | 0.94 |

In section 2.4.2 a methodology for calculation of separation distances from hydrogen jet fires was presented (Molkov, 2012). The engineering tool is based on the definition of harm criteria for people following the exposure at a certain temperature. In the present case, it is not possible to investigate the temperature distribution at distances greater than 2 m from the release point due to the limitation of the domain and the presence of the exhaust gases removal system, which would certainly affect the temperature distribution. Therefore, the separation distances were calculated from the jet fire flame length, as presented in Molkov (2012). The average of the calculation for temperature 1300 K and 1500 K was considered, as this is the region on the jet axis where the flame tip is generally located. Results for the 5 tests are presented in Table 4.5. It is shown that the distance from the release point indicated for "no harm" of people can vary from 2.43 m for test 1 to 3.33 m for test 5. The tool allows calculation of separation distances only along the axis of the jet fires. No information is given with regards to the sides of the jet fire, which could be of essential importance for first responders intervention in case of fire involving a FCHV. Moreover, the originated jet fires may be characterised by longer flames, due to the higher storage pressure and greater nozzle diameter. Therefore, calculation of separation distances on the sides of the jet fire will be addressed in the following section, through the evaluation of the thermal dose.

Table 4.5 Separation distances calculated according to the harm criteria for people considering the jet fire flame length

| *Test No.* | *1* | *2* | *3* | *4* | *5* |
|---|---|---|---|---|---|
| *average calculated flame, m* | 0.70 | 0.75 | 0.80 | 0.88 | 0.95 |
| *"no harm" limit, m* | 2.43 | 2.63 | 2.78 | 3.08 | 3.33 |
| *"pain" limit, m* | 2.09 | 2.25 | 2.39 | 2.64 | 2.85 |
| *"death" limit, m* | 1.39 | 1.50 | 1.59 | 1.76 | 1.90 |

### 4.2.5 Thermal dose evaluation

The thermal dose was evaluated for the free jet fire configuration resulting from section 4.2.3.1, as this would be the scenario of an accidental release in open space. Figure 4.17 shows the thermal dose distribution at several times of exposure for test 4. Maximum thermal dose was recorded inside the flame and it varied from $2.1 \cdot 10^5$ to $2.5 \cdot 10^7$ $(kW/m^2)^{4/3}s$ in the range of time 2-240 s. The graph legend is limited to maximum value 870 $(kW/m^2)^{4/3}s$, to represent distinctively the range of values characterising the thresholds defined in LaChance (2010), which are reported in Table 2.2 of Chapter 2. Higher thermal doses are represented in red as for 870 $(kW/m^2)^{4/3}s$. Unfortunately, the limitation of the domain to 0.5 m prevents the evaluation of thermal dose for a further distance. However, it is noticeable that 60 s exposition would result in first degree burns within 0.5 m from the jet flame axis. Figure 4.18 shows the thermal dose classified by the associated harm criteria for test 1, 2 and 4. As shown in Figure 4.17, the thermal dose is not uniformly distributed around the jet fire due to the changing properties and width along the flame, and its radial distribution depends on the distance from the release point. The maximum values in Figure 4.18 are calculated from maximum thermal dose recorded along the all flame height at a certain radial distance. It is possible to notice that the maximum exposure time to not be "harmed" by the flame within 0.5 m is lower than 30 s for all the 3 tests. At the same distance, 4 minutes results to be the maximum exposure time before third degree burns occurrence. It must be considered that radiation level in the surroundings of the jet is affected by the presence of water vapour in atmosphere, which in the present case corresponded to mass fraction equal to 0.008.

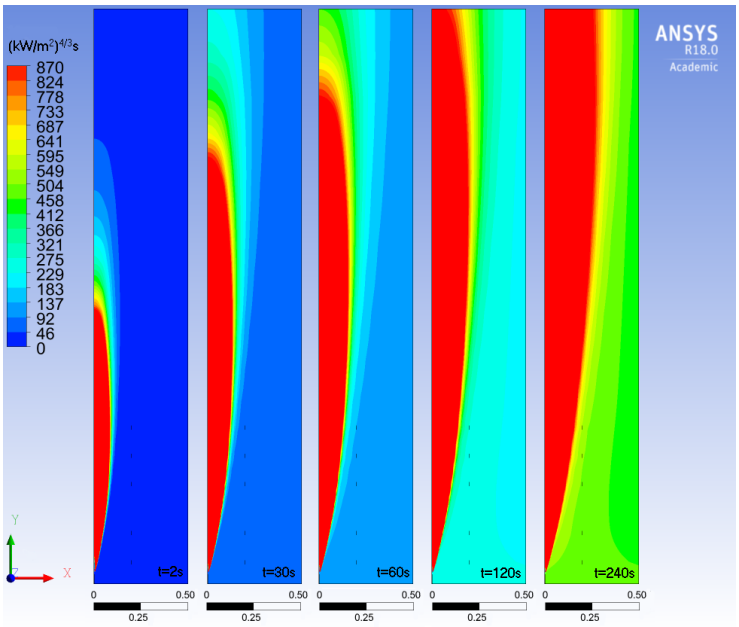


Figure 4.17 Calculated thermal dose distribution for test 4

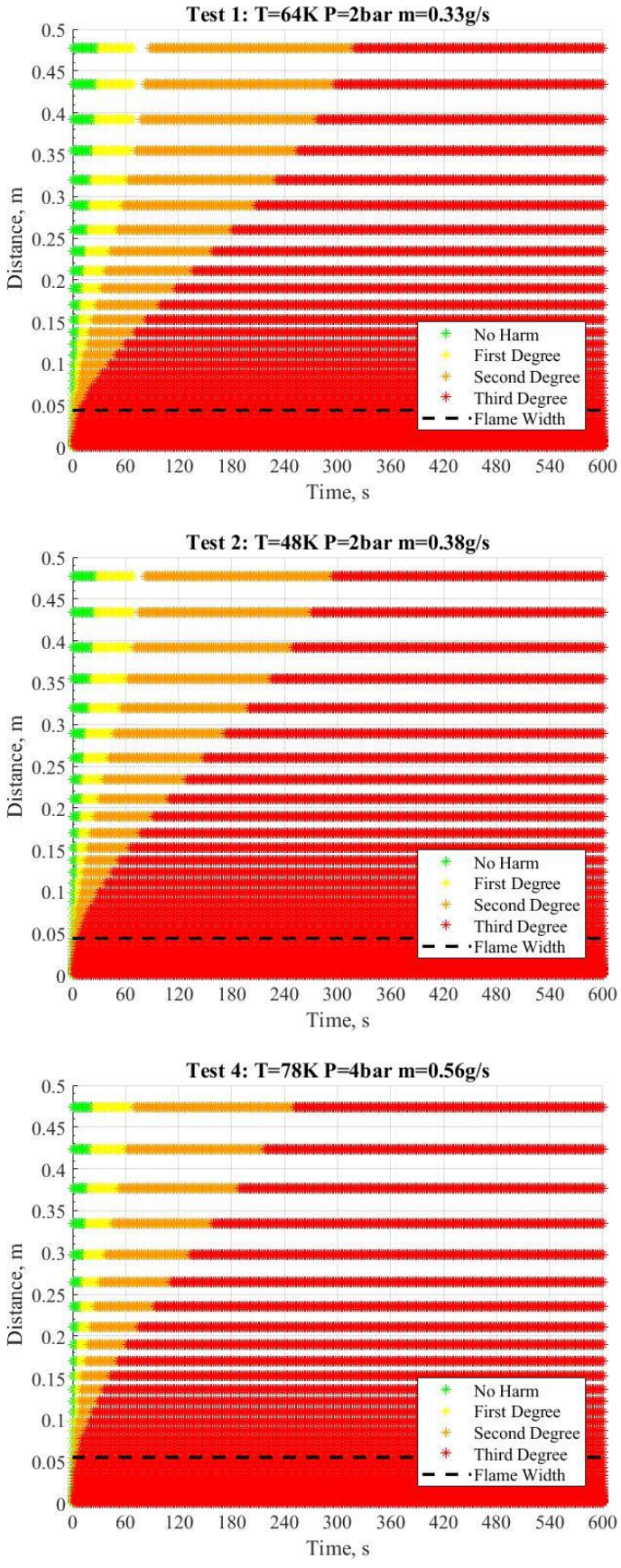


Figure 4.18 Thermal dose hazard distances: time versus distance for tests 1, 2 and 4

### 4.2.6 Concluding remarks

Simulations of cryogenic hydrogen jet fires were conducted to develop a predictive CFD model for assessment of thermal hazards. The simulations were validated against experiments in the range of pressures 2-5 bar abs and temperatures 48-82 K. Release source was modelled using the notional nozzle theory (Molkov, 2012). Three turbulence models were compared and realizable k-ε model demonstrated the best performance in reproducing the measured flame length and radiative heat flux. A sensitivity analysis of different parameters in simulations on thermal radiation from the jet fires has been carried out. The angular divisions' refinement for radiation model and humidity in air are shown to affect considerably the simulated radiative heat flux. 10x10 angular divisions' number was found to be the resolution, which provides independence of simulations on further refinement, for the problem under study. The presence of water vapour in air demonstrated a strong effect on the flame thermal radiation, causing variations up to 13%. Larger variations were found for different velocities at the hood for releases with higher hydrogen mass flow rate. Therefore, it is fundamental for experimental studies to make available exact measurements of test conditions to develop and validate predictive CFD models. The hydrogen inlet turbulence parameters, the absorption coefficient and turbulent Schmidt number showed to have a minor effect on radiative quantities. Turbulence intensity of 25% and turbulent length scale of $0.07 \cdot D_{eff}$ at the inlet, Hubbard and Tien's absorption coefficient model and $Sc_t$=0.9 were selected to describe the jet fires. Five cryogenic jet fire tests were used to validate the CFD model. For all five tests experimental radiative heat flux at 5 sensors along the jet flame was predicted within ±15% accuracy, with few exceptions. During the study, the Abel Noble EOS was found to be applicable to cryogenic releases only for low pressure (< 6 bar). Further research should be conducted to extend the domain of the CFD model applicability to high pressure cryogenic releases. In the final portion of the study the hazard distances along and on the sides of the jet axis were calculated considering the temperature distribution and thermal dose.

## 4.3 High pressure jet fires

This section is based on the conference publication "Simulation of thermal radiation from hydrogen under-expanded jet fire" (Cirrone et al., 2017b), submitted to the International Journal of Hydrogen Energy.

### 4.3.1 Description of the experiment

The CFD study is aimed to simulate the horizontal jet fire experiment conducted at INERIS in France (Proust et al., 2011). The experimental facility is shown in Figure 4.19. The release system was arranged in an 80 m long gallery with cross section dimensions 3x4 m. The gallery was open at one end and a chimney with square cross section was located at the opposite blind

extremis (Proust, Private Communication, 2016). Hydrogen was released from a 25 l tank with initial pressure 930 bar. The release system consisted of 10 m long pipe with internal diameter 10 mm, connecting the tank to the release point. The release nozzle was located on the centre-line of the gallery and 1.5 m above the ground, the nozzle orifice diameter was 2 mm. A fire proof wall approximately 1.7 m tall and 1.2 m wide was located behind the release nozzle to protect the hydrogen tank. A recess with dimensions 4×4×4 m was present in proximity of the release (Studer, Private Communication, 2016). Figure 4.20 shows the detail of the recess area and locations of five sensors measuring the radiative heat flux from the flame. The radiometers were located on a line forming a 45º angle with jet axis. The sensing surfaces had dimensions 2x2 cm and 180° view angle. The flame length was measured through a video camera positioned at 5 m distance from the flame. Uncertainty of measurements was assessed to be about ±20 cm. Tank temperature and pressure were recorded during the entire release duration.

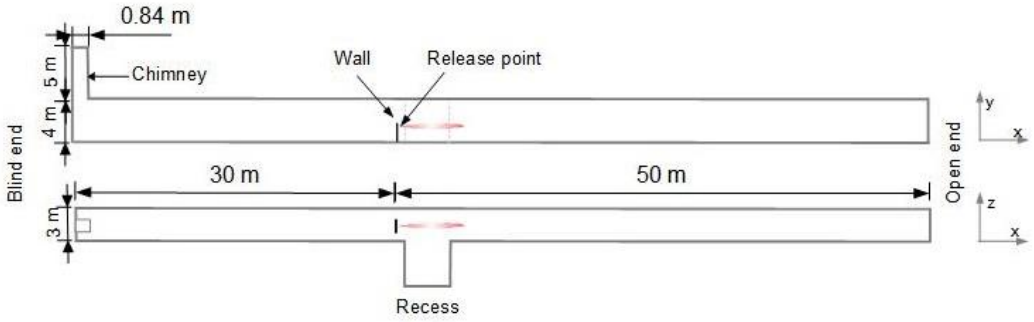


Figure 4.19 General view (top) and plan view (bottom) of the experimental facility

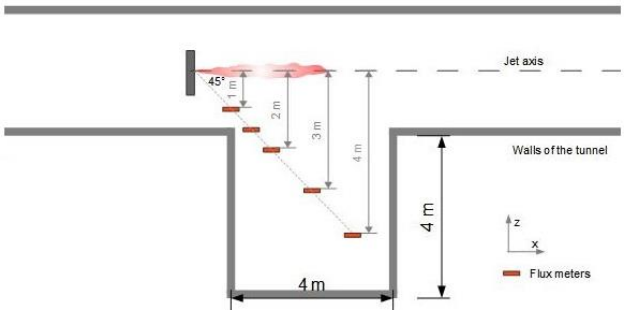


Figure 4.20 Detail of recess area and sensors position

### 4.3.2 Numerical details

4.3.2.1 Governing equations

The model is based on the Reynolds-Averaged Navier-Stokes (RANS) conservation equations for mass, momentum, energy and species indicated in section 3.1 (Equation 3.1-3.4). Realizable k-ε model (Shih et al., 1995) was used for turbulence modelling because of its better capability to predict the spreading rate of axisymmetric jets (ANSYS Fluent, Theory Guide, 2016). The model solves the transport equations for turbulence kinetic energy, *k*, and turbulent

dissipation rate, $\varepsilon$, as shown in Equations (3.5) and (3.11). Combustion is modelled through the Eddy Dissipation Concept model (Magnussen, 1981). The specifics of the model and related equations are discussed in section 3.4.2. The Discrete Ordinates model is employed for radiation (Murthy and Mathur, 1998).

4.3.2.2 Blowdown dynamics

The release from the high-pressure hydrogen storage (930 bar) results in an under-expanded jet. The area where the flow expands to ambient pressure is characterised by the presence of shock waves and supersonic velocities, preventing the use of incompressible codes and requiring highly refined numerical grids. Therefore, the release source was modelled through the Ulster notional nozzle approach (Molkov, 2012). The model is based on mass and energy conservation equations, accounts the non-ideal behaviour of hydrogen at extremely high pressure through the Abel-Noble equation of state, and describes the expansion process as isentropic. The flow is characterized by uniform sonic velocity and ambient pressure at the notional nozzle, simplifying significantly the problem by allowing to skip simulation of shock structures and considering the jet flow at the notional nozzle as completely expanded. Complete description of the approach and employed equations are available in (Molkov et al., 2009) The described above notional nozzle approach was applied to simulate the under-expanded jet properties dynamics during the tank blowdown. A discharge coefficient, $C_d$, equal to 0.7 was used to evaluate the mass flow rate as follow: $\dot{m} = C_d \cdot \rho \cdot u \cdot A$. In a first analysis, the blowdown was treated as adiabatic. However, there is an experimental evidence, see Schefer et al. (2007), that heat transfer between the storage system and the surroundings can affect the blowdown dynamics: during blowdown process from a 43 l tank the stagnation temperature in the tank started to increase after about 140 s. Therefore, a second case was investigated, treating the blowdown as adiabatic in the first phase of the release and as isothermal when temperature decreased to 215 K, to mimic the experimental trend (Proust et al., 2011). Comparison of reservoir temperature dynamics for the two limiting simulated cases and experimental observations for tank temperature is shown in Figure 4.21. Pressure dynamics is shown in Figure 4.22. The adiabatic calculation seems to be closer to the experimental pressure curve, although the difference between the two simulated cases is negligible. This may be attributed to the not long enough discharge time for the heat transfer to affect the blowdown dynamics. The same observations could be made for the mass flow rate shown as function of overpressure in Figure 4.23, where it can be seen that the mass flow rate for the adiabatic case is slightly larger than the adiabatic to isothermal case when the overpressure drops to 200 bar (after ~12 s). The adiabatic to isothermal formulation was chosen to represent the problem under study, as it gave better correspondence to the experimental

temperature in the reservoir, which affects, along with pressure, the jet properties evaluated at the real and notional nozzles.

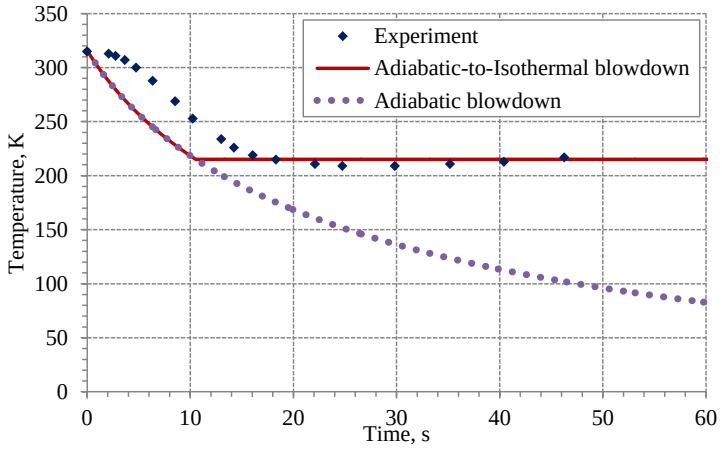


Figure 4.21 Temperature in the reservoir during tank blowdown

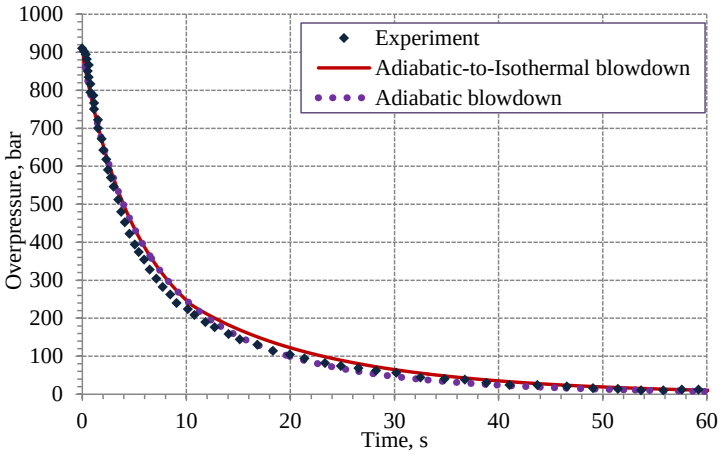


Figure 4.22 Pressure in the reservoir during tank blowdown

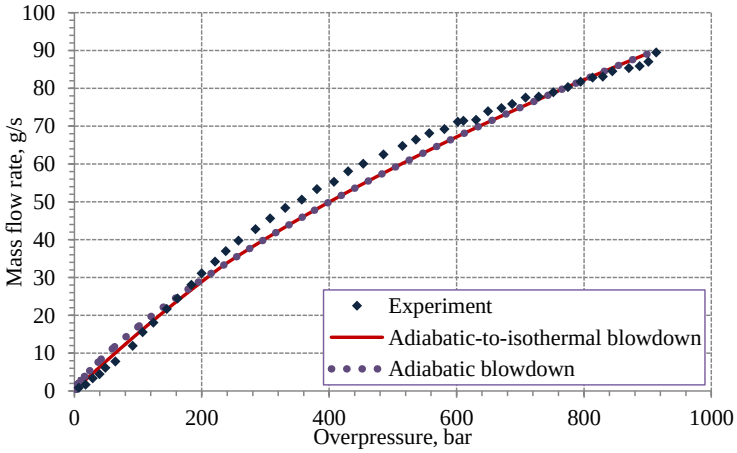


Figure 4.23 Mass flow rate released during tank blowdown

4.3.2.3 Computational domain and numerical details

Employing the notional nozzle diameter as inflow boundary with specified flow velocity would require a change of the numerical grid because the release conditions in the notional nozzle and its diameter are changing during blowdown process. To avoid the change of grid, the release of hydrogen was reproduced through the volumetric source implementation of the notional nozzle approach (Molkov et al., 2009). This approach is based on the evaluation of source terms for mass, momentum, energy, turbulent kinetic energy and turbulent dissipation rate depending on the dynamics of properties at the notional nozzle. Source terms are applied to a constant cylinder volume, thus responsible for the hydrogen release. The equilateral cylinder diameter is 3.1 cm and it corresponds to the value of the notional nozzle at the beginning of the blowdown. The range of validity of the volumetric source approach is limited to $Size_{VS} \leq 4d_{eff}$, meaning that at least about 35 s of release can be simulated without any further modification of the mesh. This limitation to the simulation is accepted, as the most dangerous phase of the release, characterized by longer flame length and radiative heat flux, is contained within this time, and at 35s, pressure in the tank has already dropped to about 50 bar from initial value 900 bar. The calculation domain includes the entire 80 m gallery. The fire-proof wall dimensions were approximated as 1.2x1.7x0.1 m. The recess was assumed to be located at 1 m from the release point, as this is the position that better allows the placement of five radiative heat flux sensors. The chimney was assumed to be at the centre of the gallery blind end. The solid ground was meshed to include the evaluation of conjugate heat transfer with the flame. Control volumes size varied from about 2 mm at the release to 3 m toward the end of the gallery. Smaller control volume sizes (0.5 mm) were used in the solid body for the layer of cells of the ground surface, so that it would be sufficiently refined to resolve the conduction heat transfer across the body. The expansion ratio between neighbouring control volumes was limited to 1.1 in proximity of the release, whereas it was increased to 1.2 in the far field. The total number of control volumes was 1,260,049. The fluid part consisted of 965,445 CVs while the remaining CVs formed the solid ground. The minimum orthogonal quality and the skewness of the mesh were 0.49, in agreement with the minimum numerical requirements defined in (Molkov and Shentsov, 2014) for modelling hydrogen release and dispersion. Figure 4.24a shows the mesh section corresponding to the plane where the release exit is located (x=0). Figure 4.24b shows in detail the release volume, indicated in green, and the short tube separating the release volume and the wall. The gallery walls and ground were considered as no slip surfaces made of concrete. Density was considered equal to 2300 kg/m$^3$, specific heat of 900 J/kgK and thermal conductivity equal to 1.95 W/mK (Reddy et al., 2015). Emissivity was fixed equal to 0.94 (Mikron, 2016). Kirchhoff's law was applied; thus, emissivity of the surface is equal to the absorptivity of incident radiation. The wall behind the

release nozzle was considered to be highly reflective with emissivity equal to 0.09, as indicated for aluminium foils (Mikron, 2016). The radiometers were modelled as 10x10 cm surfaces, so that the dimensions would coincide with the numerical grid size in the space where they are located. The sensors were modelled as isothermal no slip walls with emissivity 1. The isothermal assumption prevents the increase of sensors temperature because of absorbed radiation. Emissivity equal to 1 imposes that the entire received radiation is absorbed and not reflected and that the sensors emit as black bodies. However, temperature of sensors will be equal to that of environment, 288 K, thus, there will be no radiation losses from radiometers to their surroundings, which would affect the net radiation received by the sensors. The chimney opening and the gallery open end were modelled as pressure-outlet with gauge pressure equal to 0 Pa. The ambient conditions were 288 K and 1 bar. Moist air was considered for the simulation. Water vapour mass fraction was imposed equal to 0.006 (1% by volume), indicated as typical value for atmosphere (NASA, 2016).

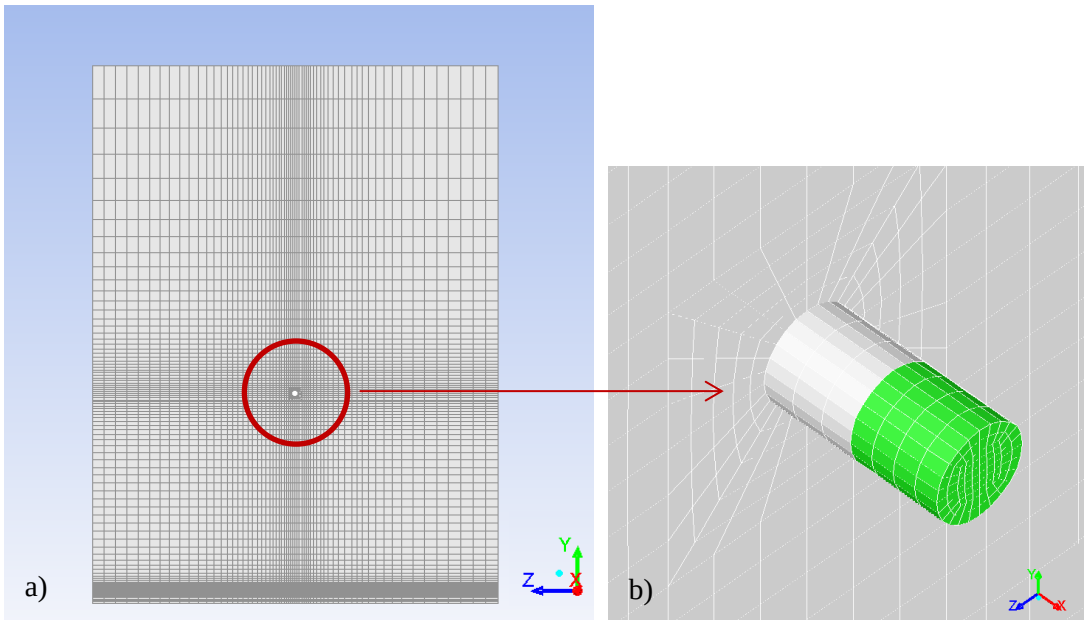


Figure 4.24 Calculation domain and numerical mesh: a) cross section at $x = 0$; b) enlargement of the volumetric source area and numerical mesh

Water vapour was considered as a media participating in radiative heat transfer with mean Planck absorption coefficient evaluated as function of temperature and partial pressure according to the experimental data presented by Hubbard and Tien (1978). Scattering was neglected. RTE was discretised employing 5x5 angular divisions and 3x3 pixels, as suggested in ANSYS Fluent (2016) for problems involving large gradients of temperature in space. Pressure-based solver was employed along with the incompressible gas assumption. SIMPLE procedure was chosen for velocity-pressure coupling, whereas convective terms were discretized using the second order upwind. Time step equal to $10^{-3}$ s was applied at the initial

stage of simulations (up to about 2 s) and it was increased with the simulation advancement in time up to 0.01s.

### 4.3.3 Results and discussion

The received radiative heat flux was monitored at five sensors located at different distances from the flame, as discussed and shown in section 4.3.1. Figure 4.25 shows the comparison between the experimental radiative heat fluxes, indicated by continuous lines, and the simulated ones, indicated by dashed lines. The numeration of the sensors denotes the distance from the jet axis. During the first 10 seconds and except for sensor 1, the simulation misrepresents the experimental radiative heat flux dynamics, resulting in significant underestimation. The dissimilarity may be attributed to both physical and numerical factors. First of all, the sudden release and combustion of the high-pressure hydrogen may cause the movement and entrainment of dust or other particles present on the gallery ground, which would affect the emitting volume and radiation intensity. Secondly, experimental observations on ignition of high pressure gas releases showed a spherical broadening of the jet fire head during the first stage of the release (0-400 ms). The spherical zone was characterized by intense radiation in the studies by Kessler et al. (2014) and Studer et al. (2009). Those dynamics and flame stages were not detected in the simulations. Conversely, the simulated ignited release immediately stabilised into a jet fire. The reason may be due to either the time step not being sufficiently low to correctly resolve the flame propagation, or the use of pressure-based incompressible solver. The need of a fine mesh to represent correctly the release source, the choice of time step to limit the required computational time and high speed of the release resulted in high CFL number (over 100). This may affect the predictive capability of the simulation during the initial instants of the jet fire. The total mass imbalance was monitored during the simulation and resulted to be less than 0.5% at 36 s (end of the simulation). However, it is believed that the hydrogen mass balance shall be examined to have a precise idea of the simulation quality; this analysis could not be conducted because of absence of all the required data. Albeit the radiative heat flux discrepancies during the first phase of the release (about 10 s), the second phase shows a better agreement between the experimental and simulated thermal radiation fluxes. Further remarks should be reported on the resolution of the computational mesh. As discussed in section 4.3.2.3, the grid was designed heeding the grid refinement where higher gradients and complexity of the flow are expected, according to the available best practices and numerical requirements formulated for this class of problems. Possible numerical diffusion was addressed using a second order upwind scheme. However, it would be beneficial to further extend the analysis with a grid sensitivity study, to ensure the grid independency.

The simulated flame length was calculated as the region of the flame characterised by range of temperature 1300-1500 K, according to the experimental observations on visible flame length made in Schefer et al. (2004). The resulting distance is represented by red bars in Figure 4.26, where simulations are compared to the experimental measurements made through a video camera. Flame length is well reproduced for a wide range of pressure decay in the tank, whereas it is over-predicted during the final phase of the release ($p$<200 bar). This final trend can be attributed to the analogous mass flow rate overestimation (Figure 4.23). However, a sort of discontinuity in the experimental flame length trend around 100 bar should be noted, which may be due to measurements inaccuracy. The flame width followed the same trend as in experiment, resulting in approximately 1/6 of the flame length along the blowdown duration.

The sensitivity of simulation results to variation of turbulent flow characteristics at the release source was analysed. It was found that the change of turbulence intensity (TI) and turbulent length scale (TLS) from TI=30% and TLS=0.33$D_{eff}$ to TI=4% and TLS=0.07$D_{eff}$ has a considerable effect (up to 30% decrease) on the monitored radiative heat flux in the closest sensors at distances 1.0-1.5 m. The set of turbulence characteristics were defined according to a parametric study conducted at HySAFER on hydrogen concentration jet decay (TI=30%, TLS=0.33$D_{eff}$) and experimental data on air under-expanded jets (TI=4% and TLS=0.07$D_{eff}$) (Chuech et al., 1989). Minor effect of turbulent characteristics on radiative heat flux was found for steady state cryogenic jet fires where maximum variation was 15% (section 4.2.3.1.3). This difference is presumed to be due to the different source modelling technique, as the volumetric source is more sensitive to the applied turbulence characteristics whereas they have minor effect for the constant diameter notional nozzle implementation with specified velocity at inflow boundary condition. The water vapour in air was found to have a greater effect on the thermal radiation absorbed in the surroundings of the flame. The effect was seen to be larger with the increase of distance from the flame.

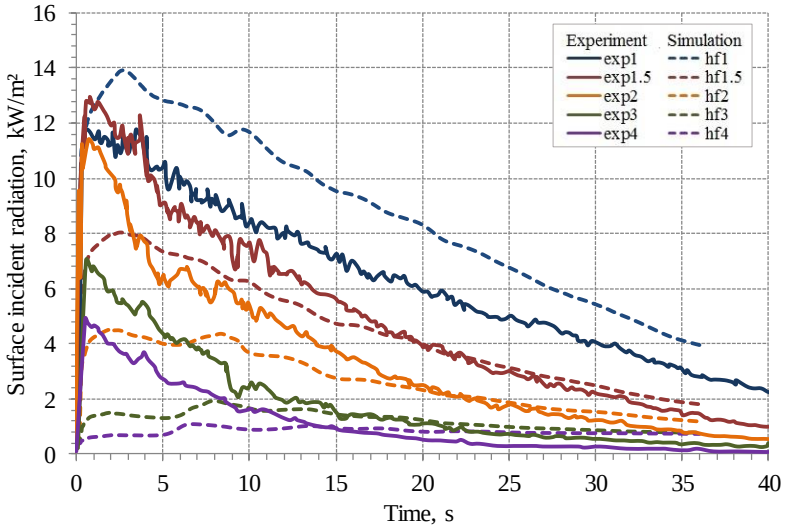


Figure 4.25 Radiative heat flux: simulation versus experiment

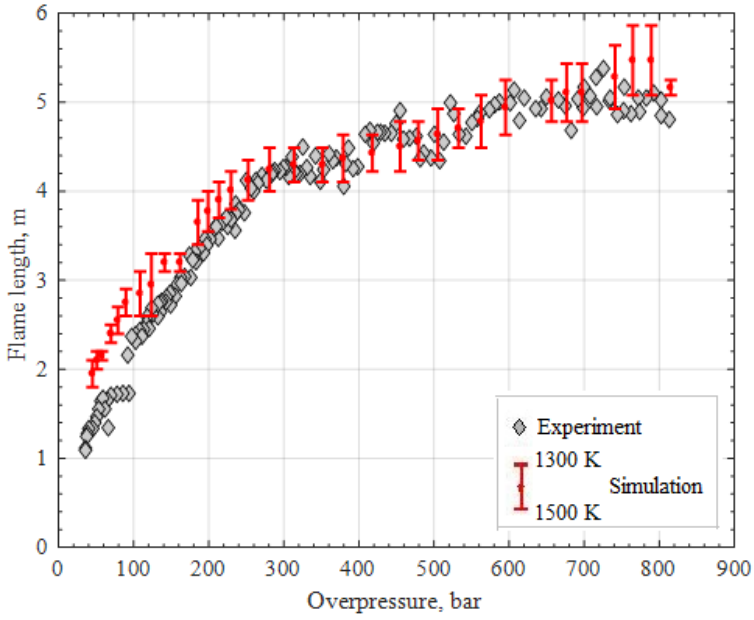


Figure 4.26 Flame length: simulation vs experiment

### 4.3.4 Concluding remarks

The thermal hazards from a high pressure (900 bar) hydrogen jet fire have been investigated numerically. Realizable k-ε turbulence model was applied along with Eddy Dissipation Concept for combustion and DO model for radiation simulations. The blowdown from a high-pressure hydrogen storage tank was modelled as first adiabatic and then isothermal process to account heat transfer with environment, and the mass flow rate was evaluated using discharge coefficient $C_d$ equal to 0.7. The transient release was modelled via the volumetric source implementation of the notional nozzle. Simulation results show excellent CFD model

capability to predict flame dynamics with pressure decrease for a large part of the blowdown process with slight overestimation for lower tank overpressures. In spite of close agreement between the experimental and simulated flame lengths, modelling of radiative heat flux had a twofold limited predictive capability during the first stage of hydrogen release ($t$=0-10 s) and quite a good agreement at later stage ($t$=10-35 s). This may suggest that the experimental radiation was affected by some physical processes not unaccounted in CFD model, e.g. entrainment in jet flame and radiation of dust. However, the first stage of the release results to be the most dangerous, as it is characterized by the highest thermal radiation and flame length. It is therefore of primary importance to perform further numerical investigations to obtain better reproduction of the experiment.

# 5 Spark ignition of stoichiometric hydrogen-air mixture

## 5.1 Introduction

Hydrogen release in air can easily ignite due to the low Minimum Ignition Energy (MIE) and wide flammability range (4-75% vol). If MIE is usually greater than 0.1 mJ for other flammable gases, such as methane or ethane (Lewis Von Elbe, 1961), MIE for hydrogen in air in standard conditions is as low as 0.017 mJ (ISO, 2004). However, it can decrease below 0.0012 mJ for ignition in oxygen. Therefore, it can be deduced that the potential of ignition for hydrogen-air mixtures is greater, thus more dangerous, than other fuels. The standard technique to determine MIE for flammable gases is the spark capacitive discharge (Babrauskas, 2003). Furthermore, the deployment of Fuel Cell Vehicles makes the study of electrostatic discharge hazards of primary importance. Several experimental studies have investigated the measurement of MIE for different hydrogen-air mixtures by capacitive discharge, such as Ono et al. (2007) and Kumamoto et al. (2011). It was observed that, besides the hydrogen composition and oxygen enrichment, the MIE is strictly dependent on the gap distance between electrodes, with minimal energy for 0.5 mm. Thiele et al. (2002) investigated the flame propagation in lean hydrogen-air mixtures. For 20% $H_2$ by vol., it was observed that in a first phase the flame propagation is dominated by the expansion of the high temperature kernel. This preponderance was observed up to about 80 μs after breakdown. After a short transition phase, the propagation is governed by the flame speed. The flame development was further investigated numerically by the authors through a 2D-model simulation. Han et al. (2011) conducted an extensive numerical study investigating the effect of several parameters on the calculation of MIE, such as energy supply procedure or electrodes size. It was found that the electrodes size does not affect significantly the MIE for gap distances greater than the quenching distance (0.66 mm). Furthermore, it was observed that for spark channels with a radius lower than 0.15 mm and stoichiometric mixture, the numerical MIE levelled off to 0.04 mJ, overestimating by over 135% the experimental results. In all the numerical investigations, it was underlined that numerical reproduction of spark ignition represents an utmost challenge because of the complex interaction among plasma and chemical kinetics, high temperature, short duration of the process, etc..., resulting in a high stiffness problem. The study aims at the 3D modelling of stoichiometric hydrogen-air mixture ignition by spark. The final aim is to determine by simulation the MIE.

## 5.2 Numerical model

### 5.2.1 Governing equations

The mass conservation equations for mass, momentum, energy and species (3.1-3.4) are solved for the laminar flow. The rate of reaction is computed through the laminar finite rate model, which employs the generalized finite-rate formulation for reaction modelling. A subset of Peters and Rogg's kinetic mechanism (Peters and Rogg, 1993), including 13 chemical species and 37-step reduced chemical reaction, was considered for hydrogen combustion in air.

### 5.2.2 Problem assumptions and numerical details

Only the capacitive component of the spark discharge was considered, as it is the most frequent technique to measure MIE (Kumamoto et al. 2011). Furthermore, as discussed in Babrauskas (2003), the nominal energy is generally measured taking account of the capacitance and voltage in the system, confirming the validity of the model assumption to consider that energy is released uniquely as capacity component. The duration of the spark was assumed to be 1 μs, according to the computational study conducted by Yuasa et al. (2002) on methane/air mixtures. The energy was released uniformly in time, following the conclusions of the experimental study performed by Ono et al. (2007): the authors observed that the MIE is approximately constant for spark duration in the range 5ns-1ms. Dissipation of energy due to circuit resistance circuit was neglected. Therefore, all the nominal storage energy was considered available to ignite the mixture. The electrodes were not considered in the simulation, thus neglecting the heat losses towards them. Kumamoto et al. (2011) found that the IE in $H_2$-air mixtures is dependent on the gap between electrodes. The MIE was measured for gap distance equal to 0.5 mm. Therefore, this value was considered as length of the cylinder where energy was released in simulation. The radius was assumed 60 μm. Energy was released through addition of a source term to the energy equation. Energy was assumed to be homogeneously distributed throughout the cylindric volume. ICEM CFD 18.0 was used to build the numerical grid. The computational domain was assumed to be spherical with radius 2 mm. Given the symmetrical nature of the problem, the domain was reduced to a latitudinal slice of the sphere with angle 12°. Consequently, any possible effect of buoyancy was still included, even if in such a small scale. If the use of such a small angle was beneficial for reducing the final number of CVs, it implicated cells skewness up to 0.78 and minimum orthogonal quality of 0.21. Even if not optimal, these values are still within the acceptable ranges (skewness<0.95 and minimum orthogonal quality>0.01) suggested by ANSYS Fluent User's Guide (2016) and the potential time saving is considerable. The hexahedral numerical grid had control volume size of 2 μm where the spark channel is located, to address the spatial resolution of chemistry through the finite rate model. A maximum expansion ratio of 1.05 was

maintained, resulting in maximum CV size of 20 μm towards the boundaries and total number of control volumes equal to 331,696. The numerical grid is shown in Figure 5.1. The external boundary of the computational domain was modelled as non-reflecting pressure-outlet with gauge pressure equal to 0 Pa. The pressure-based solver was employed, along with the compressible formulation for the mixture, so that the formation of the combustion wave during the kernel formation could be captured. However, doing so requires the employment of low time step to maintain an adequate acoustic CFL (about $10^{-10}$ s), otherwise the phenomena would not be properly represented. An additional analysis investigated the application of the incompressible solver disregarding the development of the pressure wave. Simulation resulted in divergence of the solution, despite the attempts to stabilise it, such as lowering of under-relaxation factors (URFs) or variation of numerical schemes. It was concluded that the significant rise in temperature (thousands of K) and velocity may prevent the use of the incompressible solver, as it is not more possible to neglect the compressibility effects, density variation with temperature, pressure and velocity rise, as they become too important to be neglected. Therefore, the compressible solver was maintained in the present analysis. PISO procedure was used for pressure-velocity coupling, as suggested for transient simulations, and second order upwind was employed for discretization of convective terms. A time step equal to $10^{-8}$ s was implemented in the initial phase of the simulation, so at least 100 time steps could be guaranteed during the spark duration. The stiff chemistry solver was employed for the solution of species transport equations involving reaction time scales much faster than convection ad diffusion time scales, such as for the radicals in the multi-step reaction mechanisms. The time step was then increased in several stages to reduce the computational time required by the simulation.

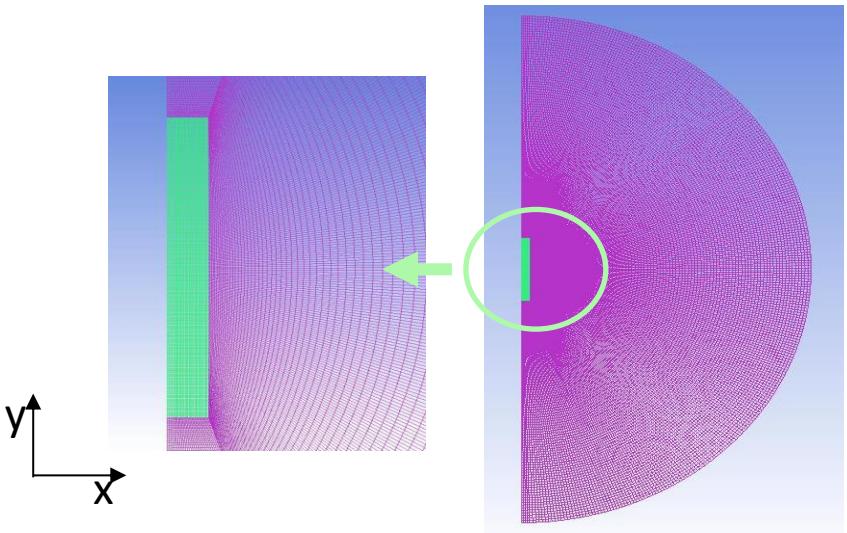


Figure 5.1 Numerical grid with detail of spark channel volume indicated in green

## 5.3 Results and discussion

### 5.3.1 Flame kernel growth for 17 µJ

The first stage of the analysis is aimed to the reproduction of the stoichiometric hydrogen-air mixture ignition and flame propagation for the MIE reported in literature, i.e. 17 µJ. An energy source term evaluated as $S_E = \frac{MIE}{\Delta t \cdot V_{spark}} = 3.007 \cdot 10^{12} \frac{W}{m^3}$ was applied in the spark channel to reproduce the release of energy. The temperature and OH radical profiles were monitored as indication of the flame development. Figures 5.2 and 5.3 show the profiles evolution in time for, respectively, x and y directions. The laminar flame speed is 2.2 m/s and it was calculated through Cantera (2018). Including the effect of thermal expansion, the analytical visible flame velocity corresponds to about 14.3 m/s. As shown in Figures 5.2 and 5.3, simulations resulted in flame propagation speeds approximately 11.0 m/s and 12.5 m/s on x and y directions respectively, which are slightly lower than the expected theoretical values. The properties distributions are characterised by notable oscillations on the y symmetry axis. It must be remarked that the employment of such a narrow symmetry angle has the disadvantage of resulting in low quality and highly skewed cells along the y-axis. Therefore, it is concluded that such instabilities are caused by the poor-quality mesh even if still within Fluent recommended values. However, since the computational time saving is considerable, and it is believed that the presence of such oscillations does not affect significantly the flame propagation or ignition probability, the same mesh is maintained for the following calculations.

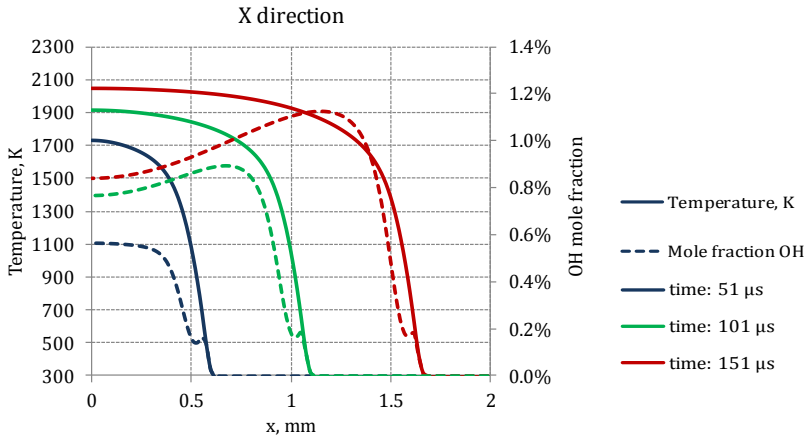


Figure 5.2 Temperature and OH profiles on x-axis for IE=17 µJ

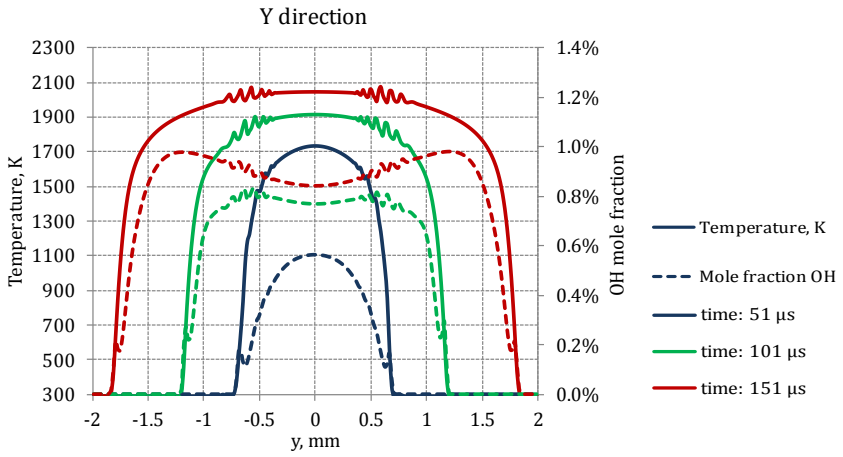


Figure 5.3 Temperature and OH profiles on y-axis for IE=17 µJ

Figure 5.4 shows the OH mole fraction and temperature contours in space for several times. The OH radical distribution shows the effect of the cylindrical channel shape on the final flame propagation, indicating a more pronounced front towards the x-direction, perpendicular to the channel axis. The boundaries are reached in about 180 µs of simulated time.

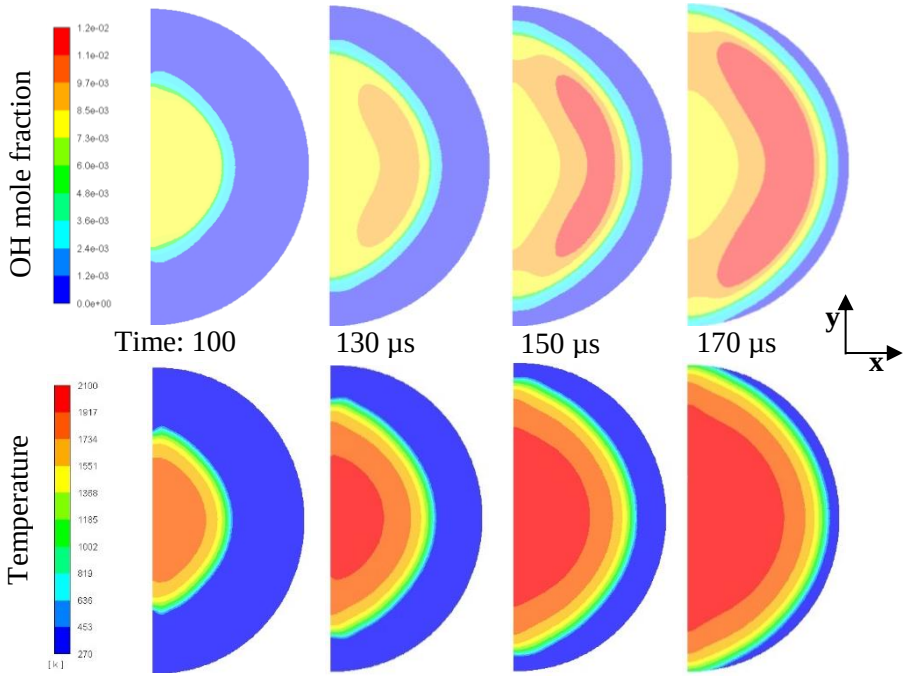


Figure 5.4 Flame propagation for IE=17 µJ

### 5.3.2 Numerical evaluation of MIE

Several simulations have been performed to evaluate the MIE in a quiescent stoichiometric hydrogen-air mixture. The procedure was simply based on gradual decrease of the applied

energy source until ignition was not more observed. The criteria to determine the failure of ignition were: temperature decrease to temperature lower than 600 K, not sustainment of OH radical production and no accumulation of $H_2O$ in the domain. All the mentioned factors were considered as indication of not sustainment of combustion. As shown in Figures 5.5-5.7, this circumstance was observed for IE=5.67 μJ (⅓ experimental MIE). The sudden energy release caused an increase of temperature to 3000 K and correspondingly OH mole fraction, but it was insufficient to ignite the mixture and resulted in its dissipation without formation of the flame kernel. The simulation was stopped after 60 μs. The same parameters are presented in the same graphs for IE=9 μJ, which resulted to be successful in triggering the ignition of the mixture. The maximum temperature in the domain reached 7000 K during the energy release and then stabilised at 2100 K.

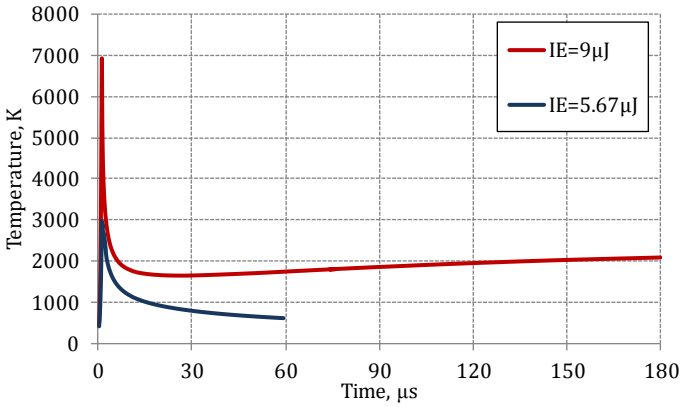


Figure 5.5 Maximum temperature in the domain

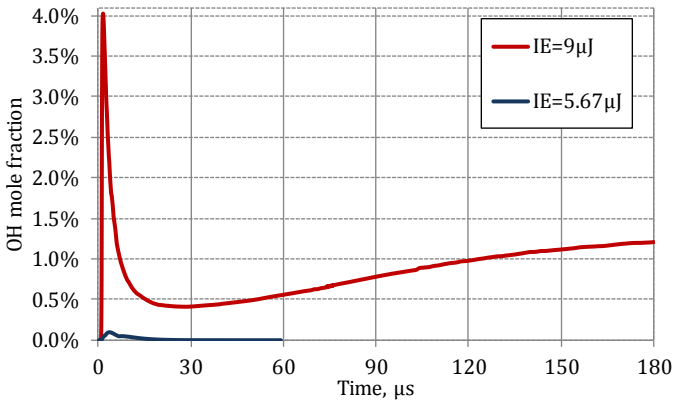


Figure 5.6 Maximum OH mole fraction in the domain

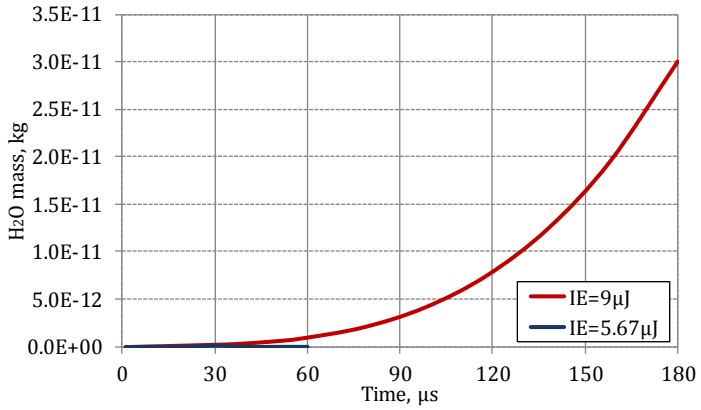


Figure 5.7 Water vapour mass accumulation in the domain

Figure 5.8 shows the results of the numerical investigation against the experimental MIE curve reported by Ono et al. (2007) and Lewis and von Elbe (1961). Ignition was successful for IE=17, 12 and 9 µJ. Therefore, the numerically determined MIE is 9 µJ (~1/2 experimental MIE). Several reasons can be behind the discrepancy between calculations and experiments. As mentioned in the problem formulation, the heat conduction to the electrodes is not considered, as they are not included in the numerical grid. Furthermore, the losses in the circuit resistance are neglected. Roth et al. (1951) attempted to measure the energy delivered into the gas directly, reporting 95%. However, as reported by Babrauskas (2003), later studies found out that the actual energy dissipated in the spark generally decreases with increasing resistance, although not monotonically. For instance, Rose and Priede (1958) found that, for a 5pF capacitance and resistor 50 kΩ, only 50% of the stored energy is delivered into the gap, compared to 90% for 100 Ω resistor. However, these may be extreme cases as generally capacitive sparks release nearly all the stored energy (more than 95%) during discharge.

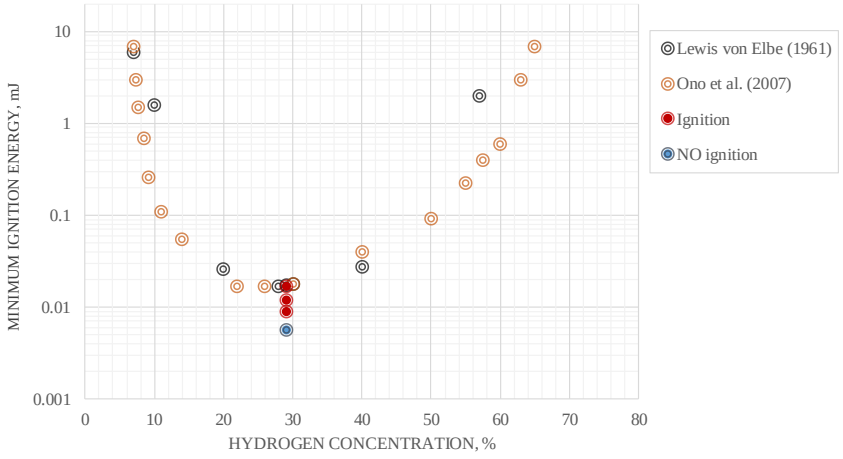


Figure 5.8 MIE calculation: simulation versus experiments

## 5.4 Concluding remarks

A CFD approach was developed to numerically assess the spark ignition dynamics in a stoichiometric hydrogen-air mixture. The flame propagation was investigated, and its velocity was found to be within the range 11.0 - 12.5 m/s, reproducing well the calculation performed through Cantera. Several numerical experiments were performed with progressively lower ignition energy to numerically estimate the minimum value leading to ignition. The MIE for stoichiometric hydrogen-air mixture was found to be 9 μJ ($<1/2$ experimental MIE). The CFD model should be enhanced and extended to the assessment of MIE for lean hydrogen-air mixtures, so that a tool for prediction of MIE in arbitrary conditions can be developed and applied for the relevant technology.

# 6 Dispersion and delayed ignition

## 6.1 Introduction

An unintended release from high pressure hydrogen storage systems produces an under-expanded jet. Accurate prediction of the gas dispersion is fundamental for the assessment of separation distances from the release source. In particular, one scenario to avoid is the delayed ignition of the jet and the associated overpressure hazards. Two studies are conducted on dispersion of hydrogen released at 200 bar and 40 bar. Simulations provide insights into the effect of the release system and numerical features of the model. Results for the 40 bar release are validated against experiments. The hydrogen jet is characterised by non-uniform hydrogen distribution and high turbulence level. Overpressure and flame propagation behaviour in case of ignition may be significantly different from combustion dynamics in uniform or initially quiescent mixtures, as supported by experimental evidences in (Shirvill et al., 2007), (Takeno et al., 2007), (Royle and Willoughby, 2011a). The second section of this chapter assesses the applicability of two combustion models for predicting delayed ignition hazards of the simulated 200 and 40 bar releases.

## 6.2 Description of experimental tests

### 6.2.1 HSL test

The experiment regards a 200 bar horizontal hydrogen free jet fire (Royle and Willoughby, 2011b). The release point was located 1.2 m above the ground. The ground of the facility was constituted by a 10 m x 10 m concrete pad installed on a 24 m x 18 m tarmac pad. A wall was located behind the release point. Wall dimensions are considered 5.4 x 4 x 0.6 m. A scheme of the HSL facility with the relative dimensions is shown in Figure 6.1. The jet was ignited through a pyrotechnic source located on the jet axis at 2 m from the release point. The ignition delay was 800 ms. However, the time required by the valve to pass from close to fully open configuration was 260 ms (Royle and Willoughby, 2011a). Two radiant heat flux sensors were located at 1.5 m from the jet axis, with distance, respectively, 2.6 and 5.2 from the release point. 5 pressure sensors were located in the surroundings of the jet. However, pressure dynamics is available for only one sensor located at 1.5 m from the jet axis and 0.8 m from the ignition point.

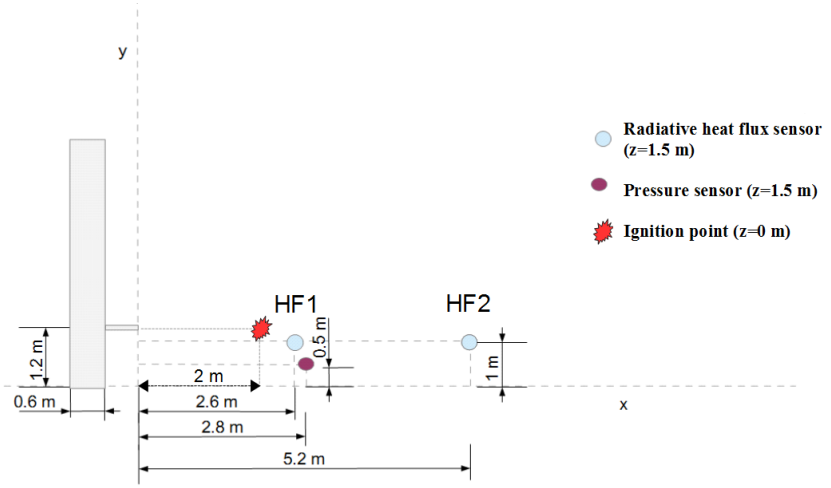


Figure 6.1 Scheme of HSL experimental set up, plane x-y

### 6.2.2 INERIS test

The experimental test examined a horizontal hydrogen jet released from a 5 $m^3$ storage tank with pressure equal to 40 bars. The release had diameter 12 mm and it was located 1.5 m above the ground. The dispersion phase had the aim to investigate hydrogen concentration distribution and turbulence characteristics of the jet. 9 probes for measuring hydrogen concentration were located on an instrumented mast perpendicular to the jet axis. The mast was moved from 1.25 m to 10 m from the release point, to sample concentration at different distances. Instantaneous velocity was deduced from sensors measuring the instantaneous dynamic pressure. Velocity fluctuations were calculated from measurements at the same probe for different time. These data were then used along with the mean velocity to calculate the turbulent intensity in the jet. The jet was ignited 5 s after the start of the release. The distance between the release point and ignition source was 1.8 m. The flame originated by pyrotechnical ignition of a $H_2/O_2$ stoichiometric mixture released 20 cm below the jet axis was used to ignite the hydrogen jet. 3 pressure sensors were employed to measure the overpressure originated by the delayed ignition of the jet. Two of them were located 20 cm below the jet axis, the first at 20 cm and the second at 3.8 m from the release point. A third sensor was located on the side of the jet, precisely at 1.5 m from the jet axis. A high-speed video camera was used to record the flame propagation within 5 m from the release point. The device was located 10 m from the jet axis.

## 6.3 Unignited releases and dispersion

### 6.3.1 HSL test: 200 bar release

6.3.1.1 Numerical details

The Reynolds-Averaged Navier-Stokes (RANS) conservation equations for mass, momentum, energy and species (3.1)-(3.4) were used to describe the flow. The description of the equations is given in section 3.1. Two additional transport equations are added for turbulent kinetic energy and turbulent dissipation rate. Two turbulence models were selected and compared to solve the equations for *k* and ε. In case 1 RNG k-ε model by (Yakhot and Orszag, 1986) was employed, as it provides enhanced accuracy for swirling flows and portions of the flow characterised by low-Reynolds number. Realizable k-ε (Shih et al., 1995) was used in case 2, as it provides better performances in representing axisymmetric jets (ANSYS Fluent, Theory Guide, 2016). Details and equations of the models are given in sections 3.3.1.2 and 3.3.1.3. The release at high-pressure (20 MPa) produces an under-expanded jet. Solving the generated shock waves would need a really fine grid for the numerical simulations, as shown in previous work on under-expanded jets, such as in Xu et al. (2005), Taira et al. (2015) and Cumber et al. (1995). It has also to be considered that the transient simulation would require a much smaller time step to capture the shock waves. Therefore, the notional nozzle approach presented and employed for the free jet fires investigated in Chapter 4 results to be the best solution to optimise the computational resources and speed up simulations. Equations presented in Molkov et al. (2009) are solved to obtain the flow characteristics at the real and notional nozzle. Results are reported in Table 6.1.

Table 6.1 Gas properties in the storage, real and notional nozzles for a 200 bar release

| *Parameter* | *Storage* | *Real nozzle* | *Notional nozzle* |
|---|---|---|---|
| *Pressure, Pa* | 20000000 | 9637721 | 101325 |
| *Temperature, K* | 288 | 234 | 240 |
| *Density, kg/m$^3$* | 14.908 | 9.282 | 0.102 |
| *Velocity, m/s* | - | 1251 | 1177 |
| *Mass flow rate, kg/s* | - | 0.37 | 0.37 |
| *Diameter, cm* | - | 0.64 | 6.28 |

A first analysis assuming a constant release was conducted. These cases are indicated as 1a and 2a in Table 6.2. The release source was modelled as a square nozzle with length 5.6 m, which section is equal to the notional nozzle area, so that the same mass flow rate can be maintained. 8x8 cells were used to discretise the notional nozzle. The nozzle was considered

as a velocity inlet with imposed temperature and velocity as indicated for the notional nozzle conditions in Table 6.1. Turbulence intensity and turbulent length scale were defined as, respectively, 30% and $0.33D_{not}$, as suggested by a parametric study conducted at HySAFER. During the release, storage conditions are expected to change because of tank blowdown. Consequently, the diameter of the notional nozzle is expected to vary too, requiring the variation of the release nozzle in the numerical grid and furtherly complicating the problem. Therefore, a second problem formulation (cases 1b and 2b) included the blowdown dynamics in simulations through the volumetric source employment. The approach, described in Molkov et al. (2009) and in section 4.3 of the present work, allows to reproduce the variation of the notional nozzle and flow characteristics in simulations. The source terms were applied to a cube with length equal to the notional nozzle size. In case 2b, 4x4x4 CVs were used to represent the volumetric source, therefore increasing the cell size from 0.7 cm to 1.4 cm. All the meshes were characterised by a cell growth rate of maximum 1.1 in the proximity of the release, following the CFD best practices indicated in Molkov and Shentsov (2014). 1.2 was employed at further distances. Several changes were made in the mesh, along with turbulence or release model, when shifting from one case to another, resulting in slightly different total number of control volumes. Details of the numerical grids are given in Table 6.2. In general, the numerical grid was subdivided in two domains. Representation of the structure is given in Figure 6.2. The numerical grid was realized through a hexahedral mesh and had size 25 x 8 x 10 m. This is the zone where the release system was located, as indicated in Figure 6.3. In order to minimize the effect of boundaries on the primary area of the release, a second domain consisting of a hemisphere with radius 50 m was built around the hexahedral domain. A tetrahedral and coarser mesh was employed to reduce the number of control volumes, as there is no need to accurately solve the flow in this portion of the domain as for the proximity of the release. The two numerical grids were coupled through an interface. Details on the mesh size, refinement level and quality for each of the analysed case are given in Table 6.2. The flow is considered as an incompressible ideal-gas. The assumption follows the conclusions by Makarov and Molkov (2013) that the effect of compressibility can be neglected for Mach number in the range 1-0.3 with limited error on density evaluation (±0.7%). The pressure-based solver was employed along with SIMPLE pressure correction algorithm. Convective terms were discretized using the second order upwind scheme, with exception of turbulent kinetic energy and dissipation rate ($1^{st}$ order upwind). The ground and wall behind the release were modelled as no-slip adiabatic surfaces. The external hemispherical boundary is modelled as a pressure outlet. Initial conditions of the simulations were quiescent air with pressure equal to 1 bar, temperature of 288 K and approximately 0.01 water vapour content. Time step equal to $10^{-3}$ s was used for the release simulation along with $1^{st}$ order time implicit transient formulation. It is assumed that the valve is fully opened when the release starts. Therefore, the

simulated time for the unignited release was 540 ms, corresponding to the ignition delay time minus the time required by the valve to open.

Table 6.2 Numerical details of the analysed cases

| *Case* | *Turbulence model* | *Release modelling* | *Mesh size* | *Cells at the nozzle* |
|---|---|---|---|---|
| 1-a | RNG k-ε | Notional nozzle | 975502 | 8x8 |
| 1-b | RNG k-ε | Volumetric source | 975502 | 8x8 |
| 2-a | Realizable k-ε | Notional nozzle | 921714 | 8x8 |
| 2-b | Realizable k-ε | Volumetric source | 883571 | 4x4x4 |

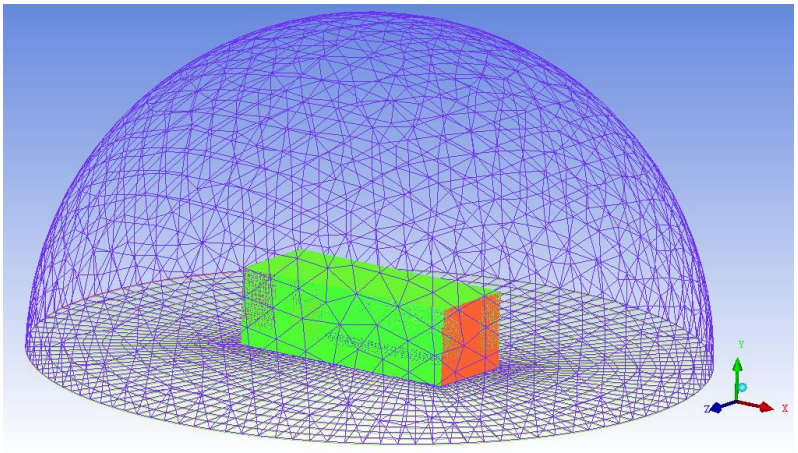

Figure 6.2 Hexahedral and tetrahedral numerical grids structure

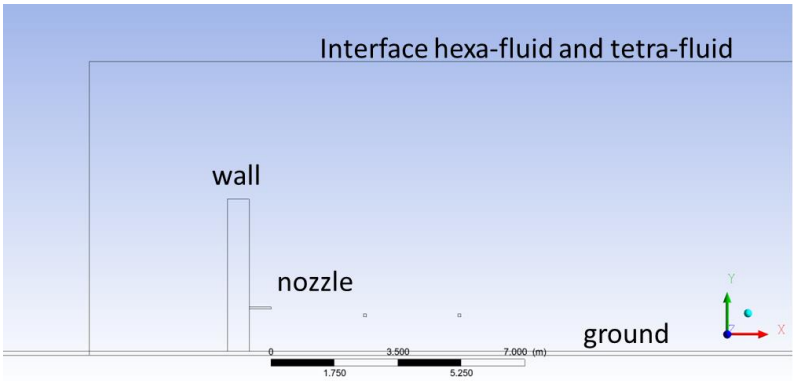


Figure 6.3 Features of the domain in proximity of the release point

6.3.1.2 Results and discussion

The following section presents the results for the unignited release. In a first stage the effect of turbulence and release modelling were analysed. In a second stage, the time step independency and validity of flow incompressibility assumption were verified. Finally, the

ignition delay time effect on the distribution was investigated. The obtained hydrogen distribution was then considered as initial condition for the study on ignition of the turbulent jet in section 6.4.1.

Realizable and RNG k-ε models were employed and compared. RNG k-ε model resulted in a faster jet, reaching 12% greater distances than realizable at 540 ms and in a slightly higher hydrogen concentration along the jet, as shown in Figure 6.4. Mass flow rate at the inlet was practically the same for both the models and equal to 0.378 kg/s, which well agrees with prediction of notional nozzle theory. Figure 6.4 also compares the results obtained employing either the notional nozzle or the volumetric source. RNG k-ε shows a faster axial decay for the volumetric source, which appears visible beyond 5 m. Indeed, radial distributions at 2 and 4 m in Figure 6.5 do not show yet any difference between the two formulations. On the other hand, realizable presents a slightly higher concentration for the volumetric source, with about 6% difference at 2 m from the release. The two curves progressively overlap towards the end of the jet, showing minor deviation at 4 m and same value towards the end of the jet. Both the turbulence models are relatively new compared to standard k-ε, so it is not yet defined in which conditions realizable may outperform RNG model (ANSYS Fluent, Theory Guide, 2016). This statement seems to be confirmed by the results obtained on the unignited jet. However, it is extensively discussed that realizable k-ε model provides a better prediction of axisymmetric round jets, due to the improved turbulent dissipation rate equation. Furthermore, it was shown in section 4.2 on simulation of free jet fires that realizable k-ε model provided better prediction of flame length. Since the following step will be the ignited jet analysis, realizable appears as the most suitable turbulence model to be used further on for the study. The aim of the analysis is to build a CFD model that could extensively be applied to different scenarios. Therefore, the volumetric source formulation was selected as it is considered the most representative of the jet flow characteristics in case of longer ignition delay times during which change in storage conditions may intensively affect the jet parameters. Figure 6.6 shows the resulting hydrogen mole fraction distribution on plane z=0. Radial distribution of hydrogen at 2, 4, 6 and 8 m for 540 ms ignition delay is shown in Figure 6.10, along with results for a longer delay of 800 ms. Distributions indicate that where and when ignition is triggered, hydrogen-air mixture is rich, with 43% by vol of $H_2$. Stoichiometric composition is reached approximately at 3.5 m while the LFL is achieved at about 7 m (time=540 ms). Velocity in proximity of the ignition point is included in the range 55-60 m/s, implying that flame speed should be higher than 60 m/s to have backward propagation of the flame. The width of the jet is approximately 1 m, resulting in a jet opening angle of 14°, which agrees well with general considerations on jet spreading angles. All the simulations required a computational time of approximately 24 h on a 48 CPU machine.

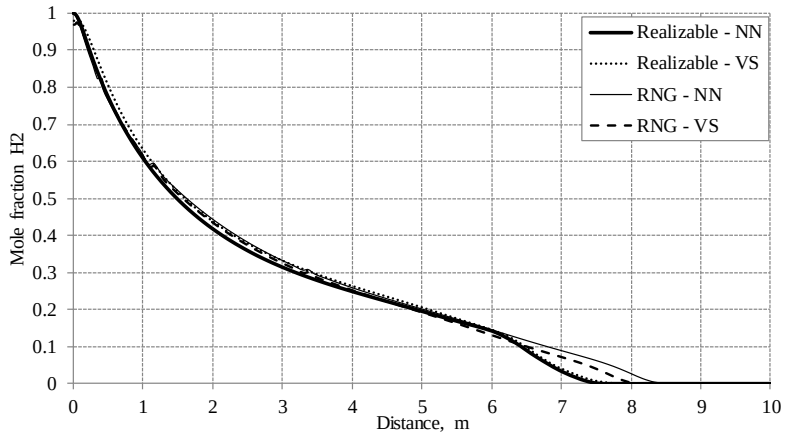


Figure 6.4 Axial hydrogen mole fraction employing realizable and RNG k-ε models for notional nozzle (NN) and volumetric source (VS) formulations (Time=540ms)

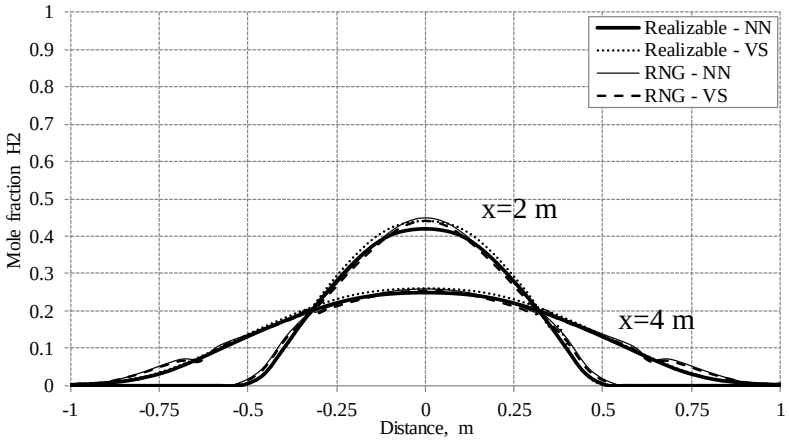


Figure 6.5 Radial hydrogen mole fraction employing realizable and RNG k-ε models for notional nozzle (NN) and volumetric source (VS) formulations at 2 and 4 m from the nozzle (Time=540ms)

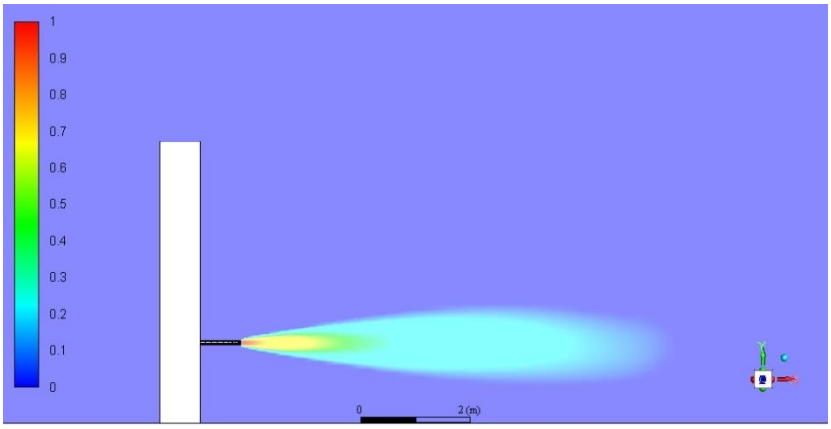

Figure 6.6 Hydrogen mole fraction distribution on plane z=0 for case 2-b

*6.3.1.2.1 Time discretisation sensitivity*

Stability and accuracy of numerical simulations may be affected by the choice of time step. Therefore, it is fundamental to verify the time step independency of the solution, to confirm that the selected time step is suitable for representation of the physics of the problem. Time step independence was verified comparing the simulation results along the centreline and at several distances from the nozzle for time steps $10^{-3}$ s and $5 \cdot 10^{-4}$ s. The independence from the temporal scheme was analysed for the case with smaller time step, $5 \cdot 10^{-4}$ s. Order of discretization was increased to the 2nd order to test the accuracy of the solution, in addition to a bounded formulation of the scheme to enhance its stability. Results show a limited effect of temporal discretization, mainly towards the extremity of the jet (5-6 m), where the flow is not yet established and is diffusing in air. Figure 6.7 presents hydrogen mole fraction radial distributions at 2 and 5 m from the nozzle.

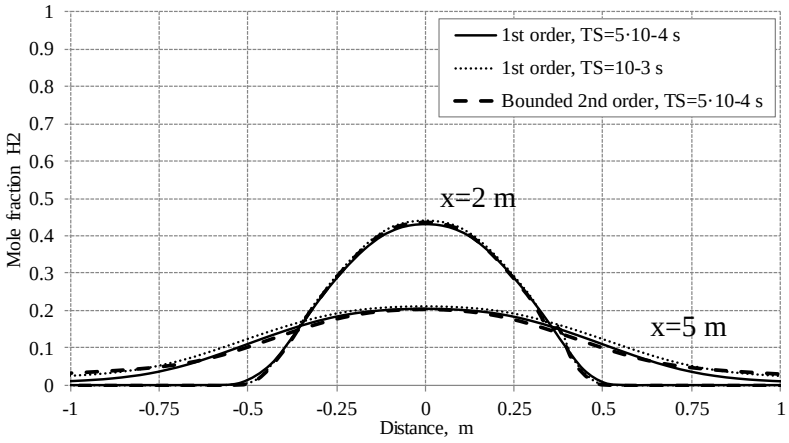


Figure 6.7 Hydrogen mole fraction radial distribution at 2 and 5 m from the nozzle (Time=540ms)

*6.3.1.2.2 Compressibility effect*

As described in section 6.3.1.1, the flow was modelled as incompressible, thanks to the implementation of the notional nozzle. However, there is still an area in the proximity of the release where Mach number is nearly equal to 1 and it decreases to 0.3 only beyond 0.8 m from the nozzle position. Therefore, change in density can still be significant and compressibility effects cannot be ignored. Figure 6.8 presents the hydrogen mole fraction distribution along the centreline of the jet at 540 ms. Dissimilarities in distributions are still visible to distance up to 3 m. However, maximum deviation does not exceed 7%. Between 3 and 6 m difference in mole fraction is negligible, while it increases for distance greater than 6 m indicating that the compressible solver gives a slightly faster flow. Figure 6.9 shows the hydrogen mole fraction along the radius at 2 m from the nozzle, where the ignitor is located. From this graph, it can be observed that the compressible flow is characterised by a narrower

jet, which could be the cause of a slower decay of velocity along the jet line and, consequently, higher concentration for distance over 6 m. Considering that difference in distribution is limited to 7% in the area of interest where ignition will be triggered, the incompressible formulation is confirmed a valid assumption for the problem under study. Results well agree with the conclusions of Makarov and Molkov's (2013) study on numerical simulations of round and plane jets, where they observed that effect of compressibility can be neglected for Mach number in the range 1-0.3, as it induces a limited error on density evaluation of ±0.7 %.

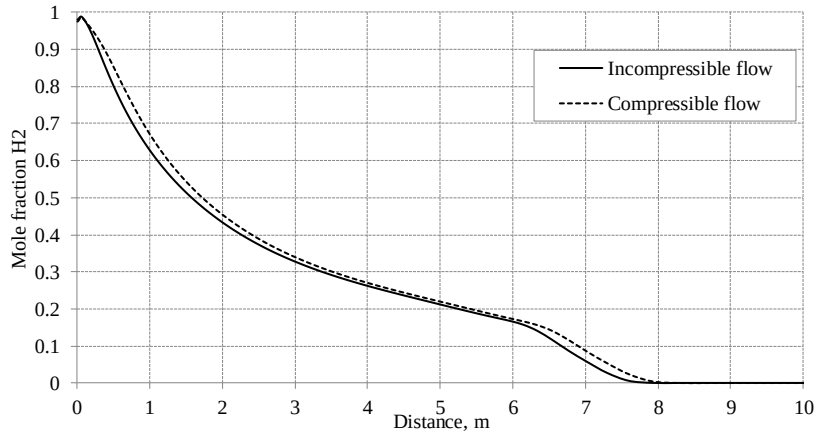


Figure 6.8 Hydrogen mole fraction distribution along the jet centreline: incompressible versus compressible flow (Time=540ms)

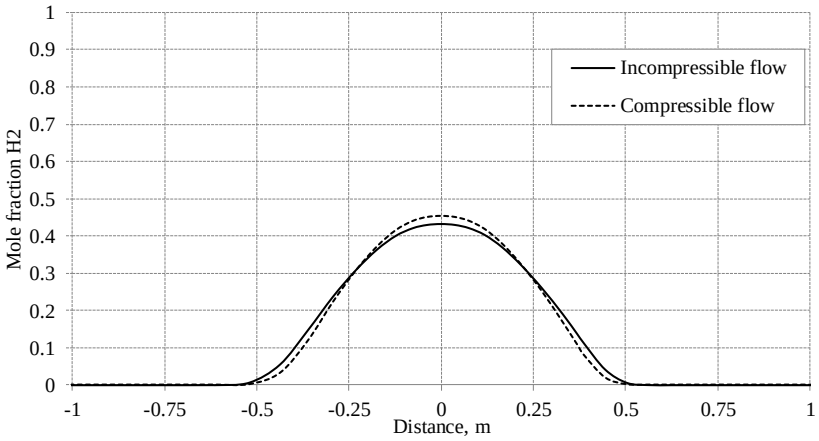


Figure 6.9 Hydrogen mole fraction distribution along the jet radius at 2 m from the nozzle: incompressible versus compressible flow (Time=540ms)

*6.3.1.2.3 Unignited release duration*

As discussed in the problem formulation, the valve is assumed to be fully open when the release begins and the ignition delay time is calculated accordingly. The time considered may however affect the hydrogen distributions and jet properties because of the tank blowdown. The ideal would be to model the valve opening, changing the characteristics of the flow

according to the time and section. However, to simplify calculations, two limit cases are considered:

- Ignition delay=540 ms, valve opening time is excluded;
- Ignition delay=800 ms, valve opening time is included in the ignition delay but valve is assumed fully open for all the 800 ms duration.

Distributions of hydrogen mole fraction for the two ignition delay times are given in Figure 6.10 at several distances x from the nozzle. The real scenario will be located between the two extreme cases with minimum and maximum ignition delay for a fully opened valve. Hydrogen concentrations do not show notable difference up to 6 m, indicating that the flow has already established at 540 ms and that blowdown does not affect significantly the jet characteristics during this period of time. Difference is clear at 8 m, as the jet at 540 ms has not yet arrived to 8 m; conversely, at 800 ms hydrogen concentration reaches the LFL at about 8.5 m. However, ignition is triggered at 2 m. Up to 4 m, concentration curves for 540 ms and 800 ms practically overlap, whereas difference is negligible for 6 m.

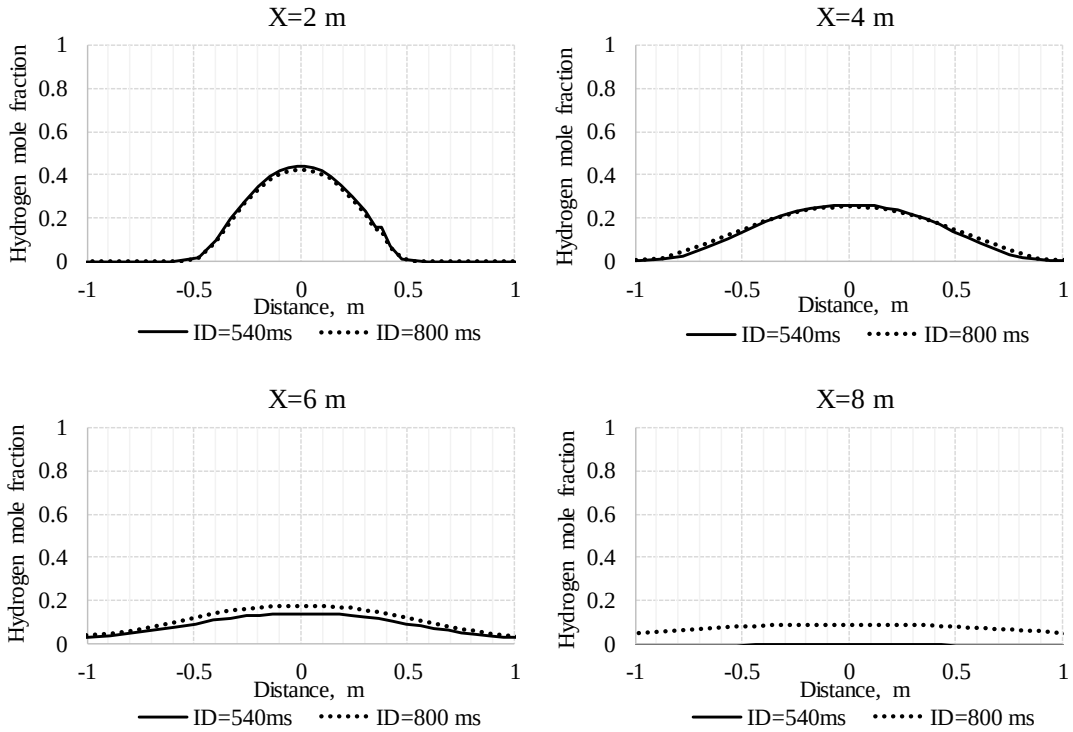


Figure 6.10 Hydrogen mole fraction distribution at several distances x from the nozzle for 540 ms and 800 ms ignition delay

6.3.1.3 Restrictor effect on the release

The release system consists of a stainless steel tube with diameter 11.9 mm, where a series of valves with 9.5 mm internal diameter was located. The 6.4 mm restrictor is located upstream the release valve. A complete scheme of the gas supply is available in Royle and Willoughby (2009). The complex release system causes few complications with regards to the assumptions made in the under-expanded jet theory, as the length and losses in the pipe between storage and nozzle may not be negligible. Indeed, the diameter at the release point is different from the restrictor one, which determines the mass flow rate of the release. It has also to be considered that the presence of several components and changes of diameters in the hydrogen path down to the release point can lead to formation of shock waves inside the pipe. This section is aimed to investigate the effect of release system configuration on the under-expanded jet characteristics. The study is limited to the near field to the nozzle. Two release configurations have been assumed and compared, to assess the effect given by the insertion of a tube with greater diameter between the restrictor and the actual release in atmosphere. In both the configurations, a portion of tube with length 80 mm was assumed upstream the restrictor. In configuration 1, it is assumed that hydrogen is directly released through the restrictor of 6.4 mm diameter into the atmosphere. In configuration 2, a further portion of 80 mm length tube is added downstream the restrictor orifice. In this case the gas is released into the atmosphere through an 11.9 mm diameter. The two configurations are shown in Figure 6.11. The tube thickness was assumed 4 mm in both configurations.

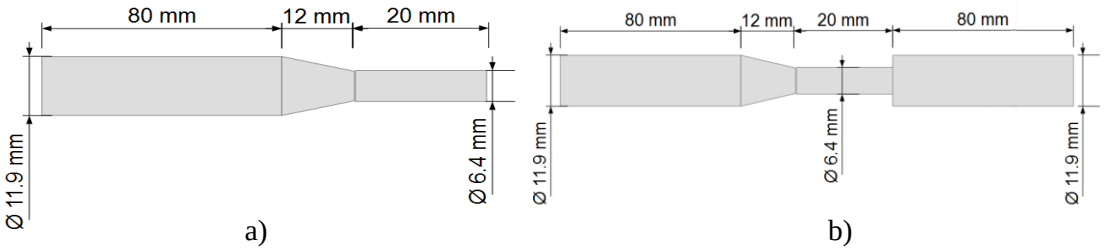


Figure 6.11 a) Configuration 1: only restrictor; b) Configuration 2: restrictor and tube

*6.3.1.3.1 Numerical details*

The CFD model consists of the Reynolds-Averaged Navier-Stokes (RANS) conservation equations for mass, momentum, energy and species (3.1)-(3.4), described in section 3.1 of the present work. The density-based solver was employed for calculations, as, originally, this approach was developed for high speed compressible flows. Therefore, it is expected a higher level of accuracy in solving the shock structures produced in the under-expanded jet (Fluent, 2016). Two additional equations for the turbulent kinetic energy and turbulent dissipation rate are solved and they are given by the realizable k-ε model (Eq. 3.5, 3.11). A steady state flow

was considered, as they aim of the study is to analyse the converged distributions for the two release system configurations shown in Figure 6.11. The dimensions of the computational domain were determined in proportion to the notional nozzle calculated for the release characteristics. A rectangular domain was employed for configuration 1. 16 divisions were used at the release point and minimum cell size was approximately 0.4 mm. The domain had size 0.315 x 0.315 x 0.616 m. Total number of CVs was approximately 650,000. A cylindrical domain was employed for the 2nd configuration, in order to decrease the total number of CVs to about 450,000 even if having a larger domain (0.48 x 0.792 m). The use of the O-grid technique to mesh the release orifice allowed a better refinement of the section (20 divisions along diameter) and saving of CVs. Graphical representation of the mesh is given in Figure 6.12. The computational domain was initialised with air at temperature equal to 288 K and pressure 101325 Pa. The inlet condition for the hydrogen flow was defined as pressure inlet, with absolute pressure equal to 20 MPa. The turbulence intensity for the hydrogen flow was imposed 20% while the turbulence length scale was evaluated as 0.07D, assuming a fully developed turbulent flow. Gauge pressure equal to 0 was defined at the external boundaries. An implicit formulation was employed to calculate the solution. Roe flux-difference splitting was employed for convective fluxes and least square cell based as spatial discretization for gradients. The first order upwind scheme was used to discretise the flow, turbulent kinetic energy and turbulent dissipation rate.

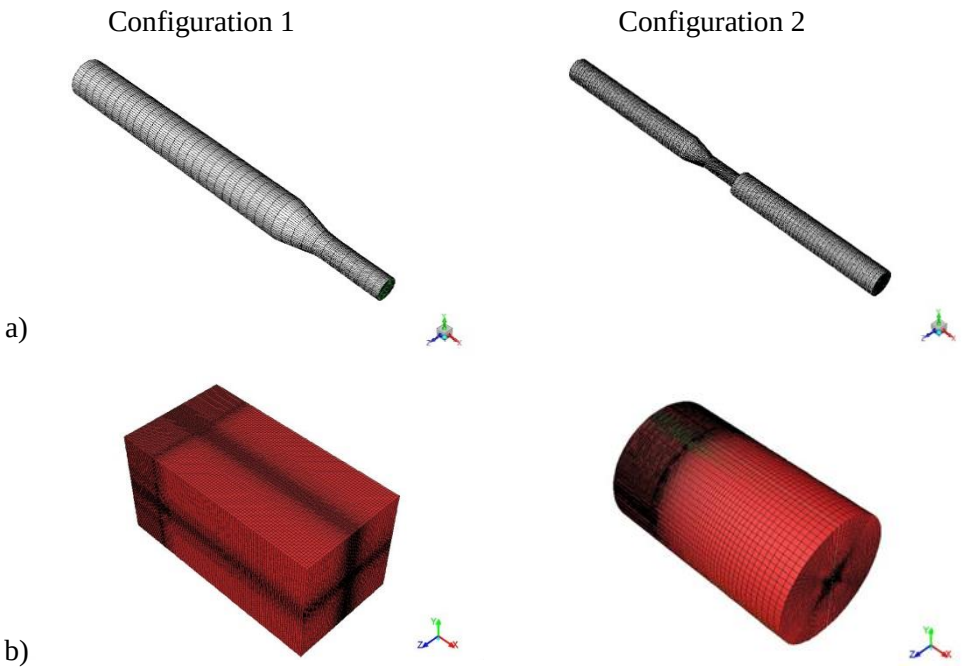


Figure 6.12 Numerical grid details: a) release system, b) overall domain

*6.3.1.3.2 Results and discussion*

Convergence of the simulations was determined by examining the evolution of hydrogen mass fraction and velocity magnitude distributions as the steady state solution was iterated. The parameters were monitored along the radius of the jet at 0, 0.1, 0.3 and 0.5 m downstream of the release, and along the jet centreline. A steady mass flow rate at the nozzle exit and overall domain mass balance were considered as further convergence criteria. Figure 6.13 presents the convergence analysis for the hydrogen mass fraction radial evolution at 0.5 m from the release, which corresponds to the further monitored distribution from the nozzle. Configuration 1 reaches a converged solution in 65,000 iterations. The real time required by the converged simulation is around 95h, which corresponds to approximately 15h per 10,000 it. Configuration 2 reaches a stable solution in 90,000 iterations. In this case, the real time needed by the simulation is around 110h, corresponding to an average of 12h per 10,000 it, which is lower than the previous case due to the reduced number of control volumes in the domain. Distributions of the converged solutions are shown in Figures 6.14-6.17 as contours of the main flow characteristics and as distribution of $H_2$ mole faction and velocity in Figure 6.18.

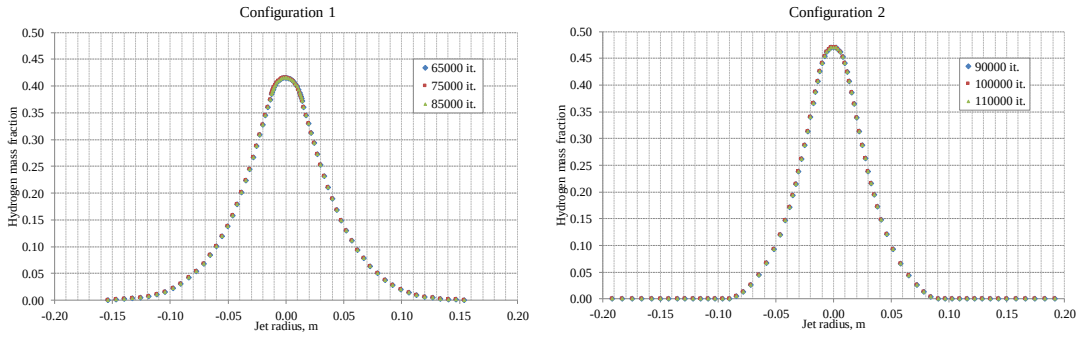


Figure 6.13 Convergence analysis: hydrogen mass fraction radial distribution at 0.5 m from the nozzle exit

The calculated mass flow rate at the nozzle is 0.359 kg/s for configuration 1 and 0.362 kg/s for configuration 2, which agrees well with the mass flow rate calculated as 0.373 by the notional nozzle theory. As shown in Figure 6.14, expansion of the jet begins immediately at the exit of the restrictor, with following expansion into atmosphere for configuration 1 and in the second portion of tube for configuration 2. In the second case, density at the nozzle is roughly 3 times lower than case 1. Figure 6.15 shows distribution for hydrogen mole fraction. At a first glance, it is possible to observe that the release from configuration 1 results in a wider jet, which will be characterized by higher entrainment of air and faster $H_2$ concentration decay along the axis, as shown in Figure 6.19. It is worth noting that the shorter distance between the jet axis and the domain boundaries may also affect air entrainment. Examining the velocity and Mach number contours in Figure 6.16 and Figure 6.17, it is not possible to

satisfactorily recognise the typical barrel shock in the near field to the nozzle for configuration 1 and it is almost absent for configuration 2. Therefore, it can be concluded that the geometry considered can deeply affect the characteristics of the under-expanded jet in the immediate proximity of the release. However, the main aim of the analysis is to assess if the release configuration affects significantly the jet at greater distances from the nozzle. Thus, the hydrogen and velocity magnitude were investigated along the centreline and along the jet radius at several distances from the release. Results are shown in Figures 6.18-6.19. The flow characteristics at the release present similar distributions. Dissimilarity between the two configurations is maximum 0.1 m from the nozzle, showing a wider jet for configuration 1 as already observed in Figure 6.15. It must be considered that different meshing techniques were employed in the two cases, and this may be the reason of deviation between the results of the two configurations. However, the difference between the two distributions decreases as the distance from the orifice increases, but at 0.5 m is still consistent. Configuration 1 (only restrictor) agrees well with the notional nozzle predictions for compressible flow at 0.5 m from the release point (4% difference). This observation agrees with the findings by Schefer et al. (2006): prediction of blowdown dynamics through a 3.175 mm restrictor better represented experiments compared to considering the release from the diameter of the tube it was inserted in. In conclusion, the release system configuration was shown to affect flow properties in the near field to the nozzle, highlighting the importance of detailed descriptions on release systems by experimentalists.

Configuration 1 Configuration 2

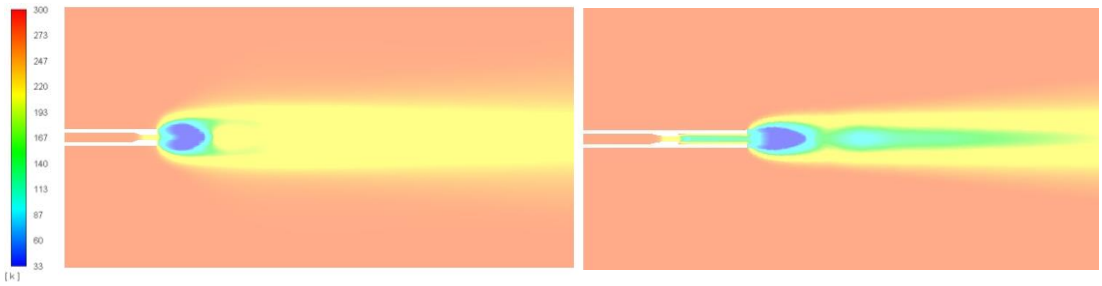


Figure 6.14 Temperature distribution on z=0 plane

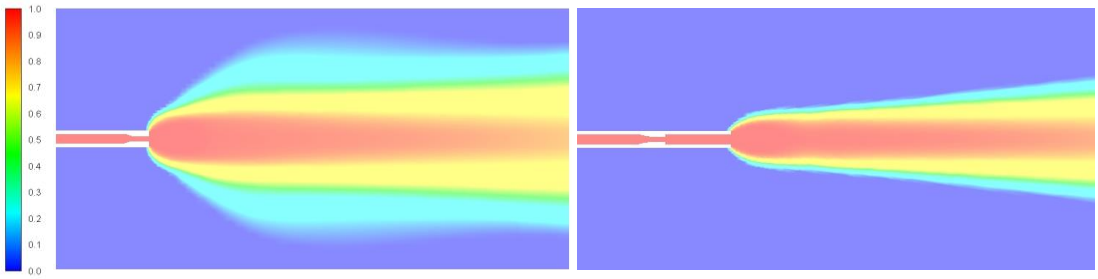


Figure 6.15 $H_2$ mole fraction distribution on z=0 plane

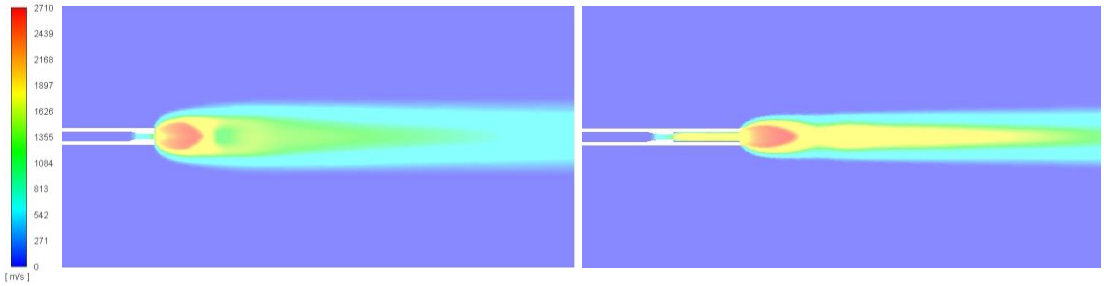


Figure 6.16 Velocity magnitude distribution on z=0 plane

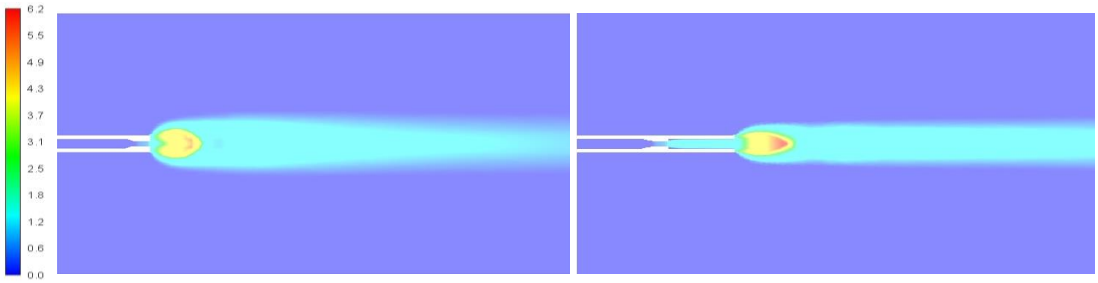


Figure 6.17 Mach number distribution on z=0 plane

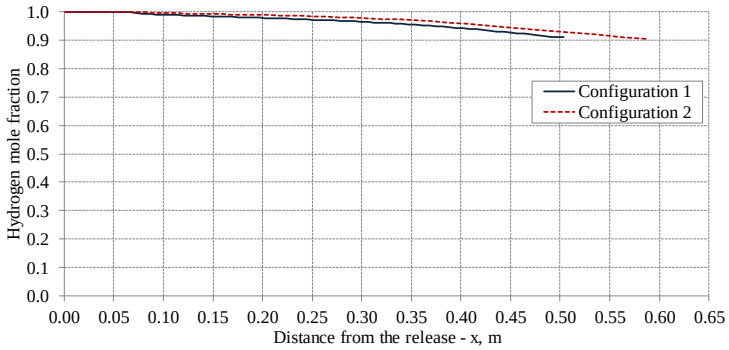


Figure 6.18 Hydrogen mole fraction distribution along the jet axis

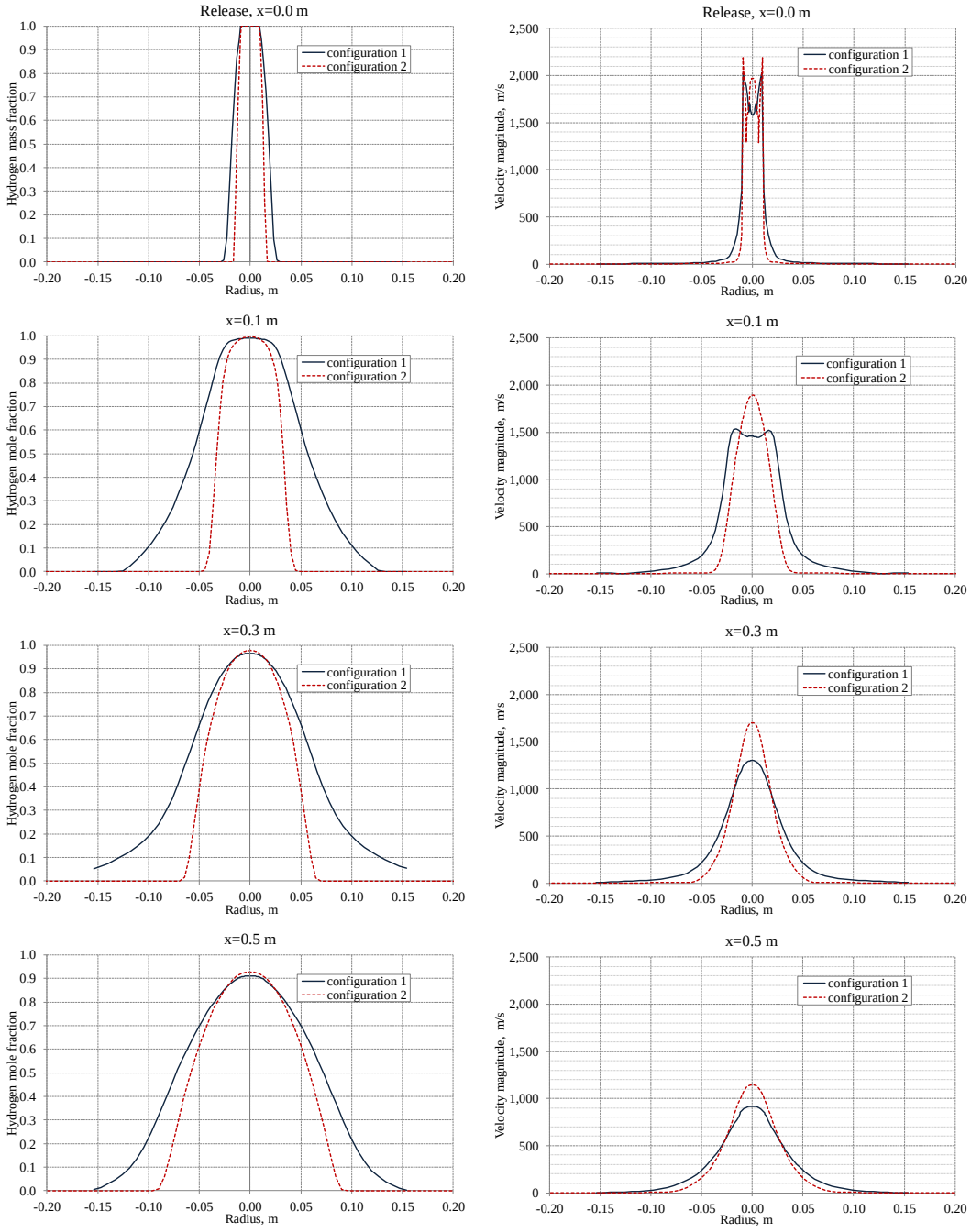


Figure 6.19 Radial distributions of hydrogen mole fraction and velocity magnitude at 0.0, 0.1, 0.3 and 0.5 m from the release point

### 6.3.2 INERIS test: 40 bar release

#### 6.3.2.1 Numerical details

The CFD model consists of the Reynolds-Averaged Navier-Stokes (RANS) conservation equations for mass, momentum, energy and species (3.1)-(3.4) reported in section 3.1 of the present work. RNG k-ε (Yakhot and Orszag, 1986) and realizable k-ε turbulence models (Shih et al., 1995) were employed and results were compared. The gas was assumed as incompressible and ideal for the study on dispersion of the jet. A segregated solver was

employed on ANSYS Fluent 14.5 and 16.2 as computational engine. The release source was modelled through the notional nozzle approach (Molkov, 2012). A square orifice with section equal to the notional nozzle area was employed in the numerical grid. The nozzle had length 4.4 cm and it was defined as a velocity inlet. Inlet velocity and temperature were imposed equal to 1199 m/s and 247.8 K respectively, as calculated through the notional nozzle theory (Shentsov, 2017). A turbulence intensity equal to 25% and turbulent length scale equal to $0.07D_{eff}$ were imposed as inlet turbulence parameters, according to the conclusions drawn in the study (Brennan et al., 2009). 2x2 cells were employed to subdivide the release source, as it was shown in previous studies to be a sufficient discretization for jets (Chapter 4, Venetsanos and Giannissi, 2016). The hexahedral numerical grid was built from the domain elaborated by Shentsov (2017). It was maintained uniform in the zone 1.2 x 1.2 x 4 m from the ignition point, as this is the zone where the hydrogen concentration is expected within the range 0.2-0.6. Cell size in this region was included in the range 2.3-2.5 cm. A cell growth ratio of 1.1 was employed outside this zone. The hexahedral domain had size 9x4.5x15 m and 939,000 control volumes. A second hemispherical domain (355,000 tetrahedral cells) surrounded the hexahedral domain, as for the mesh shown in Figure 6.2, to distance the domain boundaries and limit their effect on the simulation results. The two numerical grids were coupled as interfaces. The domain boundary was defined as pressure outlet with gauge pressure equal to 0 Pa. The domain was initialized with temperature equal to 298 K, ambient pressure and normal air composition. The SIMPLE pressure-velocity scheme was employed. A second order upwind scheme was used for resolution of the convective terms. A bounded second order implicit scheme was used for the advancement of solution in time. A time step equal to $10^{-3}$s was selected, as it was seen to provide a time step independent solution for the 200 bar release in section 6.3.1.2.1.

#### 6.3.2.2 Results and discussion

Results of hydrogen mole fraction distribution at 5 s are presented in Figure 6.20 for RNG k-ε turbulence model and in Figure 6.21 for realizable k-ε turbulence model. RNG κ-ε model shows an accurate concentration calculation along the jet. There is a rapid decrease of radial concentration at 1.25 m, as observed in experiment. The jet results to be wider at short distances from the nozzle (up to 3 m), providing a slightly higher hydrogen concentration on the sides of the jet. Reasons for this discrepancy may be both numerical and experimental. A finer discretization of the release source may affect dispersion calculation in the near field. Grid sensitivity tests conducted on cryogenic jet fires showed that the effect could be neglected beyond approximately $30 \cdot D_{eff}$, which in this case would correspond to ~1.4 m from the release point. Other possible reasons are associated to the experimental set-up. It was already shown that the exact release configuration may affect the hydrogen concentration and velocity

profiles in the near field (see restrictor effect paragraph 6.3.1.3). Furthermore, the authors of the experiments indicated that the measurements scattering may be affected by the slight difference in storage pressure between the performed tests (Daubech et al., 2015). However, discrepancies between simulations and experiments disappear beyond 3 m, and simulation reproduces well the overall hydrogen concentration. Realizable results in a slower axial concentration decay, providing at the ignition point a concentration 25% higher than experiment, which is close to stoichiometric hydrogen-air composition. Both the models achieved a "steady-state" distribution within the calculated 5 s in the region where concentration is sampled (up to 10.5 m). At 20 m hydrogen concentration is higher than the LFL. It is interesting to notice that the difference between the two turbulence models results is significant, opposite to what observed for the 200 bar release study. The increase of release pressure causes an increase of the turbulence level of the jet. Turbulence viscosity in RNG k-ε model for high Reynolds number limit is calculated similarly to realizable k-ε model, yielding to similar results for the 200 bar release. A further reason is related to the employed numerical grid, which is coarser for the INERIS test simulation. This may have led to smoother changes in concentration distribution when switching from one turbulence model to another. Hydrogen mass flow rate is 0.249 kg/s. Hydrogen mass imbalance at 5 s is 0.025% for the simulation employing RNG k-ε model, whilst it is 0.007% for realizable k-ε model. Both the simulations required approximately 30 h to calculate the 5 s release on a 48 CPU machine.

Velocity follows a decay similar to concentration for the respective models. Velocity profiles are given in Figure 6.22. Axial velocity between 1.25 and 2 m is included in the range 60-40 m/s for RNG k-ε model, whereas it is within 85-55 m/s for realizable k-ε model. The ignition point is located at 1.8 m. Therefore, flame speed is required to be higher than the mentioned values to oppose the flow field and propagate upstream the ignition location.

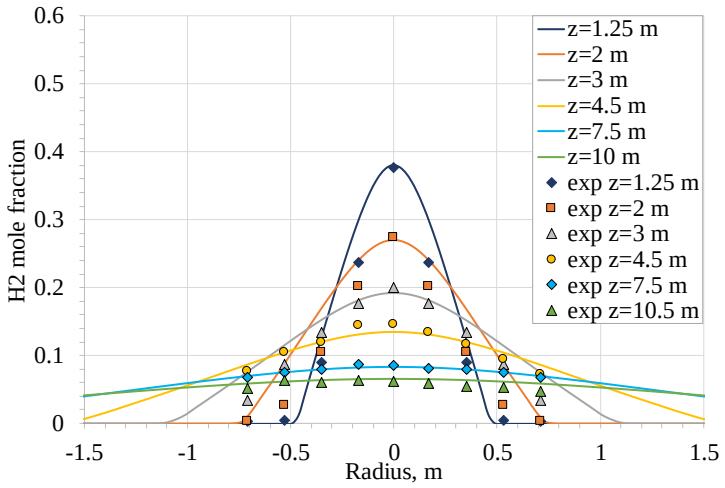


Figure 6.20 Hydrogen mole fraction radial distribution: RNG k-ε calculation versus experiment

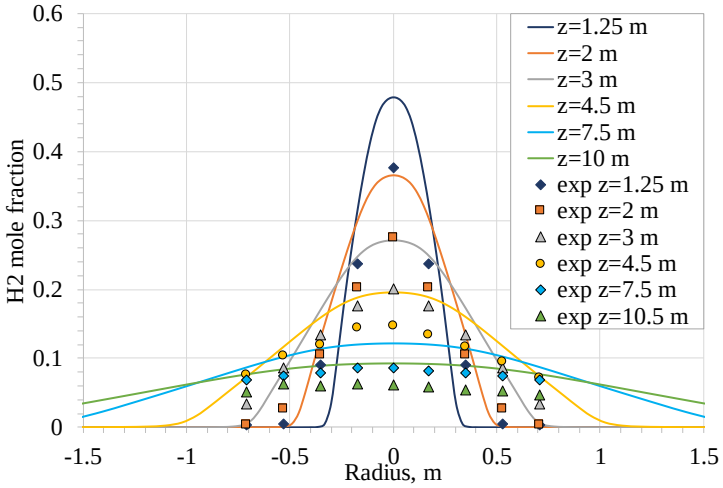


Figure 6.21 Hydrogen mole fraction radial distribution: realizable k-ε calculation versus experiment

A correct representation of turbulence inside the jet is fundamental when conducting studies on delayed ignition as shown by experimental evidences (see Takeno et al., 2007). Therefore, the simulated turbulence mapping was compared to the experimental measurements. In calculations employing k-ε, the velocity fluctuating component was calculated as $u' = \sqrt{2/3 \cdot k}$. Results for the two turbulence k-ε models are given in Figure 6.23. RNG k-ε provides a turbulence intensity (TI) included in the range 30-35% along the jet, whereas the TI calculated by realizable k-ε stabilises at 25%, which better agrees with Hinze's approximations (Daubech et al., 2015). In both the cases, TI increases with the radius normalised to the axial distance. Realizable k-ε model provides a more pronounced growth with the increase of the radius, reaching a maximum which is about twice the value obtained by RNG k-ε model. Reason for this different growing trend can be given by the differential calculation of turbulent viscosity provided for RNG k-ε model, which should improve the performance of the model for the low-Reynolds number regions of the flow.

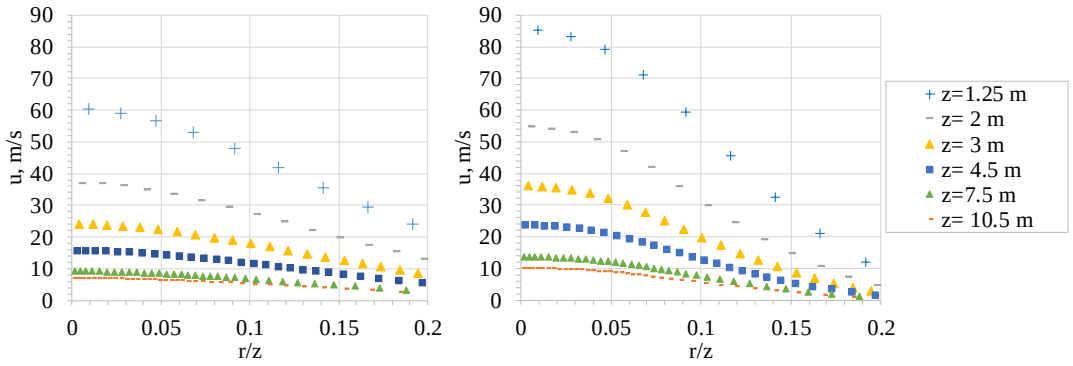


Figure 6.22 Radial velocity profiles for RNG k-ε model (left) and realizable k-ε model (right)

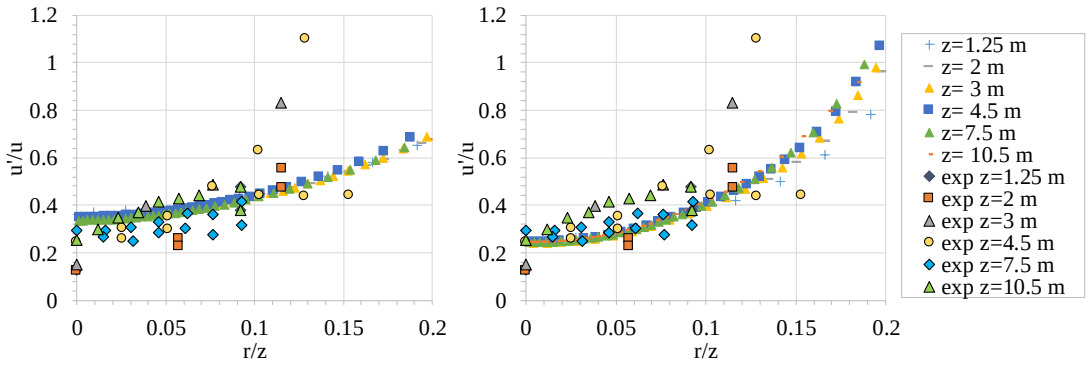


Figure 6.23 Turbulence mapping of the hydrogen jet for RNG k-ε model (left) and realizable k-ε model (right)

A further analysis employing a LES approach was conducted. Dynamic Smagorinsky-Lilly was employed as turbulence sub-model. Results on hydrogen concentration distribution are reported in Figure 6.24. Concentration of hydrogen and velocity were sampled every time step to calculate the average distributions. Reason for the slightly quivery curves at greater distances may be that the solution has not yet reached a "pseudo" steady state distribution. The axial concentration is slightly underestimated between 2 and 4.5 m, but in general concentration is well reproduced by the LES approach. Figure 6.25 shows the velocity profiles at the same locations of the concentration sensors.

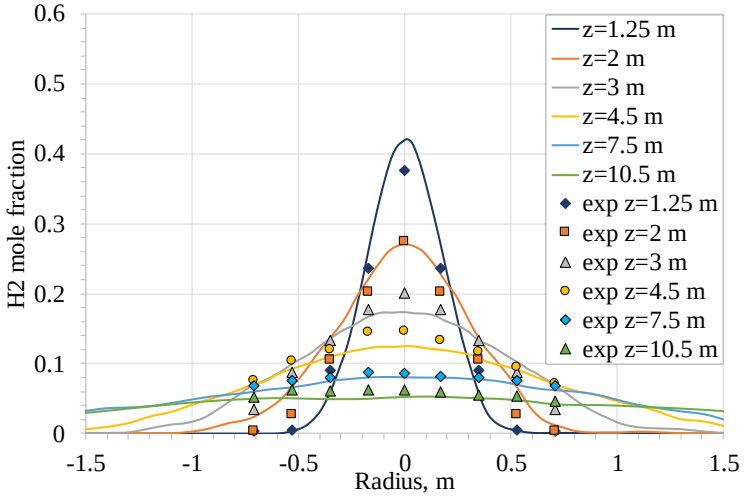


Figure 6.24 Hydrogen mole fraction radial distributions: LES approach calculation versus experiment

Calculation of turbulent intensity for the LES approach is more challenging than RANS calculations. A first calculation treated the turbulence intensity as a sub-grid scale property. The turbulent velocity was calculated as $u'_{sgs} = \sqrt{\frac{2}{3}} \cdot \mu_{t,sgs} / (\rho \cdot L_{sgs})$ on a sub-grid scale. The associated turbulence intensity results approximately one order of magnitude less than the experimental TI of the flow, as reported in Figure 6.26 (left). In Figure 6.26 (right) the

turbulent intensity was calculated as ratio of the root mean square velocity to the mean velocity of the flow. Axial TI is included in the range 50-80%, which is significantly higher than what observed in experiment and in k-ε models calculations. Reason for such high TI may be given by the not sufficient sampled time, 5 s. Generally, samplings 5 times greater than the characteristic time of the flow are suggested to obtain representative statistics of flow parameters in LES simulations, most of all at further distances from the release point. If it is considered that the velocity field reaches velocities equal to ~6 m/s beyond 10.5 m, approximately 9 s could be considered as the characteristic flow time to be simulated.

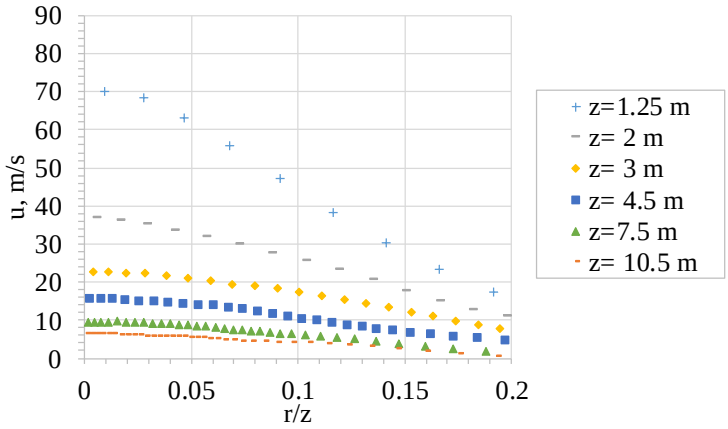


Figure 6.25 Radial velocity profiles for LES model

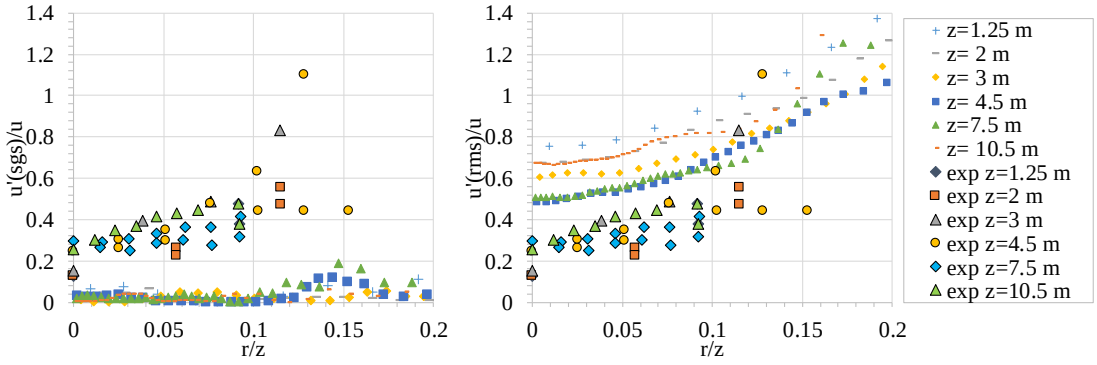


Figure 6.26 Turbulence mapping of the hydrogen jet for LES Smagorinsky-Lilly model: SGS turbulent intensity (left) and RMS turbulent intensity (right)

## 6.4 Aspects of numerical modelling of jet delayed ignition

Reproduction of hazards in delayed ignition simulations may be a challenge in numerical simulations. Experimental evidence has shown that the turbulence level of the jet may have greater effect than the total mass released on the explosion overpressure, see (Takeno et al., 2007), (Royle and Willoughby, 2011a). Accurate reproduction of the unignited jet hydrogen concentration and turbulence is of utmost importance to reproduce the flame and overpressure dynamics after ignition. This study considers two approaches to simulate the delayed ignition

of high pressure turbulent jets and analyses their performances and suitability to represent the physics of the problem under study. Details of the CFD models and results will be presented in the following section.

### 6.4.1 HSL test: finite rate model

The present section investigates the applicability of the finite rate chemistry to directly determine the rate of reaction. The finite rate model is generally suggested for laminar flows or for turbulent flows involving a fast turbulence time scale relative to chemistry time scales. These conditions are likely in detonation applications rather than deflagrations. The finite chemistry model response to application in this class of problems was analysed. Description of the model can be found in section 3.4.1 of the present work. The reaction sources for the burning mixture were calculated as in Equations (3.15)-(3.19). 9 species and 18-step reduced chemical reaction mechanism were considered for hydrogen combustion in air (Peters and Rogg, 1993). The Discrete Ordinate model was activated to include radiation in simulation. 5x5 angular divisions and 3x3 pixels were employed to discretise the RTE (Equation 3.38), as suggested in (ANSYS Fluent, User's Guide, 2016) for problems involving large gradients of temperature in space. The water vapour absorption coefficient was analytically calculated as function of temperature and partial pressure in each control volume, following an exponential function built on the results of Hubbard and Tien's study (Hubbard and Tien, 1978). The fluid is considered as a compressible ideal gas. The numerical grid and results of the dispersion simulation conducted in section 6.3.1 were employed for the delayed ignition simulation (Time=540 ms). At the ignition point, the cloud has hydrogen concentration between 0.40 and 0.45 while velocity is included in the range 55-60 m/s. Ignition of the jet at 2 m from the release point was accomplished assigning temperature equal to 2200 K, OH and H2O mole fraction equal to 0.01 in a region with size 10 cm. PISO scheme was used for pressure-velocity coupling, as recommended for higher stability of transient flow calculations (ANSYS Fluent, User's Guide, 2016). Second order upwind was used for all the flow parameters with exception of the discrete ordinate model. Under-relaxation factors (URFs) in the range 0.1-0.2 were used for pressure, density, momentum and species, while 0.8 was used for turbulence properties. Time step equal to $5 \cdot 10^{-5}$ s was considered, as generally orders of $10^{-5}$ or $10^{-6}$ s are indicated for deflagration studies. Iterations were limited to 20 per time step. Bounded 2$^{nd}$ order implicit formulation was employed for advancement in time, as a time discretisation ensuring bounds for variables is generally recommended when better stability is required. Simulations were run on Fluent software versions 14.0 and 14.5. The numerical parameters not mentioned in the present section were maintained the same as in section 6.3.1.1 for simulation of the unignited phase.

6.4.1.1 Simulation results

Maximum CFL was ~14 and it was recorded at the release source. It remained approximately constant throughout the simulation, given that the elapsed time was not great enough to observe a significant change in release velocity during the tank blowdown. The maximum CFL is accepted as it is below the maximum value recommended by ANSYS Fluent (2016) for pressure-based solver and because it rapidly decays with distance, due to the increase of the cell size and decay of velocity. CFL in the region where ignition takes place is approximately 1. Figure 6.27 shows the pressure dynamics at the sensor. It is not clear from the experimental reports if the pressure dynamics was recorded from the time of ignition, so the simulated pressure curve was shifted in time to correspond to the recorded peaks. There is a good agreement between simulations and experiments. Difference in pressure for the maximum peak is negligible, while the second peak is slightly overestimated. Position of the flame at the time of arrival of the pressure wave to the sensor is shown in Figure 6.28. It can be observed that flame 8 ms after ignition is mainly affected by transport of products due to the jet field velocity and flame has propagated back by almost 1 m.

Despite a good agreement between simulations and experiments, a preliminary analysis on time step independence showed deviation of the solution with decrease in time step. The reason for such performance of the combustion model is explained as follow: given the large time step employed and grid refinement level, all the fuel in the cell burns as the flame propagates. A very thin flame front is artificially produced. However, the use of a lower time step leads to a progressive combustion of the fuel in the cell, resulting in a propagating thickened flame front occupying 3-5 CVs which causes an increase of the explosion pressure. Due to limitation on the flame front visualization and resolution of the grid, this argument could not be verified.

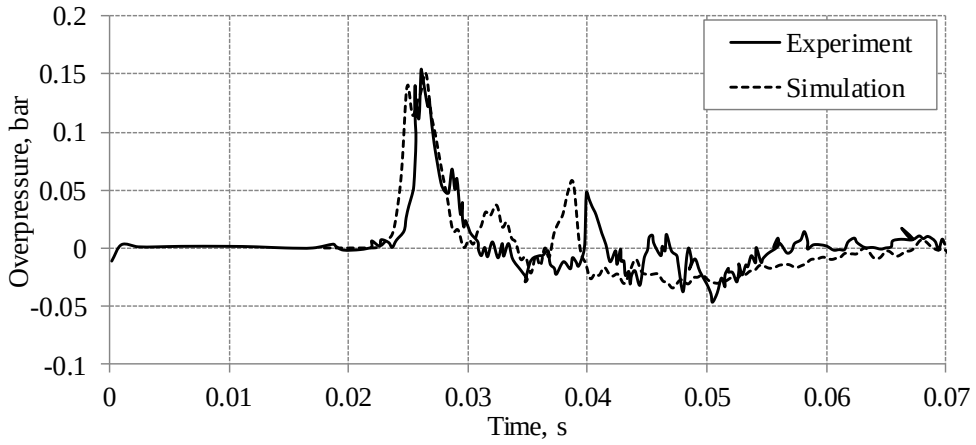


Figure 6.27 Pressure dynamics for time step equal to $5 \cdot 10^{-5}$ s and bounded second order time advancement scheme

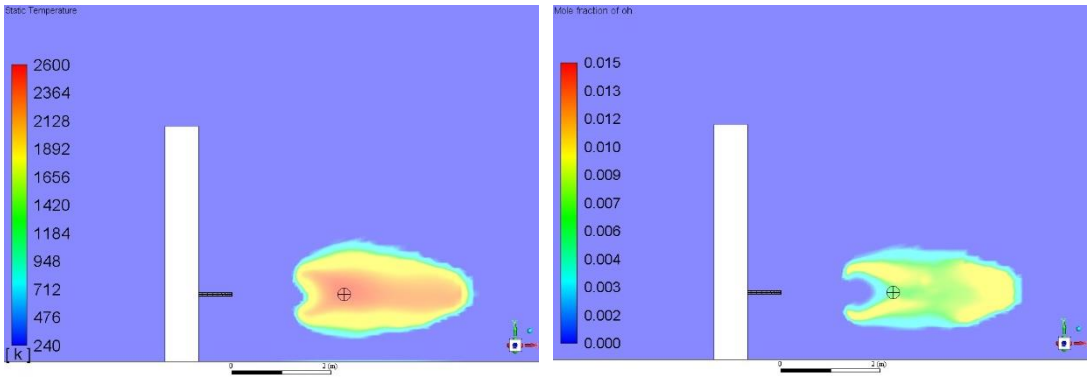


Figure 6.28 Temperature (left) and OH mole fraction (right) distributions at 8 ms after ignition for time step equal to $5 \cdot 10^{-5}$ s and bounded second order time advancement scheme

### 6.4.2 INERIS test: multi-phenomena deflagration model

A second approach for modelling the non-uniform premixed flame propagation was considered. The multi-phenomena deflagration model developed by Verbecke et al. (2009) and described in section 3.4.3 was here employed. The model was modified to take account of the highly turbulent state of the jet at the moment of ignition. Equation (3.32) was considered for the turbulent flame speed calculation. The approach was applied to simulate delayed ignition in a 40 bar hydrogen release (INERIS test). The distribution resulting from the dispersed phase at 5 s was used as an initial condition. The gas was assumed as compressible and ideal. A coupled solver was employed along with an explicit time-stepping formulation. CFL equal to 0.3 was imposed. However, time step is defined by the maximum velocity, which is recorded at the inlet nozzle, therefore a lower CFL will be expected in the region where the flame propagates. The Advection Upstream Splitting Method (AUSM) was employed as convective flux type, as it is considered to provide exact resolution of contact and shock discontinuities (ANSYS Fluent, User's guide, 2016). The second order upwind scheme was maintained for the convective terms. Ignition was realised by increasing linearly the progress variable, *c*, from 0 to 1 in a group of 4x4x4 cells located at 1.8 m. The ignition duration was assumed to be equal to the time needed by the flow to cross 1 CV at 1.8 m (0.4 ms).

#### 6.4.2.1 Simulation results

Given the high velocity of the hydrogen release (1199 m/s), the maximum CFL is recorded at the release point. The time step calculated from CFL=0.3 is approximately equal to $1.5 \cdot 10^{-6}$ s. This value is maintained for all the calculation as the velocity at the nozzle does not change in time. In the flame propagation zone CFL generally maintains <=0.2. Figure 6.29 shows the pressure transients at the three sensors for the calculations employing RNG and realizable κ-ε models. The dispersion solutions for the corresponding turbulence models were employed as

initial conditions. Both the numerical calculations result in an earlier arrival of pressure at the sensors. This may be a direct consequence of the ignition duration and technique. Therefore, this aspect is investigated in the following section. RNG k-ε model reproduces well the experimental pressure peaks at the sensors located downstream and on the side of the ignition location. Peak at P1 sensor is overestimated. The cause can be associated to the higher TI prediction: velocity increases towards the release point, leading to higher $u'$ calculation and, consequently, higher Yakhot's factor. Pressure, temperature and products mass fraction distributions in time, shown in Figure 6.30 and Figure 6.31, elucidate the cause of the resulting pressure transients. It can be observed from Figure 6.30 that the second pressure peak is given by reflection of the pressure wave on the ground. Figure 6.29 shows that calculated first pressure peak width is narrower than in experiment for P1 and P2 sensors, indicating that the model results in a faster combustion and pressure drops to atmospheric before being caught up by the reflected pressure wave. Ignition in experiments was performed using a premixed flame of stoichiometric oxygen-hydrogen mixture. The release point was located 0.2 m below the jet axis and the flame had length approximately equal to 0.4 m. The experimental ignition technique affects the resulting pressure and flame propagation dynamics, increasing the turbulence level of the mixture and modifying its composition. The combustion products of the "ignition flame" itself may work as diluents of the reactants, slowing down the overall rate of reaction and widening the extension in time of the first pressure peak (time 8-9 ms in experiments). On the other hand, experimental negative pressure is well reproduced at both the sensors. Pressure at P3 did not show any negative phase, while in experiment the measured negative pressure was even greater than the positive peak. However, this portion of measurements is considered to not be entirely reliable and to be caused by some damage to the sensor, because of both the value of achieved negative pressure and the following increase to a positive value comparable to the pressure peak given by deflagration.

Temperature and products mass fraction distribution (Figure 6.31) illustrates the flame propagation in time. The highest temperature zone is located close to the release nozzle, where mixture is continuously fed with hydrogen by the jet inlet. Turbulent flame speed increases from approximately 20 m/s at 2.5 ms to 80 m/s at 15 ms. The wrinkling factors mainly contributing to increase the turbulent flame speed are associated to the flow turbulence and fractal-like flame wrinkling, respectively $\Xi_{rng}$ and $\Xi_{fract}$. $\Xi_{rng}$ is included in the range 6-8 in the region around the propagating flame. However, the factor increases up to 50 at the limiting sides of the jet (r/z>0.2), where the flow is characterised by high turbulence ($u'$) and low turbulent flame speed because of the low hydrogen concentration. $\Xi_{fract}$ can vary from 1 to 4 within 4 m from the release point.

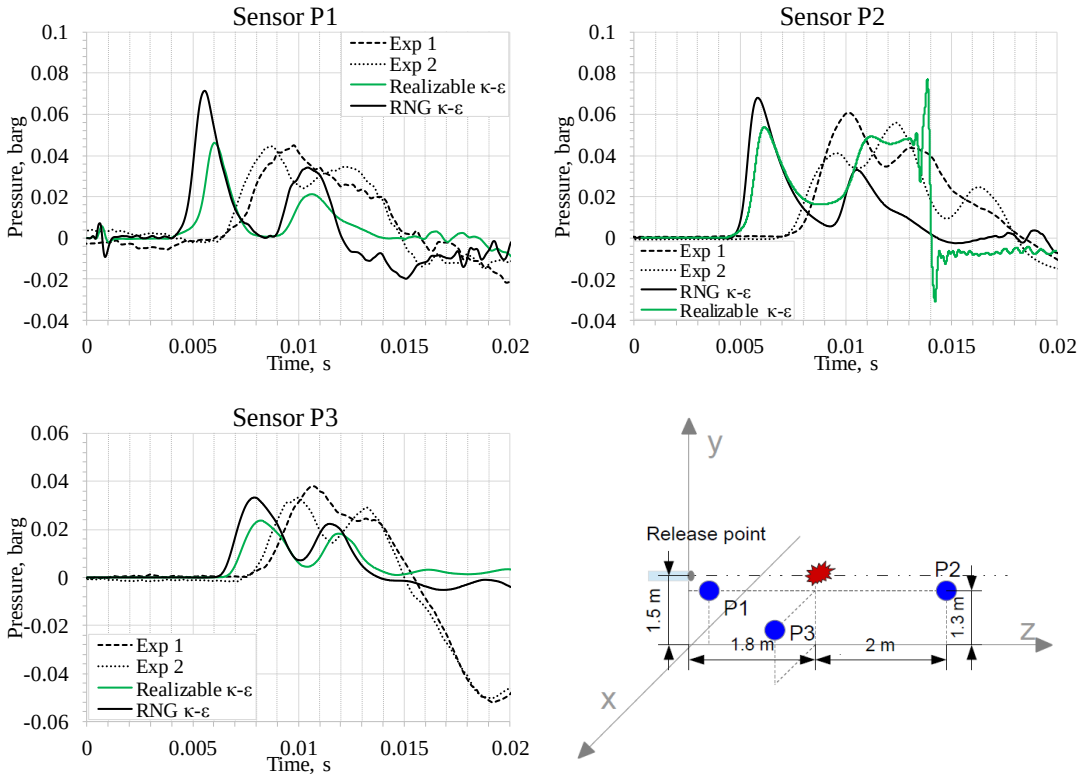


Figure 6.29 Pressure transients for realizable and RNG k-ε models: simulations versus experiment

Figure 6.29 provides a comparison to the results obtained employing a realizable k-ε model. In general, the pressure calculated at the sensors is lower than RNG k-ε model estimation. The cause is given by ignition of the jet in a richer zone. Indeed, realizable k-ε model resulted in a slower decay of hydrogen mole fraction (see Figure 6.21). The jet is ignited in a zone with fuel concentration approximately 40%, conversely to the calculation for RNG k-ε model which provides a near to stoichiometric composition at 1.8 m. Therefore, the calculated Karlovitz wrinkling factor of the turbulent flame speed will be lower, along with the calculated flame temperature. Furthermore, as seen in Figure 6.23, turbulence intensity levels along the jet are lower, too. This would translate in lower $\Xi_{rng}$, which as discussed for RNG k-ε model results is among the main contributors to the increase of turbulent flame speed. Combustion downstream the ignition point is enhanced because of the higher hydrogen concentration, causing the cohesion of the two pressure peaks at sensor P2, rather than having a pressure drop as for RNG k-ε model. However, large oscillations of pressure were recorded at P2 at about 14 ms. Pressure within 13 and 16 ms is presented in Figure 6.29 as an average over 250 steps, but wide variations are still visible. These oscillations are due to the passage of the flame at the sensor location.

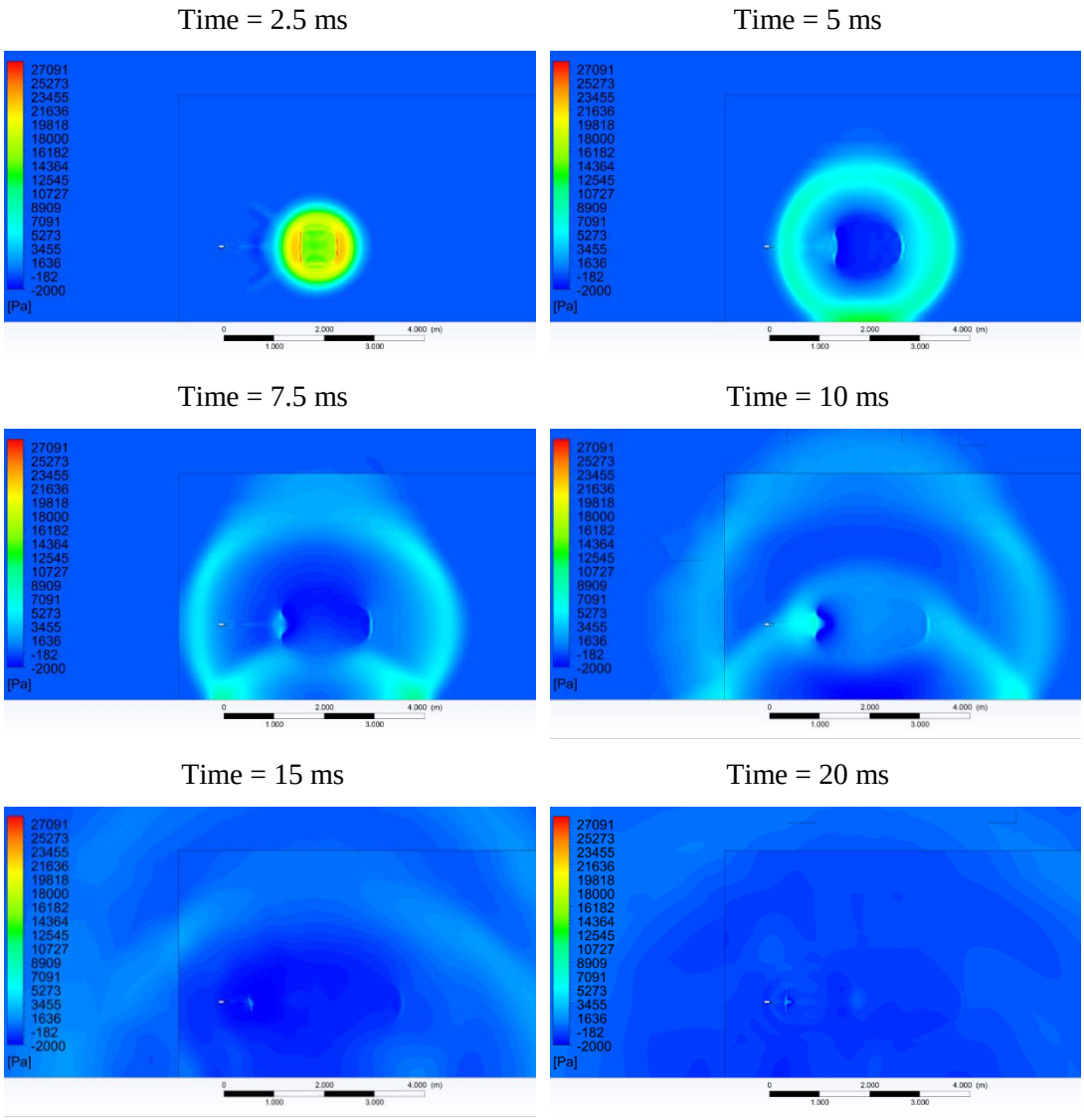


Figure 6.30 Relative pressure distribution on yz plane for RNG k-ε model calculation

The arrival time of the pressure wave to the sensors may be affected by numerous factors. One of them is the ignition process that in this section is investigated in terms of ignition duration. The ignition time was varied from 0.4 ms to 1 and 2 ms and results are shown in Figure 6.32. The higher is the ignition time, the longer is the pressure wave arrival time. For an ignition time equal to 2 ms a 20% decrease was observed at the sensors, due to a minor effect of the products expansion during ignition. However, it is unlikely that the ignition process would take as long as 2 ms, therefore this is presented as a limit scenario. Both RNG k-ε and realizable k-ε models required approximately 16 h to calculate 30 ms of simulated time on a 48 CPU machine.

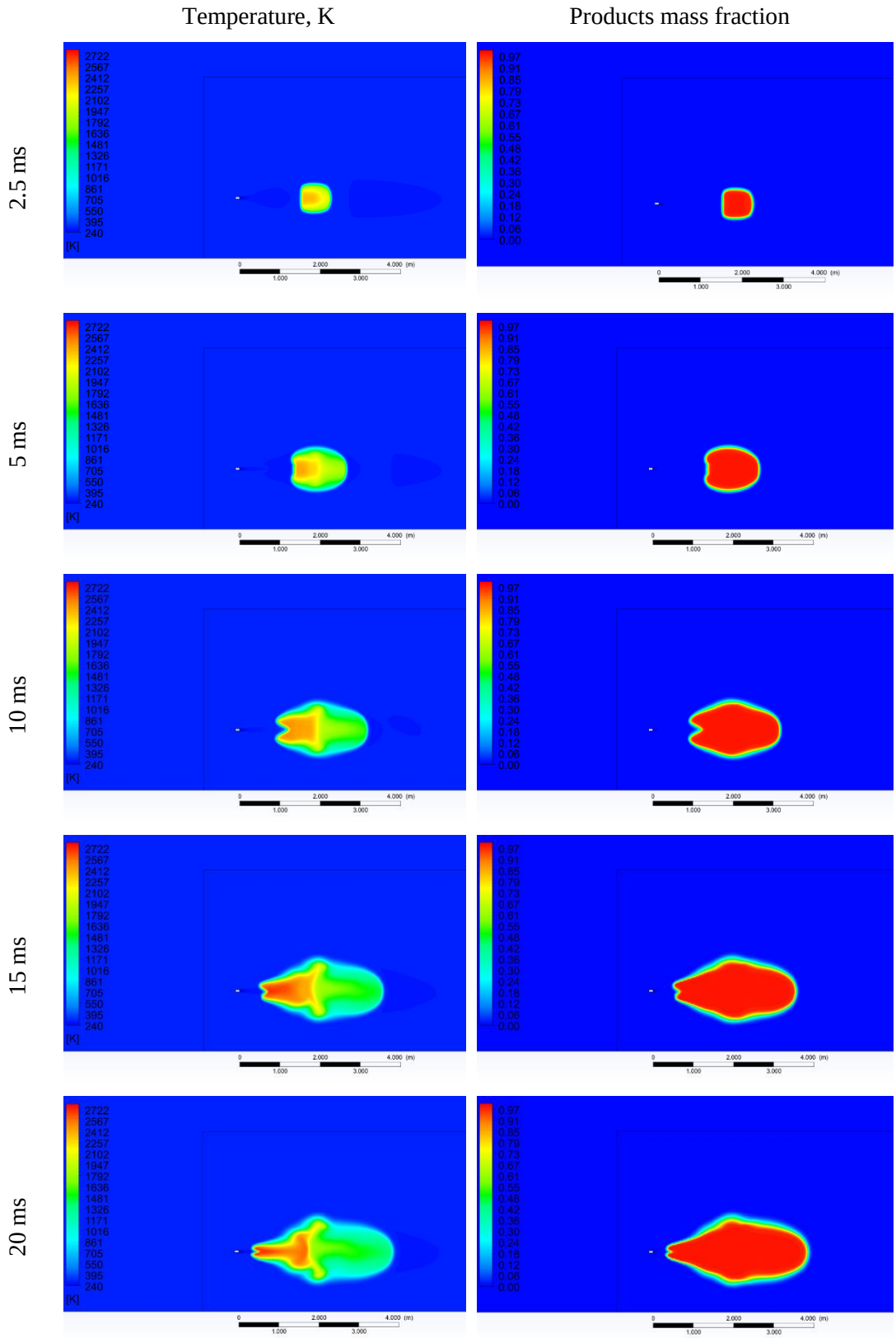


Figure 6.31 Temperature and products distribution on yz plane for RNG k-ε model calculation

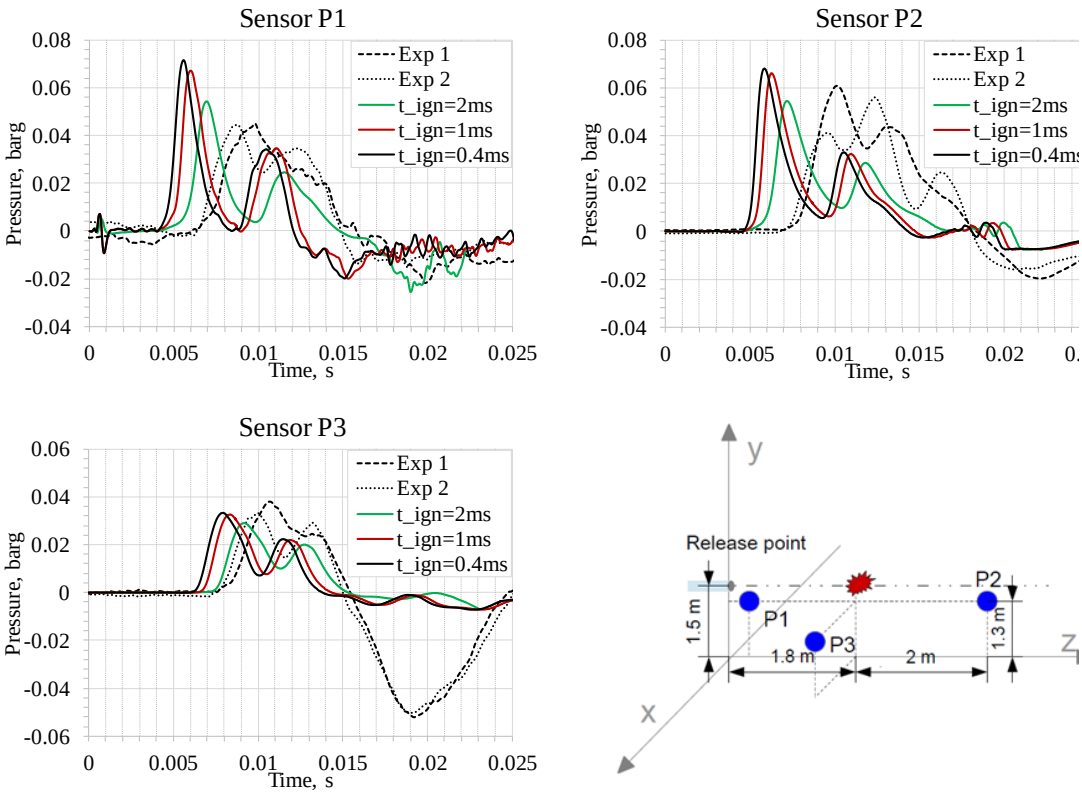


Figure 6.32 Effect of ignition duration on pressure transients for RNG k-ε model

The possible effect of numerical errors and inaccuracy on the obtained solution was assessed through two sensitivities studies. A first CFL sensitivity test was conducted. CFL was halved, as suggested by the CFD evaluation protocol (Baraldi et al., 2017). The ignition time considered for this analysis was 1 ms. Comparison of results for CFL equal to 0.3 and 0.15 is given for sensor P1 and P2 in Figure 6.33. The pressure transients coincide, confirming the time independency of the solution. The second sensitivity study should be conducted on the grid independency of the solution. However, as presented in section 6.3.2.1, the numerical grid already counts about 1.28 million cells. The numerical diffusion was addressed by a fine mesh in the region where the hydrogen disperses (cell size ~2.3-2.5 cm) and by the use of a second order upwind scheme for convective terms. A full sensitivity study would be unpractical given the already numerous control volumes. An increase of the convective numerical scheme order was employed to quantify the accuracy and stability of the solution as an alternative to the grid independence test, following the guidelines given in the CFD evaluation protocol. The scheme was changed from second order upwind to third order MUSCL. Maximum deviation in pressure resulted to be <8% and it was recorded at the maximum peak, whereas the pressure dynamics followed the same trend as the second order scheme. It is considered that the deviation is acceptable for engineering calculations.

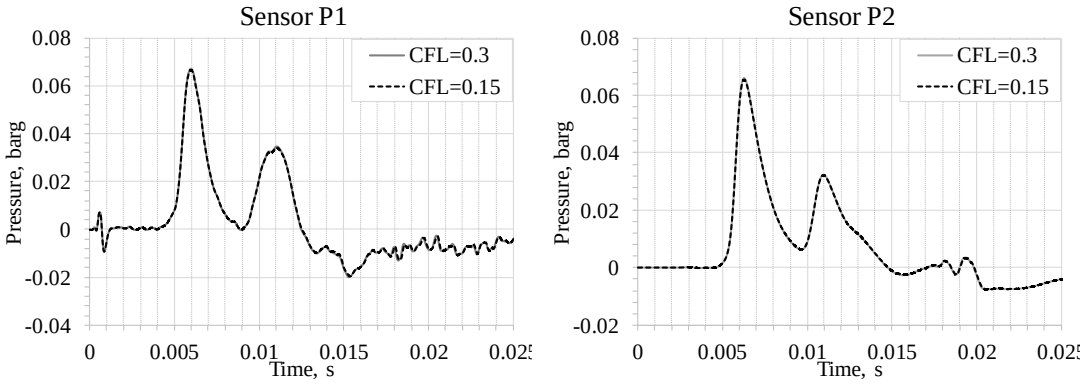


Figure 6.33 CFL sensitivity test: pressure transients for RNG k-ε model

From the analysis above, it was seen that the fractal-like wrinkling factor may affect considerably the turbulent flame speed. In the following section, $\Xi_{fract}$ is considered as function of the control volume size and the Kolmogorov length scale, as described in Equation (3.33). Results are given in Figure 6.34 and they present a decrease of overpressure at all the sensors. Deviation between simulations and experiment can be associated to the assumption of resolving the quantity $\frac{R_{flame}}{Cv\ size}$, which may not be exact for RANS simulations. This assumption is more appropriate for a LES approach, where larger eddies are resolved and what is below the sub-grid scale is modelled. $\Xi_{fract}$ as described in Equation (3.35) was employed for calculation of the turbulent flame speed. The distribution obtained in a parallel study conducted at HySAFER (Shentsov, 2017) was employed for the simulation of ignition. The quasi steady state dispersion results, obtained through dynamic Smagorinsky-Lilly turbulence sub-model (~12 s of simulated time), were in good agreement with experiments and they were interpolated on the mesh used for the present study. Results on pressure transients are shown in Figure 6.34. Pressure oscillations similar to realizable k-ε model can be observed when the flame crosses the location of the sensor P2. LES is shown to provide worse performance than RANS models. The reason may be given by a mesh too coarse to accurately resolve turbulence in LES, whilst in RANS averaging of the flow parameters allows a smoother reproduction of pressure. Furthermore, it should be considered that LES allows resolution of only 10% of the flame wrinkling, as observed for spherical flame propagation for uniform hydrogen-mixtures. The computational time for LES calculation was approximately the same as for RANS simulations.

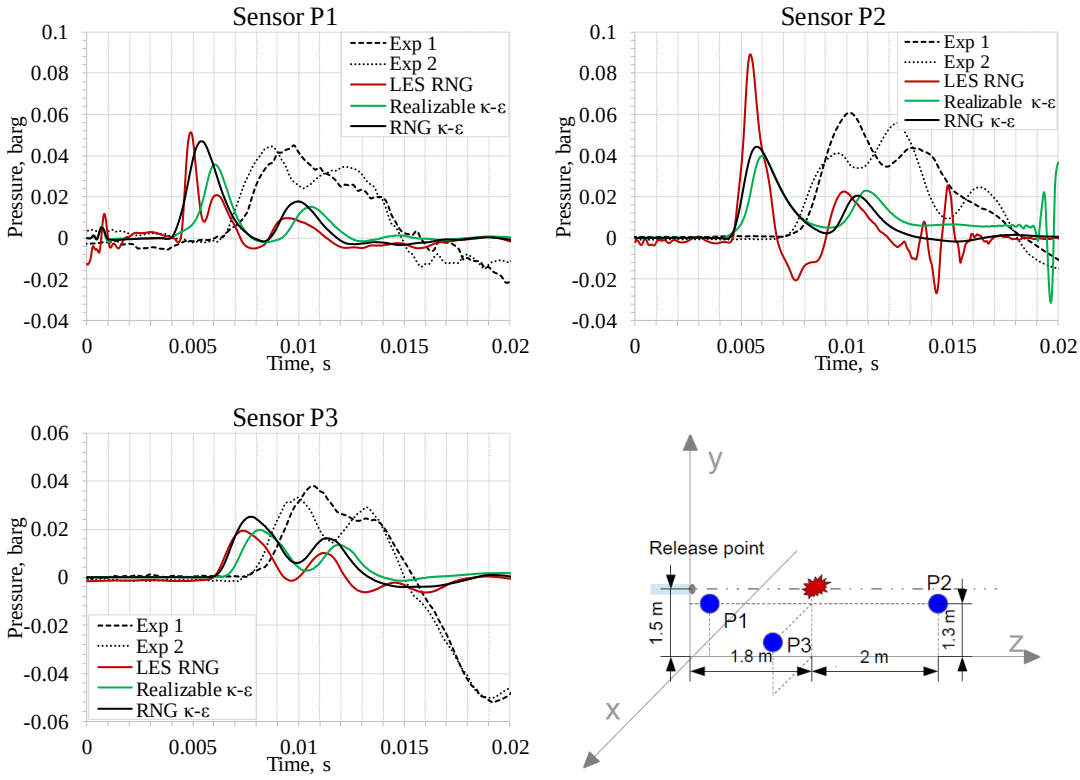


Figure 6.34 Pressure transients for realizable k-ε model, RNG k-ε model and LES: simulations versus experiment

## 6.5 Concluding remarks

The dispersion of hydrogen releases from storage at 40 bar and 200 bar was simulated. The turbulence model was found to affect the hydrogen jet at 40 bar. RNG k-ε model and LES Smagorinsky-Lilly yielded similar results and gave better reproduction of experimental distribution. However, among the two, RNG k-ε better approximated turbulence within the jet. Realizable k-ε turbulence model was found to consistently differ from the other turbulence models' prediction by over 25%. For higher release pressure (200 bar), the effect of the turbulence model on hydrogen concentration was found to be limited to a maximum variation equal to 6%. Two approaches for simulating delayed ignition overpressure and flame propagation were considered and tested. The finite rate model was found to agree with experimental results for overpressure originated by ignition of the 200 bar jet; however, the model presented inconsistency with variation of time step. The multi-phenomena deflagration model was proposed as an approach. The model was adapted to non-uniform and turbulent mixtures derived by hydrogen jets. Applicability of the approach was tested on the 40 bar hydrogen release experiment performed at INERIS laboratories. The model presented better reproduction of experiments for wrinkling factor associated to fractals as function of the flame extension and for RNG k-ε model.

# 7 Rupture of a tank in a fire

## 7.1 Introduction

Installation of a thermally activated pressure relief device (TPRD) on high-pressure hydrogen tanks is required by Regulations (ISO/TR 15869:2009 and GTR 2013). In case of a continuous and/or established fire involving the tank, the device activates venting the gas and preventing the catastrophic failure of the tank. This scenario would result in a jet fire and it was investigated in Chapter 4. However, a second scenario involves the TPRD failure to activate and an inadequate thermal protection of the tank to withstand the fire. In this case the tank can catastrophically rupture with a devastating blast wave and fireball, leading to life safety and property protection issues. Several examples of such scenarios are available in the accident history of CNG vehicles. In 2002 an incident with the following dynamics was recorded: the impingement on the cylinder of the flame from the vehicle interior did not encompass the TPRD and the strength of the cylinder was compromised earlier than the TPRD reached the activation temperature. A similar circumstance was observed in 2007. In this case the tank exploded while the first responders were responding to the fire involving several adjacent vehicles (Zalosh, 2008). No accidents have been recorded yet for hydrogen powered vehicles but it should be considered the limited number of deployed units. Dadashzadeh et al. (2018) calculated that if the fire resistance rating (FRR) of the onboard storage tank is below 47 minutes the risk is higher than $10^{-5}$ fatality/vehicle/year, which is considered as an acceptable risk level. Precisely, the risk can be up to two orders of magnitude higher if FRR=8 min. Therefore, it is of primary importance to achieve an extended understanding of two main hazards from a tank rupture: blast wave and fireball. This chapter addresses the development and validation of a CFD approach for modelling the blast wave and the fireball dynamics observed for rupture of stand-alone tanks. The CFD model aims to give insights into the formation and dynamics of the blast wave and the fireball and to provide a contemporary tool for hydrogen safety engineering. This study is an extension of the numerical investigations performed in Kim et al. (2015) and Shentsov et al. (2015). Two CFD approaches are developed and compared against 3 experiments conducted on a 35 MPa and two 70 MPa storage tanks (type III and type IV), as they constitute the current state of the art for vehicular purposes.

## 7.2 Preliminary simulations on a 35 MPa tank rupture in a fire

### 7.2.1 Description of experimental set-up

The experiment was conducted on a type IV storage tank with 72.4 l volume and 34.5 MPa as initial pressure (Weyandt, 2005). The storage system was located in open atmosphere and in a stand-alone configuration, as shown in Figure 7.1. The tank internal temperature was 27°C at the beginning of the test. TPRD was removed to achieve the catastrophic rupture of the tank exposed to a propane fire with heat release rate approximately 370 kW. During the fire exposure, the temperature inside the tank increased to 39°C, while the pressure measurements indicated an increase to 35.7 MPa. The tank ruptured after 6 min and 27 sec. The blast wave pressure was measured at 4 different locations. Three sensors were located in perpendicular direction to the cylinder axis at the distances 1.9 m, 4.2 m and 6.5 m. A further sensor was located in the cylinder axial direction at 4.2 m distance. The fireball size was captured through a high-speed video camera.

Figure 7.1 Hydrogen fuel tank test setup (Zalosh, 2007)

### 7.2.2 CFD Model and numerical details

The governing equations included the Reynolds-Averaged Navier-Stokes (RANS) conservation equations for mass, momentum, energy and species as presented in Equations (3.1)-(3.4). Flow turbulence was included in the model through the RNG k-ε model developed by Yakhot and Orszag (1986). The model solves the transport equations for turbulent kinetic energy and turbulent dissipation rate as presented in Equations (3.9) and (3.10). The Eddy Dissipation Concept by Magnussen (1981) was selected to include detailed chemical mechanisms in the turbulent combustion. A subset of Peters and Rogg's kinetic mechanism was considered (Peters and Rogg, 1993): 13 species and 37-step reduced chemical reaction mechanism for hydrogen combustion in air. The rate of reaction for each specie is evaluated as in Equation (3.22). Details of the model can be found in paragraph 3.4.2. The radiative heat

transfer was taken into considerations through the Discrete Ordinates model (Murthy and Mathur, 1998).

7.2.2.1 Computational domain and grid

The same numerical grid as in Shentsov et al. (2015) was employed for the study. A polyhedral mesh was used, as the major number of cells surrounding a control volume provides a better representation of pressure gradients (Li et al., 2015). The hydrogen tank was located at the centre of a hemisphere with radius equal to 50 m, to assure that the external boundaries would be located at a sufficient distance. The grid was characterised by different refinement zones, from a finer grid for the hydrogen tank to a coarser mesh towards the domain boundaries, resulting in a total number of CVs equal to 172199. Figure 7.2 shows the numerical grid at the different refinement levels. The domain boundaries were modelled as pressure outlet with gauge pressure=0. The soil was modelled as a no slip adiabatic wall. Moist air with composition in mass fractions: 0.23 $O_2$, 0.0001 H2O and ~0.77 $N_2$ was considered. The domain was initialised as quiescent fluid with temperature 293 K and atmospheric pressure. Pressure and $H_2$ mass fraction equal to respectively 35 MPa and 1 were imposed in the volume representing the hydrogen tank. The implicit density-based solver was employed. Two simulations were conducted using, respectively, the ideal gas and Redlich-Kwong EOS. Results are presented and compared in section 7.2.3. The mixture thermal conductivity and viscosity were calculated employing the mass weighted mixing law, while the mass diffusivity was calculated through the kinetic theory. A constant absorption coefficient equal to 3.6 m/s was assigned to the gas mixture. The parameter was calculated according to the data on mean Planck absorption coefficient for water vapour by Sparrow and Chess (1978), assuming flame temperature equal to 1200 K and stoichiometric combustion. RTE (Eq. 3.38) in DO model was discretised by 5x5 rays, as suggested for problems involving large temperature gradients. The Green Gauss Cell Based model was used for gradients, as indicated for a polyhedral mesh (ANSYS Fluent, User's Guide, 2016). The PISO algorithm was employed for pressure-velocity coupling. The first order upwind was employed for spatial discretization of the turbulent kinetic energy, turbulent dissipation rate and discrete ordinates. The second order upwind was used for the flow resolution. An initial time step equal to $10^{-7}$ s was employed. During the calculation, the time step was gradually increased (see Table 7.1) maintaining the CFL number below 1 and monitoring the residuals as indication of the effect on the solution.

Table 7.1 Time step size variation during simulation

| *Time, s* | 0 | $6.8 \cdot 10^{-5}$ | $1.9 \cdot 10^{-3}$ | $3.2 \cdot 10^{-3}$ |
|---|---|---|---|---|
| *Time step, s* | $10^{-7}$ | $10^{-6}$ | $2 \cdot 10^{-6}$ | $4 \cdot 10^{-6}$ |

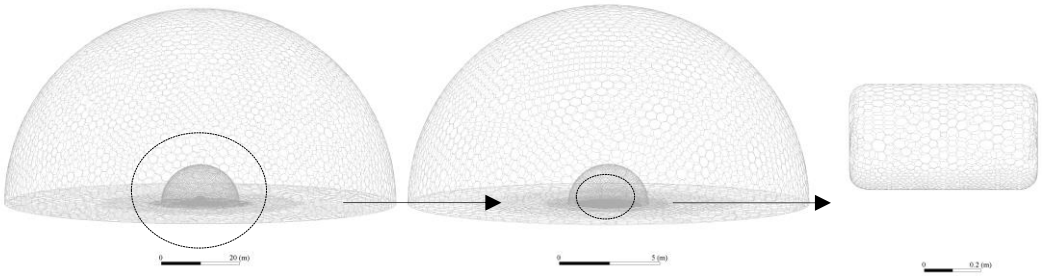

Figure 7.2 Numerical grid and different refinement levels: entire domain hemisphere (left), inner refined hemisphere (centre), tank surface (right)

### 7.2.3 Results and discussion

Figure 7.3 shows the comparison between the experimental overpressure and the calculations performed employing the real gas EOS and ideal gas EOS. The pressure wave was overestimated in the near field (sensor at 1.9 m) for both ideal and real gas EOSs. The model employing the real gas EOS reached a peak equal to 374 kPa, while the ideal gas formulation provided a pressure peak equal to 352 kPa at 1.9 m. Conversely, overpressure was considerably underestimated for the further sensors. The reason may be the absence or low contribution of combustion to the blast wave, as discussed in the following section. It is noticeable that the two EOSs result in similar pressure dynamics for the sensor at 4.2 m. From Figure 7.4, it can be observed that the two EOSs maximum overpressure decay curves overlap after 2.5 m. Same figure compares the simulation results to the analytical predictions by Molkov and Kashkarov (2015), confirming the underestimating trend of simulations. Figure 7.5 shows the comparison between the pressure transients at the sensors distances in direction perpendicular and parallel to the tank axis for the real gas calculation. There is a large deviation for distance equal to 1.9 m, whereas the difference in maximum overpressure disappears for greater distances, even if the pressure transients in x direction are slightly translated forward in time. Figure 7.7 and Figure 7.8 show the distribution of pressure, temperature, $H_2$ and OH mole fraction on the plane where the tank axis is located for the real gas calculation. At 1 ms the primary pressure wave is formed. Between 1 and 4 ms, pressure wave is reflected on the ground and it moves towards the primary wave, until they unite in a unique front (8 ms). Temperature decreases in the zone of expanding hydrogen, as indicated by the $H_2$ distribution as well. Higher temperature is recorded towards the ground, where combustion is triggered and maintained as suggested by the distribution of OH mole fraction. Simulations employing the real gas EOS required approximately 50 days to simulate 15 ms on a 32 parallel processors machine. Figure 7.6 shows the property distribution at 4 ms for the ideal gas calculation. The maximum temperature is 500 K, which indicates along with the absence of OH that there is no combustion of the mixture. Ideal gas calculation was stopped after the sensor at 4.2 m was

reached, as it was observed that approximately 14% of hydrogen was consumed. Since no combustion was observed, this 14% represents a "numerical loss" of the simulation, undermining the reliability and accuracy of the overall simulation. A similar conclusion can be drawn for the real gas calculation: within 1 ms 14% of hydrogen was consumed, while approximately 16% was absent at the end of the calculation (15 ms). Since the major presence of combustion was noticed after 1 ms, it could indicate that the 2% difference is given by the hydrogen reaction, while 14% of hydrogen was "lost" due to numerical instabilities and inaccuracy in the first stage of simulation, when the highest gradients are present. The reason may be consequence of a too large time step to describe the problem. Therefore, a time step sensitivity study should be performed. On the other hand, reduction of time step would lead to unfeasible calculation time, which represents already an issue for initial time step $10^{-7}$ s. Furthermore, the passage from a smaller to larger time step to speed up simulations as indicated in Table 7.1, could lead to numerical issues in case of a too large variation. It also constitutes a somehow arbitrary technique that cannot be universally applied since it does not follow established criteria. Results on hydrogen presence highlights the importance of assessing hydrogen mass balance and not only the overall mass balance throughout the calculation. Finally, a constant radiation absorption coefficient should not be used, as the emitted radiation depends strongly on the mixture temperature and water vapour presence. Conversely, it should be calculated for each control volume. All the mentioned issues need to be addressed to develop a reliable and solid CFD model to perform accurate calculations. Shenstov et al. (2016) addressed the more accurate modelling of radiation and the use of the pressure-based solver for the same experiment calculation. The mean Planck absorption coefficient was calculated as function of the cell water vapour mole fraction and temperature according to Yan et al. (2015)'s data. The experimental pressure transient was well reproduced, with a slight underestimation for the sensor located at 6.5 m. However, it is considered to be within the experimental accuracy. It is challenging to determine the reason behind such a different pressure dynamics between the results given in Shentsov et al. (2016) and the simulation conducted in the present study. Indeed, different time steps were used along with the solver and absorption coefficient formulation. The fireball size was slightly underestimated, with a maximum horizontal extension of 7 m, whereas 7.7 m was measured in experiment. However, this is believed to be due to the entrainment and momentum of the ground particles, which are not considered in the simulation. The burner surface presence in experiment may also have affected the fireball size. Despite the good agreement between simulation and experiment, some of the questions raised during the calculation employing the density-based solver still remain open. First of all, the need of a time discretization formulation that would follow an established criterion at each time step, instead of increasing it on the basis of user observations on the CFL. A time step that would well resolve the shock wave in the

initial stage would require a significant calculation time if applied to the entire simulation. Secondly, the calculation time should be reduced. Even increasing the time step during the calculation, approximately 50 days were required to simulate 15 ms. Once these issues are solved, a study on the independence of the solution from the time discretization and numerical grid shall be performed, to assure compliance with the CFD protocol defined by Baraldi et al. (2017). These issues will be addressed in the following sections.

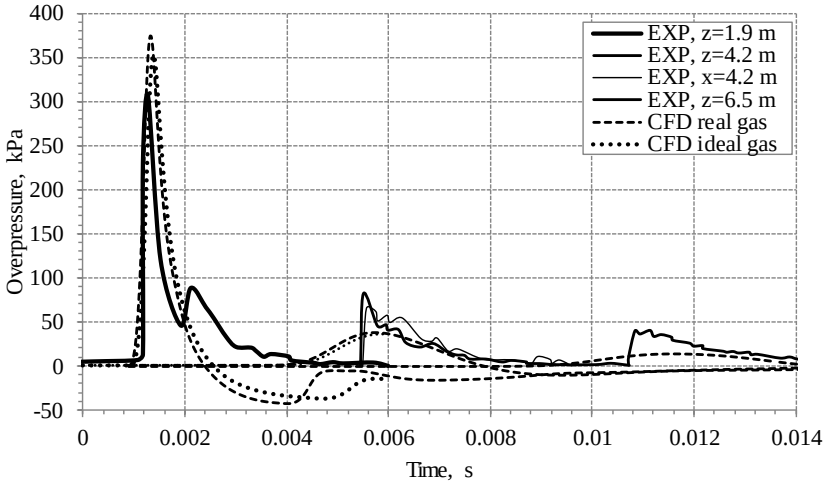


Figure 7.3 Experimental versus simulations (only z direction) pressure transients

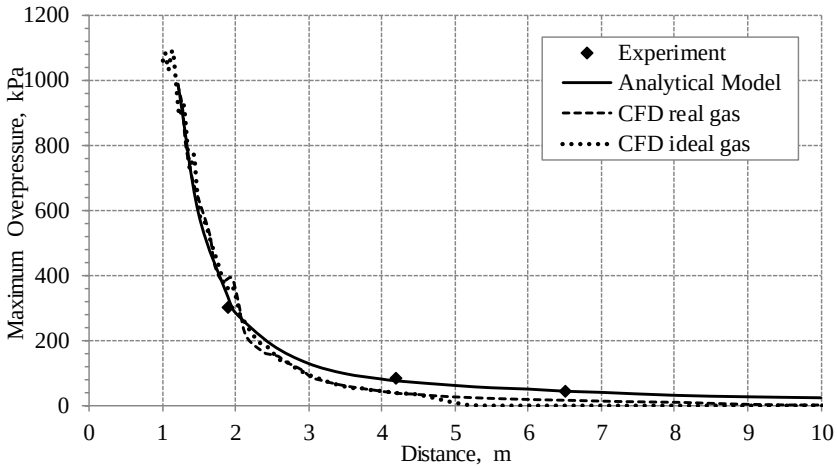


Figure 7.4 Maximum pressure as a function of distance from the tank in direction perpendicular to the tank axis

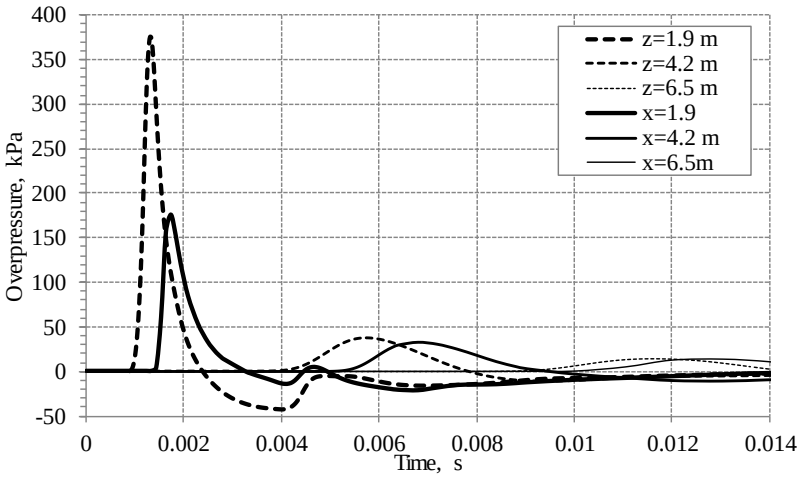


Figure 7.5 Real gas simulation: pressure transients in direction perpendicular (z) and parallel to the tank axis (x)

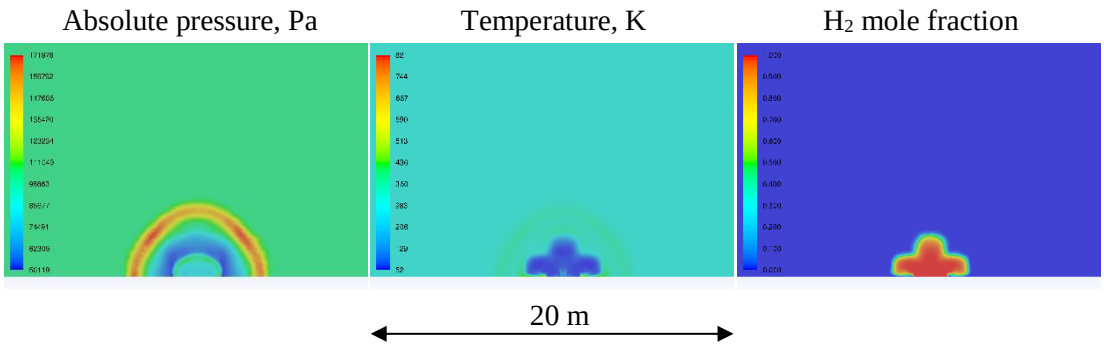


Figure 7.6 Ideal gas simulation: pressure, temperature and $H_2$ mole fraction distributions on plane z=0 at 4 ms

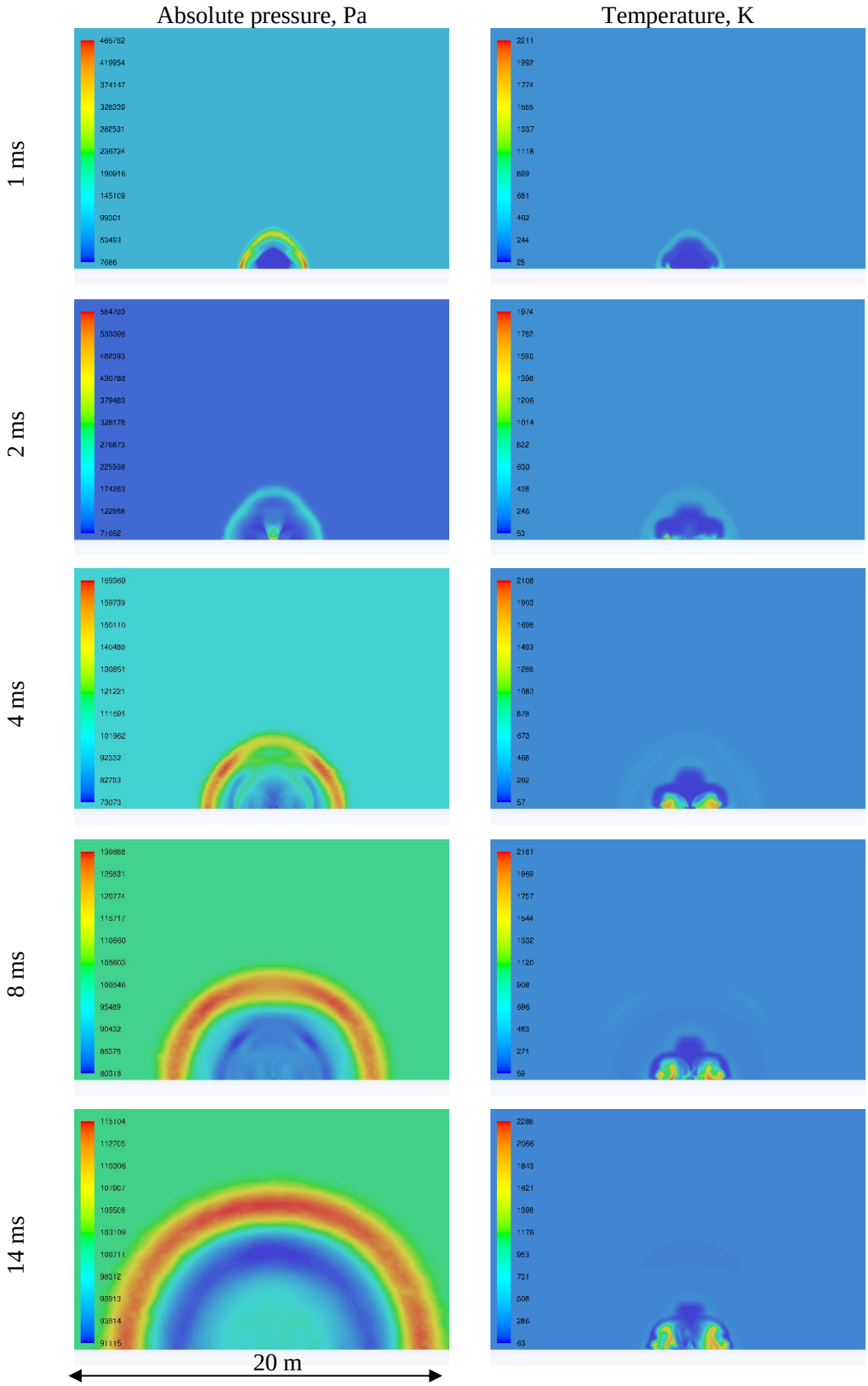


Figure 7.7 Real gas simulation: pressure and temperature distribution on plane z=0

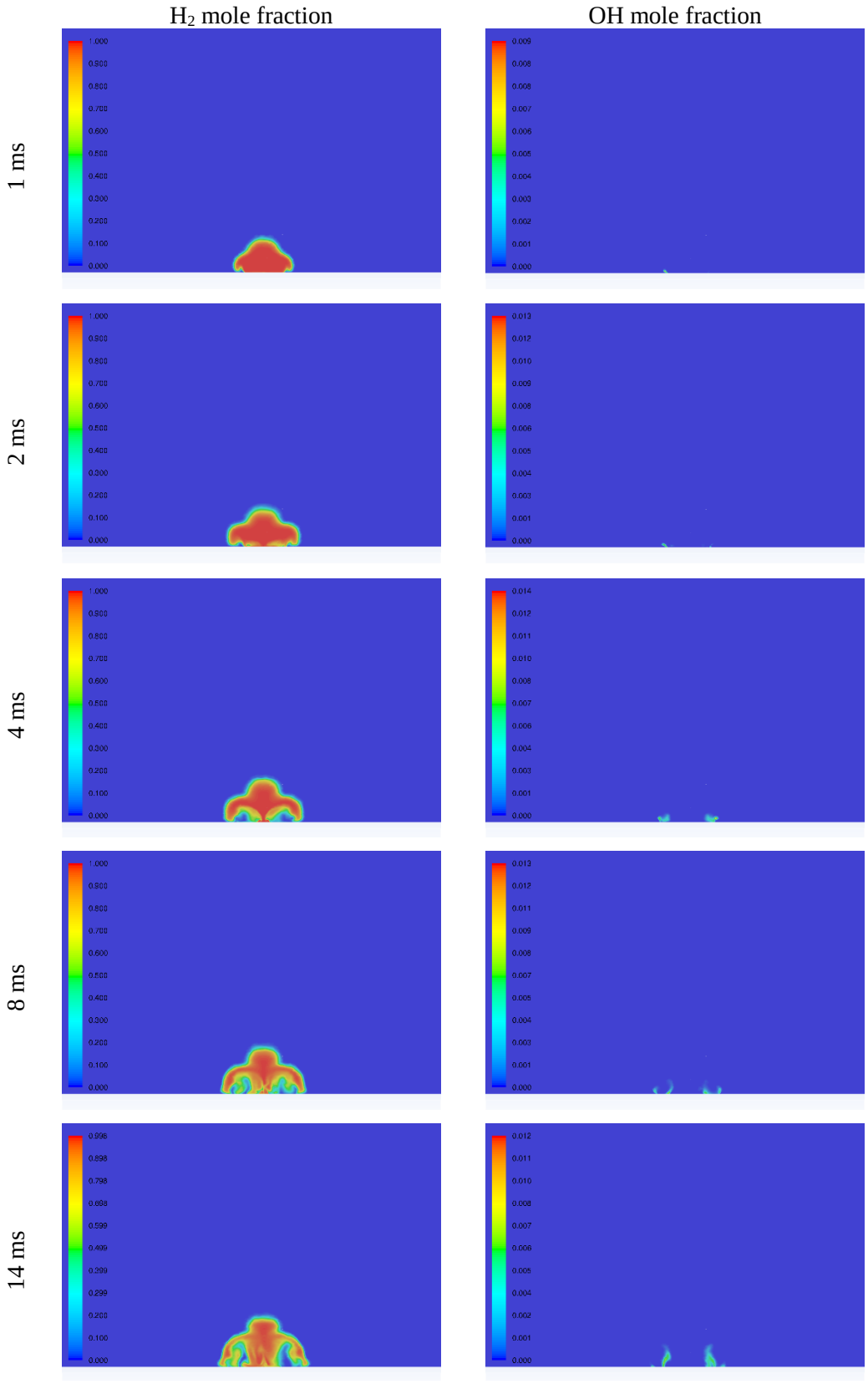


Figure 7.8 Real gas simulation: $H_2$ and OH mole fraction distribution on plane z=0

## 7.3 Quasi 1-D test for 70 MPa hydrogen charge

The conclusions of the simulations on rupture of a 35 MPa tank highlighted the presence of issues in the elaborated numerical model. Investigating them on the same case as section 7.2 would require significant computational efforts. Therefore, a simpler problem was formulated to investigate the parameters affecting the solution and formulate the basis for a CFD approach to simulate rupture of a 70 MPa tank. Hydrogen gas at 70 MPa is suddenly released in a tube with dimensions 3cm x 3cm x 10m. The originated pressure wave, hydrogen mass balance and combustion are analysed for varying time step and solver.

### 7.3.1 Numerical model

A LES approach implemented in a density-based solver was chosen for the following analysis. The governing equations for conservation of mass, momentum, energy and species were solved (Eq. 3.1-3.4). The RNG SGS model by (Yakhot and Orszag, 1986) was implemented. In a first stage of the analysis, combustion modelling was not included (section 7.3.2.1). In a second stage, reaction modelling of the 13 species and 37-step reaction was considered through the Finite Rate model (Eq. 3.14-3.17). The real gas equation as formulated by Peng-Robinson (Equation 3.42, Peng and Robinson, 1976) was employed for the study, as it better reproduces the specific heat for high pressure and low temperature as calculated through NIST EOS. The calculation domain was a tube (see Figure 7.9) constituted by 9000 control volumes (3x3x1000) with size 1x1x1cm. The domain had temperature 300 K. The hydrogen charge was located in a region 20x3x3cm, which was initialised with pressure equal to 70 MPa. The rest of the domain was initialised with pressure 101325 Pa and normal air composition. The governing equations were solved explicitly in space, while the second order implicit was employed for the transient formulation. The Advection Upstream Splitting method (AUSM) was used for convective fluxes, while the second order upwind for diffusion terms. The starting time step considered for the calculation is $10^{-7}$s, evaluated considering CFL~0.1 for the hydrogen shock speed at 70 MPa. Fluent 16.2 was used for the calculations.

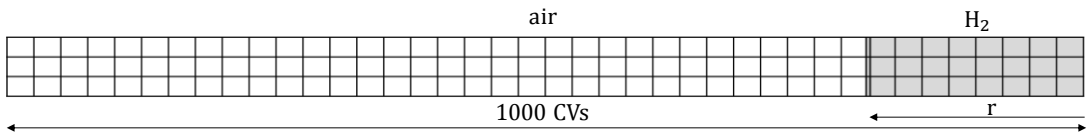


Figure 7.9 Numerical grid

### 7.3.2 Results and discussion

7.3.2.1 Unignited test

A first test is conducted without including combustion modelling. Figure 7.10 shows the pressure distribution along the tube axis within 20 and 240 μs. The shock wave well reproduces

the shock pressure 5.46 MPa calculated for the ideal gas assumption, while it underestimates the shock pressure employing the real gas assumption (8.56 MPa). The time step sensitivity test is conducted increasing progressively its size up to $10^{-6}$ s. Figure 7.11 shows the pressure distribution as monitor of solution convergence for $6 \cdot 10^{-7}$ s, which corresponds to approximately a CFL equal to 0.45. Deviations starts to appear for ts > $8 \cdot 10^{-7}$ s. Above this value, hydrogen mass imbalance becomes considerable, approaching -3% within 0.8 ms of simulated time, as shown in Figure 7.12.

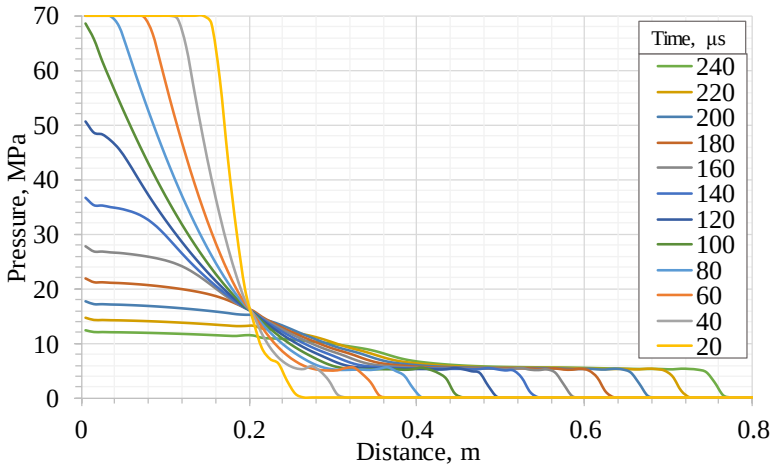


Figure 7.10 Unignited test: pressure distribution on the tube axis within 20 and 240 µs for ts=$10^{-7}$ s

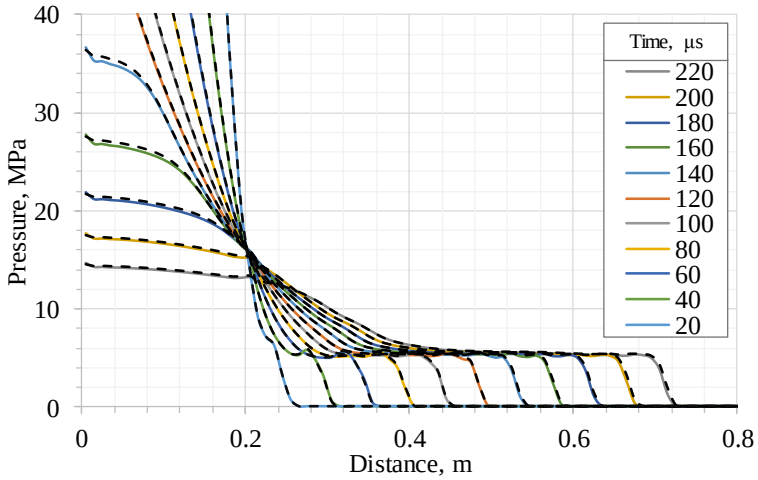


Figure 7.11 Unignited test: pressure distribution for $10^{-7}$ s (solid line) and $6 \cdot 10^{-7}$ s (dashed line)

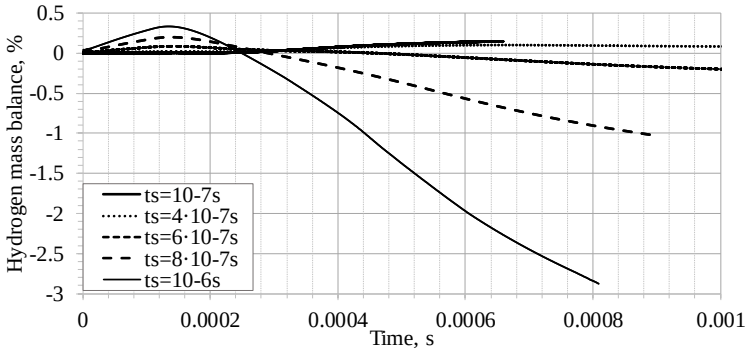


Figure 7.12 Unignited test: hydrogen mass balance for time step sensitivity study

7.3.2.2 Ignited test

In the present section, the time step sensitivity study was repeated for the test including reaction modelling in the CFD approach. Presence of combustion causes higher peaks of the shock wave as soon as the mixture ignites. Figure 7.13 shows the pressure distribution comparison between the unignited and ignited tests. The pressure axis is limited to 40 MPa to make visible the variation of the curves at low pressure. It can be observed that the shock is faster due to the rise of temperature in the mixture.

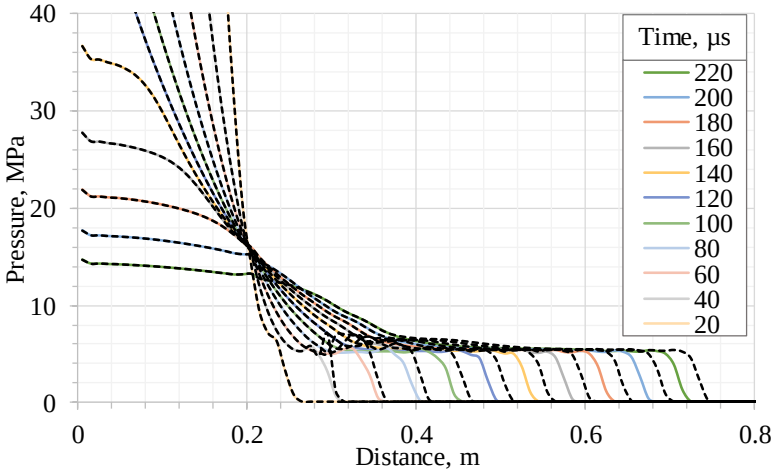


Figure 7.13 Pressure distribution along the tube axis for ts=$10^{-7}$s: unignited (solid line) versus ignited test (dashed line)

Time step was varied in the range $5\cdot10^{-8}$s - $8\cdot10^{-7}$s. Pressure dynamics did not show significant difference for time step increased to $4\cdot10^{-7}$s, as well as the burnt hydrogen and mass imbalance. Figure 7.14 shows the comparison between the axial pressure distribution for time step equal to $10^{-7}$s and $6\cdot10^{-7}$s. Deviations can be observed in the range 40-80 µs. Afterwards, they disappear, and the pressure curves overlap for the two time steps. Hydrogen mass imbalance is kept under control (below 0.5%) up to 1 ms, as shown in Figure 7.15. It can be noticed to be greater than the unignited case. For time step equal to $8\cdot10^{-7}$s, deviations in pressure are

observed throughout the simulated time, and mass imbalance increases over 1% within 1 ms of simulation. Burnt hydrogen is approximately the same among the different time steps up to 3 ms, whereas it is shown to be lower for ts=$8 \cdot 10^{-7}$s beyond that time. The simulated case approximates a quasi 1D shock wave propagation. However, a 3D application may be affected by larger imbalances and effect of the time step. The study in paragraph 7.2 employed a time step ranging between $10^{-7}$ s and $4 \cdot 10^{-6}$ s, achieving a time step that caused large mass imbalance even for the simpler quasi 1D case. Therefore, it is concluded that the disappeared hydrogen was "numerically lost" and it may have been the cause of the large pressure underestimation at the further sensors. Indeed, the disappeared hydrogen does not participate in combustion and does not contribute to increase the strength of the blast wave.

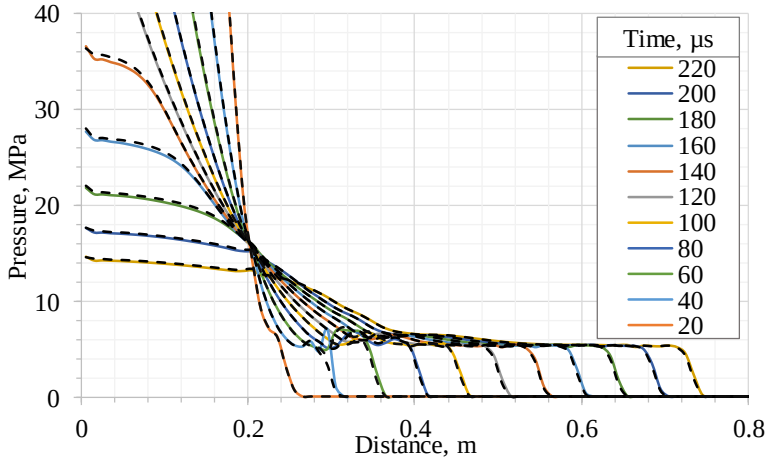


Figure 7.14 Ignited test: pressure distribution for $10^{-7}$ s (solid line) and $6 \cdot 10^{-7}$ s (dashed line)

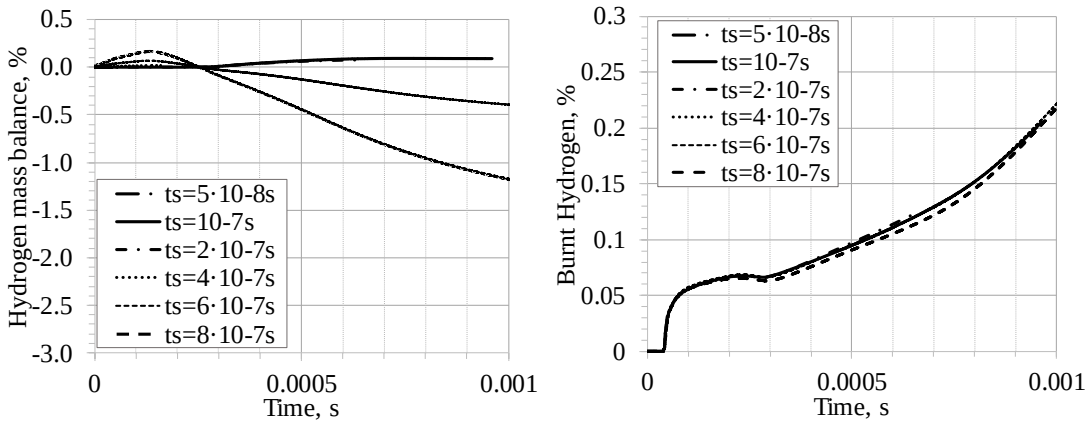


Figure 7.15 Ignited test: $H_2$ mass balance (left) and burnt $H_2$ (right) for time step sensitivity study

The density based solver requires a low time step to provide convergence of the solution and a limited hydrogen mass imbalance. The time step can be as low as $10^{-8}$ s, as suggested by (ANSYS Fluent, Service Request, 2016). This limitation would cause a large calculation time on a 32 or 64 parallel processors machine (see paragraph 7.2.3). The density based (coupled,

indicated as db in figures) solver solution was compared to the pressure-based solver (indicated as pb in figures), which is based on a segregated algorithm. Time step for the pressure-based solver was increased from $10^{-7}$ s to $1.2 \cdot 10^{-6}$ s and no significant difference was observed in the results with exception of the time range 20-40 μs, as per the coupled solver. Figure 7.16 compares the pressure distribution for the highest time steps employed for the two solvers up to 2 ms. The two models present few dissimilarities in the near field, approximately within 0.2 m from the location of the 70 MPa "charge". The deviation becomes negligible for greater distance and simulated time. Figure 7.17 presents the hydrogen mass balance and combustion for the analysed time steps and segregated solver (pb). Results are compared to the solution obtained for coupled solver and time step equal to $6 \cdot 10^{-7}$ s (db). Trend of burnt hydrogen is slightly different between the two solvers. Hydrogen mass balance is improved by the segregated algorithm employment, and it is maintained below 0.25% even for a time step twice the maximum limit given by the coupled solver. Given the capability of the pressure based solver to reproduce the same pressure dynamics as the coupled solver and maintain an acceptable hydrogen mass imbalance even for higher time steps, it is selected for the numerical approach developed in the following section (7.4) which aims to simulate the rupture of a 70 MPa hydrogen storage tank. Furthermore, it was seen that, although the real gas EOS was employed, the resulting shock pressure is closer to the ideal gas calculation rather than the real gas. In a similar analysis conducted at HySAFER (Shentsov, 2017), it was seen that ideal gas law reproduces the corresponding shock pressure (5.46 MPa). Therefore, it will be used in the following study.

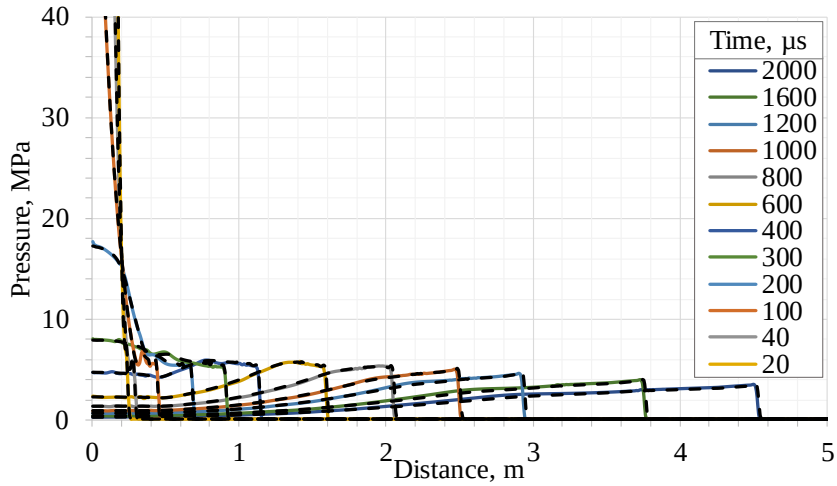


Figure 7.16 Ignited test: pressure distribution for $6 \cdot 10^{-7}$ s db (solid line) and $1.2 \cdot 10^{-6}$ s pb (dashed line)

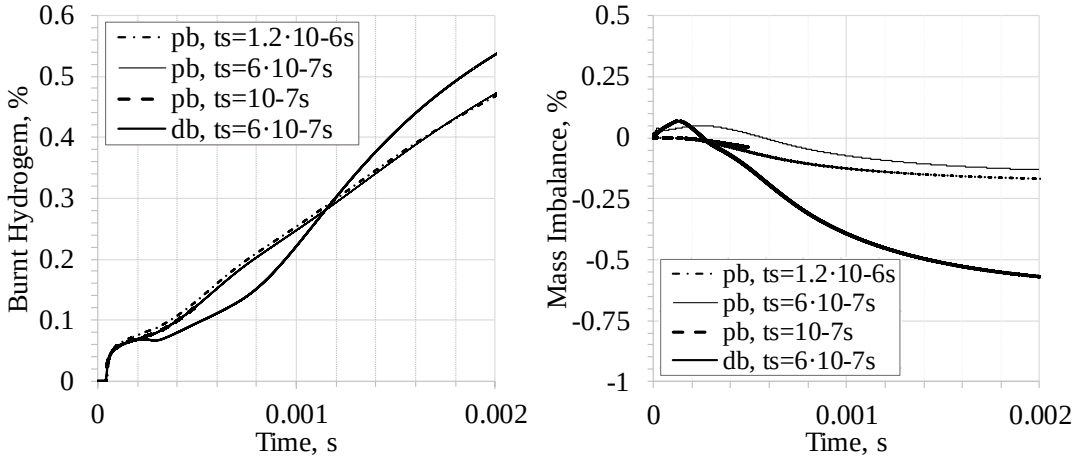


Figure 7.17 Ignited test: $H_2$ mass balance (left) and burned $H_2$ (right) for time step sensitivity study with segregated solver (pb)

## 7.4 Blast wave and fireball dynamics for 70 MPa tank rupture in a fire

This study aims at the development of a CFD approach to simulate blast wave and fireball dynamics after a 70 MPa hydrogen tank rupture in a fire. A parametric study is performed, to provide insights into the effect of sub-models, numerical methods and parameters on the convergence of the simulations and reproduction of experimental data. Simulation results were validated against two experimental tests conducted in Japan (Kim, 2017). During the analysis, it was assessed the effect of hydrogen combustion and tank opening on the blast wave strength. Results of the present chapter were included in Molkov et al. (2018).

### 7.4.1 Description of experimental set-up

Two bonfire tests were conducted on tanks with initial storage pressure 70 MPa. The blast wave was monitored at 5 and 10 m in perpendicular direction to the storage tank axis. An Infrared camera and a set of video cameras were used to assess the dimension of the fireball. Details of the two tests are presented in Table 7.2. The first test was conducted on a type IV tank with volume equal to 35 l. The tank ruptured after about 21 min of exposure to the bonfire and the last recorded measurement of pressure in the tank was 94.54 MPa. The maximum overpressure recorded at 5 and 10 m was, respectively, 110.5 and 23.4 kPa. The second test was conducted on a type III tank with 36 l volume. The pressure measured before burst was equal to 99.47 MPa. In this case, the tank required about 11 min to rupture, approximately half of the time needed in test 1. The difference could be related to the heat release rate of the bonfire along with the tank typology. However, no experimental data are available on the fire sources, thus, it is not possible to draw exact conclusions. The maximum overpressure recorded at the probe sensors was 110.5 kPa at 5 m and 74.3 kPa at 10 m. In test 2, the

maximum overpressure recorded at the closest sensor was roughly 30% less than test 1, despite the slightly bigger volume and pressure before burst. Both the tests resulted in a fireball with diameter approximately 20 m.

Table 7.2 Summary of experimental conditions and measurements

| *Test N.* | *1* | *2* |
|---|---|---|
| Tank type | IV | III |
| Volume, l | 35 | 36 |
| Ambient temperature, K | 282.15 | 280.15 |
| Pressure, MPa | 70.23 | 70.69 |
| Pressure before burst, MPa | 94.54 | 99.47 |
| Rupture time, s | 1281 | 654 |
| Blast wave peak at 5 m, kPa | 110.5 | 74.3 |
| Blast wave peak at 10 m, kPa | 23.4 | 23.4 |
| Fireball diameter, m | ~20 | ~20 |
| Fragment scattering distance, m | ~20 | ~200 |

### 7.4.2 Analytical evaluations

The first stage of the analysis is the prediction of the pressure wave at the sensors through the analytical methodologies available in literature, starting with the predictive model by Baker et al. (1975). Following the definition given by Crowl (2003), a physical explosion is the sudden release of mechanical energy. In the present case, it is linked to the release of the high pressure compressed gas. If the gas is considered as ideal, the mechanical energy can be evaluated as in Brode's model (1959):

$$E_m = \frac{V \cdot (P_g - P_s)}{\gamma - 1} \tag{7.1}$$

where $V$ and $P_g$ are the volume and pressure of the tank, $P_s$ is the pressure of the surroundings and $\gamma$ is the ratio of specific heats. The mechanical energy obtained considering the pressure before burst is 8.48 MJ for test 1 and 9.17 MJ for test 2. The explosion takes place almost at the level of the ground, therefore the energy is released in a hemisphere and not a sphere. This is considered including a mechanical energy coefficient $\alpha = 2$ into the calculations. However, given that part of the energy is lost because of cratering, burner destruction, etc. a lower coefficient, $\alpha = 1.8$ is suggested in Baker et al. (1975). The starting shock overpressure depends on the speed of sound and pressure of the gas and surroundings, therefore it will be the same for the two tests: 55.33 bar. However, if the pressure and temperature before burst

are considered, starting shock overpressure increases to 75.02 bar and 78.62 for test 1 and test 2 respectively.

Calculating the mass of hydrogen through the ideal gas equation of state can lead to significant overestimation of the mass for hydrogen high-pressure storage, leading to higher mechanical energy and hence undermining the predictive capability of the model. Comparison of mass calculations for ideal gas and Abel Noble real gas equation of state is reported in Table 7.3. The difference in the evaluations is approximately 30% for both test 1 and test 2, and a similar overestimation is expected for the mechanical energy.

Table 7.3 Calculated hydrogen mass

| *Calculated mass* | *Test 1* | *Test 2* |
|---|---|---|
| Ideal gas, kg | 2.10 | 2.21 |
| Real gas, kg | 1.44 | 1.48 |

If the gas is considered as real, the starting shock overpressure shall be recalculated. Indeed, the real gas velocity of sound is higher than ideal, leading to almost twice the starting shock if the conditions before burst are considered. Results are summarised in Table 7.4.

Table 7.4 Starting shock pressure calculations

| *Test N.* | *Gas EOS* | *Storage pressure, MPa* | *Storage temperature, K* | *Starting shock pressure, MPa* |
|---|---|---|---|---|
| *1* | *Ideal gas* | 70.00 | 288 | 5.56 |
| | | 94.54 | 380 | 7.50 |
| | *Real Gas – Abel Noble* | 70.00 | 288 | 8.64 |
| | | 94.54 | 380 | 11.66 |
| *2* | *Ideal gas* | 70.00 | 288 | 5.63 |
| | | 99.47 | 397 | 7.86 |
| | *Real Gas – Abel Noble* | 70.00 | 288 | 8.67 |
| | | 99.47 | 397 | 12.26 |

The compressed real gas mechanical energy should be considered, as proposed by Molkov and Kashkarov (2015) who employed the Abel Noble equation of state:

$$E_m = \frac{\alpha \cdot (V - mb) \cdot (P_g - P_s)}{\gamma - 1} \tag{7.2}$$

The resulting mechanical energy is 5.80 MJ and 6.27 MJ for test 1 and 2, respectively. Once the mechanical energy has been evaluated, it can be used for the calculation of the equivalent spherical vessel radius $r_v = \left(\frac{3 \cdot V}{4\pi}\right)^{1/3}$, which is employed to calculate the dimensionless distance $\bar{r} = r_v \left(\frac{P_s}{\alpha \cdot E_m}\right)^{1/3}$. The dimensionless distance is used in Figure 7.18 for the calculation of non-dimensional overpressure $\bar{P}$, which is then used to calculate the overpressure at distance *r* as $\Delta P = \bar{P} \cdot P_s$. Example is given for test 1 and distance 5 m for both the ideal gas and real gas assumption.

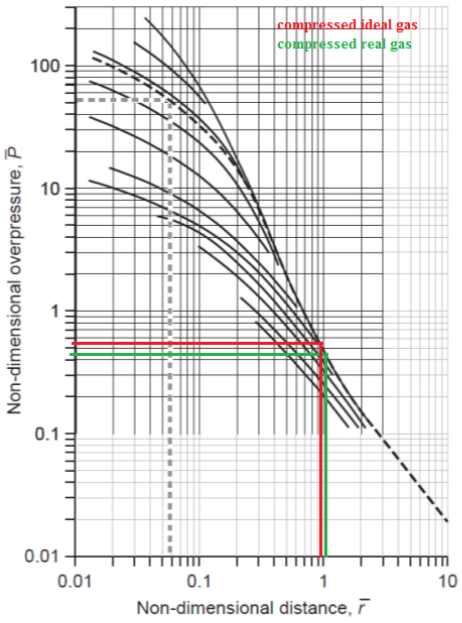


Figure 7.18 Example application of Baker's methodology to test 1 for distance r=5 m

Table 7.5 reports the blast wave overpressures evaluated according to Baker et al.'s methodology, for both ideal and real gas assumptions in $E_m$ calculation. At a first glance, it can be observed that experimental overpressure at 5 m for test 1 is higher than test 2, despite the slightly lower burst pressure and tank volume. Therefore, test 1 resulted in a significant overpressure underestimation, approximately 50% even when the gas is considered as ideal. Underestimation was observed also for test 2 overpressure at sensor 1: approximately 25% if the ideal gas formulation is employed and 39% if the real gas is considered. In Baker's methodology, only the mechanical energy is indicated to contribute to the blast wave strength, as it is considered that the blast wave is faster than the pressure wave provoked by combustion, therefore it will detach from the contact surface before combustion can contribute.

Table 7.5 Overpressure predictions at 5 and 10 m according to Baker's methodology

| *Test N.* | *Test 1* | | *Test 2* | |
|---|---|---|---|---|
| Sensor position, m | 5 | 10 | 5 | 10 |
| Blast wave – Experiment, kPa | 110.5 | 23.4 | 74.3 | 23.4 |
| Blast wave – Ideal gas, kPa | 55.7 | 18.2 | 55.7 | 19.2 |
| Blast wave –Real gas, kPa | 45.6 | 15.2 | 45.6 | 15.2 |

Molkov and Kashkarov (2015) refined the methodology presented in Baker et al. (1975) including the contribution of combustion into the blast wave strength and the non-ideal behaviour of the gas, as discussed above. A fraction $\beta$ of the total associated chemical energy $E_{ch}$, is considered to contribute to the blast wave. The dimensionless radius to be used in Figure 7.18 is calculated as:

$$\bar{r} \quad = r \left( \frac{P_s}{\alpha E_m + \beta \left( \frac{r_{sh}}{r_b} \right)^3 E_{ch}} \right)^{\frac{1}{3}} \tag{7.3}$$

where $r_{sh}$ and $r_b$ are, respectively, the radius of the hemisphere behind the shock and the hemisphere that would be occupied by the products in case of stoichiometric combustion. The authors found that coefficients for a stand-alone tank with volume 72 l and pressure 35 MPa are α=1.8 and β=0.052. However, combustion contribution may be different for a lower volume and higher pressure of the storage. Hence, the chemical coefficient will be changed in the range 0.052-0.25 to quantify the effect on the resulting overpressure. Results for both ideal and real gas assumptions are given in Table 7.6. Since the analytical methodology takes account of solely tank pressure and volume, overpressure for test 1 will be correspondingly lower than test 2. However, the opposite was observed in experiment as discussed above. Coefficient α=1.8 and β=0.052 led to underestimation of the overpressure for both the sensors. Test 2 overpressures at the two sensors were better reproduced for combustion contribution equal to 10%. Overpressure variation from experiment was contained within 15%. Calculations on test 1 indicated that the combustion contribution should rise to 25% to reproduce the pressure peak at sensor 1. However, the corresponding pressure at sensor 2 would be overestimated by over 30%. Since difference in the storage conditions of the two tests is not significant, the author considers that the cause of different pressure at the first sensor may be due to either the tank rupture process or other experimental settings, implying that the effect is less sensed in the far field as for sensor at 10 m. Further investigations need to be conducted to assess the effect of other parameters on blast wave overpressure. Analytical methodologies take account of solely tank pressure and volume, precluding the possibility to

investigate the effect of other factors. On the other hand, CFD modelling allows to analyse a broader set of scenarios, resulting to be the perfect tool to conduct further investigations.

Table 7.6 Overpressure predictions at 5 and 10 m according to Molkov and Kashkarov's methodology for chemical coefficient β in the range 0.05-0.25

| *Test N.* | | *Test 1* | | *Test 2* | |
|---|---|---|---|---|---|
| *Sensor position, m* | | 5 | 10 | 5 | 10 |
| *Blast wave – Experiment, kPa* | | 110.5 | 23.4 | 74.3 | 23.4 |
| *Blast wave – α=1.8 and β=0.052, kPa* | *Ideal gas* | 65.9 | 25.33 | 67.4 | 27.4 |
| | *Real gas* | 55.7 | 22.8 | 57.8 | 24.3 |
| *Blast wave – α=1.8 and β=0.10, kPa* | *Ideal gas* | 76.0 | 29.4 | 77.5 | 31.4 |
| | *Real gas* | 70.4 | 25.8 | 71.4 | 26.9 |
| *Blast wave – α=1.8 and β=0.15, kPa* | *Ideal gas* | 90.2 | 35.0 | 92.2 | 36.0 |
| | *Real gas* | 76.5 | 27.9 | 79.0 | 28.9 |
| *Blast wave – α=1.8 and β=0.20, kPa* | *Ideal gas* | 104.4 | 37.0 | 109.4 | 38.5 |
| | *Real gas* | 91.2 | 30.9 | 94.2 | 31.9 |
| *Blast wave – α=1.8 and β=0.25, kPa,* | *Ideal gas* | 116.5 | 39.0 | 119.6 | 43.6 |
| | *Real gas* | 110.4 | 35.0 | 111.5 | 35.5 |

The energy of explosion can also be expressed in terms of equivalent TNT mass. However, the methodology is mainly used for Vapour Cloud Explosions and it is considered obsolete by many (Lee's, 1996). Once the equivalent mass is calculated, the overpressure is estimated from correlations based on explosions of TNT or other fuels. Several methodologies to calculate the equivalent TNT mass are available and results are reported in Table 7.7:

- ME: In the report of the Major Hazards Assessment Panel, the equivalent mass of TNT for pressure vessels considers only the compressed gas energy (Mechanical Energy) and it is calculated as $m_{TNT} = \alpha \frac{E_m}{E_{TNT}}$, where $E_m$ is calculated as in Equation (7.1) and $E_{TNT}$=4.65 MJ/kg (Major Hazards Assessment Panel, 1994).
- CE: The equivalent mass of TNT considers the full amount of chemical energy (Molkov, 2012) and it is calculated as: $m_{TNT} = \frac{m_{fuel} \cdot H_c}{E_{TNT}}$.
- BS: The equivalent mass of TNT considers a fraction of the chemical energy through inclusion of a Yield Factor, YF, as $m_{TNT} = YF \frac{m_{fuel} \cdot H_c}{E_{TNT}}$ (Brasie and Simpson, 1968). YF=0.05 is indicated as conservative yield factor for the far field (Lees, 1996).

Table 7.7 Evaluations of TNT equivalent mass for the two tests

| *Test N.* | *Test 1* | *Test 2* |
|---|---|---|
| $m_{fuel}$ Abel Noble EOS, kg | 1.44 | 1.48 |
| $m_{eq}$ – $TNT_{ME}$, kg | 2.27 | 2.45 |
| $m_{eq}$ – $TNT_{CE,}$ kg | 37.01 | 38.24 |
| $m_{eq}$ – $TNT_{BS}$ YF=0.05, kg | 1.85 | 1.91 |
| $m_{eq}$ – $TNT_{BS}$ YF=0.06, kg | 2.22 | 2.29 |
| meq – TNTBS YF=0.065, kg | 2.41 | 2.49 |
| $m_{eq}$ – $TNT_{BS}$ YF=0.07, kg | 2.59 | 2.68 |

The TNT equivalent masses given in Table 7.7 are used to estimate overpressure at 5 and 10 m through the Kingery-Bulmash equations, widely accepted as an authoritative engineering tool for prediction of overpressure for hemispherical and on ground explosions in a free-field (UN Safer Guard, 2018). Results are given in Table 7.8. Overpressure predictions considering the mechanical energy well agrees with experiments, with the exception of sensor 1 for test 1. A yield factor equal to 0.07 was found to give the best agreement between calculations and experiments when the chemical energy is employed to calculate the equivalent mass of TNT. For both the tests, time of arrival of the shock front is calculated as approximately 6.9 ms and 19.7 ms for sensors 1 and 2, respectively. Also for calculations according to the TNT methodology, pressure predictions at sensors had a reasonable agreement with experiments with the exception of measurement at sensor 1 for test 1, confirming the need to further investigate the blast wave dynamics through mean of CFD modelling.

Table 7.8 Analytical overpressure predictions at 5 and 10 m for tests 1 and 2 according to TNT methodology

| *Test N.* | *Test 1* | | *Test 2* | |
|---|---|---|---|---|
| Sensor position, m | 5 | 10 | 5 | 10 |
| Blast wave – Experiment, kPa | 110.5 | 23.4 | 74.3 | 23.4 |
| Blast wave –$TNT_{ME}$, kPa | 71.48 | 21.91 | 75.12 | 22.77 |
| Blast wave – $TNT_{CE}$, kPa | 562.42 | 115.61 | 562.42 | 118.30 |
| Blast wave – $TNT_{BS}$ YF=0.05, kPa | 62.71 | 19.81 | 64.0 | 20.12 |
| Blast wave – $TNT_{BS}$ YF=0.07, kPa | 74.31 | 22.58 | 75.92 | 22.95 |

### 7.4.3 CFD Model and numerical details

#### 7.4.3.1 Governing equations

A Large Eddy Simulation approach has been implemented as CFD model. In LES approach, structures are filtered through the grid size: those smaller than the grid size are modelled employing sub-grid scale (SGS) models, whereas larger structures are explicitly resolved. The governing equations are based on the filtered conservation equations for mass, momentum, and energy in their compressible form, presented in Equations (3.1)-(3.4). The SGS turbulence model is based on the renormalisation group (RNG) theory developed by Yakhot and Orszag

(1986). In the model, an analytical-derived differential formula is employed to calculate effective viscosity, accommodating to low-Reynolds number flows. Details of the model are given in section 3.3.2.3. Finite rate chemistry was employed for combustion modelling, following the indications by ANSYS Fluent (2016) for problems involving explosions where the combustible mixture is ignited by the heat behind a shock wave. The chemical source term was calculated through the Arrhenius reaction rate for 1-step kinetic reaction. Details of the combustion model are given in section 3.4.1.

7.4.3.2 Computational domain and grid

The hydrogen and air mixture is considered as a compressible ideal gas. The mixing law is employed to calculate the specific heat of the mixture. Viscosity and thermal conductivity are defined through the mass weighted mixing law, while mass diffusivity is calculated through the kinetic theory. The volume of the tanks was geometrically scaled when transitioning from real gas tank volume ($V_{real}$) to the ideal gas tank volume ($V_{ideal}$), to conserve the mechanical energy of compressed hydrogen as calculated for the real gas. The mechanical energy was 8.48 MJ for test 1 and 9.17 MJ for test 2. Scaling followed the formulae based on the Able-Noble EOS: $V_{ideal} = V_{real} - mb$, where $m$ is the mass of hydrogen, and $b$ is the co-volume constant. Test 1 tank volume was scaled from 35 l to 23.9 l, whereas test 2 volume from 36 l to 24.6 l. A hexahedral mesh is chosen to describe the domain. The tank is discretised by 10 cells along the diameter (~28 cm) and 16 along the axis (~48 cm). The domain smallest cells are located in the tank and they are characterised by dimension ~3 cm. A maximum expansion ratio of 1.1 is used in proximity of the tank, while 1.2 is used for distances greater than 10 m (2$^{nd}$ sensor location), leading to a maximum cell aspect ratio of 9.8 for the cells adjacent the boundaries. The extent of the domain is approximately 50 m, to assure the minimum effect of boundaries and to assess the decay of the blast wave with distance. The same structure as in section 7.2.2 was used, with several levels of refinement towards the tank location. The resulting numerical grid is composed by 147104 CVs and is shown in Figure 7.19. Minimum orthogonal quality is 0.33 in 4 cells inside the tank, while it is above 0.4 in the rest of the domain.

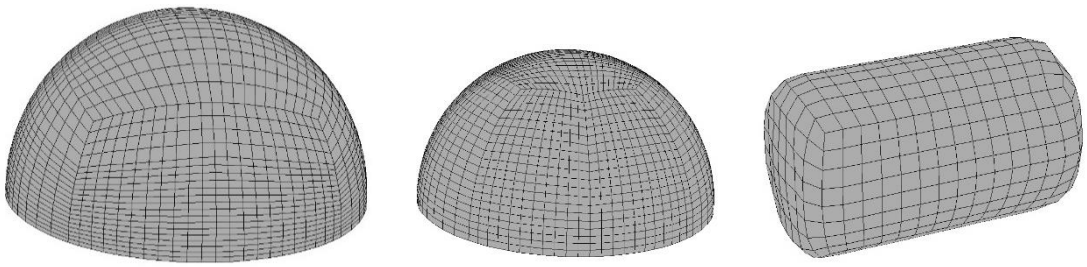

Figure 7.19 Numerical grid and different refinement levels: entire domain hemisphere (left), inner refined hemisphere (centre), tank surface (right)

The ground is specified as an adiabatic no slip wall. The external boundary is defined as pressure outlet with gauge pressure equal to 0. The domain is initialized with pressure equal to 101325 Pa, temperature 282 K and air composition. The region corresponding to the tank is initialised with hydrogen mass fraction equal to 1 and the pressure measured before burst, i.e. 94.54 MPa and 99.47 MPa for test 1 and test 2 respectively. The temperature in the tank before burst was not measured, so it was calculated from the Abel-Noble EOS for the given tank volume and pressure. Simulation initial conditions are given in Table 7.9. PISO scheme is used for coupling pressure and velocity. The second order discretization scheme was used for pressure, to improve accuracy and as recommended by (Ansys Fluent, 2016) for compressible flows. The second order upwind scheme was used for convective terms. The set-up involves the use of the first order as time advancement scheme. The time step adapting technique was employed to maintain a constant CFL. The time step size, $\Delta t$, was calculated through an UDF (User Defined Function) developed at HySAFER (Shentsov, 2017). The CFL was calculated including the speed of sound from the following equation: $CFL = (u + c) \cdot \Delta t / \Delta x$, where $u$ is the speed of the flow, $c$ is the speed of sound and $\Delta x$ is the size of the control volume. The imposed CFL was selected according to the conclusions of Zbikowski's study on detonation modelling: CFL=0.2 was the maximum value providing convergence and stability of the solution. CFL was decreased to 0.05 and no difference in the calculated overpressure was noticed (Zbikowski, 2010). However, the CFL convergence for the present study will be verified in the following section. ANSYS Fluent 16.2 was used as platform for the computations.

Table 7.9 Simulation initial conditions

| *Parameter* | *Test 1* | *Test 2* |
|---|---|---|
| Experimental tank volume, l | 35 | 36 |
| Scaled tank volume, l | 23.9 | 24.6 |
| Pressure, MPa | 94.54 | 99.47 |
| Temperature, K | 376 | 397 |
| Hydrogen mass, kg | 1.44 | 1.48 |

### 7.4.4 Results and discussion

#### 7.4.4.1 Convergence of time discretization scheme

Prior to proceeding with the calculation of the blast wave and fireball dynamics, a convergence study on the time discretization scheme was conducted to assure time independency of the solution. Firstly, a CFL sensitivity test was performed. The CFL number was decreased from 0.2 to 0.02. Given the increase of time needed by simulations with the decrease of maximum CFL (calculation of 1ms required 1.5h for CFL=0.2 and 8h for CFL=0.02), convergence of the results is investigated through comparison of pressure transients along the directions

perpendicular (z) and parallel (x) to the tank axis for the initial stage of the explosion. Indeed, it is considered that the initial phase is the more unstable and difficult to converge, as it is characterised by higher gradients of velocity, pressure and temperature. Therefore, it is believed that if convergence is achieved in this stage, it will be confirmed at later stages too. Results are shown in Figure 7.20. No significant difference was noticed, confirming time independency of the results. A slight increase of burnt hydrogen was observed for CFL=0.2 (about 0.04% more) compared to solutions for lower CFL, while no difference was observed for CFL<=0.1. However, deviation for CFL=0.2 is considered to be negligible and the saved computational time is significant. Therefore, it is employed for the following calculations. Conclusions on CFL sensitivity tests agree well with the study conducted by Zbikowski (2010), which indicated 0.2 as maximum CFL for detonation in quasi 1-D explicit modelling. The parametric study presented in section 7.3 on a quasi 1-D blast wave propagation from 70 MPa source indicated that convergence of results was given by CFL~0.9 for a pressure-based solver. The author considers that the different CFL convergence is caused by the passage from quasi 1-D to 3-D geometry, which can lead to a different stability and convergence of the solution as the blast wave and flow directions may not be aligned to the numerical grid.

As shown in section 7.4.3.2, the current CFL formulation for the implicit solver includes the speed of sound in calculation of the time step, as in explicit solvers. Implicit formulations are unconditionally stable, and choice of time step is not limited by a stability criterion as for explicit formulations. Therefore, it would be possible to increase CFL depending on the complexity of the problem (ANSYS Fluent, 2016). Higher CFL is an attractive option when simulations of blast wave in larger domain are needed, such as for explosions in tunnels. In this case, the number of control volumes and, consequently, simulation time can increase significantly. The CFL was changed from 0.2 to 0.6, 1 and 2. From Figure 7.20 it is possible to observe that solution for CFL=0.6 starts to deviate from CFL<0.2. Up to 10% higher peak pressure was observed at 2 ms for CFL=2. However, deviation decreases with the increase of time and travelled distance, becoming negligible when the pressure wave reaches the first sensor at 5 m. Burned hydrogen and mass imbalance increase with the increase of CFL. At 20 ms, the portion of burned hydrogen increased from about 8.7% for CFL=0.2 to 11% for CFL=2. However, the increase is not great enough to affect the pressure recorded at the sensors in z direction. Furthermore, the relative difference in burnt hydrogen among different CFLs decreases with the increase of elapsed time. The size of the time step affects the number of iterations needed by the solution to converge at each time step. However, the number of iterations is limited for all the cases to 20. As a consequence, higher solution residuals are expected with the increase of CFL. This leads to an increase of mass imbalance, which anyway is maintained below 0.5%. Therefore, it is concluded that for simulations involving pressure

dynamics in the far field, CFL can be furtherly increased, reducing significantly the calculation time from days to hours.

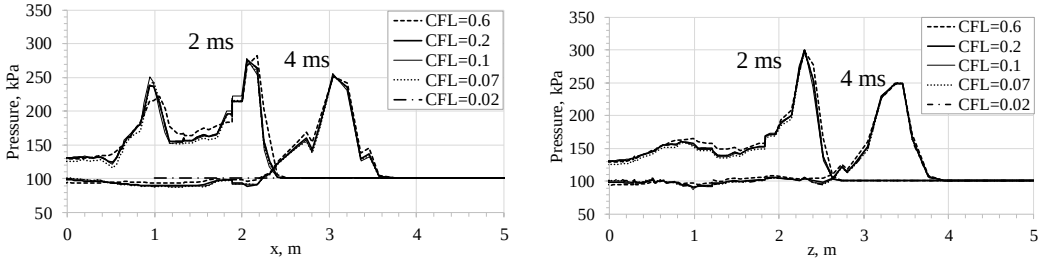


Figure 7.20 CFL convergence test: pressure distribution in x (along tank axis) and z (perpendicular to the tank axis) direction at 2 ms and 4 ms (Test 1)

The advantage of using adaptive time step techniques to maintain a constant CFL is still an open question for CFD codes employing implicit schemes, given that they are unconditionally stable and the time step is not limited by stability criterion (limit to CFL) as in explicit schemes. The solution provided by the adapting time step technique was compared to the solution obtained maintaining a constant time step, to give more insights on the benefits of using which of the two techniques. The analysis is conducted on experimental test 1, as it is considered that the obtained conclusions are the same for the two tests given the similarity of the initial conditions. Assuming the gas as ideal, the shock speed for hydrogen with pressure 94.5 MPa and temperature 380 K is 2511 m/s. Considering that the minimum cell size is approximately 2 cm, a time step equal to $10^{-6}$ s is imposed to have CFL below 0.2. A further case with half of the time step is considered ($5 \cdot 10^{-7}$ s), to assure independency of the solution with decrease of the time step. Results are reported in Figure 7.21 for pressure transients in z and x directions and they are compared to the solution obtained for CFL=0.02. No significant difference was noticed with regards to the pressure distribution or the burnt hydrogen. As a consequence, no difference was observed for pressure dynamics at the sensors. However, implementation of the adapting time step improves hydrogen mass balance by approximately one order of magnitude, highlighting that the two techniques are equivalent in terms of numerical results but slightly different in terms of convergence and stability of the solution. Furthermore, maximum velocity in the domain decreases with the elapsed time and the blast wave moves towards cells with greater size. As a consequence, the adapted time step progressively increases, shortening the calculation time. Indeed, implementation of CFL=0.2 requires about 44 h to simulate 50 ms; conversely, implementation of constant time step=$10^{-6}$ s leads to simulation of only 15 ms for the same calculation time. In conclusion, the adaptive time step technique is selected to proceed with the calculations as it gives the best performance in terms of hydrogen mass balance and calculation time.

To assure that the obtained solution is accurate, the time advancement scheme was upgraded from the first to the second order. The second order is applicable only for a formulation using a constant time step. Since the simulations for time steps $10^{-6}$ s and $5 \cdot 10^{-7}$ s did not give any difference in the results, time step equal to $10^{-6}$ s was selected to shorten the calculation time. Results are given for test 1 and they are shown in Figure 7.22 in terms of pressure distribution along z and x directions for 2 and 4 ms. No significant pressure difference can be discerned between the time advancement schemes. Difference in burnt hydrogen is negligible while 2nd order shows a better hydrogen mass balance.

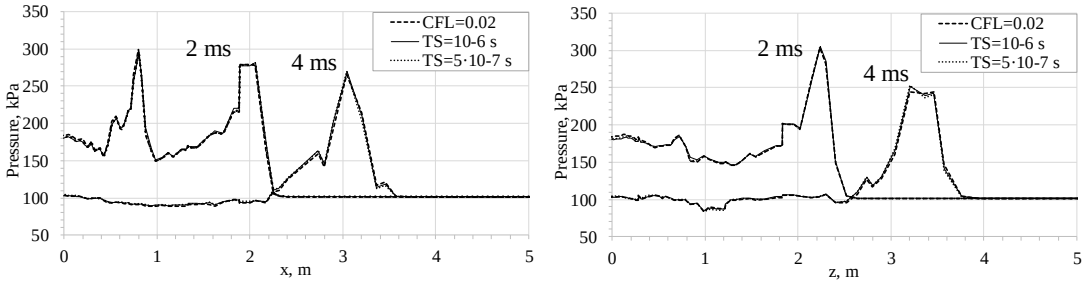


Figure 7.21 Time step sensitivity: pressure distributions in z and x directions at 2 and 4 ms (test 1)

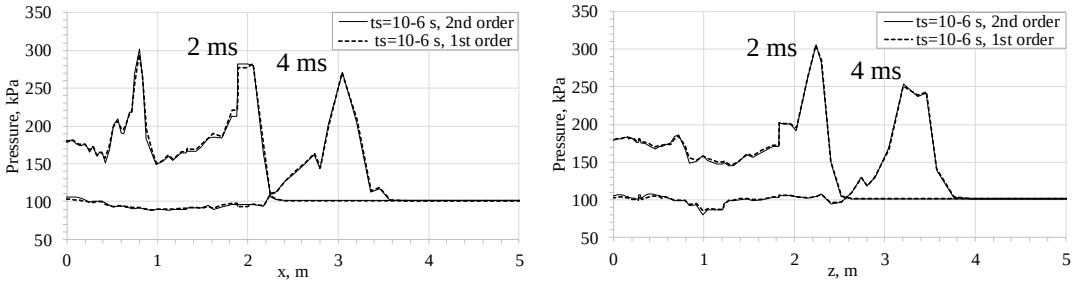


Figure 7.22 Time advancement scheme sensitivity: pressure distributions in z and x directions for 2 and 4 ms (test 1)

A further convergence parameter is the number of iterations per time step. The implicit formulation for time dependent problems requires multiple iterations for each time step. If the convergence criteria, defined by the residuals, are met before the limit of iterations per time step is reached, the solution advances to the following time step. Otherwise, all the iterations are performed and the solution advances by time step regardless the calculated residuals. To assess the accuracy and convergence of the solution, the maximum number of iterations per time step was changed from 20 to 50. The selected case had CFL=0.07, as a smaller time step would more easily lead to convergence. Residuals were equal to $10^{-5}$. The solution converged according to the imposed residuals for each time step within the 50 iterations. During the first stage of the simulation, approximately 45 iterations were needed to achieve convergence. During the final stage of simulated time, the number of iterations required to achieve

convergence decreased to 35. Simulation time increased by a factor equal to 1.9. The burnt hydrogen did not show any difference between the two cases, while the hydrogen mass balance slightly improved from -0.05 % to -0.03%. No difference in overpressure was observed along x and z directions (Figure 7.23), indicating that the error propagation is minimum and leading to an accurate solution. Therefore, the limit of 20 it/ts was maintained for the following calculations.

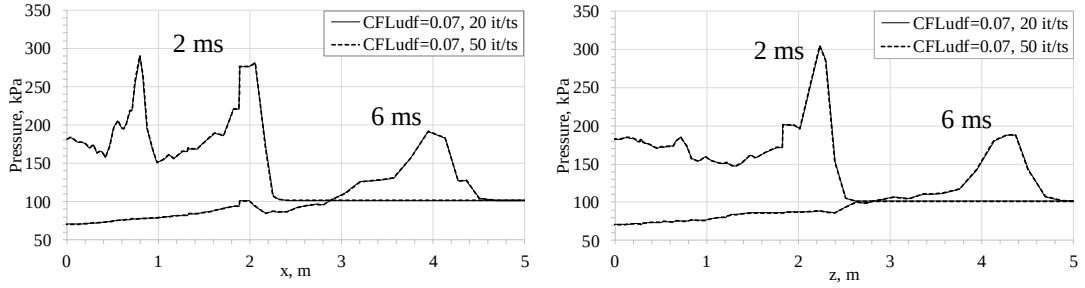


Figure 7.23 Iterations per time step sensitivity: pressure distributions in z and x directions for 2 and 6 ms (test 1)

7.4.4.2 Blast wave dynamics for test 1 and test 2

After the convergence study on the time discretization scheme, the results for the blast wave dynamics are analysed. At time=0 s, the wall of the tank is instantaneously removed, producing the starting shock which propagates outwards. Figure 7.24 shows propagation of the pressure wave along the tank axis for test 2. It is difficult to exactly assess the starting shock in simulations, as a much finer mesh would be required for more accurate calculations. Furthermore, it has to be considered that in the real case, the hydrogen charge is cylindrical, causing an anisotropic starting shock as shown in Figure 7.24. The results agree with the observations on the directional effects on pressure vessel burst by Geng et al. (2011). In their study, pressure on the side of the tank resulted to be higher than the pressure recorded along the cylinder axis. The starting shock along z direction is between 60 and 80 bar, well agreeing with the value of 78.6 bar calculated according to Baker et al. (1975).

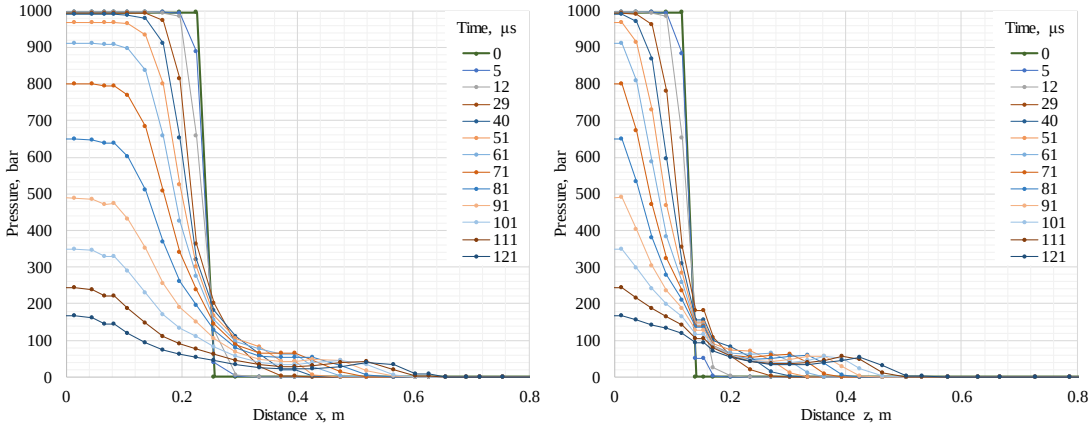


Figure 7.24 Pressure distributions along x and z direction for test 2

Figure 7.25 shows the dynamics of the blast wave in the tank surroundings for test 2. Legend limits are different from figure to figure, due to the great variation in ranging values. The blast reaches the ground at approximately 0.5 ms. Afterwards the blast is reflected, and it moves with higher velocity compared to the primary blast wave and in a region characterised by higher temperature as shown by the velocity and temperature distributions at 2 ms (Figure 7.26). The reflected wave catches up the primary wave and they combine in a singular front at approximately 5 ms. The blast wave has a hemispherical shape with higher pressure recorded in proximity of the ground, most likely because of the tank location 1 m above it, as suggested in Kim et al. (2015). Combustion is triggered immediately after rupture, due to the high-pressure compression and mixing of air and hydrogen. Temperature dynamics in the tank surroundings is shown in Figure 7.26. The blast wave adiabatically compresses air, causing an increase of temperature and exceeding 3000 K when the pressure wave reaches and reflects off the ground. In the meanwhile, temperature in the region of the tank drops, because of hydrogen expansion. Conversely to the quasi-hemispherical pressure wave shape, temperature presents different patterns according to the considered plane. Figure 7.27 shows the comparison of the temperature distributions on plane z=0 and plane x=0 respectively perpendicular and parallel to the tank axis at time equal to 4 ms. It can be noticed that on plane z=0 turbulent mixing is enhanced increasing the extension of the high temperature region because of the tank cylindrical shape.

Figure 7.28 shows the comparison between the experimental and calculated overpressure dynamics at the two sensors for test 1. It is not clear from experimental reports the time elapsed between the rupture of the tank and the verification of the pressure peaks, but time is 0 s when the pressure starts to be recorded at the sensor at 5 m. Hence, the experimental curves were shifted in time by 7.2 ms, so that the first peak timing would correspond to the time it is obtained in simulation. However, simulation well reproduce the time required by the blast wave to move from the first sensor to the second one in experiments. Furthermore, simulated

blast arrival time at the two sensors well reproduces the time calculated through the TNT theory discussed in section 7.4.2 (6.9 ms and 19.7 ms for sensors at 5 m and 10 m respectively). Therefore, it is concluded that simulations well reproduce the time of arrival of the blast wave at the two sensors. Same conclusions can be drawn for test 2. Overpressure at 5 m is underestimated for test 1. However, the negative pressure phase is well reproduced in time and magnitude. The second peak is well reproduced, and it is smoother than the first one. Reason for this behaviour may be the numerical grid, as cell size in z direction at 10 m is almost twice the cell size at 5 m. As shown in Figure 7.30, more than 5% of hydrogen burns within 1 ms, due to the high pressure and temperature given by the blast wave compression. When the sensor at 10 m is reached, the burnt hydrogen achieves 8.7%. However, analytical calculations on combustion contribution to the blast wave concluded that approximately 10-15% of hydrogen should have burnt when the blast wave reaches the sensors (Table 7.6).

Time=0.5 ms

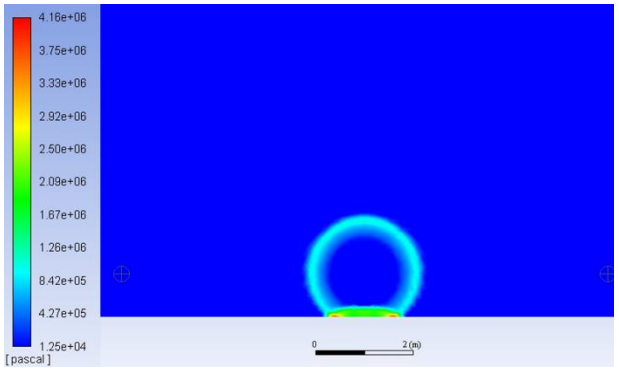


Time=1 ms

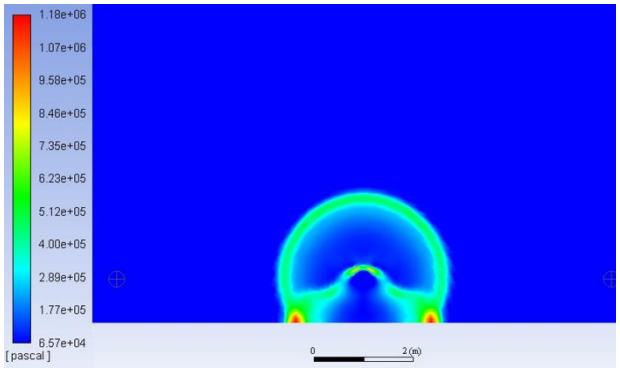


Time=2 ms

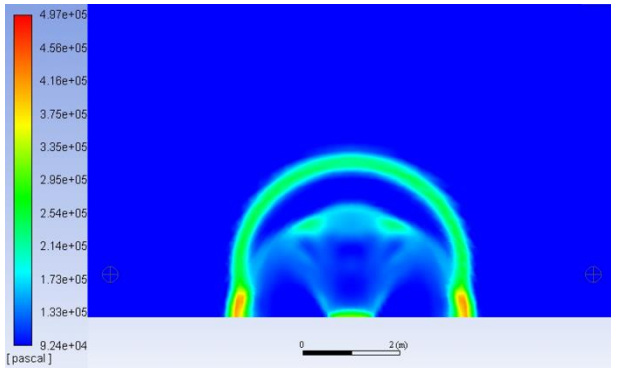


Time=4 ms

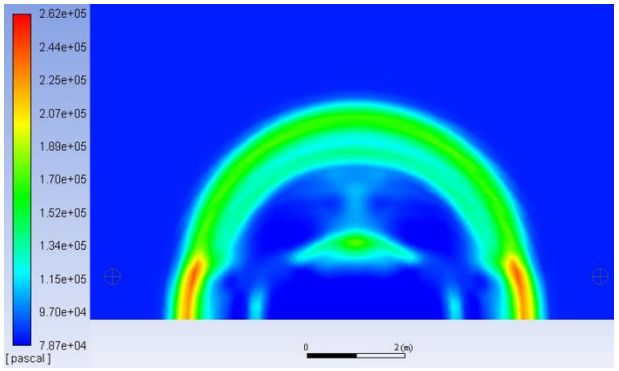


Time=6 ms

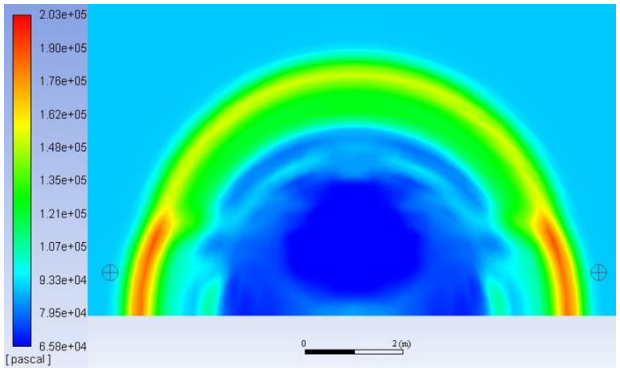


Time=8 ms

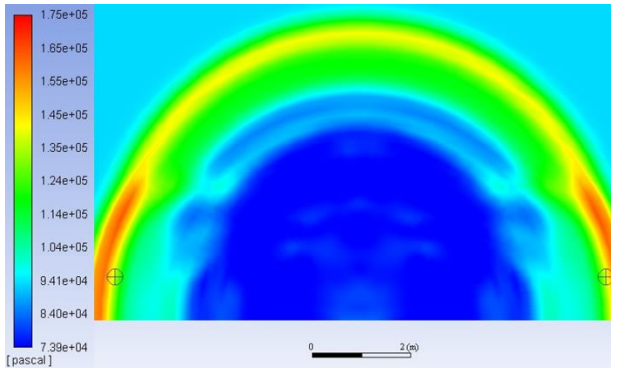


Figure 7.25 Pressure wave dynamics on plane x=0 for test 2

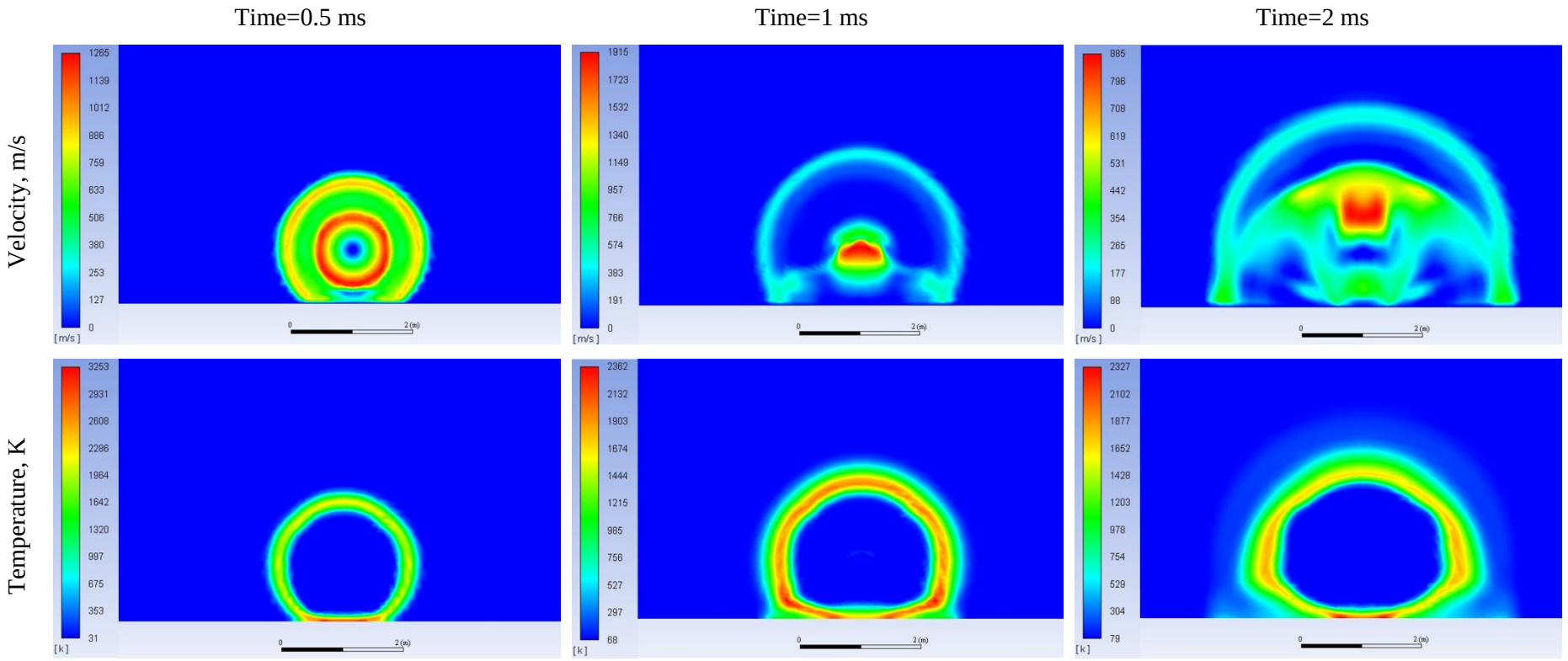


Figure 7.26 Velocity (top) and temperature (bottom) distributions on plane x=0 for test 2

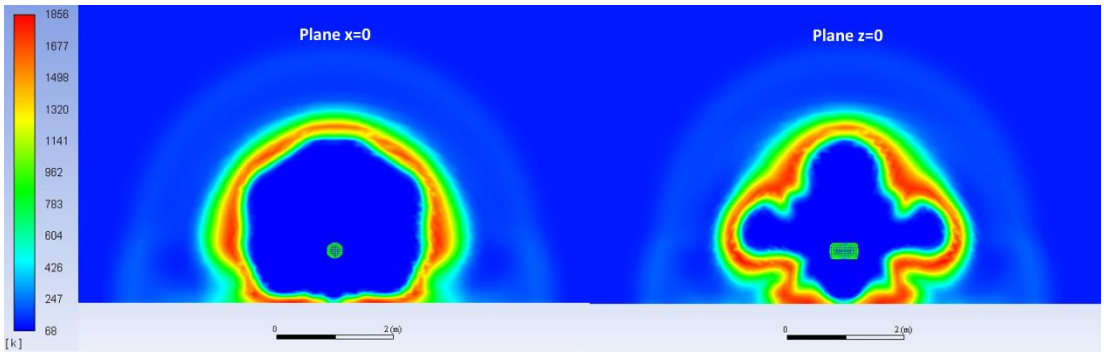


Figure 7.27 Temperature distribution on plane x=0 (left) and plane z=0 (right) at 4 ms for test 2

The mass balance is shown to be under control and below 0.1% up to 50 ms simulation. Test 2 pressure dynamics is shown in Figure 7.29. Pressure peaks are well reproduced, as well as the overall dynamics during the 50 ms shown. As expected, burnt hydrogen is not different from test 1 (Figure 7.30). Hydrogen mass imbalance is below 0.1 % and it follows the same trend as per test 1, confirming the good accuracy of the results. Overall, numerical simulations reached similar conclusions to the analytical calculations performed in section 7.4.2. The author considers that blast wave at 5 m for test 1 is affected by experimental settings or a specific explosion dynamics rather than the amount of mechanical and chemical energy released initially. Possible cases of such high overpressure are investigated in the following sections. The time needed by the simulation of 50 ms was approximately 40 h on a 32 parallel processors machine. Time step during the simulation increased from $1.7 \cdot 10^{-6}$ to $5.9 \cdot 10^{-6}$ s.

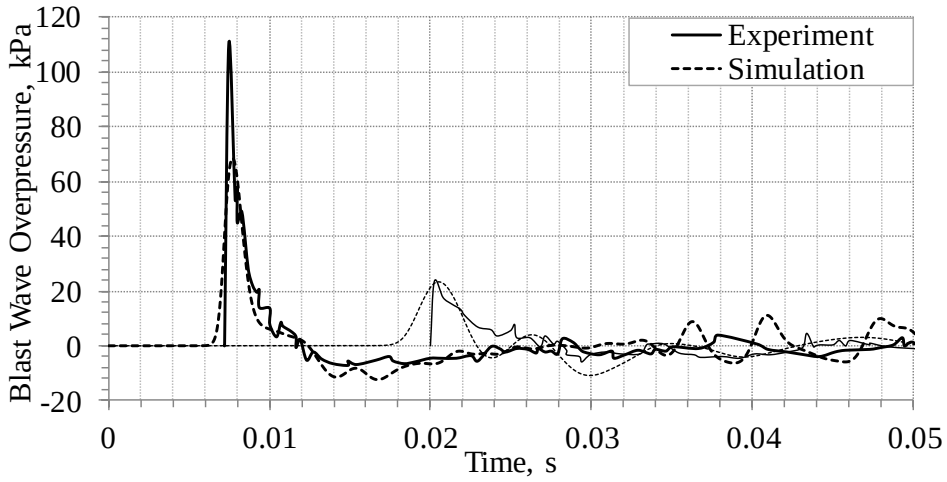


Figure 7.28 Pressure dynamics for test 1: simulation versus experiment

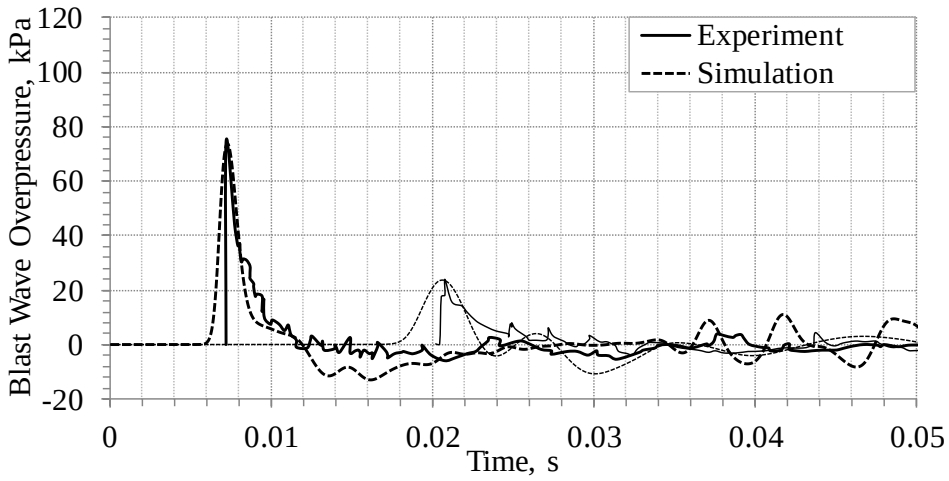


Figure 7.29 Pressure dynamics for test 2: simulation versus experiment

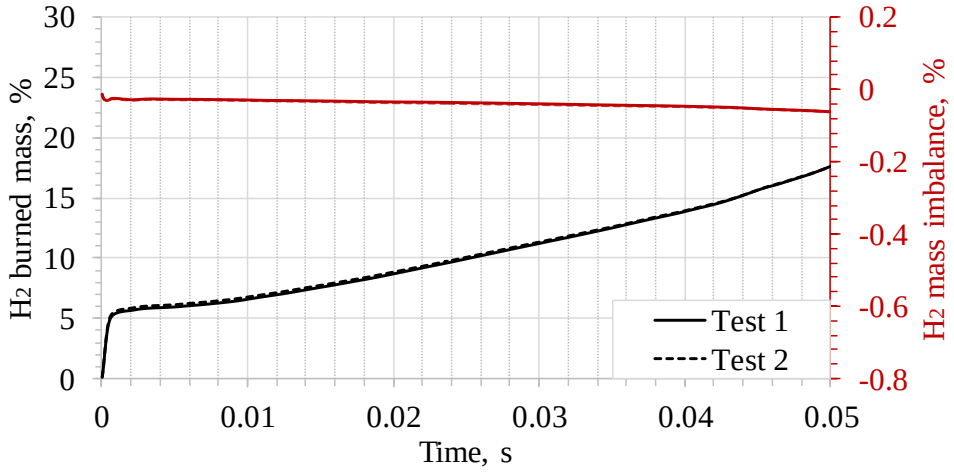


Figure 7.30 Burned hydrogen (black) and hydrogen mass imbalance (red) for test 1 (solid line) and test 2 (dashed line)

7.4.4.3 Combustion contribution to the blast wave

Molkov and Kashkarov (2015) widely discussed the importance of accounting chemical energy along with the stored mechanical energy. Their calculations stated that the ratio of chemical to mechanical energy released to feed the blast wave was 1.4 for a 35 MPa stand-alone tank, leading to an increase by 30% of the maximum overpressure at 6.5 m from the tank. To quantify the contribution of combustion to the blast wave, the case with only release of mechanical energy was considered deactivating the combustion model. As shown in Figure 7.31, pressure peaks for the case without combustion well agree with the maximum overpressures at 5 m and 10 m calculated according to Baker et al.' s methodology, respectively 45.6 kPa and 15.2 kPa (Table 7.5). Combustion contributes to the blast wave strength increasing it by 35% at 5 m. The blast wave arrival time is affected by the absence of combustion and therefore high temperature zones, showing a shift of about 1 ms for the first

sensor and 2 ms for the second sensor. A similar behaviour is expected for test 2. Therefore, the same conclusion as in Molkov and Kashkarov (2015) is reached: contribution of the released hydrogen combustion to the blast wave strength cannot be neglected to accurately predict the blast wave decay.

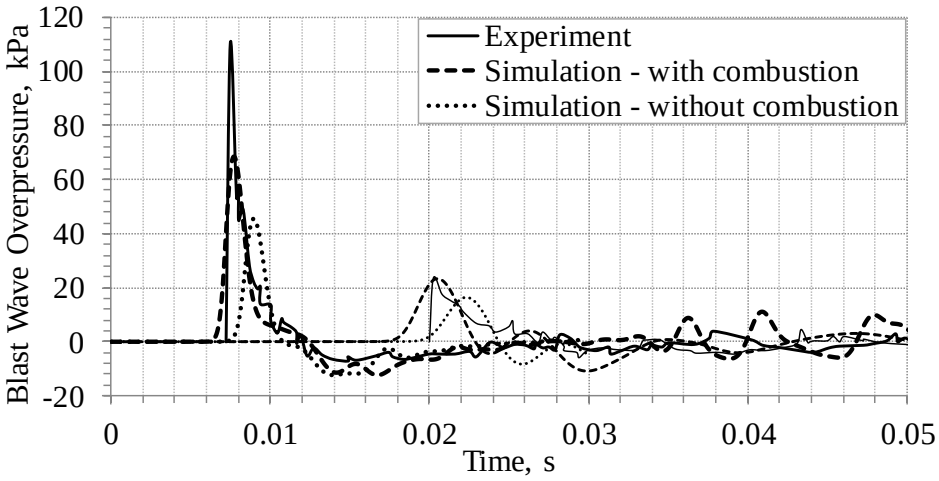


Figure 7.31 Pressure dynamics for test 1: combustion contribution to blast wave

In the present model one reaction for the hydrogen-air mixture was employed. However, combustion may be affected by the considered chemical mechanisms. To quantify this effect, a case employing a subset of Peters and Rogg's kinetic mechanism with 9 species and 18-step reduced kinetic reaction mechanism was considered for hydrogen combustion in air (Peters and Rogg, 1993). The aid of products and temperature patch around the tank was needed to exceed the activation energy threshold and maintain combustion. A region with dimensions 1.5x0.9x0.9 m was initialised with $mf_{OH}$=0.001 and T=900K. The model employing 18 reactions and 9 species resulted in a slight higher burnt hydrogen (+0.5%), perhaps because of the numerical ignition aid. Pressure at sensors did not show significant differences in dynamics. It is therefore concluded that the solution is not affected by the level of detail of the employed chemical mechanisms.

7.4.4.4 Grid sensitivity test

Results may be affected by the resolution of the computational grid. Therefore, a grid sensitivity study was conducted. The length of the computational cells was halved, as suggested in the CFD protocol elaborated by Baraldi et al. (2017). The refinement focused on the tank volume, the surrounding area and the zone where the sensors are located. 24 divisions were employed along the tank diameter and 32 along the tank axis. The resulting mesh had 723044 control volumes and the simulation was conducted with CFL equal to 0.1. Figure 7.32a shows the pressure dynamics comparison between the coarse and fine grid. No significant difference is noticeable for the sensor at 5 m. Sensor at 10 m recorded a lower (~10%) and

slower pressure wave. This is thought to be associated with the reduced combustion for the finer grid (-2%), shown in Figure 7.32b. The simulated flame front requires 4-5 CVs. Varying the length of the cell causes a reduction of the space occupied by the contact surface, with consequent decrease of burnt hydrogen. The effect decreases with the elapsed time, as combustion does not interest anymore only the propagating flame front but all the area where hydrogen and air mix. Simulation for finer grid required approximately 10 days to simulate 30 ms while less than 2 days were needed for the coarse grid simulation with CFL=0.1. Since it is presumed that the difference in the results is given by the resolution of the contact surface and the saving of time is significant, the coarse mesh is maintained for the following calculations.

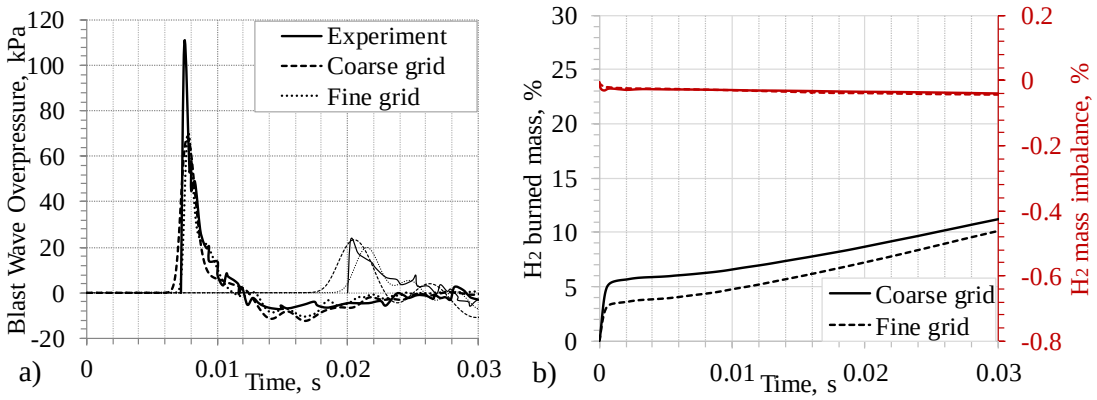


Figure 7.32 Grid sensitivity: pressure dynamics (a) and hydrogen mass balances (b) for test 1

7.4.4.5 Effect of experimental settings on test 1

As discussed above, test 1 shows an overpressure peak at the first sensor which is not believed to be exclusively linked to the initial mechanical and chemical energy, but it is considered to be associated to particular experimental conditions or exact dynamics of the tank rupture. First of all, a burner was located beneath the tank to provide the established fire surrounding the tank and leading to its rupture. The burner platform and the fire around the tank, which initializes and enhances combustion, were not considered in simulations. The case including the burner in the numerical grid was firstly considered. A solid body with dimensions 1 x 0.04 x 0.6 m was introduced 20 cm below the tank. Blast wave front showed effect of the burner presence during the first 4 ms. Afterwards, the effect is reduced. On the other hand, the combustion zone was affected throughout the simulated time (40 ms). The presence of burner enhanced combustion, rising the burnt hydrogen from 8.7% to 10% at 20 ms (time of arrival of the blast to the further sensor). However, no significant difference of overpressure at sensors was observed. A second factor that was considered was the presence of the fire surrounding the tank. The fire was introduced in simulations by patching a region of dimensions 1.5x0.9x0.9 m with temperature=900 K and water vapour mass fraction equal to 0.001. The

presence of the fire enhanced combustion but not significantly. Burnt hydrogen at 20 ms was 9.6%, compared to the 8.7% of the case without fire presence. As for the case considering the burner presence, the variation and enhancement of combustion were not enough to cause any variation of overpressure at the sensors. A further aspect that has not been investigated yet is the modality of rupture of the tank. Indeed, the type of tank employed for the two tests is different, specifically type IV for test 1 and type III for test 2. Type IV tanks are composite vessels made of polymer liner with carbon fibre windings all over the cylinder, whereas type III tanks are vessels made of metal matrix composite with fibre resin. At the moment of rupture, the tank fractures in fragments. The different material employed for type IV tank may lead to a different fragmentation from type III tank. Boyer (1960) observed through Schlieren images a high level of turbulence in the contact region due to the presence of fragments in the area of the high-pressure gas expansion. However, this scenario may last for a brief interval of time compared to the time scale of the problem. To investigate this eventuality, a new mesh was realised with the segmentation of the external surface of the tank (Shentsov, 2017). The tank wall is chequered with periodic open and closed squares, as shown in Figure 7.33 in green and red respectively. Simulation was run for CFL=0.1. Results shown a slight increase of hydrogen combustion (almost 10% at 20 ms) but not a significant difference in pressure at the sensor located at 5 m.

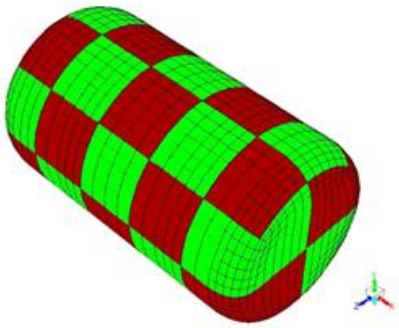

Figure 7.33 Fragmented tank: open segments in green and closed segments in red

A final scenario to be investigated interests the not entire instantaneous rupture of the tank. Experiment on a type IV tank reported by Zalosh (2007) has shown that the largest fragment was a half portion of the ruptured cylinder and it was found at 82 m of distance (Figure 7.34a). A similar circumstance was observed in all the tests conducted by Pittman (1976). In this case, the author reconstructed the vessel burst histories, estimating the directions of the maximum gas motion, denominated jetting, on the horizontal plane. Direct consequence of the jetting is an asymmetrical blast wave field. Such asymmetry could be remarkably pronounced in certain directions: data for a 100 MPa tank showed that pressure at 5 m could vary by approximately 50% within a range of 60° angle. What observed in Zalosh (2007) and Pittman (1976) can be

the cause of the high experimental pressure at 5 m for test 1. To investigate this scenario, a limiting case was considered in the CFD simulation. The external surface of the tank was cut along the cylinder axis in two equal portions. The corresponding numerical grid is shown in Figure 7.34b. The part in direction of the sensors was defined as interior, so that it could be immediately crossed by the suddenly released high-pressure hydrogen. The opposite portion was defined as a no-slip adiabatic wall. The wall surface was removed after 0.688 ms, which was calculated as the time spent by the inertial forces to move the tank from its initial position to twice its diameter.

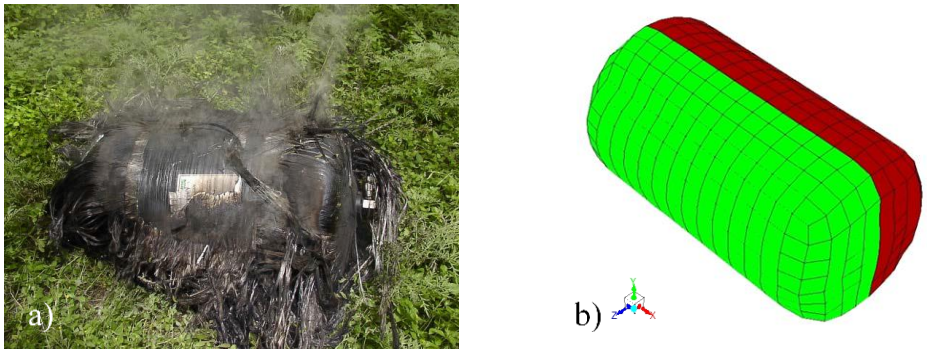


Figure 7.34 a) Fragment from cylinder for a stand-alone type IV 35 MPa tank (Zalosh, 2007); b) Numerical grid of half tank open in z direction (green) and half tank closed surface (red)

Figure 7.35 shows the dynamics of the blast wave and combustion through pressure and temperature distribution on the plane perpendicular to the cylinder axis. Time equal to 0.6 ms shows distribution before the half-closed tank wall removal. Opening of only half of the tank causes a more powerful blast wave in z direction. Combustion is significantly affected by the initial presence of the half tank wall. It is deduced that the presence of the wall enhances the turbulent mixing of hydrogen with air, leading to an intense combustion even after its disappearance. This compensates the lack of combustion of half of the hydrogen cloud because it cannot enter in contact with oxygen due to the half tank wall presence during the first 0.688 ms. Figure 7.36 shows the effect of opening of solely half of the tank on overpressure at the two sensors. Pressure increased by 40% at 5 m, reproducing the experimental peak. The blast wave arrival time to the sensors is anticipated by approximately 2 ms compared to the case with the tank entirely open since the beginning. Experimental arrival time to the sensor was not available, but it was adjusted according to the simulated pressure curve. Pressure dynamics follows the same trend in time, but a greater negative phase is reached. A 30% increase is noticeable for pressure at 10 m, which overestimates experimental peak. It has to be considered that in simulation the tank wall suddenly disappears. In experiment, there might be a loss of energy to push away the tank wall, which is not accounted in simulation. This may be the cause of the pressure overestimation at 10 m. No significant difference was observed in the

quantity of burnt hydrogen between the simulated cases for entire and half open tank. On the other hand, hydrogen mass imbalance slightly worsened for the case with opening of only half of the tank, but it was contained within 0.1%. The investigated case with exactly half of the tank open is certainly an idealised limit condition, but it is expected that the real case will be an intermediate state between the two alternatives shown in Figure 7.36. It is concluded that the high pressure at 5 m recorded for test 1 is associated to the tank rupture dynamics. Figure 7.37 and Figure 7.38 compare the temperature profiles on the perpendicular and parallel planes to the tank axis at 40 ms. The opening technique of the tank is shown to deeply affect the fireball dynamics, even if the half tank wall disappears within 1 ms from the rupture. The fireball enlarges towards the ground, instead of expanding towards the top of the domain as occurring for the instantaneous opening of the tank. The effect is believed to be more pronounced in experiments, due to the fragmentation of the tank.

A further case in which the half tank wall was not removed was analysed. No difference was observed in the monitored parameters, indicating that the solution is independent from the time selected for the tank wall disappearance. To complete the set of possible scenarios, a final case with opening of the half tank in x direction was considered. In this case, the increase of pressure recorded at 5 m in x direction was limited to 32%.

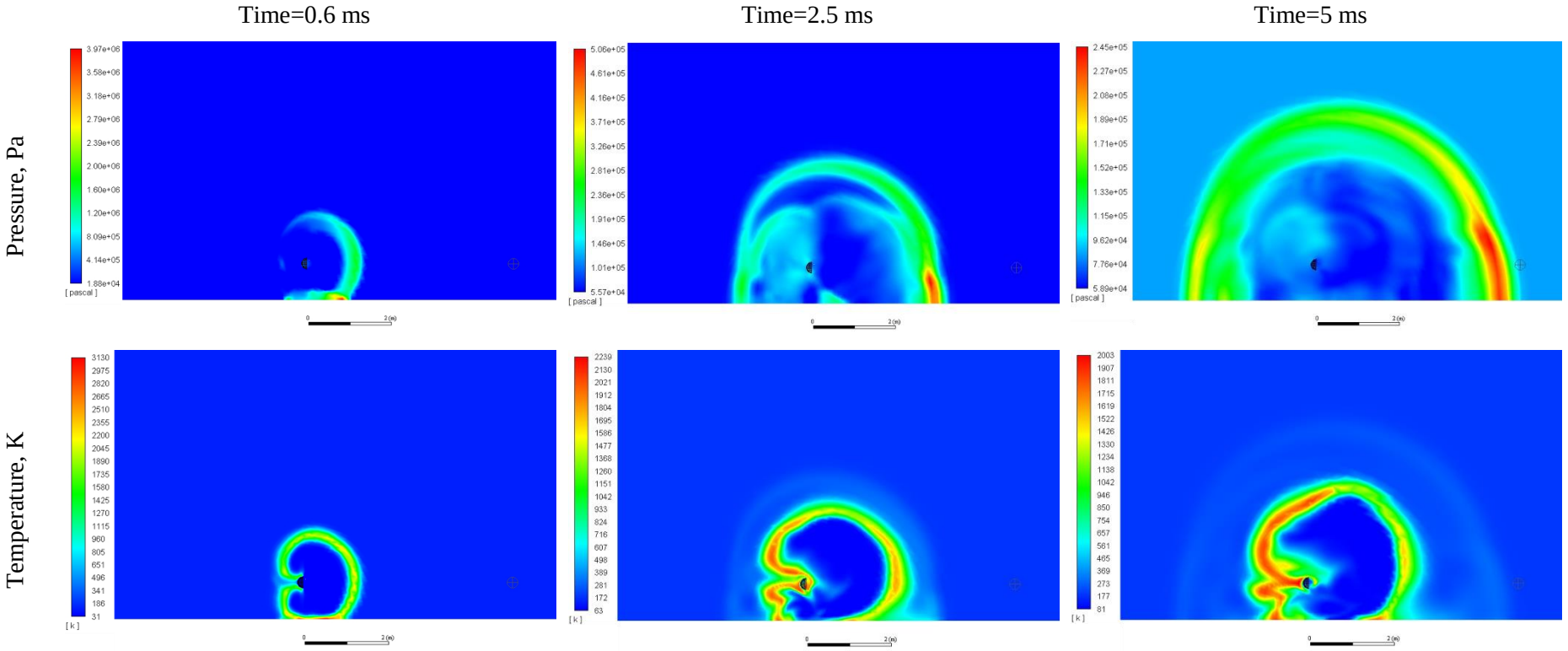


Figure 7.35 Pressure (top) and temperature (bottom) distributions on plane x=0 for test 1: effect of half tank opening

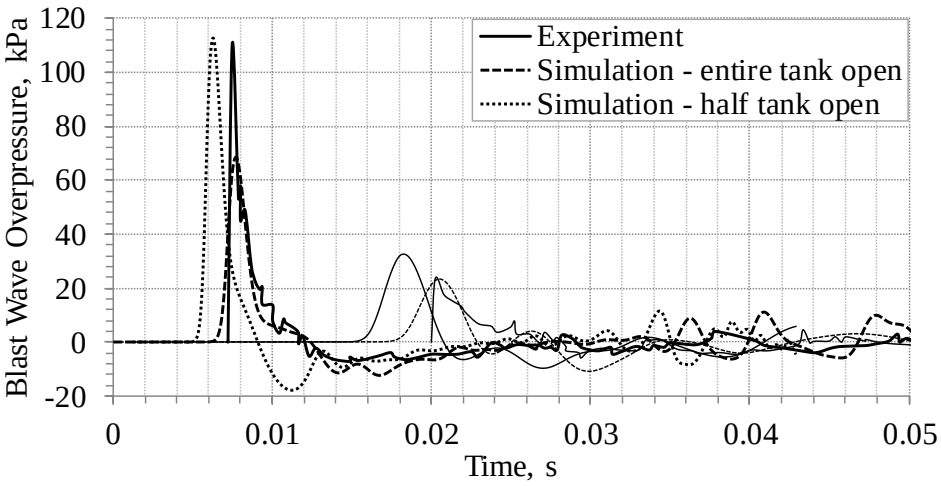


Figure 7.36 Pressure dynamics for test 1: effect of half tank opening

Instantaneous opening

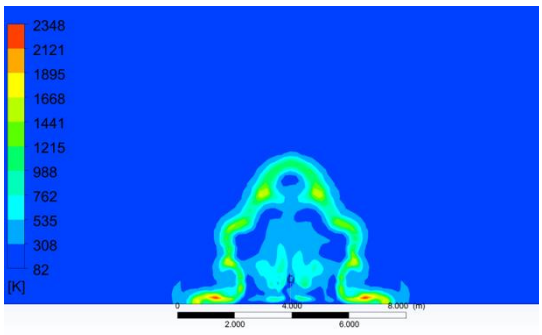


Half tank opening

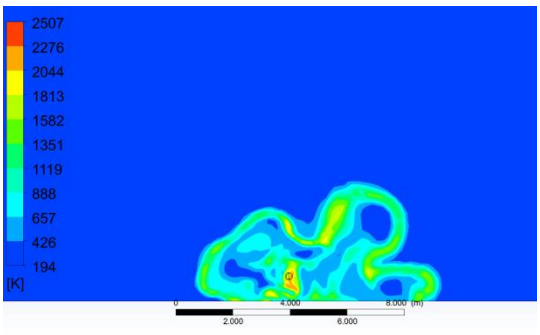


Figure 7.37 Comparison instantaneous and half tank opening: temperature distribution on plane perpendicular to the tank axis (x=0) at t=40 ms

Instantaneous opening

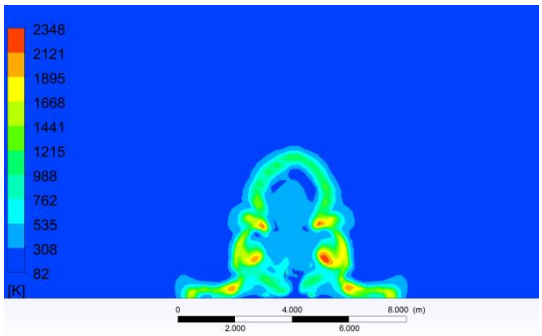


Half tank opening

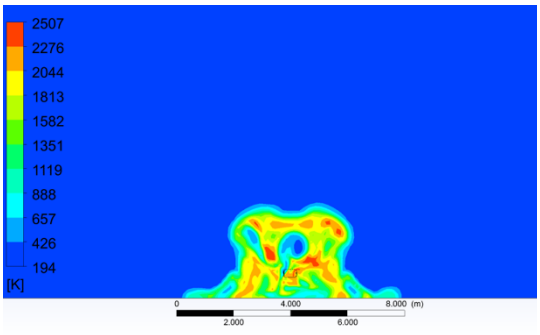


Figure 7.38 Comparison instantaneous and half tank opening: temperature distribution on plane parallel to the tank axis (z=0) at t=40 ms

7.4.4.6 Effect of turbulence model

In the present section, LES RNG subgrid-scale model (Eq. 3.13-3.14) is compared to LES Smagorinsky-Lilly (Eq. 3.12). Results of the comparison are shown in Figure 7.39. The switch of subgrid-scale model did not lead to significant variation in pressure dynamics. This result can be associated with the limited role of turbulence in propagation of the blast wave. However, turbulence has a greater effect on combustion behind the shock wave, as shown in Figure 7.40. Smagorinsky-Lilly model results in a higher combustion of hydrogen and the model is selected for the following calculations, as it better reproduces the burnt hydrogen percentage predicted by the analytical model (10-15%). The employment of a dynamic Smagorinsky constant for transitional flows did not cause any sensitive change to the results. Therefore, the "traditional" Smagorinsky-Lilly formulation is maintained for the following analysis.

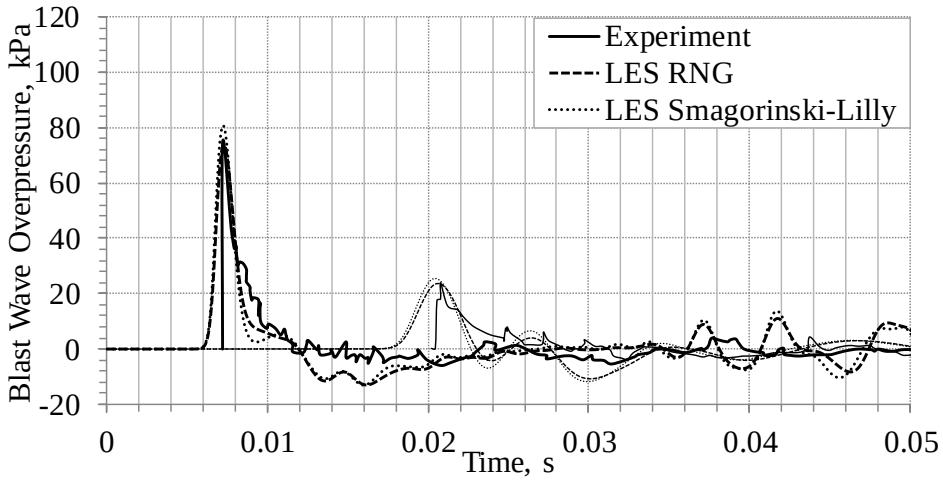


Figure 7.39 Turbulence subgrid-scale model sensitivity: pressure dynamics (test 2)

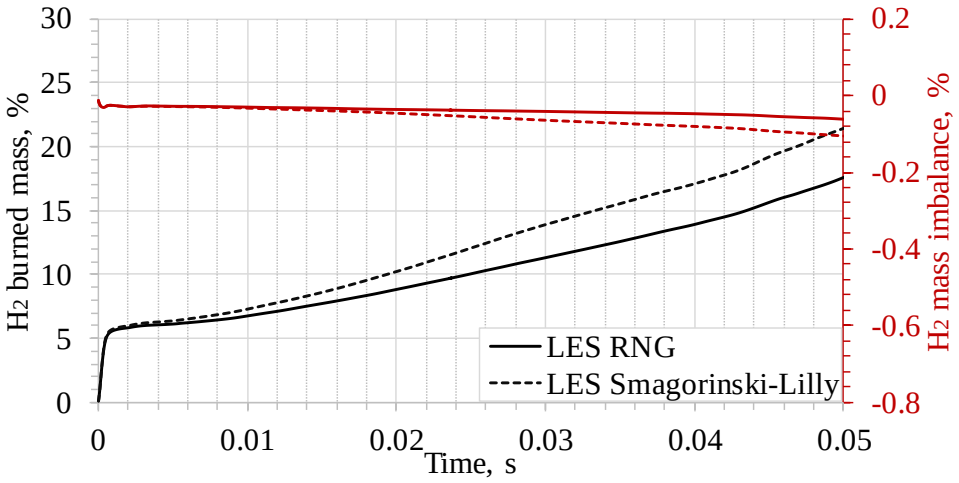


Figure 7.40 Turbulence subgrid-scale model sensitivity: burned hydrogen and hydrogen mass balance (test 2)

7.4.4.7 Effect of combustion model

The reaction rate in turbulent combustion is controlled by the turbulent mixing of reactants. Eddy Dissipation Concept by Magnussen (1981) includes detailed chemical mechanisms in turbulent flows. Details of the model can be found in section 3.4.2. The EDC was applied to the present case and results are compared to the Finite Rate model in Figure 7.41. Pressure transients are not significantly affected by the modification of the combustion model, maintaining the same overpressure peaks and overall dynamics. A slight effect can be observed in burnt hydrogen between 0.05 and 0.25 ms (Figure 7.42). It can be concluded that since combustion mainly interests the contact surface behind the shock, there is a limited effect of turbulent mixing on combustion feeding the blast wave.

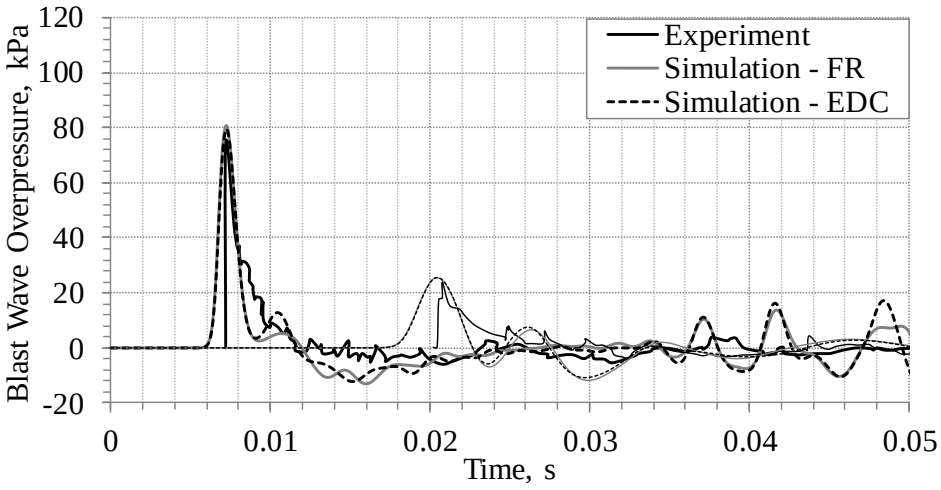


Figure 7.41 Combustion model sensitivity: pressure dynamics (test 2)

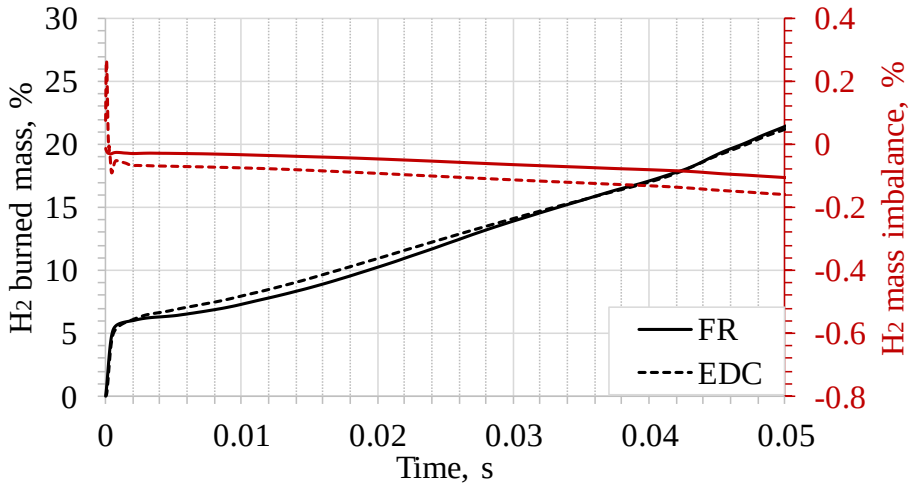


Figure 7.42 Combustion model sensitivity: burned hydrogen and hydrogen mass balance (test 2)

7.4.4.8 Inclusion of radiation in the model

Radiation losses may affect the pressure simulated at the sensor. Moreover, inclusion of radiation model is fundamental for quantification of the thermal hazards in terms of radiative heat flux from the fireball. In the present section, the Discrete Ordinates model, presented in section 3.5, was included in the LES approach. Yan et al. (2015)'s data were employed for the calculation of the water vapour mean absorption coefficient. As shown in Figure 7.43, radiation model did not affect the pressure dynamics at the sensors. Combustion and hydrogen mass balance did not show any effect either.

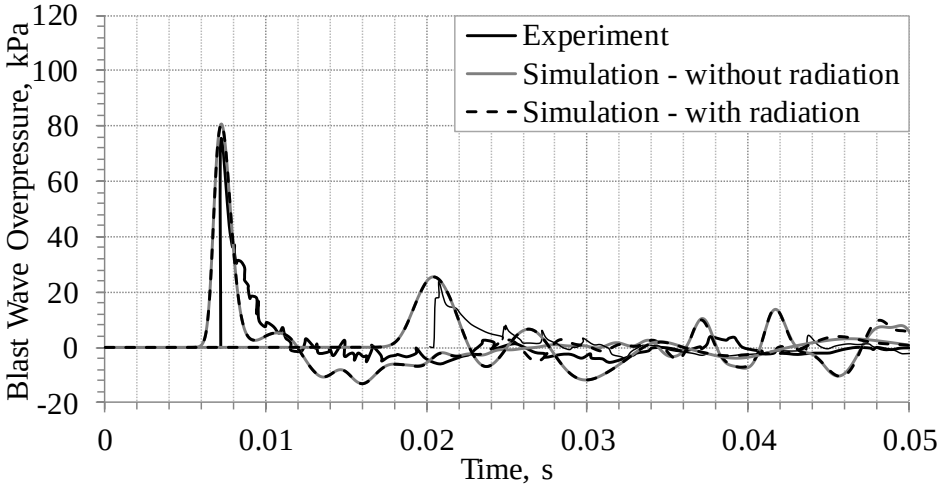


Figure 7.43 Radiation model inclusion: pressure dynamics for test 2

CFL equal to 0.2 was employed for the simulation of the blast wave. Maintaining a CFL=0.2 to simulate the fireball development until its disappearance (~1.5-2s) would require a too long calculation time. Moreover, usually higher CFL are employed when the problem does not aim to simulation of shock wave propagation. At 80 ms the shock wave becomes weak and it approaches the domain boundaries where cell size is longer than 0.5 m. Furthermore, the highest CFL is recorded in the combustion region, where the highest temperature and lowest cell lengths are recorded. Therefore, the imposed CFL was gradually increased by 10 times in 10 ms, to avoid a sharp change that could be cause of solution instabilities. The hydrogen mass balance was monitored, and it was observed that the increase of CFL did not cause any variation to its trend (Figure 7.44). The blast wave and fireball dynamics is shown in Figure 7.46-Figure 7.49. Figure 7.46 reports the pressure and temperature distribution up to 21 ms, when the blast wave reaches the second sensor. At 4 ms the pressure wave reflected from the ground has not yet reached the primary pressure wave, while after they are unified in a unique front. Temperature distribution at 2 ms shows the initial stage of detachment between the blast wave and contact surface, which appear completely separated after that moment. Detailed description and representation of the time range 0.5-8 ms is given in Figure 7.25 and is not

repeated in the present section. Water vapour and hydrogen distributions show that in the initial stage combustion interests mainly the contact surface where the expanding hydrogen starts to mix with oxygen, while afterwards the turbulent mixing increases and combustion interests the entire hydrogen cloud. The following fireball development is investigated in terms of temperature and water vapour in the interval of time 30 ms-1.8 s. The fireball assumes the classical "mushroom" shape after 30 ms. At approximately 0.4 s the cloud of hot products detaches from the main combustion zone, which remains close to the ground where the hydrogen is located. The maximum diameter of the fireball was 11 m. The result underestimates the diameter reported by experimentalists (20 m). However, photographs of the fireball showed a maximum size of approximately 13 m for both tests 1 and 2. The main cause of underestimation is believed to be associated with the tank "opening" process. Experimental evidence, see Boyer (1960), showed that turbulence in proximity of the tank surface is particularly enhanced because of its fragmentation. This along with the rupture in large fragments, see Zalosh (2007) and Pittman (1976), can deeply affect the fireball development. Figure 7.37 and Figure 7.38 showed the effect of opening of only half tank in direction perpendicular to the tank axis. The fireball grew more horizontally rather than in vertical direction as for the instantaneous opening. The author believes that the effect can become more pronounced with time. Furthermore, it must be considered that in experiments the largest fragment was seen to be the top part of the tank, which along with the burner presence may affect the spreading of the combustion zone on the horizontal plane, causing an enlargement of the fireball size. The presence of the fire leading to rupture may also have affected the resulting fireball dimensions, following the conclusions of Robert's study (Roberts, 1981). Figure 7.44 shows the burned hydrogen trend during the entire duration of the simulation, i.e. until the end of combustion. Hydrogen mass balance was maintained below 0.5% until the simulation was complete. The total time required by the simulation was approximately 14 days on a 32 parallel processors machine. Figure 7.45 shows the blast wave decay in perpendicular and parallel direction to the jet axis. Pressure decay depends on the considered direction in the near field to the tank. Higher overpressure was recorded on the sides of the cylinder. The difference disappears for distances greater than 4 m. This value agrees with the conclusions of the study on vessel pressure burst directional effects conducted by Geng et al. (2011). The authors identified as near field the distance resulting in a scaled stand-off distance lower than 1. According to this definition, the near field for the present case corresponds to distance lower than 4.5 m. The hazard distances for people outdoors are determined by the blast wave pressure threshold as defined in (Molkov and Kashkarov, 2015) and presented in Table 2.3. The "fatality" pressure limit is reached at about 4.5 m from the tank, whereas the "injury" limit is recorded at approximately 12 m. The limited size of the

domain and the refinement level of the numerical grid towards the boundary did not allow a precise calculation of the distance associated to the "no harm" pressure limit.

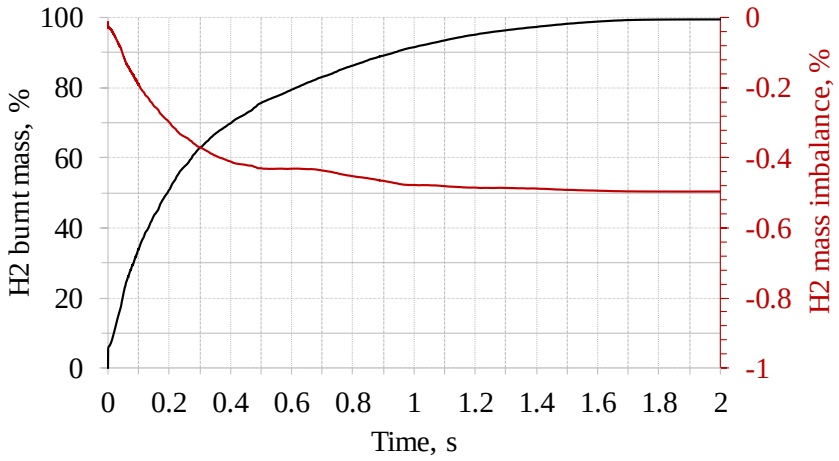


Figure 7.44 Burnt hydrogen (black) and hydrogen mass imbalance (red) for test 2

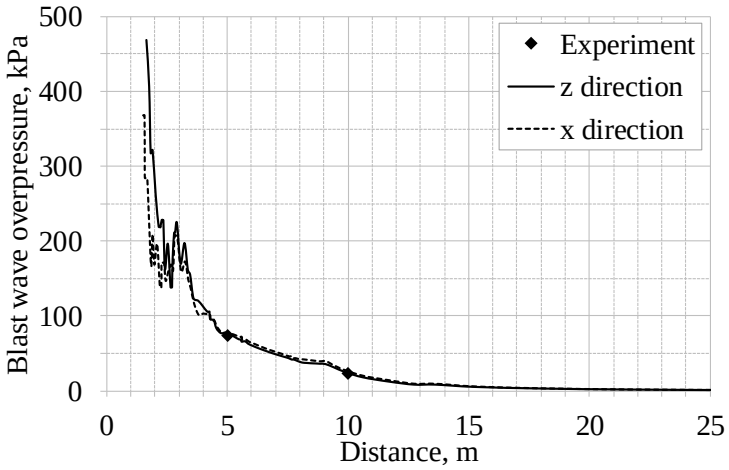


Figure 7.45 Blast wave decay: experiment versus simulation for test 2

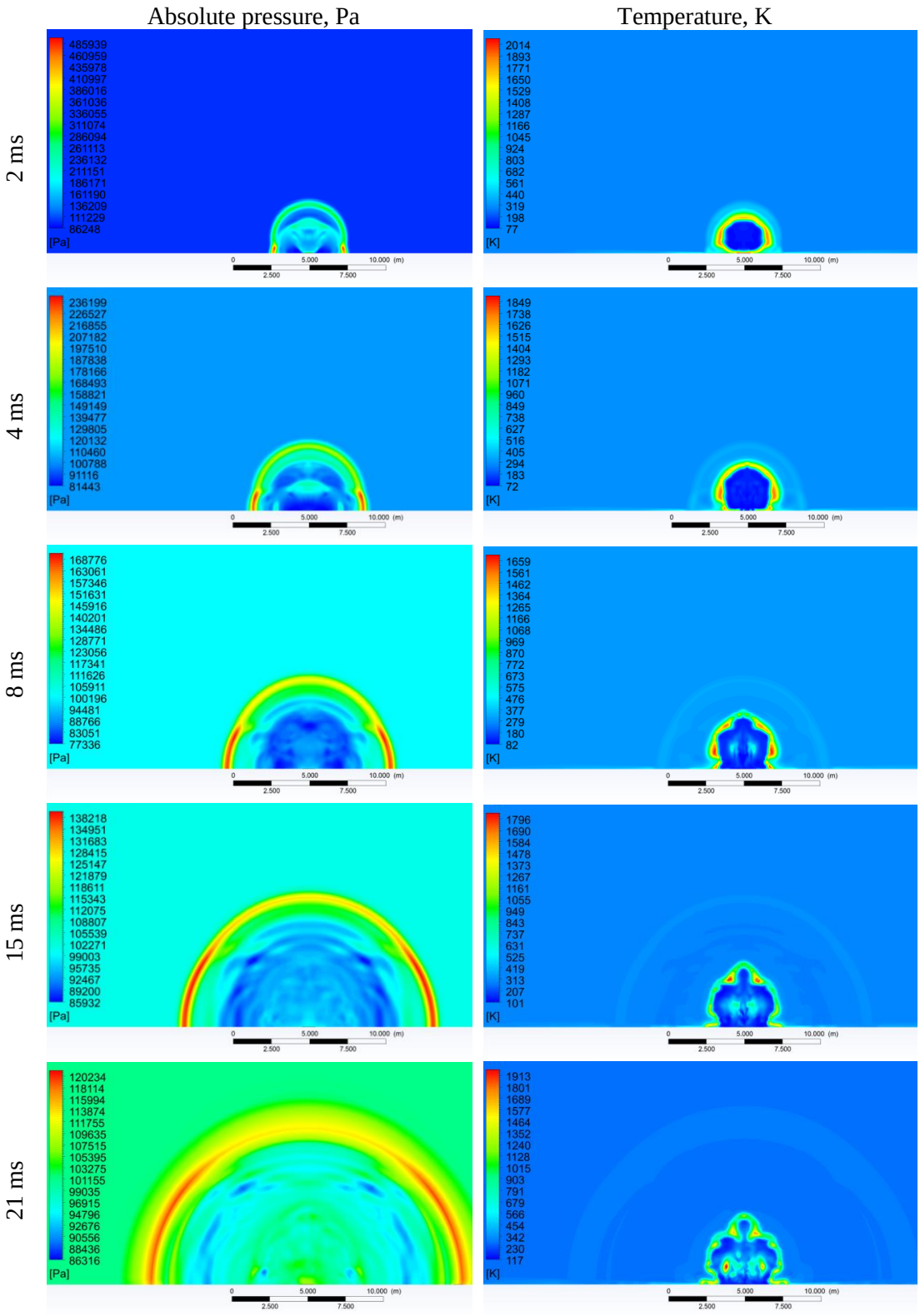


Figure 7.46 Pressure and temperature distribution between 2 ms and 21 ms (test 2)

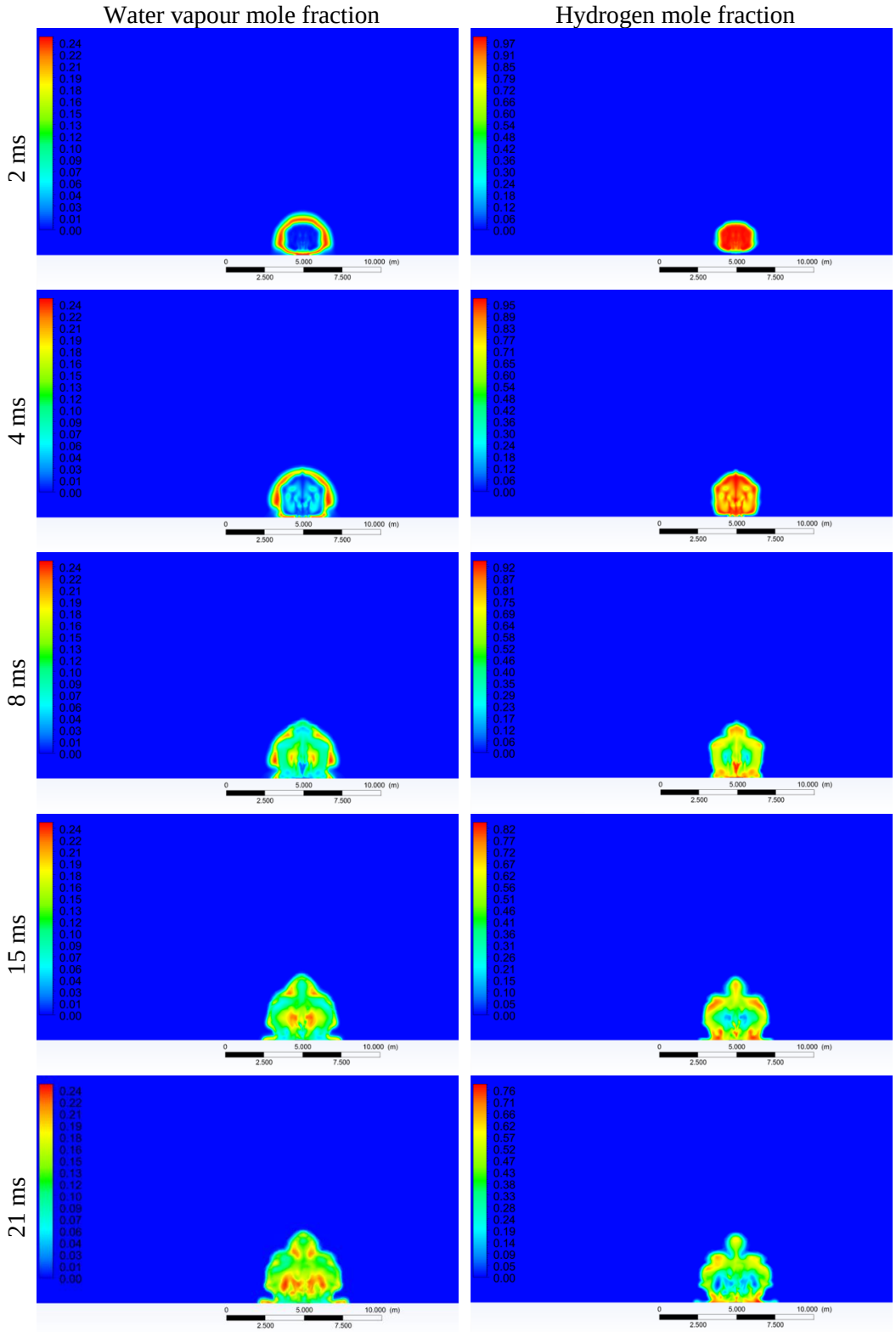


Figure 7.47 Water vapour and hydrogen distribution between 2 ms and 21 ms (test 2)

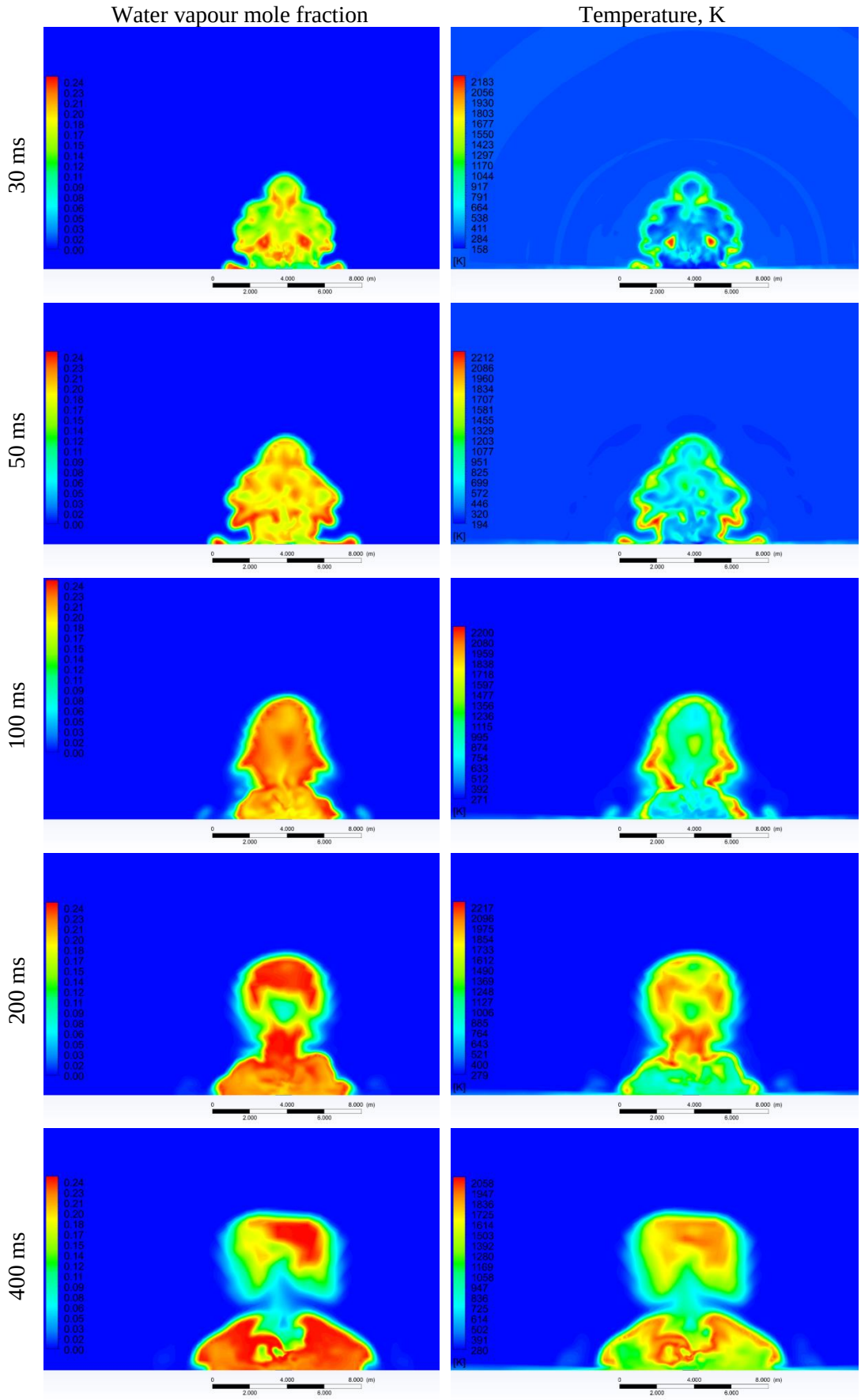


Figure 7.48 Water vapour and temperature distribution between 30 ms and 400 ms (test 2)

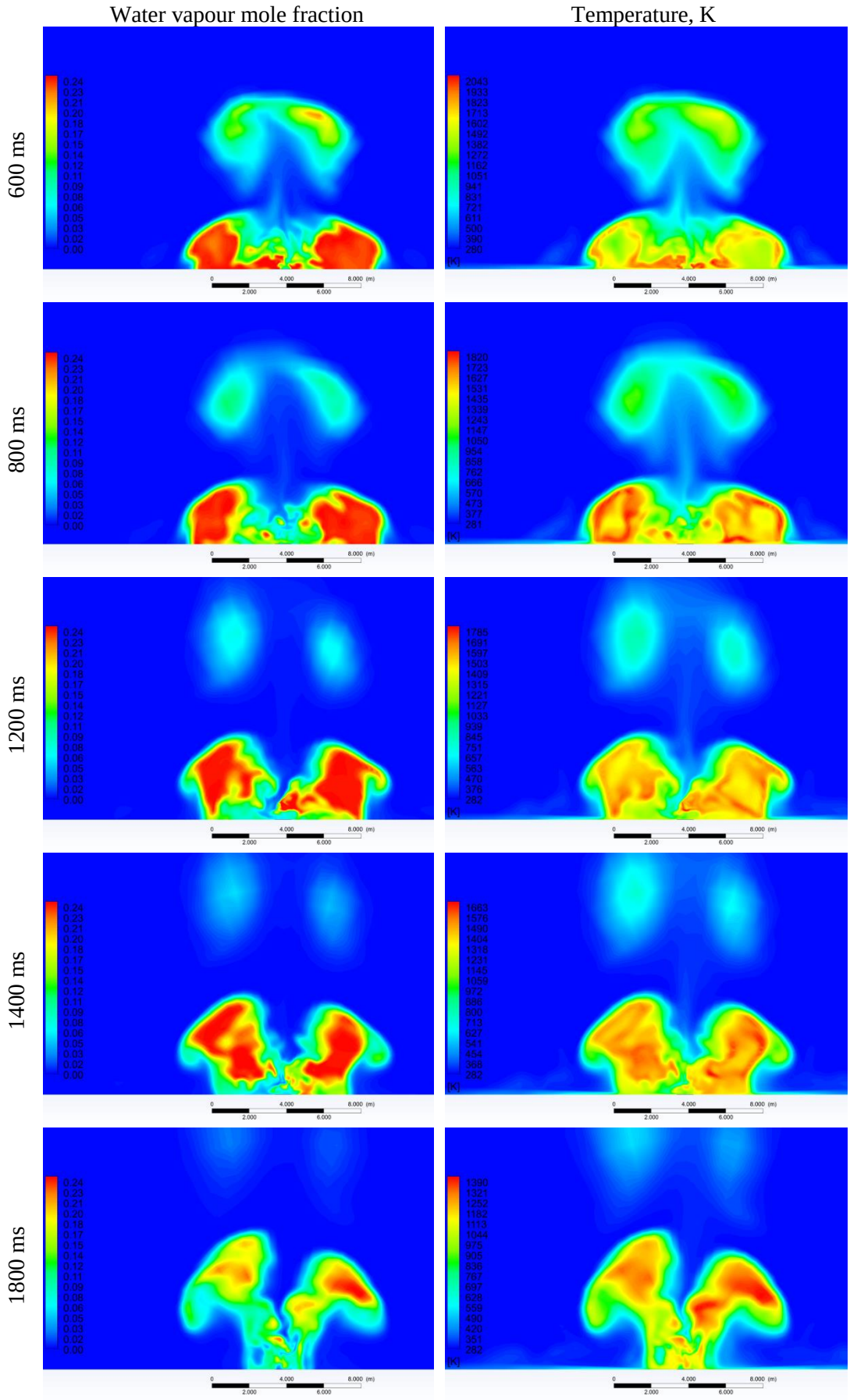


Figure 7.49 Water vapour and temperature distribution between 0.6 s and 1.8 s (test 2)

### 7.4.5 Application of the CFD model to rupture of 35 MPa storage tank

The CFD model developed in the previous section was applied to simulate the experimental test on a 35 MPa storage tank described in section 7.2.1 in Molkov et al. (2018). The storage tank was geometrically scaled, as done for the 70 MPa test, to conserve the stored mechanical energy as calculated for the real gas. Dimensions of the cylinder used in simulations were 68.4 cm in length and 37.7 cm in diameter. The eddy dissipation concept was employed as combustion model to simulate the turbulence-chemistry interactions. However, it was highlighted in section 7.4.4.7 that Finite Rate and EDC provide similar results in modelling blast wave. The computational domain consisted of 311,114 control volumes on a hexahedral grid with diameter 100 m. A region with dimensions 1.5x0.7x0.9 m around the tank was initialized with temperature and water vapour mole fraction as in section 7.4.4.3 to provide numerical ignition. Convergence of the solution was achieved for CFL<=0.1. Results of maximum overpressure along and perpendicular to the tank axis are presented in Figure 7.50. The difference between the two directions is significant for the sensor located at 1.9 m, while it decreases with distance until it disappears for distance greater than 6 m. 4.3% of the initial hydrogen mass burned when the blast wave reached sensor at 6.5 m. Simulation deviates from experiment in the tank near field. However, the CFD approach well reproduces pressure at further distances, including the blast wave time of arrival and dynamics in time, further validating the developed CFD model.

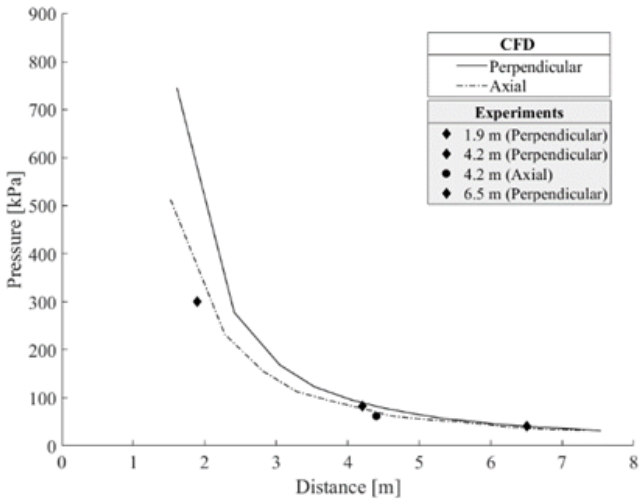


Figure 7.50 Maximum pressure as a function of distance from the tank in directions along and perpendicular to the tank axis (Molkov et al., 2018)

## 7.5 Concluding remarks

A CFD model to simulate blast wave and fireball after rupture of high-pressure storage tanks was developed. A parametric study was performed to assess the effect of both numerical and experimental parameters. The CFL sensitivity study resulted in convergence of the solution for a CFL number below the range 0.7-0.9, which is usually used for deflagration modelling. Variation of the combustion sub-model and introduction of radiation modelling were not found to affect the blast wave strength. Smagorinsky-Lilly model resulted in higher hydrogen combustion, better reproducing predictions by analytical calculations. Simulations comparing the instantaneous to the half tank opening gave insights into the effect on the blast wave dynamics. The model was validated against two experimental tests on storage tanks with initial pressure 70 MPa. Blast wave dynamics were accurately reproduced in test 2, whereas, in test 1, simulation results agree well with experiments when considering half tank opening. Further investigations on the tank opening process and bonfire effect should be conducted to better reproduce the fireball dynamics and dimension, as the current methodology resulted in underestimation of its diameter. The same CFD model was applied to modelling of an experimental test on a 35 MPa hydrogen tank (Molkov et al., 2018). Simulation well reproduced experimental tests, confirming the validity of the developed predictive tool.

# 8 Conclusions

This doctoral study was aimed to close a number of knowledge gaps identified in hydrogen safety engineering associated with the employment of high pressure hydrogen storage systems. Analytical and numerical methods, including computational fluid dynamics (CFD), were used as a contemporary tool to investigate the hazards from catastrophic failure of such systems.

The main research outcomes of this study include but are not limited to a deeper understanding of the relevant phenomena bearing risks that could affect the safety of people, property and environment, and the development and validation of numerical models capable of predicting the entity of such hazards and associated risks. The produced knowledge and engineering tools will support the development of safety strategies, evaluation of hazard distances and engineering solutions for an inherently safer deployment of hydrogen and fuel cell technologies using high-pressure storage systems.

Firstly, an extensive literature survey was conducted on the state of the art of hydrogen storage systems and applications, and the related safety science. The covered phenomena included dispersion and combustion of hydrogen unintended releases, ignition in quiescent hydrogen-air mixture and ignition in turbulent high-pressure hydrogen jet, rupture of the tank in a fire. During the review process, attention was paid to existing analytical and modelling studies, underlining where missing.

The **scientific novelties**, **impact** and **contributions** of the doctoral study are the following:

- Development of a CFD tool for prediction of hydrogen jet fires behaviour, including scaling and radiation properties. The CFD approach was applied and validated against releases from several storage conditions. A first investigation looked at jet fires originated by cryogenic releases at pressure up to 6 bar. Simulations were compared against five experimental tests conducted at SNL. For all five tests experimental radiative heat flux at 5 sensors along the jet flame was predicted within ±15% accuracy, with few exceptions. A second investigation examined the jet fire test performed at INERIS facility and originated by a high-pressure release (900 bar). The volumetric source approach was implemented to model the release characteristics during the tank blowdown, simplifying the numerical code. Thermal radiation was found to be in good agreement with experiment after the establishment of the flame (time 10 s). In both the investigations on jet fires, flame length was well reproduced, confirming the applicability of the model to a wide range of storage conditions.
- CFD tool for calculation of thermal dose. The numerical code was extended to include thermal dose calculation and provide a tool for calculation of hazard distances on the

sides of the jet fire. This tool is complementary to the available analytical correlations to determine hazard distances on the jet axis. Knowledge of thermal dose levels on the sides of the jet fire can provide useful guidelines and separation distances for first responders when they intervene to extinguish a fire involving a FCHV. The hazard distances by thermal dose thresholds were calculated for the vertical cryogenic jet fires.

- The validated CFD model for jet fires thermal hazards provides a tool to simulate real accident scenarios such as releases from TPRD openings in hydrogen-powered vehicles or in stationary storage systems involved in a fire, and calculate hazard distances from the evaluated flame length and thermal dose. Such distances may be of utmost importance to define the strategy of intervention for the first responders approaching the accidental scene.
- A parametric study on numerical and experimental features to assess their effect on thermal hazards from hydrogen jet fires. The results led to the development of the following recommendations and guidelines for future studies:
  - The numerical grid at the release nozzle can be realized employing only 1 cell, as it was found to be sufficient to correctly represent the jet fire and provide grid independence;
  - 10x10 angular divisions should be employed in DO model for resolution of thermal radiation from small-scale jet fires, as it was the minimum resolution providing convergence of the solution;
  - Turbulence level at the release point should be carefully defined when employing the volumetric source approach for simulating blowdown, as it was found to significantly affect thermal radiation in proximity of the jet fire (up to 30% variation);
  - Exact measurements and precise experimental conditions are fundamental to develop and validate predictive CFD models, including but not limited to water vapour presence in air and volumetric flow rates at the exhaust gases removal system.
- Development of a CFD tool for calculation of minimum ignition energy in hydrogen-air mixture accounting for detailed chemical kinetics. The numerical calculations gave insights into the flame kernel formation and propagation. MIE was calculated for stoichiometric and quiescent mixture with an improved accuracy compared to previous works on spark ignition modelling. The model application can be extended to calculation of MIE by spark capacitive discharge for mixtures at arbitrary conditions, such as for unintended releases from hydrogen systems in FCHVs.

- Computational investigations on high-pressure hydrogen releases and dispersion. The performances of different turbulent models were assessed. Results for a 40 bar release were compared against the experimental tests conducted at INERIS. RNG k-ε model and LES Smagorinsky-Lilly were found to predict well experiments. It was observed that a separation distance of at least 20 m should be assured between the release source and any air intake of buildings or possible ignition source to ensure a hydrogen concentration lower than the LFL. It was observed that difference between results from different turbulence models decreases with the increase of release pressure, yielding to maximum deviation in hydrogen distribution of 6% for release pressure equal to 200 bar.
- Investigation on the applicability of existing combustion models into simulation of delayed ignition of high-pressure hydrogen releases. Flame propagation dynamics and explosion overpressure were heeded in this study. The multi-phenomena deflagration model developed at UU was refined to simulate combustion in a turbulent non-uniform hydrogen-air mixture. The model showed a good agreement with the pressure trends observed in experiments. However, the model should furtherly be improved to better reproduce the mixture combustion and pressure prediction.
- Development and validation of a CFD methodology for predicting pressure and thermal hazards from rupture of hydrogen tank in a fire. The adaptive time step technique was found to shorten significantly calculations and to improve hydrogen mass balances. Therefore, this technique is recommended for explosion simulations. Exact convergence of the results was found for a CFL $\leq$0.1; however, deviation was considered to be negligible for CFL=0.2, whilst difference in computational time was significant. Thus, it is considered acceptable for engineering calculation purposes and future applications, instead of a CFL=0.7-0.9, which is usually employed for deflagrative combustion. Simulations were performed to provide insights into the process and the effect of experimental settings. Directionality effects of the vessel burst were observed in the near field to the tank (<4.5 m). Contribution of combustion to the blast wave strength was assessed and it was found to be over 35% for the sensor located at 5 m from the tank. It was concluded that combustion contribution cannot be neglected, in agreement with the study by Molkov and Kashkarov (2015). It was demonstrated that the mode the tank opens during rupture can significantly affect the blast wave and fireball dynamics. Pressure transients at the sensors were accurately reproduced for a test on a 99.5 MPa storage pressure, whereas, in a test for a 94.5 MPa tank, simulation results well agree with experiments when considering half tank opening. Fireball diameter was underestimated by the numerical prediction. The cause is believed to be associated to the tank opening dynamics, as it was observed that half

opening of the tank can significantly affect enlargement of the fireball on horizontal direction. The same CFD approach with inclusion of detailed chemical mechanism in the turbulent flow well reproduced the experimental test on rupture of a 35 MPa vessel (Molkov et al., 2018). Therefore, it is concluded that the CFD model can be applied as a contemporary tool for hydrogen safety engineering to assess the hazards from tank rupture in a fire for several storage volumes and pressures. An example of the CFD model application can be the calculation of separation distances for stationary storage systems in refuelling stations.

The research fulfilled the appointed objectives. However, new questions arose during the study, and they can be used to propose a roadmap for **future works**:

- During the study on cryogenic jet fires, the Abel Noble EOS was found to be applicable to cryogenic releases for pressure below 6 bar. Therefore, it would be desirable to conduct further research to extend the range of applicability of the CFD model and notional nozzle theory to higher release pressure.
- The methodology defined for calculation of MIE was here applied only to a stoichiometric hydrogen-air mixture. However, it would be interesting to extend the use of the model to a different composition of the mixture and to analysis of experimental settings effect into determination of MIE.
- Further development of the multi-phenomena deflagration model to enhance overpressure predictive capability and thoroughly validation against multiple experiments.
- It was concluded that the fireball dynamics deriving from rupture of the tank in a fire may be affected by a selection of experimental settings and conditions. Thus, further numerical studies should be conducted to investigate relevant factors and configurations, such as the effect of various tank opening dynamics and bonfire size on the fireball dimensions.

# References

Adolf, J., Balzer, C., Louis, J., Schabla, U., Fischedick, M., Arnold, K., Pastowski, A., Schüwer, D. (2017), Shell Hydrogen study: Energy of the future?, Shell Deutschland Oil GmbH, Hamburg

Aleksandrov, A.O., Alekseev, V. I., Chernenko, E.V., Efimenko, A.A., Gavrikov, A.I., Mayorov, A.S., Matsukov, I.D., Schepetov, N.G., Velmakin, S.M., Zaretskiy, N.P. (2009), Experimental study of hydrogen releases combustion, *3rd International Conference on Hydrogen Safety*, Ajaccio, France Sept. 16-18

ANSYS Fluent (2016), User's guide

ANSYS Fluent (2016), Theory guide

ANSYS Fluent (2016), Service request communication

Astbury, G.R. and Hawksworth, S.J. (2007), Spontaneous ignition of hydrogen leaks: A review of postulated mechanisms, *International Journal of Hydrogen Energy* 32, 2178-2185

Babrauskas, V. (2003), *Ignition handbook*, Society of Fire Protection Engineers, Fire Science Publishers, Issaquah WA, USA

Baker, W.E., Cox, P.A., Westine, P.S., Kulesz, J.J., Strehlow, R.A. (1983), Explosion hazards and evaluation, Elsevier Scientific Publishing Company

Baker, W.E., Kulesz, J. J., Ricker, R. E., Bessey, R. L., Westine, P.S., Parr, V. B., et al., (1975), Workbook for predicting pressure wave and fragment effects of exploding propellant tanks and gas storage vessels, Technical Report NASA-CR-134906

Baraldi, D., Molkov, V., Makarov, D., Keenan, J., Shentsov, V., Brennan, S., Slater, S., Coldrick, S., Jedicke, O., Ren, K., Kotchourko, A., Tolias, I., Giannissi, S., Venetsanos, A.,Verbecke, F., Duclos, A. (2017), *The CFD Model Evaluation Protocol*, SUSANA Pro.

Barlow, R.S. and Carter, C.D. (1996), Relationship among nitric oxide, temperature and mixture fraction in hydrogen jet flames, *Combustion and Flame* 104, 288-299

Barry, T.S. (2002), *Risk-informed, performance-based industrial fire protection*, Tennessee Valley Publishing, chapter 5: Exposure profile modelling, 1-37

Barthélémy, H. (2011), Gas cylinders and pressure vessels for hydrogen storage and transport, *International Sustainable Energy Storage Conference*, Belfast

Bentaib, A., Bleyer, A., Meynet, N., Chaumeix, N., Schramm, B., Hohne, M., et al. (2014), SARNET hydrogen deflagration benchmarks: main outcomes and conclusions, *Ann Nucl Energy* 2014;74:143e52.

Birch, A.D., Brown, D.R., Dodson, M.G., Swaffield, F. (1984), The structure and Concentration Decay of High Pressure Jets of Natural Gas, *Combustion Science and Technology* 36 (5-6), 249-261

Birch, A.D., Hughes, D.J., Swaffield, F. (1987), Velocity Decay of High Pressure Jets, *Combustion Science and Technology* 52 (1-3), 161-171

Boyer, D.W. (1960), An experimental study of the explosion generated by a pressurised sphere, *Fluid Mechanics* 26(9), 401-429

Bragin, M.V., Makarov, D.V., Molkov, V.V. (2013), Pressure limit of hydrogen spontaneous ignition in a T-shaped channel, *International Journal of Hydrogen Energy*, Volume 38, Issue 19, 8039-8052

Brasie, W.C. and Simpson, D.W. (1968), Guidelines for estimating damage explosion, *Loss Prevention* 2, 91

Bray, K. N. C. (1990), Studies of the turbulent burning velocity, *Proceedings of the Royal Society of London*, Series A, 43, 315-335

Brennan, S.L., Makarov, D.V., Molkov, V. (2009), LES of high pressure hydrogen jet fire, *Journal of Loss Prevention in the Process Industries* 22, 353-359

Brode, H.L. (1959), Blast waves from a spherical charge, *Phys Fluids* 2, 217-29

Calcote, H.R., Gregory, Jr. C.A., Barnett, C.M., Gilmer, R.B. (1952), Spark ignition. Effect of molecular structure, *Ind. Eng. Chem.* 44, 2656.

Cantera (2018), Open-source suite of tools for problems involving chemical kinetics, thermodynamics, and transport processes, available at: www.cantera.org/

Chen, C. and Rodi, W. (1980), *Vertical turbulent buoyant jets – a review of experimental data*, Pergamon Press, Oxford. ISBN 0-08-024772-5

Chuech, S.G., Lai, M.C., Faeth, G. M. (1989), Structure of turbulent sonic underexpanded free jets, *AIAA J.*, vol. 27, no. 5, 549–559

Chui, E.H. and Raithby, G.D. (1993), Computation of radiant heat transfer on a nonorthogonal mesh using the finite-volume method, *Numerical heat transfer*. Part B, Fundamentals 23, 269-288

Cirrone, D, Makarov, D., Molkov, V. (2017a), Thermal radiation from cryogenic hydrogen jet fires, *International Conference on Hydrogen Safety*, Hamburg, Germany Sept. 11-13

Cirrone, D, Makarov, D., Molkov, V. (2017b), Simulation of thermal radiation from hydrogen under-expanded jet fire, *International Conference on Hydrogen Safety*, Hamburg, Germany Sept. 11-13

Coppalle, A. and Vervisch, P. (1983), The total emissivities of high-temperature flames, *Combustion and Flame* 49, 101-108

Coward, H.F. and Jones, G.W. (1952), Limits of flammability of gases and vapors, United States Department of interior, *Bureau of Mines Bullettin* 503

Crowl, D.A. (2003), *Understanding explosions*, American Institute of Chemical Explosions

Cumber, P.S., Fairweather, M., Falle, S.A.E.G., Giddings, J.R. (1995), Predictions of the structure of turbulent, highly underexpanded jets, *Journal Fluids Engineering* 117 (4), 599-604

Current Results (2016), Current Results weather and science facts, California average relative humidity, available at: www.currentresults.com/Weather/California/humidity-annual.php.

Dadashzadeh, M., Kashkarov, S., Makarov, D., Molkov, V. (2018), Risk assessment methodology for onboard hydrogen storage, *International Journal of Hydrogen Energy*, Volume 43, Issue 12, 6462-6475

Daubech, J., Hebrard, J., Jallais, S., Vyazmina, E., Jamois, D., Verbecke, F. (2015), Un-ignited and ignited high pressure hydrogen releases: Concentration – turbulence mapping and overpressure effects, *Journal of Loss Prevention in the Process Industries*, Volume 36, 439-446

Delichatsios, M.A. (1993), Transition from momentum to buoyancy-controlled turbulent jet diffusion flames and flame height relationships, *Combustion and Flame*, Volume 92, Issue 4, 349-364

DOE (2006), Technical Assessment: Cryo-Compressed Hydrogen Storage for Vehicular Applications.

Dorofeev, S.B., Sidorov, V.P., Efimenko, A.A., Kochurko, A.S., Kuznetwsov, M.S., Chaivanov, B.B., Matsukov, D. I., Pereverzev, A.K., Avenyan, V.A. (1995), Fireballs from deflagration and detonation of heterogeneous fuel-rich clouds, *Fire Safety Journal* 25, 323-336

Dorofeev, S.B., Sidorov, V.P., Kuznetsov, M.S., Dvoinishnikov, A.E., Alekseev, V. I., Efimenko, A.A (1996), Air blast and heat radiation from fuel-rich mixture detonations, *Shock Waves* 6, 21-28

Drysdale, D. (2011), *An introduction to fire dynamics*, 3rd ed., John Wiley and Sons

Ekoto, I.W., Ruggles, A.J., Creitz, L.W., Li, J. X. (2014), Updated jet flame radiation modelling with buoyancy corrections, *International Journal of Hydrogen Energy* 39, 20570-20577

Engineering Toolbox (2016), Resources, Tools and Basic Information for Engineering and Design of Technical Applications, availableat: https://www.engineeringtoolbox.com

Felske, J.D. and Tien, C.L. (1973), Calculation of the emissivity of luminous flames, *Combustion Science and Technology* 7, 25-31

Fiveland, W.A. and Jamaluddin, A.S. (1991), Three-dimensional spectral radiative heat transfer solutions by the discrete-ordinates method, *Journal of Thermophysics* 5: 335-339

Flesch, T.K. (2002), Turbulent Schmidt number from a tracer experiment, *Agricultural and Forest Meteorology* 111, 299-307

Frank, J.H., Barlow, R.S., Lundquist, C. (2000), Radiation and nitric oxide formation in turbulent non-premixed jet flames, *Proceedings of the Combustion Institute* 28, 447-454

Frendi, A. and Sibulkin, M. (1990), Dependence of minimum ignition energy on ignition parameters, *Combust. Sci. and Tech.*, Vol. 73, 395-413

Friedrich, A., Breitung, W., Stern, G., Veser, A., Kuznetsov, M., Fast, G., Oechsler, B., Kotchourko, N., Jordan, T., Travis, J. R., Xiao, J., Schwall, M., Rottenecker, M. (2012), Ignition and heat radiation of cryogenic hydrogen jets, *Int. J. Hydrogen Energy*, vol. 37, no. 22, 17589–17598

Geng, J., Baker, Q., Thomas, K. (2011), Pressure vessel burst directional effects, *Proceedings of the ASME 2011 Pressure Vessels & Piping Division conference*, July 17-21, Maryland, USA

Giannissi, S.G., and Venetsanos, A.G. (2018), "Study of key parameters in modeling liquid hydrogen release and dispersion in open environment," *International Journal of Hydrogen Energy*, 43(1), pp. 455-467

Gore, J. P., Jeng, S.M., Faeth, G. M. (1987), Spectral and total radiation properties of turbulent hydrogen/air diffusion flames, Transactions of ASME. *Journal of Heat Transfer* 109, 165-171

Grune, J., Sempert, K., Kuznetsov, M., Jordan, T. (2014), Experimental study of ignited unsteady hydrogen releases from a high pressure reservoir, *International Journal of Hydrogen Energy* 39, 6176-6183

GTR (2013), Global Technical Regulation on hydrogen and fuel cell vehicles, ECE/TRANS/180/Add.13

Hall, J.E., Hooker, P., Willoughby, D. (2014), Ignited releases of liquid hydrogen: Safety considerations of thermal and overpressure effects, *Int. J. Hydrogen Energy*, vol. 39, no. 35, 20547–20553.

Han, J., Yamashita, H., Hayashi, N. (2011), Numerical study on the spark ignition characteristics of hydrogen–air mixture using detailed chemical kinetics, *International Journal of Hydrogen Energy*, Volume 36, Issue 15

Hardee, H.C. and Lee, D.O. (1973), Thermal hazard from propane fireballs, *Transportation Planning and Technology*, 2:2, 121-128, DOI: 10.1080/03081067308717067

Hardee, H.C., Lee, D.O., Benedick, W.B. (1978), Thermal hazard from LNG fireballs, *Combustion Science and Technology*, 17: 5, 189-197

Hasegawa, K. and Sato, K. (1978), Study on the fireball following steam explosion of n-pentane, *Loss Prevention and Safety Promotion in the Process Industries: Procs 2nd International Symposium* 1977, Frankfurt: Dechema 1978, 297-304

Hawthorne, W.R., Weddell, D.S., Hottel, H.C. (1949), Mixing and combustion in turbulent gas jets, *Third International Symposium on Combustion, Flame and Explosion Phenomena*, 266-88, Baltimore, USA

He, G., Andrew, Y.G., Hsu, T. (1999), The effect of Schmidt number on turbulent scalar mixing in a jet-in-crossflow, *International Journal of Heat and Mass Transfer* 42, 3727-3738

Hottel, H. and Hawthorne, W.R. (1949), Diffusion in laminar flame jets, *Third International Symposium on Combustion, Flame and Explosion Phenomena*, 254-266, Baltimore, USA

Hottel, H. and Sarofim, A. (1967), *Radiative transfer*, McGraw-Hill, New York

Hottel, H.C., Sarofim, A.F., Farag, I.H. (1974), Chapter VI: Heat transfer from nonluminous flames in furnaces, in: Howard, B.P., Beer, J.M., *Combustion technology: some modern developments*, Academic Press, 163-187

Houf, W. and Schefer, R. (2007), Predicting radiative heat fluxes and flammability envelopes from unintended releases of hydrogen, *International Journal of Hydrogen Energy* 32, 136-151

Houf, W.G., Evans, G.H., Schefer, R.W. (2009), Analysis of jet flames and unignited jets from unintended releases of hydrogen, *International Journal of Hydrogen Energy* 34, 5961-5969

Houf, W.G., Evans, G.H., Schefer, R.W., Merilo, E., Groethe, M. (2011), A study of barrier walls for mitigation of unintended releases of hydrogen, *International Journal of Hydrogen Energy* 36, 2520-2529

Hourri, A., Angers, B. and Bénard, P. (2009), Surface effects on flammable extent of hydrogen and methane jets, *International Journal of Hydrogen Energy* 34(3), 1569-1577

Hourri, A., Angers, B., Bénard, P., Tchouvelev, A. and Agranat, V. (2011), Numerical investigation of the flammable extent of semi-confined hydrogen and methane jets, *International Journal of Hydrogen Energy* 36 (3), 2567-2572

Howell, J.R., Mengüc, M.P., Siegel, R. (2016), *Thermal radiation heat transfer,* Taylor and Francis Group, 6th edition

h2safe.net: available at: http://h2safe.net/case_safety.html [last access: 29.05.2016]

Hubbard, G. L. and Tien, C. L. (1978), Infrared mean absorption coefficients of luminous flames and smoke, Transactions of the ASME, *Journal of Heat Transfer* 100, 235-239

HySafe (2007), *Biennal Report on Hydrogen Safety, Chapter III: accidental phenomena and consequences,* available at: http://www.hysafe.org [last access: 12.05.2018]

Ichard, M., Hansen, O.R., Middha, P., Willoughby, D. (2012), CFD computations of liquid hydrogen releases, *Int. J. Hydrogen Energy*, vol. 37, no. 22, 17380–17389

Ilbas, M. (2005), The effect of thermal radiation and radiation models on hydrogen-hydrocarbon combustion modelling, *International Journal of Hydrogen Energy* 30, 1113-1126

Imamura, T., Hamada, S., Mogi, T., Wada, Y., Horiguchi, S., Miyake, A., Ogawa, T. (2008), Experimental investigation on the thermal properties of hydrogen jet flame and hot currents in the downstream region, *International Journal of Hydrogen Energy* 33, 3426-3435

Ishii, R., Fujimoto, H., Hatta, N., Umeda, Y. (1999), Experimental and numerical analysis of circular pulse jets, *J. Fluid Mech*, vol. 392, 129-153

ISO (2004), Basic considerations for the safety of hydrogen systems, ISO/TR 15916:2004

ISO (2009), Gaseous hydrogen and hydrogen blends - Land vehicle fuel tanks, ISO/TS 15869:2009, reviewed and confirmed in 2016

Jang, C. B., Choi, S-W., Baek, J-B. (2015), CFD modelling and fire damage analysis of jet fire on hydrogen pipeline in a pipe rack structure, *International Journal of Hydrogen Energy* 40, 15760-15772

Karlovitz, B., Denniston, D.W. Jr., Wells, F.E. (1951), Investigation of turbulent flames. *The Journal of Chemical Physics*, 19(5), 541-547

Kessler, A., Schreiber, A., Wassmer, C., Deimling, L., Knapp, S., Weiser, V., Sachsenheimer, K., Langer, G., Eisenreich, N. (2014), Ignition of hydrogen jet fires from high pressure storage, *Int. J. Hydrogen Energy*, vol. 39, no. 35, 20554–20559

Khaksarfard, R. and Paraschivoiu, M. (2012), Numerical simulation of high pressure hydrogen release through an expanding opening, *International Journal of Hydrogen Energy* 37(10), 8734-8743

Kim, W., Shentsov, V., Makarov, D., Molkov, V. (2015), High pressure hydrogen tank rupture: blast wave and fireball, *International Conference on Hydrogen Safety*, Yokohama

Kim, W. (2017), Private communication, Hiroshima University, Japan

Kuchta, J. M. (1985), Investigation of Fire and Explosion Accidents in the Chemical, Mining, and Fuel-Related Industries A Manual, U.S. Bureau of Mines Bulletin 680.

Kumamoto, A., Iseki, H., Ono, R., Oda, T. (2011), Measurement of minimum ignition energy in hydrogen-oxygen-nitrogen premixed gas by spark discharge, *Journal of Physics: Conference Series*, 301 (2011) 012039

Kunze, K. and Kircher, O. (2012), Cryo-compressed hydrogen storage, *Cryogenic Cluster Day*, Oxford, September 28

LaChance, J. L. (2010), Progress in risk assessment methodologies for emerging hydrogen applications. Presented at the *Sixth International Short Course and Advanced Research Workshop "Progress in Hydrogen Safety – Regulations, codes and standards",* 25-29 January 2010, Belfast, Northern Ireland, UK.

LaChance, L., Tchouvelev, A., Engebo, A. (2011), Development of uniform harm criteria for use in quantitative risk analysis of the hydrogen infrastructures, *International Journal of Hydrogen Energy* 36, 2381-2388

Lamoureux., N., Djebaili-Chaumeix, N., Paillard, C.E. (2002), Laminar flame velocity determination for H2-air-stream mixtures using the spherical bomb method, *J. Phys.* IV France, 12, Pr7-445-Pr7-458

Launder, B.E. and Spalding, D.B. (1972), *Lectures in Mathematical Models of Turbulence*. London, England: Academic Press

Leckner, B. (1972), Spectral and total emissivity of water vapor and carbon dioxide, *Combustion and Flame 19*, 33-48

Lees, F.P. (1996), *Loss Prevention in the Process Industries* (2nd Edition), Elsevier

Lewis, B. and Elbe, G. von (1961), *Combustion, flames and explosions of gases*, 2nd edition, Academic Press, Florida and London.

Li, Z. Y., Makarov, D., Keenan, D., Molkov, V. (2015), CFD study of the unignited and ignited hydrogen releases from TPRD under a fuel cell car, *International Conference on Hydrogen Safety*, Yokohama, vol. 131

Lilly, D.K. (1992), A Proposed Modification of the Germano Subgrid-Scale Closure Model, Physics of Fluids 4:633-635

Gerboni, R., Salvador, E. (2009), Hydrogen transportation systems: elements of risk analysis, *Energy* 34: 2223-2229

Giannissi, S. G., Venetsanos, A. G., Markatos, N., Bartzis, J. G. (2014), CFD modeling of hydrogen dispersion under cryogenic release conditions, *Int. J. Hydrogen Energy*, vol. 39, no. 28, 15851–15863

Magnussen, B. (1981), On the structure of turbulence and a generalized eddy dissipation concept for chemical reaction in turbulent flow, *Am. Inst. Aeronaut. Astronaut.*

Major Hazards Assessment Panel (1994), "*Explosions in the process industries, A report of the Major Hazards Assessment Panel overpressure working party*, Institution of Chemical Engineers, Warwickshire, 28-29

Makarov, D. and Molkov, V. (2013), Plane hydrogen jets, *International Journal of Hydrogen Energy*, Volume 38, Issue 19, 8068-8083,

McAdams, W. H. (1964), *Heat transmission*, McGraw-Hill, New York

Medtherm corporation (2016), Heat flux transducers and infrared radiometers for the direct measurements of heat transfer rates, available at: *http://www.dr-kubelik.de* [last access: 06.05.2018]

Mikron instrument company Inc (2016), Table of emissivity for various surfaces, available at: http://www-eng.lbl.gov/~dw/projects/DW4229_LHC_detector_analysis/calculations/emissivity2.pdf [last access: 06.05.2018]

Modak, A.T. (1979), Radiation from products of combustion, *Fire Research* 6, 339-361

Modest, M.F. (2003), *Radiative heat transfer*. 2nd ed. Academic Press.

Mogi, T. and Horiguchi, S. (2009), Experimental study on the hazards of high-pressure hydrogen jet diffusion flames, *Journal of Loss Prevention in the Process Industries* 22, 45-51

Molina, A., Schefer, R.W. and Houf, W.G. (2007), Radiative fraction and optical thickness in large-scale hydrogen-jet fires, *Proceedings of the Combustion Institute* 31, 2565-2572

Molkov, V.V., Makarov, D.V., Bragin, M.V. (2009), Physics and modelling of under-expanded jets and hydrogen dispersion in atmosphere, *Physics of extreme states of matter*

Molkov, V. and Saffers, J. (2011) The Correlation for Non-Premixed Hydrogen Jet Flame Length in Still Air, *Fire Safety Science* 10, 933–943

Molkov, V. (2012) *Fundamentals of Hydrogen Safety Engineering*, bookboon.com, free download online book

Molkov, V., Shentsov, V., Brennan, S., Makarov, D. (2014), Hydrogen non-premixed combustion in enclosure with one vent and sustained release: Numerical experiments, *Int. J. Hydrogen Energy*, vol. 39, no. 20, 10788–10801

Molkov, V. and Shentsov, V. (2014), Numerical and physical requirements to simulation of gas release and dispersion in an enclosure with one vent, *Int. J. Hydrogen Energy*, vol. 39, no. 25, 13328–13345

Molkov, V. and Bragin, M. (2015), Hydrogen–air deflagrations: Vent sizing correlation for low-strength equipment and buildings, *International Journal of Hydrogen Energy*, Volume 40, Issue 2, 1256-1266

Molkov, V. and Kashkarov, S. (2015), Blast wave from a high-pressure gas tank rupture in a fire: stand-alone and under-vehicle hydrogen tanks, *International Journal of Hydrogen Energy* 40, 12581-12603

Molkov, V., Cirrone, D.M.C., Shentsov, V., Dery, W., Makarov, D. (2018), Blast wave and fireball after hydrogen tank rupture in a fire, *11th International Colloquium on Pulsed and Continuous Detonations (ICPCD),* September 17-21, St. Petersburg, Russia

Moonis, M., Wilday, A. J., Wardman, M.J. (2010), Semi-quantitative risk assessment of commercial scale supply chain of hydrogen fuel and implications for industry and society, *Process Safety and Environmental Protection* 88, 97-108

Murthy, J. Y. and Mathur, S. R. (1998), A finite volume method for radiative heat transfer using unstructured meshes, *J. Quant. Spectrosc. Radiat. Transf.*, vol. 12, no. 12, 313–321

Muthusamy, D., Hansen, O. R., Middha, P., Royle, M., Willoughby, D. (2011), Modelling of hydrogen jet fires using CFD, *International Conference on Hydrogen Safety*, San Francisco 2011

NASA (2016), Earth fact sheet, available at:
https://nssdc.gsfc.nasa.gov/planetary/factsheet/earthfact [last access: 06.06.2016]

NIST EOS calculator, available at: http://hydrogen.pnl.gov/tools/equation-state-calculator

North, G.L. and Santavicca D.A. (1990), The fractal nature of premixed turbulent flames, *Combustion Science and Technology*, vol. 72, 215-232

Omega (2016), Emissivity of common materials, available at:
www.omega.com/literature/transactions/volume1/emissivitya.html

Ono, R., Nifuku, M., Fujiwara, S., Horiguchi, S., Oda, T. (2007), Minimum ignition energy of hydrogen–air mixture: Effects of humidity and spark duration, *Journal of Electrostatics* 65 (2007), 87–93

Owston, R. and Abraham, J. (2009), Flame propagation in stratified hydrogen–air mixtures: Spark placement effects, *International Journal of Hydrogen Energy*, Volume 34, Issue 15

Panda, P.P. (2016), Private communication, Sandia National Laboratories

Panda, P. P. and Hecht, E. S. (2016), Ignition and flame characteristics of cryogenic hydrogen releases, *Int. J. Hydrogen Energy*, vol. 42, no. 1, 775–785.

Papanikolau, E., Baraldi, D., Kuznetsov, M., Venetsanos, A. (2012), Evaluation of notional nozzle approaches for CFD simulations of free-shear under-expanded hydrogen jets, *International Journal of Hydrogen Energy* 37, 18563-18574

Peng, D.Y. and Robinson, D.B. (1976), A New Two-Constant Equation of State, *Industrial and Engineering Chemistry: Fundamentals*, 15, 59–64

Peters, N. and Rogg, B. (1993), *Reduced kinetic mechanisms for applications in combustion systems*, Berlin

Pittman, J.F. (1972), Blast and fragment hazards from bursting high pressure tanks, Rep. NOLTR 72-102, Naval Ordnance Lab., White Oak, Silver Spring, MD

Pittman, J.F. (1976), Blast and fragments from superpressure vessel rupture, Rep. NSWC/WOL/TR 75-87, Naval Surface Weapons Center, White Oak, Silver Spring, MD

Pope, S. B. (1978), An explanation of the turbulent round-jet/plane-jet anomaly, *AIAA Journal* 16, 279-281

Pratt, T. H. (2000), *Electrostatic ignitions of fires and explosions*, Center for Chemical Process Safety of the American Institute of Chemical Engineer: 3 Park Avenue, New York, NY 10016-599

Proust, C., Jamois, D., Studer, E. (2011), High pressure hydrogen fires, *International Journal of Hydrogen* Energy 36, 2367-2373.

Proust, C. (2016), Private communication, INERIS

Ramachandran, R. and Menon, R.K. (1998), An overview of industrial uses of hydrogen, *International Journal of Hydrogen Energy* 23, 593-598

Rawls, G. B., Adams, T., Newhouse, N.L. (2012), *Gaseous Hydrogen Embrittlement of Materials in Energy Technologies: The Problem, its Characterisation and Effects on Particular Alloy Classes*, Chapter 1: Hydrogen Production and containment, 3–50

Reddy, D. V., Sobhan, K. , Liu, L., Young, J. D. (2015), Size effect on fire resistance of structural concrete, *Eng. Struct.*, vol. 99, 468–478

Redlich, O. and Kwong, J. N. S. (1949), On the Thermodynamics of Solutions. An Equation of State. Fugacities of Gaseous Solutions, *Chem. Rev.* 44, 233

Reynolds, O. (1883), An experimental investigation of the circumstances which determine whether the motion of water shall be direct or sinuous, and of the law of resistance in parallel channels. *Proc Royal Soc* London, 35(224e226):84e99.

Roberts, A. F. (1981), Thermal radiation hazards from releases of LPG from pressurised storage, *Buxton: Health and Safety Executive Research and Laboratory Services Division*

Rohsenow, W. M., Hartnett, J. P., Cho, Y. I. (1998), *Handbook of heat transfer*, 3rd edition, McGraw-Hill

Rose, H. E. and Priede, T. (1958), Ignition phenomena in hydrogen-air mixtures, *Symposium (International) on Combustion*, Volume 7, Issue 1, 436-445

Roth, W., Guest, P. G., von Elbe, G., Lewis, B. (1951), Heat generation by electric sparks and rate of heat loss to the spark electrodes, *The Journal of Chemical Physics*, Volume 19, Issue 12, 1530-1535

Royle, M. and Willoughby, D.B. (2009), The interaction of hydrogen jet releases with walls and barriers, *3rd International Conference on Hydrogen Safety*, Ajaccio

Royle, M. and Willoughby, D.B. (2011a), Consequences of catastrophic releases of ignited and unignited hydrogen jet releases, *International Journal of Hydrogen Energy* 36, 2688-2692

Royle, M. and Willoughby, D.B. (2011b), The interaction of hydrogen jet releases with walls and barriers, *International Journal of Hydrogen Energy* 36, 2455-2461

Schefer, R.W., Houf, W.G., Bourne, B., Colton, J. (2004), Experimental Measurements to Characterize the Thermal and Radiation Properties of an Open-flame Hydrogen Plume, in *In Proceedings of the 15th annual hydrogen conference and hydrogen expo*

Schefer, R.W., Houf, W.G., Bourne, B., Colton, J. (2006), Spatial and radiative properties of an open-flame hydrogen plume, *International Journal of Hydrogen Energy* 31, 1332-1340

Schefer, R.W., Houf, W.G., Williams, T.C., Bourne, B., Colton J. (2007), Characterization of high-pressure, underexpanded hydrogen-jet flames, *International Journal of Hydrogen Energy* 32, 2081-2093

Schefer, R.W., Merilo, E.G., Groethe, M.A., Houf, W.G. (2011), Experimental investigation of hydrogen jet fire mitigation by barrier walls, *International Journal of Hydrogen Energy* 36, 2530-2537

SFPE (2002), *SFPE Handbook of Fire Protection Engineering*, Society of Fire Protection Engineers, National Fire Protection Association, 3rd edition

Shentsov, V., Kim, W., Makarov, D., Molkov, V. (2015), Numerical simulations of experimental fireball and blast waves from a high-pressure tank rupture in a fire, *Proceedings of the Eighth International Seminar on Fire & Explosion Hazards (ISFEH8)*

Shenstov, V., Cirrone D.M.C., Makarov, D., and Molkov, V. (2016), "Simulation of fireball and blast wave from a hydrogen tank rupture in a fire", *7th International Symposium on Non-equilibrium Processes, Plasma, Combustion, and Atmospheric Phenomena,* October, Sochi, Russia

Shenstov, V. (2017), Private communication, HySAFER, Ulster University, United Kingdom

Shih, T. H., Liou, W. W., Shabbir, A. , Yang, Z., Zhu, J. (1995), A new eddy-viscosity model for high Reynolds number turbulent flows—model development and validation, *Comput. Fluids*, vol. 24, no. 3, 227–238

Shirvill, L.C., Royle, M., Roberts., T.A. (2007), Hydrogen releases ignited in a simulated vehicle refuelling environment, *International Conference on Hydrogen Safety*, San Sebastian, Spain, 11-13 September

Sivathanu, Y. R. and Gore, J. P. (1993), Total radiative heat loss in jet flames from single point radiative flux measurements, *Combustion and Flame* 94, 265-270

Smagorinsky, J (1963), General Circulation Experiments with the Primitive Equations. I. The Basic Experiment., Month. Wea. Rev., 91, 99-164

Smith, T.F., Shen, Z.F., Friedman, J. N. (1982), Evaluation of coefficients for the weighted sum of gray gases model, *Journal of Heat Transfer* 104, 602-608

Smith, T.A. and Warwick, R.G. (1983), A survey of defects in pressure vessels in the UK for the period 1962–1978 and its relevance to nuclear primary circuits, *International Journal of Pressure Vessels and Piping*, Volume 11, Issue 3, 127-166

Spalding, D.N. (1971), Concentration fluctuations in a round turbulent free jet, *Journal of Chemical Engineering Science* 26, 95-107

Sparrow, E.M. and Cess, R.D. (1978), *Radiation heat transfer*, McGraw-Hill.

Soufiani, A. and Taine, J. (1997), High temperature gas radiative property parameters of statistical narrow-band model for $H_2O$, $CO_2$ and CO, and correlated-K model for $H_2O$ and $CO_2$, *International Journal of Heat Mass Transfer* 40, 987-991

Studer, E., Jamois, D., Jallais, S., Leroy, G., Hebrard, J., Blanchetière, V. (2009), Properties of large-scale methane/hydrogen jet fires, *International Journal of Hydrogen Energy* 34: 9611-9619

Studer, E. (2016), Private communication, CEA

Taira, Y., Saburi, T., Kubota, S., Sugiyama, Y., Matsuo, A. (2015), Numerical investigation of hydrogen leakage from a high pressure tank and its explosion, *International Conference on Hydrogen Safety*, Yokohama

Takeno, K., Okabayashi, K., Kouchi, A. Nonaka, T., Hashiguchi, K., Chitose, K. (2007), Dispersion and explosion field tests for 40MPa pressurized hydrogen, International Journal of Hydrogen Energy, Volume 32, Issue 13, 2144-2153

Taylor, P. B. and Foster, P. J. (1974), The total emissivities of luminous and non-luminous flames, *International Journal of Heat and Mass Transfer* 17, 1591-1605

Terao, K. (2007), Irreversible Phenomena: Ignitions, Combustion and Detonation Waves, Springer Berlin Heidelberg New York

Thermopedia (2016), Blackbody, available at http://www.thermopedia.com/content/66/ [last access 14.04.2016]

Thiele, M., Warnatz, J., Dreizler, A., Lindenmaier, S., Schießl, R., Maas, U., Grant, A., Ewart, P. (2002), Spark ignited hydrogen/air mixtures: two dimensional detailed modeling and laser based diagnostics, *Combustion and Flame* 128, 74–87

Tien, C. L. (1969), Thermal radiation properties of gases, *Advances in Heat Transfer* 5, 253-324

Tien, C. L., Lee, K. Y. Stretton, A. J. (2002), Radiation heat transfer, in: *SFPE Fire Protection Handbook*, 3rd edition

Tominaga, Y. and Stathopoulos, T. (2007), Turbulent Schmidt numbers for CFD analysis with various types of flowfield, *Atmos. Environ.*, vol. 41, no. 37, 8091–8099

Turns, S.R. and Myhr, F.H. (1991) Oxides of nitrogen emissions from turbulent jet flames: Part I -Fuel Effects and Flame Radiation, *Combustion and Flame* 87, 319–335

UN Safer Guard (2018), Kingery-Bulmash blast parameter calculator, available at https://www.un.org/disarmament/un-saferguard/kingery-bulmash/ [last access: 28.03.18]

Venetsanos, A. and Bartzis, J. (2007), CFD modeling of large-scale LH2 spills in open environment, *Int. J. Hydrogen Energy*, vol. 32, no. 13, 2171–2177

Venetsanos, A. G. and Giannissi, S. G. (2016), Release and dispersion modeling of cryogenic under-expanded hydrogen jets, *Int. J. Hydrogen Energy*, 1–11

Verbecke, F., Molkov, V. and Makarov, D. (2009), VLES of lean hydrogen-air deflagrations in a closed vessel 5.7 m high, *International Conference on Hydrogen Safety*, Ajaccio 2009

Viskanta, R. and Mengüc, M. P. (1987), Radiation heat transfer in combustion systems, *Progress in Energy and Combustion Science* 13, 97-160

Wang, C.J., Wen, J.X., Chen, Z.B., Dembele, S. (2014), Predicting radiative characteristics of hydrogen and hydrogen/methane jet fires using FireFOAM, *International Journal of Hydrogen Energy* 39: 20560-20569

Wen, J. X., Huang, L. Y. (2000), CFD modelling of confined jet fires under ventilation-controlled conditions, *Fire Safety Journal* 34, 1-24

Weyandt, N. (2005), Analysis of induced catastrophic failure of a 5000 psig type IV hydrogen cylinder, Southwest Research Institute Report 01.0639.01.001

Weyandt, N. (2006), Catastrophic failure of a 5000-psig hydrogen cylinder installed on a typical SUV, Southwest Research Institute Report 01.06939.01.005

Willoughby, D.B. (2015), Private communication, Health and Safety Laboratory

www.fuelcells.org [last access: 16.11.2015]

www.hyfive.eu [last access: 29.05.2016]

www.HyIndoor.eu [last access: 29.05.2016]

Xiao, J., Travis, J. R., Kuznetsov, M. (2015), Numerical investigations of heat losses to confinement structures from hydrogen-air turbulent flames in ENACCEF facility, *International Journal of Hydrogen* Energy 40, 13106-13120

Xu, B.P., Zhang, J.P., Wen, J.X., Dembele, S., Karwatzki, J. (2005), Numerical study of a highly under-expanded hydrogen jet, *International Conference on Hydrogen Safety*

Yakhot, V. and Orszag, S. A. (1986), Renormalization Group Analysis of Turbulence, *J. Sci. Comput.*, vol. 1, no. 1, 1–51

Yakhot, V. (1988), Prepagation velocity of premixed turbulent flames, *Comb. Sci. Tech*., 60, 191

Yan, L., Guangxi, Y., He, B. (2015), Development of an absorption coefficient calculation method potential for combustion and gasification simulations, *International Journal of Heat and Mass Transfer* 91, 1069-1077

Yeoh, G. H. and Yuen, K. K. (2009), *Computational fluid dynamics in fire engineering*, Butterworth-Heinemann, 1st Edition

Yuasa, T., Kadota, S., Tsue, M., Kono, M., Nomura, H., Ujiie, Y. (2002), Effects of energy deposition schedule on minimum ignition energy in spark ignition of methane/air mixtures, *Proceedings of the Combustion Institute*, Volume 29, Issue 1, 743-750

Zabetakis, M. G. and Burgess, D.S. (1961), Research on the hazards associated with the production and handling of liquid hydrogen, *United States Department of the Interior Bureau of* Mines, Report of Investigations 5707

Zalosh, R. (2007), Blast waves and fireball generated by hydrogen fuel tank rupture during fire exposure, *Proceedings of the 5$^{th}$ International Seminar on Fire and Explosion Hazards*, Edinburgh UK

Zalosh, R. (2008), CNG and Hydrogen vehicle fuel tank failure incidents, testing and preventive measures, Firexplo, Wellesley, MA

Zbikowski, M. (2010), Hydrogen deflagration-to-detonation transition and its mitigation technologies, *PhD Thesis*

Zheng, J., Bie, H., Xu, P., Liu, P., Zhao, Y., Chen, H., Liu, X., Zhao, L. (2012), Numerical simulation of high-pressure hydrogen jet flames during bonfire test, *International Journal of Hydrogen Energy* 37: 783-790

Zhiyong, L., Xiangmin, P., Jianxin, M. (2010), Harm effect distances evaluation of severe accidents for gaseous hydrogen refuelling station, *International Journal of Hydrogen Energy* 35, 1515-152

Zimont, V.L. and Lipatnikov, A.N. (1995), A numerical model of premixed turbulent combustion of gases, Chem. Phys. Reports, Vol. 14(7), 993-1025